UNIVERSITY OF MODENA AND REGGIO EMILIA

PHYSICS AND NANOSCIENCES – SCHOOL OF GRADUATE STUDIES

DOCTORAL THESIS

# *Charge transport through chiral systems*

*Author*
Andrea STEFANI

*Supervisor*
Claudio FONTANESI

A thesis submitted in fulfilment of the requirements for the degree of

*Doctor of Philosophy in Physics and Nanosciences*

October 2023

## COPYRIGHT

# Table of contents

# Abstract

This thesis experimentally investigates charge transport in chiral systems, both at the monomer level (in the classic configuration of the molecular junction: metal|molecule|metal interface), where the dominant transport mechanism is tunneling, and within more extensive and complex systems (conjugated polymers, hybrid interfaces), where the transition to incoherent transport (hopping) occurs. Transport measurements (I-V curves) are recorded in both the solid state (through mc-AFM measurements, 4-probe resistance measurements, and impedance measurements) and using the electrochemical paradigm (a 3-electrode setup, with the current being recorded between the Working Electrode (WE) and Counter Electrode (CE) via Cyclic Voltammetry (CV)). In particular, numerous transport experiments are carried out in the presence of a ferromagnetic electrode (typically Nickel) in an external magnetic field to perform spin injection into the examined chiral system. This approach allows for the assessment of the spin polarization of charge carriers downstream of the measured interface as a function of the magnetic field orientation, evaluating the so-called Chiral Induced Spin-Selectivity Effect (CISS). In the first part of this thesis, the great results achieved in terms of spin-filtering using chiral thiophene derivatives and TTF derivatives (anchored to metallic substrates exploiting the S-metal interaction) are juxtaposed with results on enantio-recognition carried out with the same interfaces (the preferential interaction of a chiral analyte with one of the two enantiomers of a chiral selector, a fundamental process in biology). Through a meticulous comparison of the experiments, which is also a result of extensive characterization of all systems used, it is concluded that spin is the hidden force governing enantio-selective interactions. The second part of the thesis focuses on the study of achiral conjugated polymers (PCPDT-BT), homochiral polymers (p-2T3N), and the induction of supramolecular chirality in normally achiral polymers (polyaniline, PANI). Additionally, an original architecture for the development of an electrochemical transistor is proposed, utilizing these polymers as organic semiconductors constituting the gate. Currently, only the commercial achiral polymer PCPDT-BT has been tested in this configuration, but the extremely promising results regarding the operation of the device using the polaronic state (p-doping) of the organic semiconductor lead us to plan the near-future implementation with chiral systems. Lastly, the central role of spin in the oxygen evolution reaction (OER, crucial for electrochemical water splitting) is investigated using metallic electrodes coupled with bulk enantiopure chiral agents.

# Acknowledgement

The first person I must acknowledge is Prof. Claudio Fontanesi, undoubtedly... or “il buon Claudio” or “il Fonta”. He chose to believe in me after I messed up the properties of integrals in his physical-chemistry exam and guided me through a beautiful research journey, always providing assistance, listening, opportunities, and friendship. If I can perform two measurements in the laboratory today, it's certainly thanks to you.

I thank Saphi for being by my side in a path full of obstacles, even in the darkest moments. Thanks for tolerating me, for giving me all your affection and determination, for putting a smile on my face when I couldn’t see the Beauty. Without you, I don't know if I would have made it.

I thank my mother, who taught me discipline and respect for duty; I thank my father for his ability to see things in perspective. You are my sources of inspiration.

I thank my friends. My second family. The relationship we've built is the thing that makes me proudest of all.

Our life is what our thoughts make it.
Legacy keeps building.
Amala.

Andrea

# 1. Introduction

This thesis concerns the experimental investigation of charge transport through chiral systems. The transmission or conduction of electrons through chiral molecules is spin dependent[1]–[5]. This sentence is the most plausible attempt to encapsulate, although in a necessarily incomplete manner, the essence of the Chiral Induced Spin Selectivity effect (CISS effect). The earliest experimental evidence is generally traced back to 1999 arising from experiments conducted by K. Ray, D. Waldeck, R. Naaman et al. [6]. Furthermore, it's essential to acknowledge the earlier influential works by Mayer and Kessler [7], as well as the discovery of magneto-chiral dichroism by Rikken and Raupach in 1997 [8], a phenomenon that "complements" the CISS effect. Following these initial studies, a multitude of confirmations has been achieved [9]. The CISS effect has been observed in various chiral molecular systems, ranging from macro [10]–[15] and small [16], [17] molecules to supramolecular polymers [18], [19], metal-organic frameworks [20], hybrid organic-inorganic perovskites [21], [22], and artificial superlattices [23], [24], employing a wide array of electrical, optical, and electrochemical techniques [25]–[32]. Despite being a relatively nascent field due to its recent discovery and the ongoing absence of a comprehensive theoretical model (especially concerning the quantitative aspects) [33] the profound and extensive implications of the evident consequential interaction between molecular chirality, electron spin, handedness, and magnetism are captivating and appealing [34]. Indeed, it's essential to recall that we inhabit a notably homochiral world: essential molecules for life, such as amino acids and sugars, are selectively used in only one handedness [35] (left-handed in the former, right-handed in the latter) [36]. This chirality extends to larger scales, from the right-handed twists of DNA helices to asymmetric organelles, cells, and entire organs [37]. This phenomenon is known as the "homochirality problem" a signature of life as we know it, dating back to its origins and persisting to this day. The cause of this broken symmetry and, consequently, the origin of life, remains a topic of debate. While previous proposals attributed the consequences of this asymmetry to circularly polarized light, fluid dynamics, or magnetic fields [38], Furkan Ozturk and Dimitar Sasselov from Harvard University have recently presented a novel theory regarding the origin of life's homochirality. They suggest that spin-polarized electrons acted as the chiral symmetry-breaking agents in reduction reactions, initiating the very first enantiomeric excess (ee) [39]. Within this picture, chiral recognition and enantioselectivity rule asymmetric processes from chemical synthesis to biological life cycles and, considering the CISS paradigm, their connection with spin-dependent transport through chiral molecules appears to be more than a mere suggestion [40]–[42]. A deeper understanding of the mechanisms underlying enantioselective interactions and spin manipulation through the engineering of chiral structures has the potential to bring about a technological revolution. Merely by contemplating the pharmaceutical sector, it is sufficient to recognize that nearly 56% of the pharmaceuticals on the market and used in therapy are chiral compounds, and among them, 88% are administered as racemates [43]. In recent years, there has been a growing trend in the demand for enantiomerically pure substances in medicinal chemistry to reduce the toxicity or side effects associated with the inactive enantiomer [44], [45]. This need is currently met with high costs and complications in producing pure homochiral substances, whether achieved through asymmetric synthesis or the separation of racemic mixtures. In this context, chirality already plays a fundamental role [46], and recent discoveries have opened the doors to the use of new strategies such as the molecularly imprinted technique (MIT) [47] and the exploitation of new materials like chiral metal–organic frameworks (CMOF) to enable chiral recognition, separation, and catalysis [48]. Still in the medical field, the benefits stemming from the control of enantio-selective interactions are giving rise to new nanotechnologies capable of harnessing the preferential handedness of our biology as an advantage rather than an obstacle. Drawing inspiration from the selectivity exhibited by chiral entities in biological systems [49], innovative synthesis methods have been developed to enable the induction of chirality in nanoparticles and quantum dots [50]–[54]. These chiral assemblies can be used as drug nanocarriers [55]. It has been demonstrated that the handedness of these devices influences their transport through protein and lipid membranes into tumor-like tissues, leading to an increased diffusion coefficient and, consequently, enhanced delivery efficiency as nanocarriers [56]. Alongside, in the field of spintronics, the ability of a chiral interface to preferentially transport one spin, resulting in downstream spin-polarized current, makes it a genuine spin injector, akin to a ferromagnetic material in the presence of an external magnetic field[14], [57]. This property of chiral molecules can be harnessed for applications in memory devices, as an alternative to the more traditional configurations involving pinning layer, pinned layer, and free layer [58]. For example, Dor et al. designed a CISS-based magnetic random access memory device (MRAM) using only a single ferromagnetic free layer, without a fixed ferromagnetic layer [59]. The spin-filter role is performed by polyalanine (PANI) with a spiral structure, which magnetizes the ferromagnet just using current, without requiring the application of a magnetic field [60]. Different spin states are generated by changing the current direction, relying on the spin-transfer torque effect [61], [62]. Similarly, in the realm of semiconductors, significant progress has been made in terms of charge injection/transport via organic molecule|semiconductor interfaces. Liu et al. created heterojunctions of “normal metal|chiral molecules|magnetic semiconductor” where spin-polarized electrons are injected into the semiconductor without the need for a permanent magnet [63]. The use of organic materials within spintronic devices offers unique potential in terms of flexibility, plasticity, tunability, scalability, and addressability. Beyond the briefly mentioned examples in drug synthesis and spintronics, the potential applications involving chirality are manifold [64]–[68]. When its orientation is adeptly controlled, spin can effectively serve as a chemical reagent to select the desired reaction pathway(s) over others, thereby enhancing or diminishing the reaction rate by tuning the involved activation energies [3], [69]–[74]. It is clear that to harness this great potential and achieve such a technological revolution, the preliminary step is to gain a deeper understanding of the mechanisms underlying spin-polarized charge transport through chiral systems, particularly concerning the parameters and conditions that affect the magnitude of the CISS effect. This thesis aims to provide an additional piece to the larger puzzle, with a specific focus on experimentally investigating the connection between spin-dependent transport and enantio-specific interaction in chiral systems (enantio-recognition).

# 2. Theoretical background

## 2.1. Charge transport at the monomer level

Since this work's purpose is to investigate charge transport through chiral systems, the first step is to understand how the charge flows through a single molecule (such as a monomeric compound). In fact, this phenomenon represents a matter of great experimental interest in the case of a single molecular layer (monolayer) involved in the architecture of nano-scale devices, but it is also the key elementary step to understand how the overall current flows in multimolecular systems.

In this scenario, the model scheme consists of the metal-molecule-metal assembly, where the molecule of interest is contacted between two metal electrodes. This system is generally addressed as the "molecular junction" and can be partitioned into three discrete parts, i.e. the molecular core and the two macroscopic electrodes on both sides, which allow to inject currents and fix voltages [75].

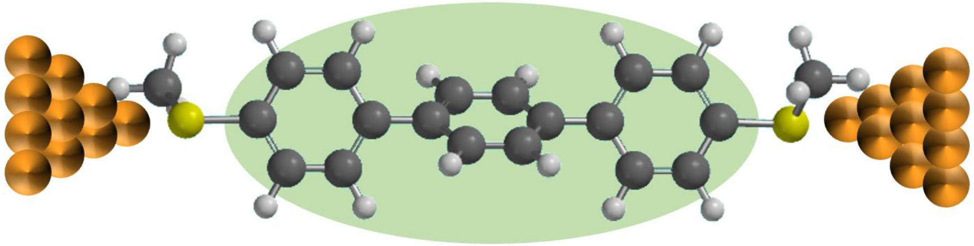

Figure 1 Schematic representation of a molecular junction: two macroscopic electrodes are connected by an organic molecule that serves as the active component. Reprinted with permission from ref [76].

At this point, a first fundamental distinction must be made between two different regimes: coherent and non-coherent transport. The distinction between these two regimes is based on the conservation (coherent) or the loss (non-coherent) of the information about the phase of the transmitted electron wavefunction. In fact, when electrons are described as "coherently going through a channel", all dissipative/phase-breaking processes are assumed to be limited to the contacts. No phase-breaking processes (such as inelastic scattering with photons, phonons, other electrons) affect the electrons flowing through the molecule, which basically acts as passive bridge with well-defined channel modes (or "sub bands"), each one having a specific energy-momentum relationship. In this picture, the molecular channel acts like a "rigid environment” and the electron elastically interacts with it, like a ping-pong ball bouncing off a truck [77].

On the other hand, inelastic interactions with the environment cause charge carriers transmitted through a molecule to experience decoherence. This leads to a complete or partial loss of quantum mechanical behavior and has important consequences for charge transport, which will be discussed in the corresponding section [78].

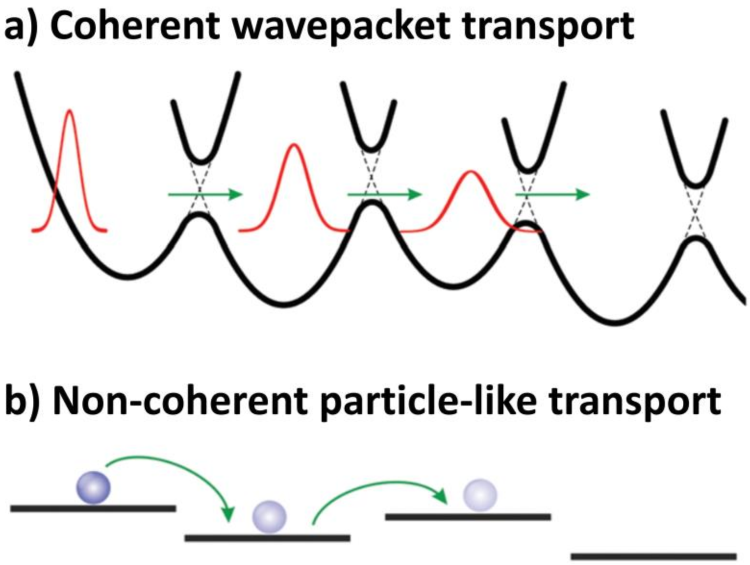

Figure 2 Comparison between **a)** coherent wavepacket transport (tunneling as the dominant mechanism vs. **b)** incoherent, particle-like transport (proceeding by hopping). Reprinted with permission from ref [79].

The conservation of charge carriers’ coherence is associated with the concept of phase correlation between the wavefunction amplitudes of spatially distant states. Phase correlation can be influenced by various parameters (e.g. the level of conjugation in a polymer) leading to different degrees of delocalization of the wavepacket [79]. Therefore, a fundamental length scale involved in the determination of the dominant transport regime is the phase-coherence length, $L_{\varphi}$, that is the distance over which the phase information of electrons is preserved. A typical $L_{\varphi}$ value for $Au$ at $T = 1K$ is around $1\ \mu m$ while at room temperature it becomes of the order of a few tens of $nm$.

Since small organic molecules are usually in the order of magnitude between $1$ and $10\ nm$ (including most of thiophene derivatives which were used in our research), the condition $L < L_{\varphi}$ is typically fulfilled in the case of a single molecule (molecular wire) or a molecular monolayer contacted between two metal electrodes. Therefore, the so called “mesoscopic regime" arises and the coherent transport, or tunneling, is the dominant charge transfer mechanism.

The tunneling transport mechanism is generally treated with the scattering formalism, or Landauer approach [80], [81], whose central idea is as follows: once the inelastic interactions can be ignored, a transport problem can always be viewed as a scattering problem. This means that transport properties, like the electrical conductance ($G$), are intimately related to the transmission probability for an electron to cross the system ($T$). This connection will be revealed by the Landauer formula in this coverage (equation 21, vide infra).

The conductance G is a familiar physical quantity, since it's featured in the macroscopic Ohm's law:

$$G = \sigma \frac{A}{L} = \frac{1}{R} \tag{1}$$

Where $A$ is the sample transverse area, $L$ is its length and $\sigma$ is the conductivity, which is a material specific property.

Unfortunately, Ohm's law as presented in equation (1) cannot be applied to mesoscopic systems like molecular junctions, and but a quantum description of conductance is needed to reveal some fundamental (and counterintuitive) characteristics. In fact, it is not obvious to note that for a single mode conduction channel (as if the electrodes were bridged by a molecule with one single energy level available for the transport of carriers) there is a maximum amount of conductance, which is a fundamental constant related to the charge of an electron and Planck's constant:

$$G_0 \equiv \frac{q^2}{h} = 38.7\ \mu S = (12.9\ k\Omega)^{-1} \tag{2}$$

$G_0$ is defined as "quantum of conductance". However small, actual channels have at least two levels (one for up spin and one for down spin) at the same energy ("degenerate" levels) making the maximum conductance equal to $2G_0$ [82].

In order to introduce the connection between $G$ and $T$, we shall present the steps leading to the Landauer formula.

In the most general view, a current is a measure of the flow (i.e. quantity per unit of time) of objects from one point in space to another; in particular, we are dealing with quantum objects (electric charges) and thus their physical state is defined by a wavefunction $\psi(x,t)$.

Since the squared modulus of $\psi$, $|\psi(x,t)|^2 = \psi^*\psi$, is the probability density, we consider its variation with respect to time:

$$\frac{\partial|\psi(x,t)|^2}{\partial t} = \psi^* \frac{\partial\psi}{\partial t} + \frac{\partial\psi^*}{\partial t}\psi \qquad (3)$$

According to the time-dependent Schrodinger equation:

$$i\hbar\frac{\partial\psi}{\partial t} = \left(\frac{\hat{p}^2}{2m} + V\right)\psi \qquad (4)$$

Where $\hat{p}$ is the momentum operator.

We can substitute the time-dependent (TD) Schrodinger equation expression in the previous equation (3), and we obtain

$$\frac{\partial|\psi(x,t)|^2}{\partial t} = \psi^* \frac{\left(\hat{p}^2/_{2m} + V\right)\psi}{i\hbar} + \psi\frac{\left(\hat{p}^2/_{2m} + V\right)\psi^*}{i\hbar} \qquad (5)$$

Simplifying

$$\frac{\partial|\psi(x,t)|^2}{\partial \mathrm{t}} = \frac{1}{2mi\hbar}(\psi^*\hat{p}^2\psi - \psi\hat{p}^2\psi^*) \qquad (6)$$

With $\hat{p} = -i\hbar\nabla_r$

$$\frac{\partial|\psi(x,t)|^2}{\partial t} = -\nabla_r \cdot \left[\frac{1}{2m}(\psi^*\hat{p}\psi - \psi\hat{p}\psi^*)\right] \qquad (7)$$

The physical meaning of the obtained relation emerges by comparing it to the familiar "continuity equation" in its differential form:

$$\frac{\partial\rho}{\partial t} + \nabla \cdot j = 0 \qquad (8)$$

Clearly, what we obtained in equation (7) is precisely the continuity equation, with the density term at the first member and the divergence of the flux density at the second member. Therefore, we found an expression for the quantum mechanical current density j:

$$j = \frac{1}{2m}(\psi^*\hat{p}\psi - \psi\hat{p}\psi^*) \qquad (9)$$

Focusing on the specific electric current, accounting for the flow of charge, we have that $\mathrm{J} = \mathrm{qj}$ so the current density expression turns into

$$J = \frac{q}{2m_e}(\psi^*\hat{p}\psi - \psi\hat{p}\psi^*) \qquad (10)$$

Where $q = 1.6 \times 10^{-19}\ C$ and $m_e = 9.1 \times 10^{-31}\ kg$ are the charge and the mass of the electron, respectively. It should be noted that, since $\psi$ has dimension of ${}^{1}/_{\sqrt{Volume}}$, the dimension of J is ${}^{A}/_{m^2}$ for 3D, ${}^{A}/_{m}$ for 2D, and $A$ for 1D current flow; also, if $\psi$ is real, then $J = 0$.

Since the molecular junction system introduced above is treated as a 1D environment, we can consider a plane wave wavefunction for a single dimension $x$, assuming $x = (0, L)$ boundary conditions. The wavefunction for a state $|k\rangle$ of definite energy $E(k)$ is

$$\psi_E(x,t) = \left(\frac{1}{\sqrt{L}}\right) e^{ikx} e^{-iE(k)\frac{t}{\hbar}} \tag{11}$$

If we substitute this latter form of $\psi$ in the quantum mechanical expression for the current density (equation 10), we can notice that the time evolution portion is not affected by the momentum operator, and therefore factors to 1. After some calculation, we end up with the equation for the current carried for a single state $|k\rangle$ (note that the current density coincides with current in 1D)

$$J(k) = I(k) = \frac{q\hbar k}{L m_e} \tag{12}$$

This equation is linked to the classical notion of current carried by a particle with velocity $v(k) = \frac{\hbar k}{m_e}$ traversing a distance $L$

$$I = \frac{q v(k)}{L} \tag{13}$$

Up until this point, we have derived an expression for the quantum current density. Now we should apply this formalism to our system of interest: the electron flowing from the first electrode (for example the left, "$L$" electrode) to the second ("$R$") crossing the organic molecule.

Firstly, let's expand the discussion to multiple k-states: we must sum the contribution from each state

$$\boldsymbol{J} = \frac{q}{L}\sum_{k} v_g(k) f(k) \tag{14}$$

Where $v_g(k)$ is the group velocity and $f(k)$ is the so called "Fermi function". The Fermi function is a probability distribution function which determines the probability that a state "$k$" is occupied by an electron. In the molecular junction, since the two macroscopic electrodes are metallic, their energy distribution is assumed to be continuous (as a consequence of Bloch's theorem). Consequently, the allowed states will be occupied up to a specific energy called electrochemical potential (Fermi level), μ, which coincides with the Fermi energy at T = 0. A typical electrochemical potential value for a noble metal is around -5 eV (vacuum level set to 0) [83]. Instead, in the in-between molecular channel, the discrete distribution of the electrons' states is much more evident and their energy is determined by the structure of the Molecular Orbitals (MO). These orbitals are full up to the highest occupied molecular orbital (HOMO), which for a characteristic molecule could be roughly −7 eV. When the Left and Right metallic electrodes are coupled to the organic molecule, some charge carriers will flow through the system leading to charge and geometric rearrangements. As a result, the electrochemical potential of the electrodes μ shifts to a common level which lies somewhere between the HOMO-LUMO gap of the molecule.

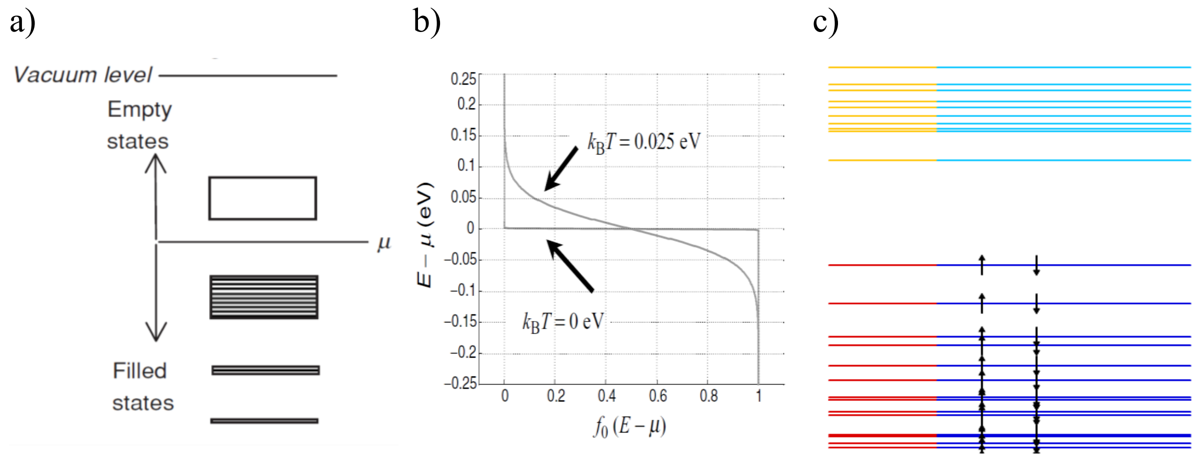

Figure 3 **a)** The Fermi function describes the allowed energy levels for the electrons. $\mu$ is the common electrochemical potential of the metallic contacts (Fermi level) coupled to the channel **b)** Fermi function distribution in the vicinity of $\mu$ **c)** Molecular Orbitals (M.O.) spectrum of 2T3N, an organic thiophene derivative studied in this work (the HOMO/LUMO region is highlighted).

In this equilibrium state, the over-time average number of electrons in any energy level (i.e. the distribution of charges in the $|k\rangle$ states) is given by the above mentioned Fermi function:

$$f_0(E-\mu) = \frac{1}{1+\exp\left(\frac{E-\mu}{k_B T}\right)} \tag{15}$$

Far below $\mu$, energy levels are always full ($f_0 = 1$), while highly above $\mu$ levels are always empty ($f_0 = 0$). Energy levels within a few $k_B T$ of μ are occasionally empty and occasionally full so that the average number of electrons lies between 0 and 1 ($0 \leq f_0 \leq 1$). This kind of equilibrium system is described by Figure 4a and can be simply represented with the model of the rectangular potential barrier (Figure 4b) which is the simplest example when dealing with quantum tunneling.

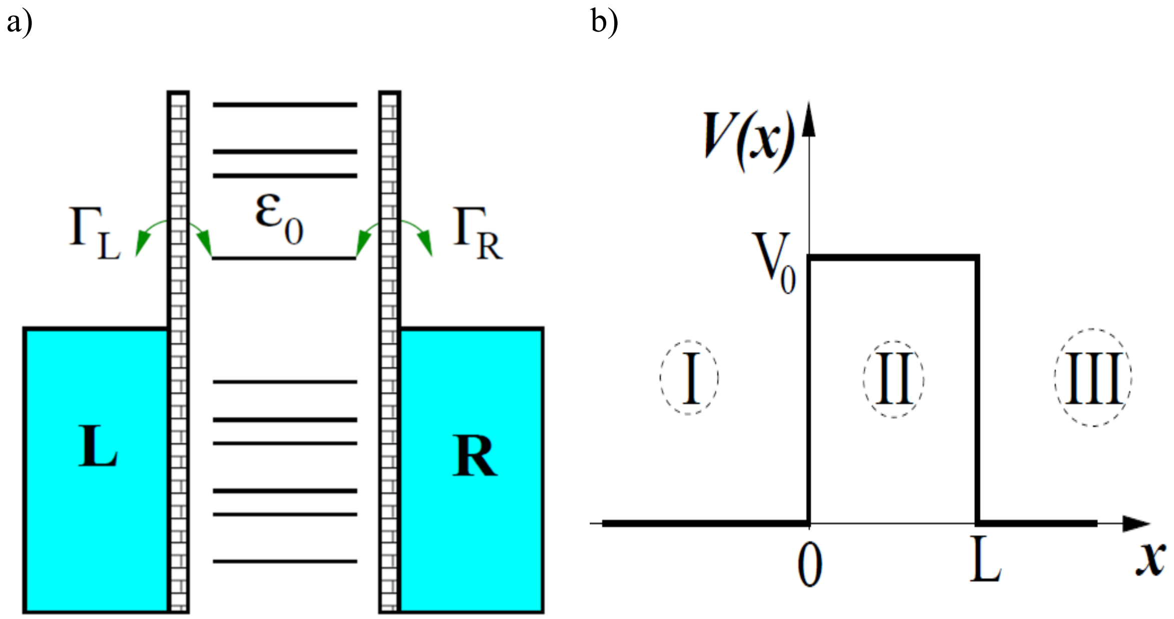

Figure 4 **a)** Energy diagram of the molecular junction: the metal has a continuum of states filled up to the Fermi level. The molecular bridge has a series of sharp resonances (the molecular orbitals) **b)** Typical rectangular potential barrier. $V_0$ is the barrier's height, $L$ is its width. Reprinted with permission from ref [82].

The potential barrier represents the molecule sandwiched between the two metal electrodes in the molecular junction: it is characterized by a width $L$ and by a height $V_0$. This height is in principle the distance between the electrochemical potential of the electrodes and the nearest molecular energy level in the molecule. In fact, even though different molecular orbitals can participate in the electron transport simultaneously, the transport is generally dominated by the one level which lies closest to the Fermi level of the metals (typically the HOMO or LUMO). This level is labelled as $\varepsilon_0$ in Figure 4a (in this case, we talk about single-level resonant tunneling model). Given the described potential barrier, the goal is to investigate the crossing probability as a function of the energy of an approaching electron ($E$). Let's consider the same plane wave of equation (11), $\psi(x,t) = \left(\frac{1}{\sqrt{L}}\right) e^{ikx}$, representing an electron flowing through the molecular junction from the Left to the Right electrode (L→R verse), across the molecular bridge.

Based on the result of equation (14), the quantum-mechanical expression for the probability current is:

$$J_{L\to R} = \frac{q}{L}\sum_{k} v_g(k)\, T(k)\, f_L(k)\ [1 - f_R(k)] \tag{16}$$

The $T(k)$ term introduced in equation (16) is precisely the transmittance term. In fact, the plane wave travelling in the L→R verse is partially reflected with a probability amplitude $r$ and partially transmitted with a probability $T = |t^2|$ when impinging the molecule's potential barrier. As it is known from quantum tunneling theory [84], the probability of transmission of a wave packet through the barrier decreases exponentially with the barrier height and also with the barrier width (which can be identified with the length of the contacted molecule: therefore, tunneling transport decreases exponentially as the length of the channel increases). This is graphically represented in Figure 5.

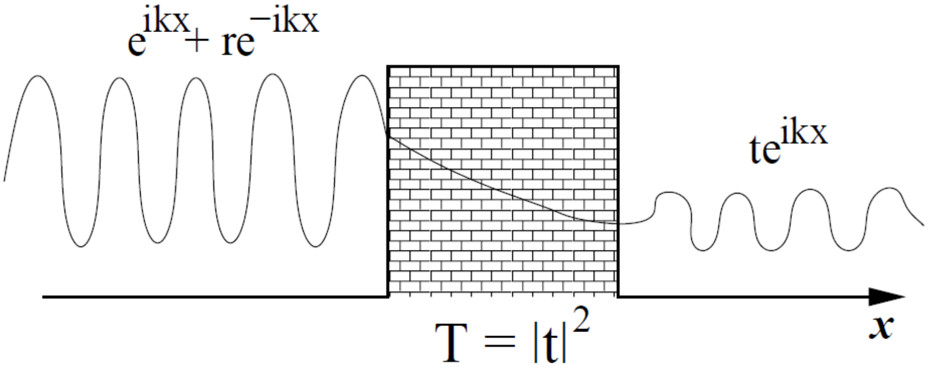

Figure 5 Wavefunction (plane wave) interacting with a potential barrier.

The $f_L(k)$ is the Fermi-function of the Left electrode (which is, in general, not equal to the Right electrode Fermi function, $f_R(k)$, as we will be discussing shortly). Thirdly, the $[1 - f_R(k)]$ factor is called the "Pauli blocking". It ensures the preservation of the Pauli exclusion principle: only those states that were initially occupied on the left and empty on the right contribute to the current flowing from left to right $J_{L\to R}$.

The sum over the k-states can be converted into an integral: the allowed states in the k-space are discrete "boxes" of each side ${}^{2\pi}/_{L}$ and therefore volume $\left({}^{2\pi}/_{L}\right)^d$ in $d$ dimensions. Since we are considering a mono-dimensional scenario we can replace ${}^{1}/_{L}\sum_k g(k)$ with ${}^{1}/_{2\pi}\int g(k)dk$ , with the cancellation of the dependance of the macroscopic dimension $L$.

We obtain

$$J_{L\to R} = \frac{q}{2\pi}\int dk\ v(k)\ T\ (k)\ f_L(k)\ [1 - f_R(k)] \tag{17}$$

Now we shall introduce the density of states (DOS), in order to change the integration variable from $k$ to $E$. A few manipulations of the DOS (which is defined as $^{dk}/_{dE}$ ) leads to:

$$\frac{dk}{dE} = \left(\frac{dE}{dk}\right)^{-1} = \frac{m}{(\hbar^2 k)} \tag{18}$$

since $E = \frac{\hbar^2 k^2}{2m}$. Equation (18) is substituted in equation (17)

$$J_{L\rightarrow R} = \frac{q}{h}\int dE\; T(E)\; f_L(E)\; [1 - f_R(E)] \tag{19}$$

We assume that the transmission coefficient $T(k)$ does not depend on the direction of current flow (the transmission probability is the same independently of the barrier's crossing direction); then, the same expression is valid for the opposite verse current $J_{R\rightarrow L}$

$$J_{R\rightarrow L} = \frac{q}{h}\int dE\; T(E)\; f_R(E)\; [1 - f_L(E)] \tag{20}$$

And the net total current, $I$, is

$$I = \frac{2q}{h}\int_{-\infty}^{\infty} dE\; T(E)\; f_R(E)\; [f_L(E) - f_R(E)] \tag{21}$$

This is the Landauer formula, which carries the connection between conductance $G$ and transmission $T$ that we were looking for.

Up until this point, we have worked towards a quantum mechanical expression of the tunneling current, but we have not addressed a fundamental question: what is the meaning of the distribution of the states? How does the density of states affect the charge transfer (and therefore the current)? At the end of the day, why do electrons flow? Qualitatively, we can already anticipate that conduction through the molecular bridge will depend on the channel's DOS around the electrochemical potential μ, since we mentioned that the height of the potential barrier is related to the distance between the energy states available for conduction in the molecule and the electrochemical potential of the metals. In this regard, let's discuss what happens to the fermi functions of the electrodes once we introduce the driving force of charge carriers' flow: an applied voltage.

A potential difference $V$ is applied between the two macroscopic electrodes. Assuming an arbitrary notation, the applied positive $V$ lowers the energy levels in the Right (R) electrode with respect to the Left one (L). This breaks the equilibrium and determines two different values of μ for the two electrodes, separated by $qV$

$$\mu_L - \mu_R = qV \tag{22}$$

As a consequence, we obtain two distinct Fermi functions for the Left and Right contacts

$$f_L(E) = \frac{1}{1 + \exp\left(\frac{E - \mu_L}{k_B T}\right)} = f_0(E - \mu_L) \tag{23}$$

$$f_R(E) = \frac{1}{1 + \exp\left(\frac{E - \mu_R}{k_B T}\right)} = f_0(E - \mu_R) \tag{24}$$

This is due to the two electrodes both "trying" to bring the molecular bridge into equilibrium with itself, and then the molecule acts like an intermediary.

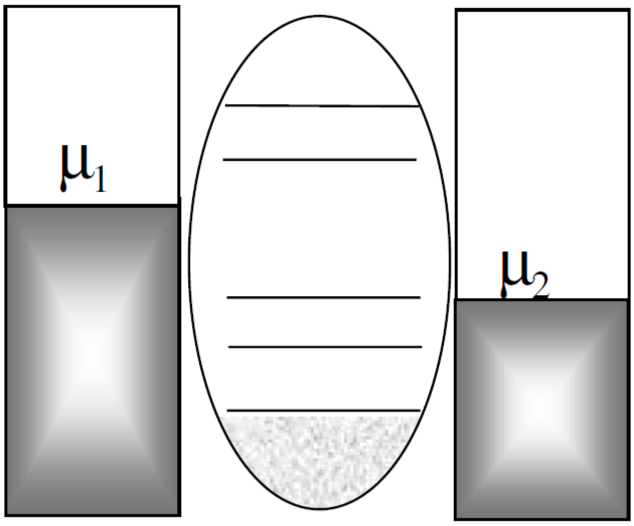

Figure 6 Applying a positive voltage V to the right (R) electrode compared to the left (L) reduces the electrochemical potential at the left. Consequently, the L and R contacts strive to establish distinct Fermi distributions, and the molecular channel goes into a state intermediate between the two. Reprinted with permission from ref [82].

Consequently, when a current flows between the two electrodes (following a specific verse, L→R or R→L) as a result of an applied voltage, we have to consider two distinct fermi functions for the two contacts of the molecular junction. At zero temperature, these fermi functions $f_L(k)$ and $f_R(k)$ are step functions: their value is 1 (full occupation) for energies below $E_F + {}^{qV}\!/_2$ and $E_F - {}^{qV}\!/_2$, respectively (where $V$ is the applied voltage) ; and 0 above this value.

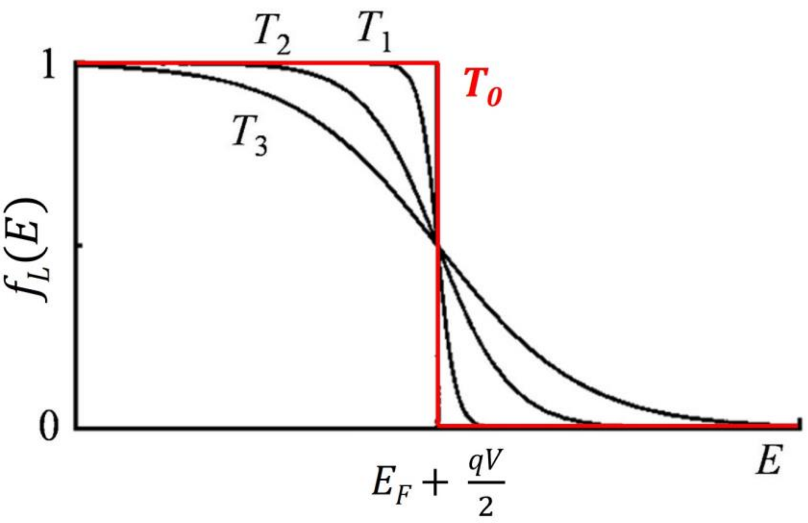

Figure 7 Fermi functions distribution at different temperatures: $T_3 > T_2 > T_1$ . At the absolute zero temperature ($T_0$), the probability of an electron to have an energy below the Fermi energy is equal to 1, while the probability to have higher energy is zero. Re-elaborated with permission from ref [85].

After the introduction of the applied external voltage, the Landauer formula can be written as

$$I(V) = \frac{2q}{h}\int_{-\infty}^{\infty} dE\, T(E,V)\ \left[f\left(E - {}^{qV}/_{2}\right) - f\left(E + {}^{qV}/_{2}\right)\right] \tag{25}$$

If we assume low applied voltages ($qV \to 0$, linear regime), the Landauer formula reduces to

$$I = GV \tag{26}$$

Then the conductance $G$ is defined as

$$G = \left(\frac{2q^2}{h}\right) T \tag{27}$$

With the Transmission $T$ evaluated at the Fermi energy.

Equation (27) is the quantum description of conductance that is required in the study of charge transport through mesoscopic systems, where conduction is transmission. In order to determine the total conductance, we have to solve the Schrödinger equation, find the current carrying eigenmodes, calculate their transmission values and sum up their contributions to obtain the total transmission $T$. Therefore, for a single perfect conduction mode ($T = 1$) the contribution to total conductance is exactly equal to one "unit of conductance" $G_0$

$$G_0 \equiv \frac{2q^2}{h}(25.8\ k\Omega)^{-1} \tag{28}$$

That is exactly equal to equation (2), the point where we started this coverage.

In order to evaluate the transmission $T$ when a voltage $V$ is applied, it is required the knowledge of its dependence on the energy and on the voltage: $T = T(E, V)$. This is crucial to the purpose of this work, since the final aim is to exploit the Landauer formula in the fitting and interpretation of the experimental current-voltage characteristics (I-V curves). In the case of a rectangular potential barrier, the computation of the transmission (and in turn of the I-V curves) is a simple problem. The effect of the applied voltage is represented in Figure 8. In the a) panel, the Right and Left Fermi levels are split and more empty states are available in the Right electrode for tunneling into. Anyway, this description is often too simple to fit any concrete experimental scenario.

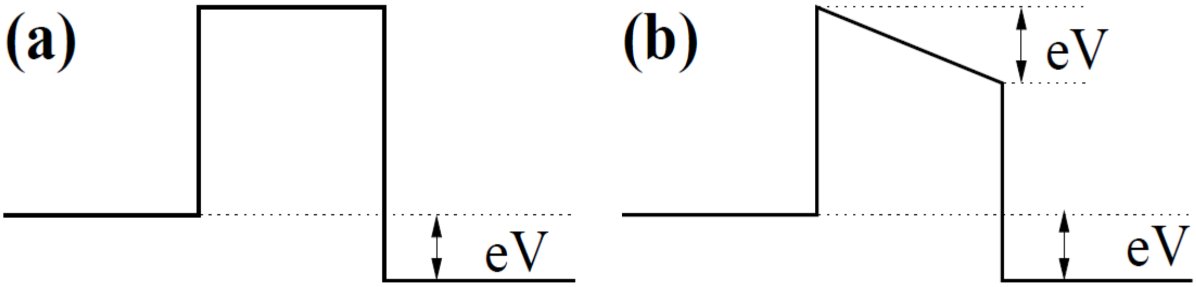

Figure 8 Effects of a voltage application on the potential barrier. **a)** Simplistic representation vs **b)** more realistic modeling. Reprinted with permission from ref [75].

A more appropriate way of describing the effect of the voltage is shown in Figure 8b, where a linear drop in the potential with the barrier region has been assumed. This kind of potential (and other arbitrary-shaped potentials) can be treated using the Simmons model, which is an application of the Landauer formula combined with the use of the Wentzel-Kramers-Brillouin approximation. In the case of a fig. 8b-like potential, Simmons showed that zero-temperature net current density can be written as

$$J = J_0\left\{\varphi_B \, exp\left(-A\sqrt{\varphi_B}\right) - (\varphi_B + eV) \, exp\left(-A\sqrt{\varphi_B + eV}\right)\right\} \tag{29}$$

Being

$$A = \frac{2\,\alpha\, s_B}{\hbar}\sqrt{2m} \tag{30}$$

$$J_0 = \frac{e}{2\pi h\, \alpha^2\, {s_B}^2} \tag{31}$$

where $\varphi_B$ is the average barrier height relative to the negative electrode and $s_B$ is the barrier width. Regarding $\alpha$, it is a dimensionless correction factor which is adjusted in fitting procedures to account for the possibility of non-rectangular barriers or an effective mass different from the bare electron mass (otherwise, it usually is of the order of 1).

Depending on the magnitude of the perturbation (the applied potential $V$), three different regimes can be distinguished in the I-V characteristics as it's schematized by Figure 9. These regimes are referred as the linear region, the resonant region and the saturation region.

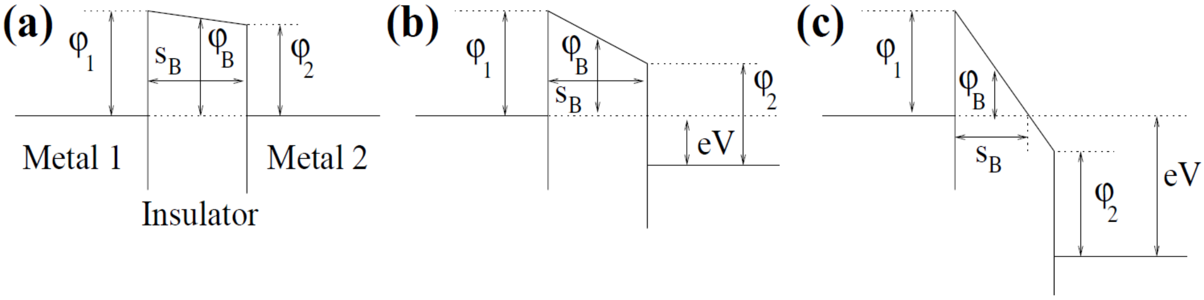

Figure 9 Tunneling across a potential barrier. Depending on the magnitude of the applied potential ($eV$), the linear, resonant and saturation regions are identified (panels **a**, **b**, and **c** respectively). Reprinted with permission from ref [75].

Although the Simmons model can be very accurate, its expression has to be simplified in three different equations (one for each different regime) in order to be used effectively in I-V curves fitting. This latter is a valid method for sure, but we proceeded to use one single equation which was derived by the Landauer formula after a series of assumptions. This allows to simulate and fit the experimental I-V characteristics with one single mathematical expression.

The main simplification of this approach is that the only contribution to the transmission comes from a single molecule's energy level (resonant level), which dominates the transport for a certain applied voltage range. This is called "single resonant level tunneling model" (SRLTM). In this context, the transmission coefficient dependence from the voltage V and the Energy E is given by the Breit-Wigner formula:

$$T(E,V) = \frac{4\,\Gamma_L\,\Gamma_R}{[E-\varepsilon_0(V)]^2+[\Gamma_L+\Gamma_R]^2} \tag{32}$$

In the latter equation, $\varepsilon_0(V)$ denotes the position of the transmission mode (in general, it depends on the voltage applied across the junction and on the way it drops at the interfaces). It's important to note that the $\varepsilon_0$ is expressed with respect to the fermi energy of the system at zero applied bias, therefore it represents the energy offset between the electrodes electronic band and the resonant tunneling level. In addition, $\Gamma_L$ and $\Gamma_R$ are the left and right reservoirs' scattering rates (assumed to be energy and voltage independent). They have the dimensions of energy, and they quantify the strength of the molecule's coupling to the metal electrodes. When the molecule is equally coupled to the electrodes ($\Gamma_L = \Gamma_R$), then the voltage drops symmetrically at the left and right interface, so $\varepsilon_0(V) = \varepsilon_0$. In addition, we must define the sum $\Gamma_L + \Gamma_R = \Gamma$, which represents the broadening of the resonant level $\varepsilon_0$. In fact, before the coupling of the molecular channel to the macroscopic electrodes, the density of states of the three elements do not affect each other and the situation is represented by Figure 10a. We have one sharp level in the channel and a continuous distribution of states in the metals. When coupled, all these states "spill over": the channel "loses" part of its state as it spreads into the contacts, but it also "gains" part of the contact states that spread into the channel. Since the loss occurs at a fixed energy ($\varepsilon_0$) while the gain is spread out over a range of energies, the overall effect is to broaden the channel DOS from its initial sharp structure into a more diffuse structure. Since the "coupling broadening" tends to be much larger than the electron Fermi broadening of the electrode, the effect of temperature on the Fermi distribution can be ignored and the Fermi function can be approximated into a step function [86].

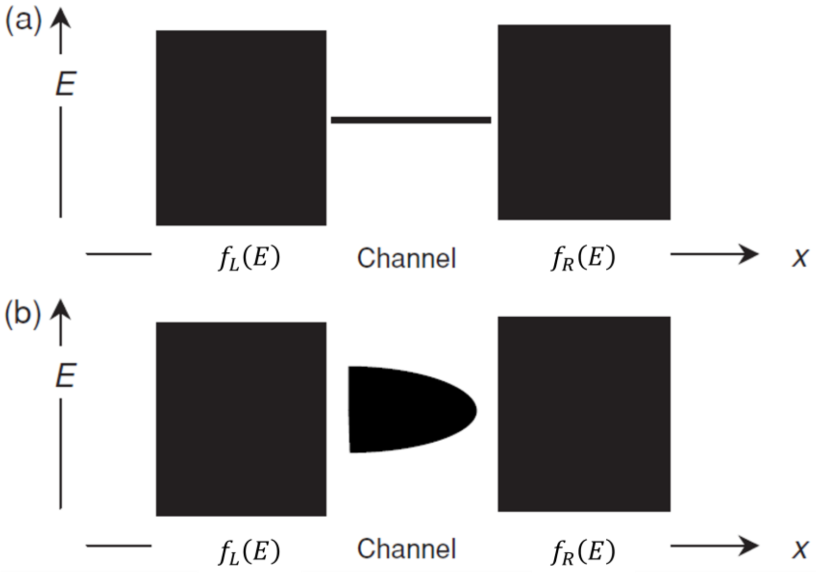

Figure 10 Density of states before **(a)** and after **(b)** the coupling of the elements in a molecular junction. The connection results in a "broadening effect," where the channel's molecular orbital loses its sharpness and partially spreads into the contacts states (and vice versa, the contacts distributions also partially spread into the channel). Reprinted with permission from ref [82].

Given these approximations, Landauer formula's integral can be solved analytically producing a temperature-independent solution.

$$I(V) = \frac{2e}{h}\frac{4\,\Gamma_L\,\Gamma_R}{\Gamma}\left[arctan\left(\frac{{}^{eV}\!/_{2} - \varepsilon_0}{\Gamma}\right) + arctan\left(\frac{{}^{eV}\!/_{2} + \varepsilon_0}{\Gamma}\right)\right] \qquad (33)$$

It is evident that the variables affecting the I-V characteristics in the tunneling mechanism are mainly the energy offset $\varepsilon_0$ and the coupling strength to the electrodes, $\Gamma_L$ and $\Gamma_R$.

Armed with this model, we can now analyze some examples of I-V curve, starting from the ones displayed in Figure 11.

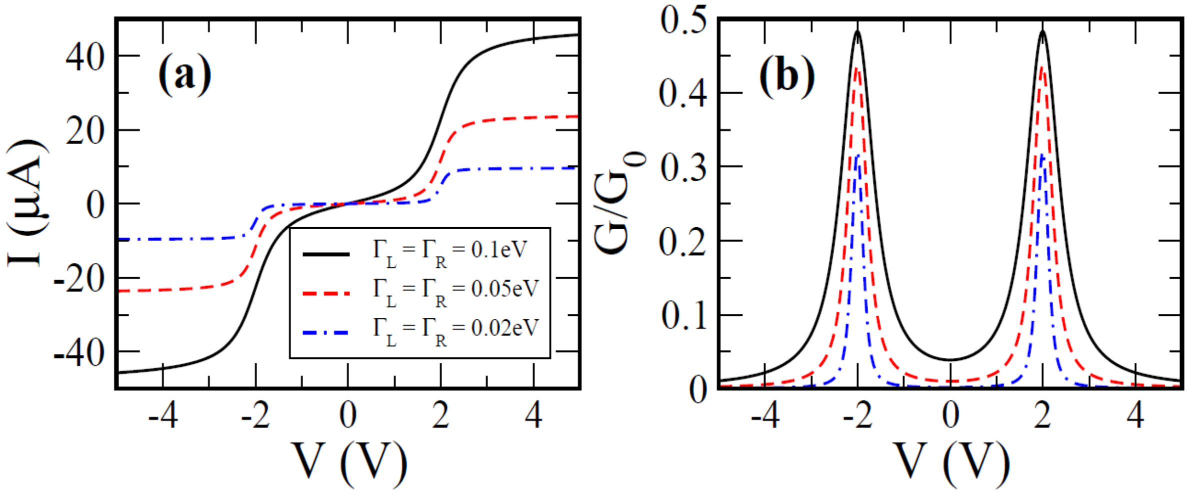

Figure 11 **a)** Examples of computed I-V curves in the resonant tunneling model, with a level position $\varepsilon_0 = 1\ eV$ (measured relatively to the Fermi energy of the electrodes) and at room temperature ($k_BT = 0.025\ eV$). The various curves represent different values of the scattering rates. **b)** The corresponding differential conductance $G = {}^{dI}/_{dV}$, normalized by $G_0 = {}^{2e^2}/_{h}$. Reprinted with permission from ref [75].

Figure 11a shows simulated I-V characteristics for different values of $\Gamma$ (in symmetric coupling conditions), and a starting position of the resonant level at $\varepsilon_0 = 1$ eV. As previously mentioned (and schematized in Figure 9), three different regions can be distinguished. The first region is at low bias, when voltage is much smaller than $|\varepsilon_0|$. In this situation the given bias is not enough to align the Fermi level and the broadened molecular level $\varepsilon_0$: resonant tunneling is not achieved and few carriers are transmitted, which traduces to very low currents. Despite the appearance, the current trend is linear in this region and its value is not a constant [86].

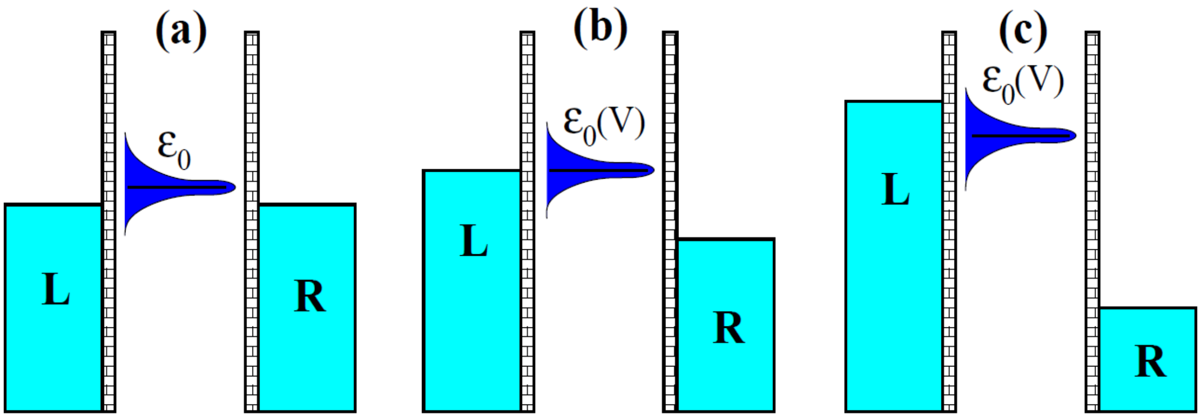

Figure 12 Alignment of the resonant level depending on the applied voltage (a finite level broadening of $\Gamma = \Gamma_L + \Gamma_R$ is considered). **a)** Zero bias region **b)** resonant region **c)** large bias region (current saturation). Reprinted with permission from ref [75].

On the other hand, current non-linearity is evident in the second region, which is defined by the resonant condition ${}^{eV}\!/_{2} = \varepsilon_0(V)$, i.e. $eV = 2\varepsilon_0(V)$. The increased bias brings the electronic level of the electrode to resonance and therefore the current rapidly increases. Finally, when the voltage is larger than $2\varepsilon_0 + |\Gamma|$, the third region is found, and the current saturates to the value $I_{sat}$

$$I_{sat} = \frac{2e}{h}\frac{4\,\Gamma_L\,\Gamma_R}{\Gamma} \tag{34}$$

An actual example of an experimental I-V characteristic is displayed in Figure 13. The presented dotted curve is taken directly from our work *Chiral recognition: a spin-driven process in chiral oligothiophene* (Stefani et al., Section 3.2 of this work) [87], and it was acquired with a magneto-conductive AFM apparatus.

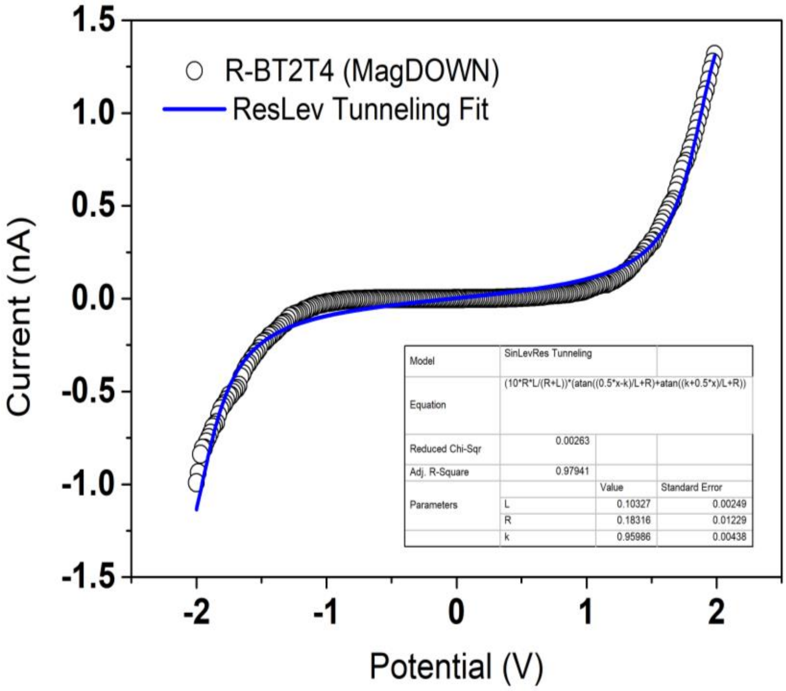

| | | | |
|---|---|---|---|
| Model | SinLevRes Tunneling | | |
| Equation | (10*R*L/(R+L))*(atan((0.5*x-k)/L+R)+atan((k+0.5*x)/L+R)) | | |
| Reduced Chi-Sqr | 0.00263 | | |
| Adj. R-Square | 0.97941 | | |
| Parameters | | Value | Standard Error |
| | L | 0.10327 | 0.00249 |
| | R | 0.18316 | 0.01229 |
| | k | 0.95986 | 0.00438 |

Figure 13 Fitting of an experimental I-V curve using the resonant tunneling model. The investigated system is a Au|molecule|Ni junction. The dotted line represents the actual experimental data obtained using a magneto-conductive atomic force microscopy (mc-AFM). The molecule under investigation is an enantiopure chiral thiophene derivative known as R-$BT_2T_4$ (please refer to Section 3.2 for more details). This molecule is adsorbed onto a Au(111) substrate on one side and contacted by the Ni AFM tip on the other side. The blue line represents the curve fitted with the resonant tunneling model, and the fitting provides the following values: $\varepsilon_0 = 0.96\ eV$, $\Gamma_R = 0.183\ eV$ (Au) and $\Gamma_L = 0.103\ eV$ (Ni).

The investigated systems consists of a chiral enantiopure thiophene derivative (R-$BT_2T_4$, its structure is reported in Figure 44a, Section 3.2) which is chemisorbed to a Au(111) oriented substrate, forming a self-assembled monolayer (SAM). The charge-transfer is measured at the level of the single molecule of the monomer by contacting the SAM via a Nickel AFM tip and by applying electrical bias in the -2 V to 2 V interval. The conductivity was also mapped as a function of the magnetic field direction (magnetizing the ferromagnetic Nickel tip, in this case “down directed” magnetic field is applied) but we are not going to focus on this further complication at the moment. The presented curve shows a linear first region with very low currents for voltage $\leq |1.0|$ V. For higher voltage values, the resonant condition is reached, and the current rapidly increases.  Based on the previous discussion, the curve can be fitted with the single-level resonant tunneling model and the results and the results are represented by the blue trace. We are aware that tunneling transport can involve more than one state and that further effects arise from the non-symmetric interface (Au|$BT_2T_4$|Ni) and the application of the magnetic field, but still the model suits very well the experimental results. The free fitting parameters are the height of the barrier ($\varepsilon_0$) and the molecule's coupling strength to the electrodes ($\Gamma_R$ and $\Gamma_L$ for Au and Ni, respectively). The effect of the barrier on the current is due to the fact that as the barrier increases, the voltage required to reach resonant tunneling increases gradually. So that the conductance decreases with tunneling barrier and the saturation current at resonance is harder to reach. On the other hand, coupling strengths affect the magnitude of the current but also the shape of the curve in the case of different values for the two contacts [86]. In fact, a smaller coupling traduces to a smaller broadening of the molecular energy level and consequent narrower distribution of the transmission spectrum, which affects the transport of electrons across the molecular junction. All things considered, the used fitting values are $\varepsilon_0 = 0.96\ eV$, $\Gamma_R = 0.183\ eV$ and $\Gamma_L = 0.103\ eV$. It's interesting to note that the ratio of the coupling strengths to the two different metals is ${}^{\Gamma_R}/_{\Gamma_L} \cong 1.78$.

Ab-initio and semi-empirical theoretical calculations were performed for the $BT_2T_4$ in our work [87]. Chemisorption of $BT_2T_4$ on both Au and Ni was modelled within the so-called embedded cluster approach and the results show a $BT_2T_4$ theoretical adsorption energy of $-120.1\ \mathrm{kcal\ mol^{-1}}$ and $-77.8\ \mathrm{kcal\ mol^{-1}}$ on Au and Ni respectively (Section 3.2.3.5 of this thesis). The ratio of these interaction energies is $\frac{-120.1\ \mathrm{kcal\ mol^{-1}}}{-77.8\ \mathrm{kcal\ mol^{-1}}} = 1.55$ which is a coherent value when compared to the emerged fitting parameters ratio 1.78 (accounting for the different interaction environment and procedure).

## 2.2. Beyond tunneling: transport mechanisms in complex systems

Up until this point, we focused on the coherent transport regime. We've come a long way, starting from the precursors expressions of current density and continued with the description of carriers proceeding elastically (without exchanging energy) through the molecular junction. What is the range of validity of the coherent picture? Intuitively, the coherent mechanism will be the dominant one as long as the time that an electron needs to cross the molecular bridge is smaller than the time that it takes to interact with other electrons or to excite vibronic degrees of freedom, i.e. the time that is needed for an electron to undergo an inelastic scattering event. This time scale is referred as "tunneling transversal time" $\tau$ : in short, the time the electron spends in the junction. In principle, $\tau$ expression depends on the distance of the molecular conduction channel from the Fermi energy of the leads (i.e. proximity of resonance condition) but a unified definition can be given with good approximation:

$$\tau = \frac{\hbar}{\sqrt{\Delta E^2 + \Gamma^2}} \tag{35}$$

Where $\Gamma = \Gamma_L + \Gamma_R$ is the coupling strength and $\Delta E$ is the injection gap (which coincides with $\varepsilon_0$ in the case of single-level resonant tunneling). The transport is mainly coherent as long as $\hbar/_\tau$ is larger than the energy scales associated with inelastic interactions, like electron-electron (Coulomb correlation, $U$) and electron-vibration ($\lambda$) i.e. $\sqrt{\Delta E^2 + \Gamma^2} > \max\{U, \lambda\}$. On the contrary, when the time needed for the electron to interact with another electron or to excite a vibrational mode is comparable to the transverse time, inelastic interactions start occurring and influencing the transport. In the case that conduction is dominated by the Coulomb interaction in the molecular bridge, particular effects are observed such as the Coulomb blockade and the Kondo effect. In extreme synthesis, the Coulomb blockade is the decrease in conductance at small bias voltages caused by the electrons' Coulomb repulsion, preventing their flowing and leading to single electron tunneling processes. This results in typical step shaped I-V characteristics (Coulomb staircase, see Figure 14c) [88]. Coulomb blockade is more likely prevailing when the molecule is weakly coupled to the electrodes i.e. there's no formation of covalent bonds (poor hybridization between the electrodes and the molecule's electronics states) and the system is brought close to resonance ($\Delta E \approx 0$). On the other hand, when the molecule's coupling strength to the leads is intermediate (not too strong, otherwise the elastic coherent tunneling dominates the transport) different higher order tunneling processes arise and can lead to the appearance of the Kondo effect.

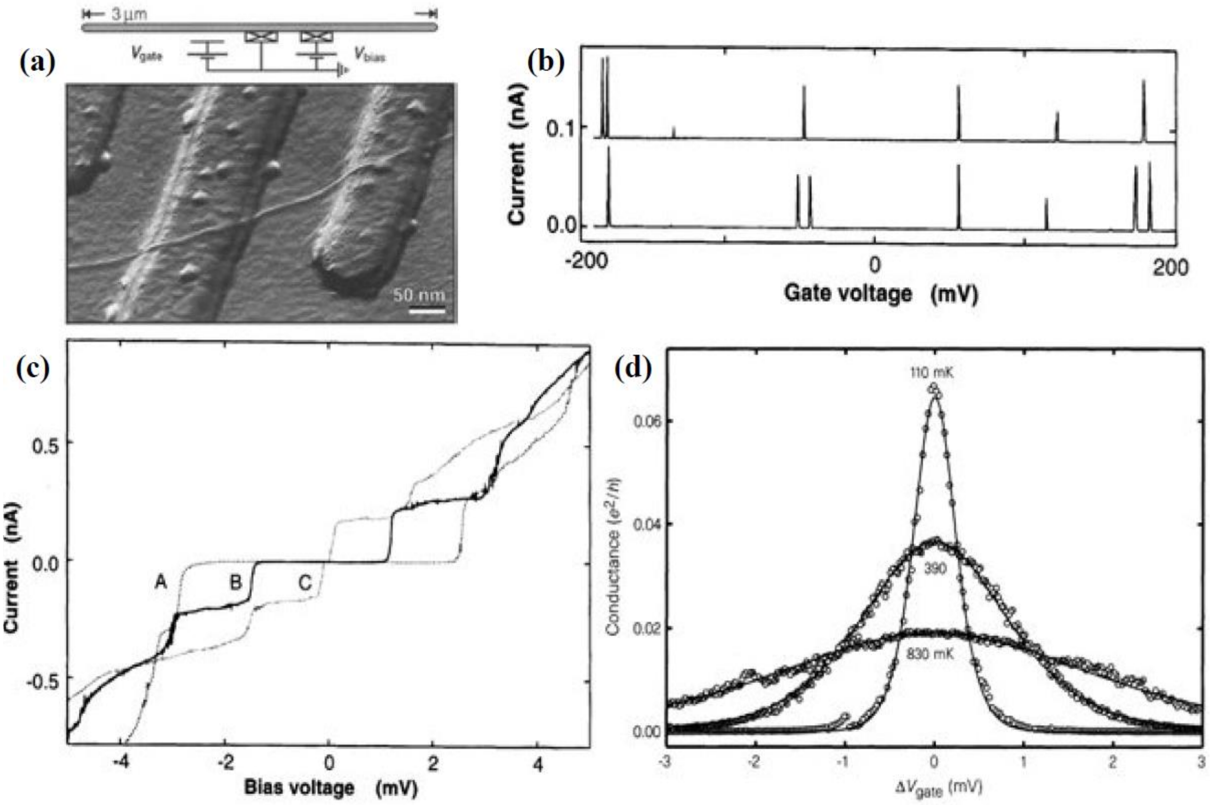

Figure 14 Coulomb blockade in a single-wall carbon nanotube (from ref. [88]) **(a)** AFM image of a carbon nanotube on top of a Si/SiO2 substrate with two 15-nm-thick Pt electrodes, and a corresponding circuit diagram. **(b)** Current versus gate voltage at $V_{bias} = 30\ \mu V$. Two traces are shown that were performed under the same conditions. **(c)** Current-voltage curves of the tube at a gate voltage of 88.2 mV (trace A), 104.1 mV (trace B) and 120.0 mV (trace C). **(d)** Conductance $G = \frac{I}{V_{bias}}$ versus $\Delta V_{gate}$ at low bias voltage $V_{bias} = 10\ \mu V$ and different temperatures. Reprinted with permission from ref [88].

The deepening of these intricate phenomena is beyond the aim of this work, but it's important to retain this general concept: these are typical coherence loss signals, as the tunneling transport mechanism starts getting "contaminated" by inelastic phenomena. In addition to Coulomb effect, electron-phonon interactions are the other possible energy-exchange mechanism in the molecular bridge. In the case of weak electron-phonon coupling, $\lambda \ll \sqrt{\Delta E^2 + \Gamma^2}$ , the excited vibrational modes generate small inelastic current that is superimposed to the elastic tunneling background. These currents' signal can be found at the energies of the excited vibrational mode of the neutral molecules inside the junction, therefore they can be exploited for local molecular spectroscopy purposes [89]. As the electron-phonon coupling and the transversal time increase (e.g. increased potential barrier width i.e. greater molecule length), vibronic effects are even more prevalent in the transport up to the point where a paradigm shift is identified since coherence is completely lost. In this instance, the orbital overlap is sufficient to ensure the conservation of the electron's wavefunction's only for limited segments. Therefore, charge transport is interpreted as sequential "hops" of the carriers (electrons or holes) between these molecular sites and it is referred as hopping regime. For comparing purposes, this hopping regime can be visualized using the same structural model previously built for coherent transport, with a single molecule sandwiched between two metal leads (see Figure 15). Unlike the previous tunneling case, now the molecule has $N$ different sites which are weakly coupled. Starting from the Left electrode, charge carriers hop incoherently between the $N$ sites when the injection energy ΔE is is provided to activate the process (ΔE being the energy difference between the first hopping state and the fermi level of the leads). The transfer rate from a starting site $i$ to an arrival site $k$ is represented by $k_{\,i,j}$.

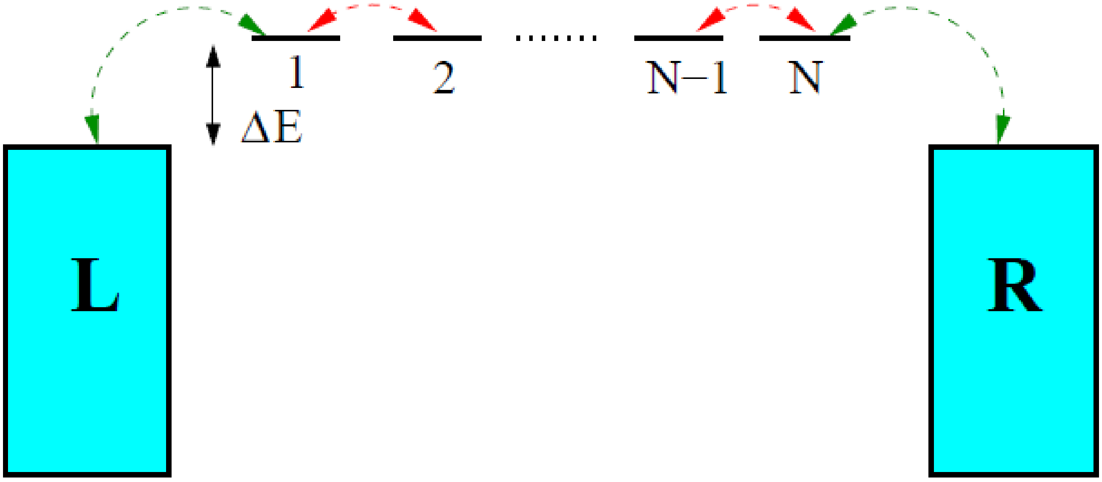

Figure 15 Representation of the described incoherent transport model. Given the nearest neighbors approximation, charge transfer is an activated process that occurs through successive jumps (hops) from one site to the next. Reprinted with permission from ref [75].

In the (strong) approximations of "nearest neighbors" (the only non-zero transfer rates are $k_{\,j,j\pm1}$) and fixed equal energy for the N molecular sites, this approach leads to the formulation of classical rate-equations for the charge transfer between two successive sites $j$ and $j+1$

$$\dot{P}_j = -\left(k_{j-1;j} + k_{j+1;j}\right)P_j + k_{j;j-1}P_{j-1} + P_j + k_{j;j+1}P_{j+1} \qquad (36)$$

with $P_j$ and $P_{j+1}$ being the sites occupation, and $\dot{P}_j = {}^{dP_j}/_{dt}$ .

Assuming the further simplification of constant internal rates in the molecule ( $k_{\,j,j\pm1} = k$ ) the expression for the current can be derived [75]

$$I = e\frac{e^{-\Delta E/k_BT}}{\left[\frac{1}{k_{Left}} + \frac{1}{k_{Right}} + \frac{(N-1)}{k}\right]}\left[e^{eV/k_BT} f_L - f_R\right] \qquad (37)$$

And consequently, the relative linear conductance can be expressed as:

$$G = \frac{e^2}{k_BT}\frac{e^{-\Delta E/k_BT}}{\left[\frac{1}{k_{Left}} + \frac{1}{k_{Right}} + \frac{(N-1)}{k}\right]} \qquad (38)$$

The presented model is inspired by the approach of Cuevas et al. in the “Organic electronics” book [75]; it gives an immediate visualization of the hopping mechanism and allows to extract the fundamental fingerprints of this conduction regime:

- The decay of conductance is linear with the length of the molecule (in contrast to tunneling, where the decay is exponential with the barrier width);
- The conductance depends on temperature following an exponential Arrhenius-type behavior.

In this scenario, we have focused on a single molecule, but the extension of this concept to longer molecular bridges, up to a polymeric chain, is straightforward. This extension is possible because activation centers (and their corresponding activation energies) can be positioned at any location along the junction. However, when dealing with this step-like transport mechanism, a critical challenge lies in determining how to describe the constant $k_{CT}$. The fundamental aspect of hopping transport involves the propensity of charges to become localized at one stage of the transport process, typically over one or a few molecular sites. This localization effect is a primary reason for the lower conductivity observed in organic semiconductors compared to electronically delocalized systems like metals. As the length of the system increases, moving from relatively small molecular bridges to longer structures such as conjugated-polymer chains, this localization effect becomes increasingly dominant. The carrier localization, in turn, exerts an influence on the interactions with vibrations, and the overall impact on nuclear degrees of freedom can be analyzed through many different models (classical, semiclassical, purely quantum). An exhaustive presentation of the possible approaches goes beyond the scope of this thesis. However, a brief introduction to the fundamental concepts for investigating the nature of the $k_{CT}$ constant is provided below. These include: the basics of Marcus theory (which has been used as a valuable approach in the investigation of charge transport processes in organic semiconductors for the last 20 years [90]), intrinsic limitations of its semiclassical nature, and the concept of a polaron.

Considering a qualitative description, as previously mentioned referring to large conjugated systems, charge carriers (electrons or holes) tend to be localized on a single lattice site. This is mainly due to structural disorder. In fact, due to weak intermolecular interactions (usually Van Der Waals interactions ) [91] most polymers solids are found in amorphous or semi-crystalline state (ordered crystalline aggregates surrounded by disordered amorphous regions) which leads to localization of the extended valence and conduction states involved in transport [92] (Anderson mechanism) [93]. This localization (i.e. oxidation or reduction of the relevant molecular site, to the point that the expression “redox sites” is used by some authors) [94] can be visualized as the charge being momentarily fixed at some point of the crystal. The transversal time tends to infinity and hence electron-lattice interactions trigger a rearrangement process involving the surrounding dielectric medium and the reorganizing nuclei. The induced displacements create a potential "well" for the electron and if this depression is significant enough, the electron will be confined to a bound state, incapable of moving independently and requiring the accompanying lattice deformation for its mobility [95]. This whole phenomenon is called “polaron formation”.

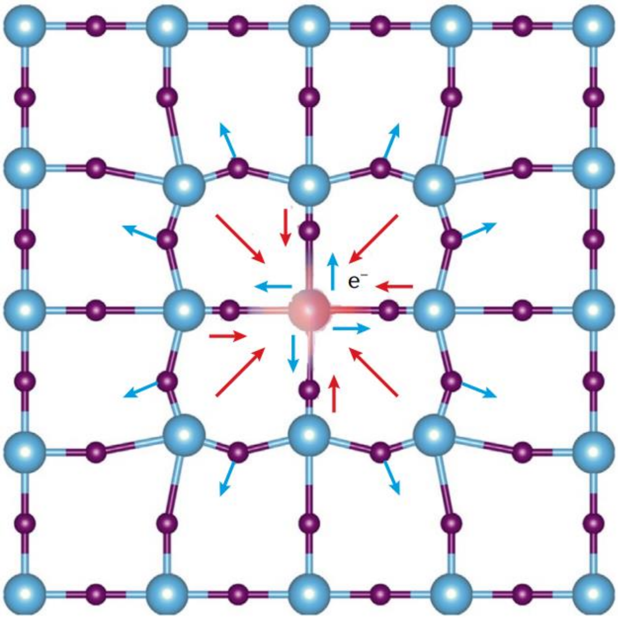

Figure 16 Simplified illustration of the polarization phenomenon induced by the self-trapping of an electron at a lattice site, resulting in the formation of a small polaron. The arrows in the symbolize the forces at play, with red arrows indicating attractive forces and blue arrows representing repulsive forces. Reprinted with permission from ref [96].

The polaron is a quasi-particle used to understand the relation between electrons and atoms in a solid material, therefore it basically consists of the electron with its self-induced polarization (it is usually described as “a charge dressed in phonons”). Consequently, in the case of large conjugated polymers, the charge transport mechanism can be defined in a more accurate way as “incoherent hopping of polarons along the molecules” [75].

While Landau is credited with introducing the concept of the polaron in 1933, the first model that consistently reproduced charge-transfer experimental results in organic semiconductors is based on Marcus theory. This theory was initially formulated to explain the rates of electron transfer reactions of solvated species in solution and introduced the practice of considering the carrier's interactions with the solvent through a potential energy surface (PES). Nevertheless, Marcus's modeling can be effortlessly extended to solid-state charge transfer (CT) between one state (reactant) to another (product). In fact, since a solid is a collection of ions oscillating around their equilibrium positions, the electron moves through a potential that continuously changes over time [97] and the relative elastic properties of the lattice are modeled through the PES. In his 1956 paper [98], Marcus notes that “when an electron is transferred from one reacting ion or molecule to another, the two new molecules or ions formed are in the wrong environment of the solvent molecules, since the nuclei do not have time to move during the rapid electron jump”. The formulation of his model arises from the correction of Libby's results in 1952, attempting to reconcile the principle of energy conservation with the Franck-Condon principle regarding vertical transitions. The key to the reasoning lies in interpreting charge transport in terms of fluctuations in both intra-molecular vibrational modes and nuclear degrees of freedom of the environment.

In general, the reactant and product states are function of the many hundreds of relevant coordinates of the system (translational, rotational and vibrational coordinates of the reacting species and of the molecules of the surrounding medium). Nevertheless, they can be visualized in a schematic and intuitive way as a function of a single “nuclear configuration” $Q$ (or the infamous “reaction coordinate”) independent variable, a function that lives in the just introduced many-variables space (we assume N dimensions for the system). This coordinate “represents any concerted motion (fluctuation) leading from any spatial configuration (on all atoms) that is suited to the electronic structure of the reactants to one suited to that for the products” [99]. A simple example of potential energy profile of the reactants ($V_R$, before electron transfer) and products ($V_P$, after electron transfer) is displayed against this “collective coordinate” in Figure 17.

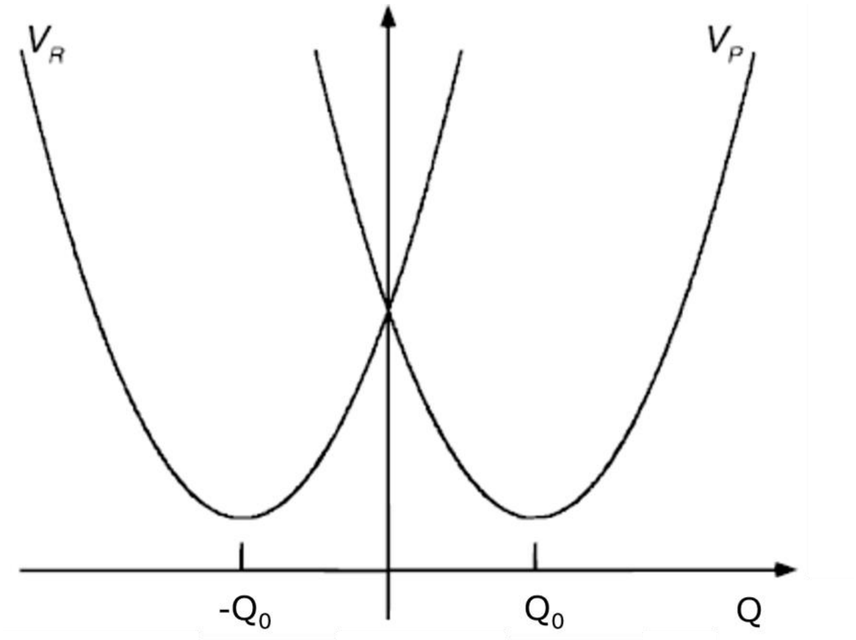

Figure 17 Diabatic potential energy surfaces (PES) for a symmetrical electron transfer reaction

The potential regions of interest in Figure 17 are depicted as identical parabolas (elastic potentials, according to the classical treatment of atomic vibrations). Assuming symmetric reactant and product ($\Delta G^0 = 0$) they can be described by equations:

$$V_R = \frac{1}{2} f (Q + Q_0)^2 \tag{39}$$

$$V_p = \frac{1}{2} f (Q - Q_0)^2 \tag{40}$$

where $f$ is a force constant. $V_R$ and $V_p$ correspond to the charge distribution before and after the electron transfer; $Q_0$ is the value of Q at the minimum. The difference between these two potential energies is given by

$$V_R - V_p = 2 f q_0 q \tag{41}$$

Consequently,

$$Q = \frac{1}{2 f Q_0} (V_R - V_p) \tag{42}$$

Therefore, the nuclear configuration Q is directly proportional to the difference in potential energies between curves $V_R$ and $V_P$. This representation is commonly referred to as the harmonic approximation, and it is one of the numerous simplifications that must be taken into account in the Marcus theory to derive a classical formulation of the transfer constant.

The same representation of the PES of Figure 17 is typically presented in a more general form (Figure 18, panels a and b), where the two identical parabolas are shifted along the ordinate axis. Furthermore, variations in entropy are neglected; as a result, the energy (or potential energy V) can be represented as the Gibbs free energy G.

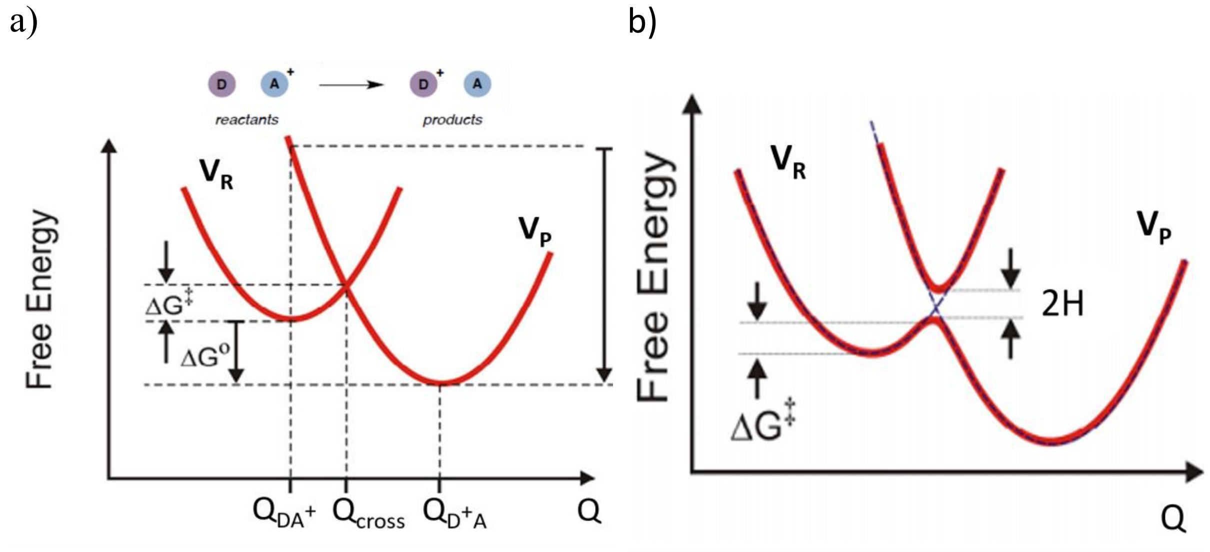

Figure 18 Diabatic **(a)** vs adiabatic **(b)** potential energy surfaces for electron transfer modeling, corresponding to low and high electronic coupling between the donor and the acceptor, respectively. In the case of diabatic states, the charge is fully localized on one of the species so no splitting occurs at the transition state. In the adiabatic case, the coupling is considerable, the 2H splitting occurs and the system stays on the lower potential energy curve. Re-elaborated with permission.

At the intersection between the two functions lies the so-called "transition state", which is characterized by the loss of one degree of freedom with respect to the reactants or products (we transition from N to N-1 dimensions) and meets the condition

$$V_R(Q_{cross}) = V_P(Q_{cross}) \tag{43}$$

Regarding the transition state, two main different scenarios must be accounted: in the case of good electronic interaction between the donor and acceptor (typically corresponding to a brief relative distance), there is a distinct splitting of the two surfaces at the intersection. This splitting is represented in Figure18b while it is omitted in Figure 18a. The splitting is addressed as 2 $H$ where $H$ is the electronic coupling (also known as the transfer integral) which plays a crucial role in governing the overall rate of electron transfer reactions and the electrical conductance of molecular wires. So, the effective coupling is defined as half of the energy splitting at the intersection of two crossing energy surfaces [100]. In the case of non-negligible $H$, the nuclear motion is coupled to electron motion and therefore as the system moves from left to right in

Figure 18b, it consistently remains on the lowest surface and this results in an adiabatic transition from the $V_R$ to the $V_P$ surface.

However, as mentioned earlier, organic semiconductors typically exhibit highly disordered environments with weak inter-molecular interactions. As a result, $H$ is very low: charges tend to be strongly localized and the increased transient time maximizes inelastic interactions furtherly leading to the charge self-trapping. This makes the splitting at the curve intersection negligible, and the transition to the product surface can only occur through the "jump" between states at the intersection ($Q_{cross}$ in Figure 18a). The crossing is allowed when the splitting between states $\frac{|G_P - G_R|}{2} = H$ is minimized (due to structural fluctuations or polarization effects of the environment) i.e. the R and P states are brought into resonance [100], and the probability that as a result of this nuclear motion the system ends up on surface P is calculated by treating this motion non-adiabatically.

Utilizing the definition of the potential energy curves, the intersection condition can be written as:

$$\frac{1}{2}f(Q_{cross} - Q_{DA^+})^2 = \Delta G^0 + \frac{1}{2}f(Q_{cross} - Q_{D^+A})^2 \tag{44}$$

Solving for the crossing point

$$Q_{cross} = \frac{\Delta G^0}{f}\left(\frac{1}{Q_{D^+A} - Q_{DA^+}}\right) + \frac{Q_{D^+A} + Q_{DA^+}}{2} \tag{45}$$

The free-energy barrier for the charge-transfer $\Delta G^{\ddagger}$ i.e. the activation energy of electrons (or holes) transfer between the initial and final localized states, is therefore expressed by

$$\Delta G^{\ddagger} = G_R(Q_{cross}) - G_R(Q_{DA^+}) = \frac{1}{2}f(Q_{cross} - Q_{DA^+})^2 = \frac{(\Delta G^0 + \lambda)^2}{4\lambda} \tag{46}$$

Where $\Delta G^0$ is the standard free energy for the reactions and $\lambda$ is the “classical” reorganization energy, defined as

$$\lambda = \frac{1}{2}f(Q_{DA^+} - Q_{D^+A})^2 \tag{47}$$

$\lambda$ is the energy to be dissipated on the acceptor surface if the electron is transferred at $Q_{DA^+}$. It can be decomposed into the solvational (“outer shell”, $\lambda_0$) and vibrational (“inner shell”, $\lambda_i$) components.

The classical expression for solvation energy is obtained using a two-sphere model representing the donor and acceptor (with radii $a_1$ and $a_2$, respectively, and at distance $R$) and considering the solvent as a dielectric continuum.

$$\lambda_0 = (\Delta e)^2 \left[\frac{1}{2a_1} + \frac{1}{2a_2} - \frac{1}{R}\right]\left[\frac{1}{\varepsilon_\infty} - \frac{1}{\varepsilon_0}\right] \tag{48}$$

$\varepsilon_\infty$ and $\varepsilon_0$ are the optical and the static dielectric constants, while $\Delta e$ is the amount of charge transferred.

The vibrational component contributing to the reorganization energy, $\lambda_i$, can be expressed using the following equation:

$$\lambda_i = \sum_l \lambda_{i,l} = \frac{1}{2}\sum_l f_l\left(\Delta Q_{e,l}\right)^2 \tag{49}$$

In this equation, the summation is performed over the coupled intramolecular vibrations. The contribution of the $l_{th}$ normal mode to the reorganization energy is determined by its constant force $f_l$ and the change in equilibrium positions between the reactants and the products, represented by $\Delta Q_{e,l} = Q_{P,e} - Q_{R,e}$.

It is evident that in the case of self-exchange reactions, i.e. $\Delta G^0 = 0$ (the “donor” and the “acceptor” are identical except for their oxidation state), equation 46 reduces to

$$G^\ddagger = \frac{\lambda}{4} \tag{50}$$

Which is the polaron activation energy [101].

Based on this classical description, the charge transfer constant from site $i$ to site $j$ (Marcus rate) is defined as [102]:

$$k_{i,j}^{Marcus} = \frac{2\pi}{\hbar} \mid H_{i,j} \mid^2 \left(\frac{1}{\sqrt{4\pi\lambda\, k_B T}} exp\left(-\frac{(\Delta G^0 + \lambda)^2}{4\lambda\ k_B T}\right)\right) \tag{51}$$

The equation (51) is an Arrhenius-type equation that describes the energy activation process of polaron hopping. This result can also be derived from different models, as demonstrated by Levich and Dogonadze in 1960 or Holstein [95], [103] in his description of small polaron motion in solids [90]. The Arrhenius-like temperature dependence is a key characteristic of this activated transport mechanism, whereas in the case of tunneling, the current-voltage (I-V) curves are essentially temperature-independent. In fact, the single-level resonant tunneling model (discussed in the previous Section 2.1) did not exhibit an explicit temperature dependence; the temperature action was mainly accounted for in the variations it induced in the Fermi functions of the electrodes, although this effect is often considered negligible.

Given this description of the hopping probability, the hopping mobility $\mu$ (in the high temperature approximation) is described by:

$$\mu = \frac{e\,a^2}{k_B T} k^{Marcus} \qquad (52)$$

Where $a$ is the intermolecular distance.

The expression of Marcus' rate (equation 51) gained popularity because it is a simple analytically solvable equation that essentially depends on only three parameters: the electronic coupling, the standard free energy of the reaction, and the reorganization energy [104]. Therefore, experimental measurements of charge-transfer rates can be quickly interpreted, provided the constraints imposed by the numerous approximations. The most evident limitation of this model lies in its temperature dependence when the high-temperature limit is not satisfied. In fact, experimental results show that the predictions of equation (51) are validated at high temperatures, where electron transfer is an activated process, but they are inconsistent for $\hbar\omega_{max} \sim k_B T$ ($\omega_{max}$ is the highest frequency of the Huang−Rhys active modes), predicting a vanishing electron transfer rate at zero temperature (which is not observed experimentally).

The main reason for this inconsistency lies in the classical description of nuclear coordinates. In fact, for organic semiconductors, both intramolecular and intermolecular vibrational modes play a fundamental role in the charge transport environment. In fact, reorganization of organic molecules typically involves particular vibrational modes (such as C-C and C=C stretchings, $\omega = 1000$ and $\omega = 1500 \div 2000$ cm$^{-1}$, respectively) coupled to charge transfer which can have such a significant zero-point fluctuation that it exerts a major influence on transport even at temperatures close to absolute zero.

The incorporation of quantum effects of nuclei into the Marcus theory, aimed at reducing limitations in the model's application, is achieved by employing the displaced harmonic oscillator (DHO) formalism or the Energy Gap Hamiltonian (EGH), along with utilizing the Fermi Golden Rule (FGR) [105]. This semi-classical approach allows for the consideration not only of electronic states (represented by the simple parabolas) but also the effects related to vibrational levels (including the possibility of overcoming the activation barrier through tunneling when donor and acceptor wavefunctions overlap) [106]. The extent of the role of tunneling depends on the extent of the vibrational overlap between the initial and final states.

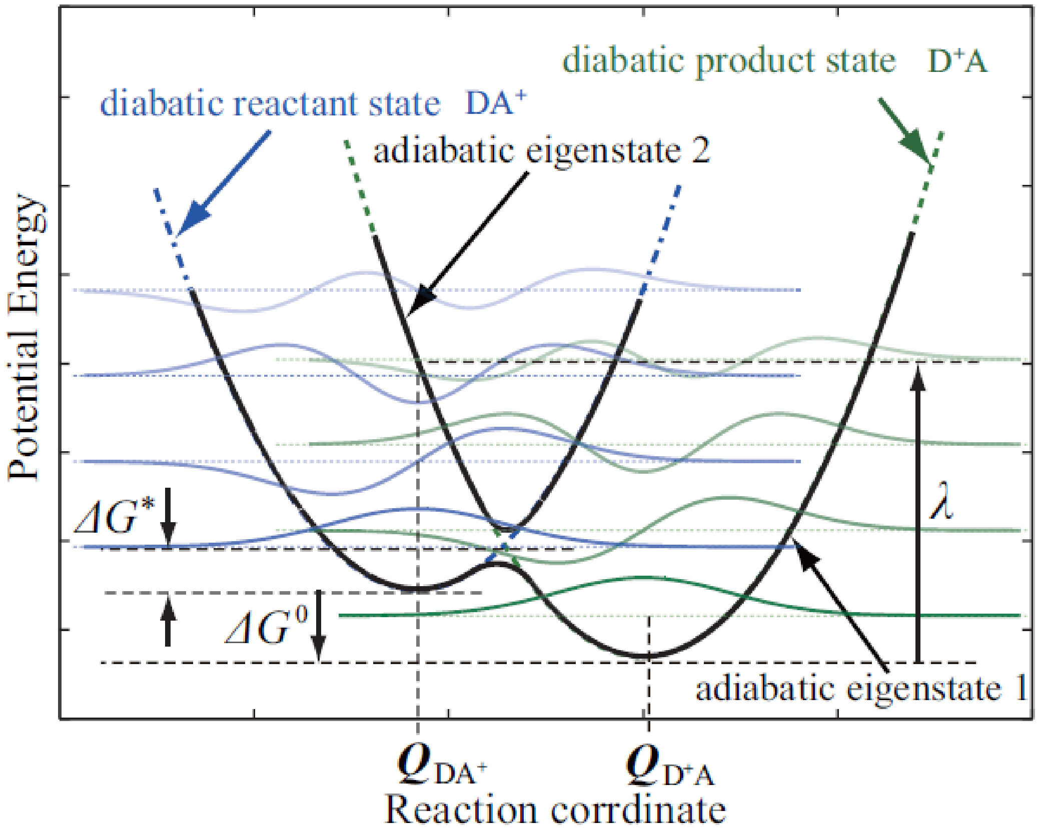

Figure 19 Representation of diabatic and adiabatic states for reactants and products (as shown in Figure 18), but now also including vibrational levels (vibronic model). Depending on the overlap of vibrational levels, the tunneling probability can be favored or hindered). Reprinted with permission from ref [102].

The Fermi Golden rule of perturbation theory, considering the full Hamiltonian of the system, leads to the charge transfer constant [107]–[109]

$$k_{i,j} = \frac{2\pi}{\hbar}\left|H_{R,P}\right|^2 |\langle r_{vib}|p_{vib}\rangle|^2 \delta\left(E_i - E_j\right) \qquad (53)$$

in terms of isolated levels for the reactant and products (with $|r_{vib}\rangle$ and $|p_{vib}\rangle$ being the vibrational states of reactant and product respectively). $H_{i,j} = \langle i|H|j\rangle$ is the electronic matrix element that mixes the donor and acceptor states (in our case $i = R$, $j = P$). The same expression can be written in terms of the density of states of the product, $\rho(E_P)$

$$k_{R,P} = \frac{2\pi}{\hbar}\left|H_{R,P}\right|^2 |\langle r_{vib}|p_{vib}\rangle|^2 \rho(E_P) \qquad (54)$$

And then in terms of the Franck-Condon weighted density of states ($FCWD$)

$$k_{R,P} = \frac{2\pi}{\hbar}\left|H_{R,P}\right|^2 (FCWD) \qquad (55)$$

Assuming the case of non-adiabatic charge transfer, in the context of the polaron model, each electronic state is coupled with a number of vibrations treated as harmonic oscillators with separated nuclear and electronic coordinates [110]–[115]. Under this assumption, the total Hamiltonian of the system can be written as:

$$H = |R\rangle\langle R|\left\{E_R^0 + \frac{1}{2}\sum_l f_l\left(Q_l - Q_{R,l}\right)^2\right\} + |P\rangle\langle P|\left\{E_P^0 + \frac{1}{2}\sum_l f_l\left(Q_l - Q_{P,l}\right)^2\right\} + (|R\rangle\langle P| + |P\rangle\langle R|)H_{R,P} \tag{56}$$

Compared to the previous expressions, the substitution $Q_R = Q_{DA^+}$ and $Q_P = Q_{D^+A}$ has been made to simplify the notation.

The term within the first curly bracket represents the potential of the left parabola, corresponding to the reactants, whereas the second term within the curly brackets represents the potential of the products. This Hamiltonian is known as the spin-boson model or the polaron model. It involves two electronic states that are coupled with numerous vibrational levels, which can be either quantum mechanical or classical. If we consider coupling with a specific vibrational mode, characterized by frequency ω and equilibrium displacement $Q$, then the reorganization energy for that vibrational mode can be written as follows:

$$\lambda_i = \frac{f}{2}(\Delta Q_e)^2 \tag{57}$$

The expression for $\lambda_i$ can be further rewritten in terms of a dimensionless quantity known as the Huang-Rhys factor (HR), which is essentially the electronic-vibrational coupling constant and takes into account the relation between the change in electronic potential energy due to the change in vibrational coordinate and the reorganization energy [106].

$$S = \frac{\lambda_i}{\hbar\omega} = \frac{f}{2\hbar\omega}(\Delta Q_e)^2 = \frac{\mu\omega}{2\hbar}(\Delta Q_e)^2 \tag{58}$$

From these considerations, given the coupling with a single vibrational mode such that $\hbar\omega \gg k_B T$, it is possible to generalize the expression of the charge transfer rate constant as [114]:

$$k_{R,P} = \frac{2\pi}{\hbar}{H_{R,P}}^2\left(\frac{1}{4\pi\lambda_0 k_B T}\right)^{1/2}(FC) \tag{59}$$

With $(FC)$ being the Franck-Condon factor:

$$(FC) = \sum_{\nu'} \exp\left(-S\right)\frac{S^{\nu'}}{\nu'!} exp\left\{\frac{-(\lambda_0 + \nu'\hbar\omega + \Delta G^0)^2}{4\lambda_0\, k_B T}\right\} \tag{60}$$

The Franck-Condon factor takes into account the sum of all possible vibrational overlap integrals for transitioning from level $\nu$ to $\nu'$. Each of these considered possibilities represents a potential channel for the reaction from $\nu$ to $\nu'$. This sum is dominated by channels where the overlap between $\nu$ and $\nu'$ is optimal, which occurs when the energy released ($\Delta G^0$) and the sum of the reorganization energies and the initial vibrational energy of the product ($\nu'\hbar\omega$) are similar. It's important to note that the expression of reorganization energies in this formulation approaches the classical version described by the previous equation (47) in the high-temperature limit. On the other hand, the portion of the equation preceding the Franck-Condon factor represents the transfer rate in the absence of a barrier; this includes $H_{R,P}$ and the classical density of states [106].

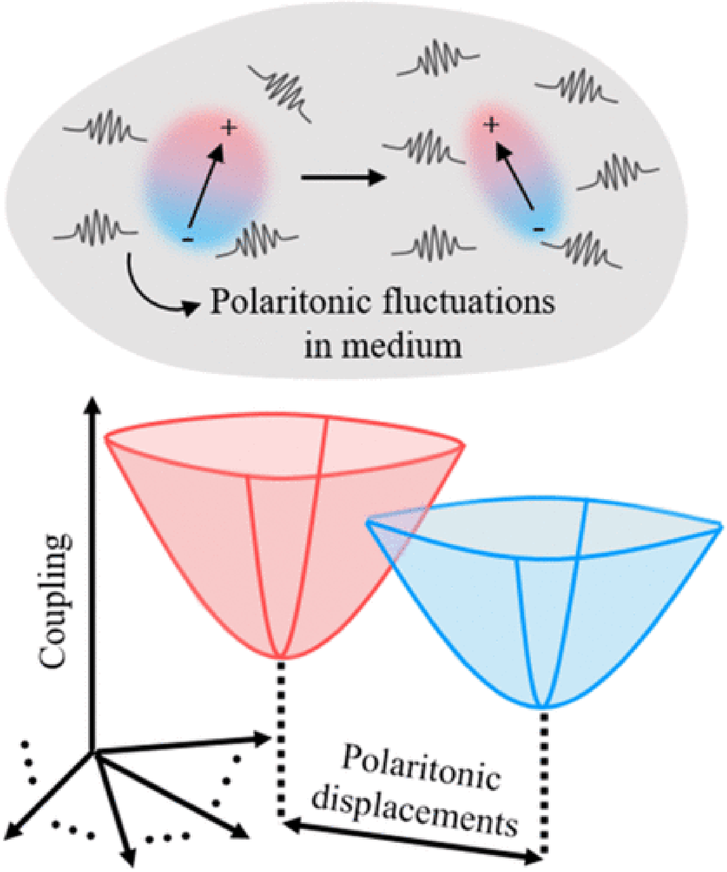

Figure 20 Schematic illustration of multiple-mode polaritronic displacements. Reprinted with permission from ref [116].

## 2.3. CISS effect: challenges and state of the art

The discovery of chirality dates back to the mid-19th century and is primarily attributed to the name of Louis Pasteur and his research on tartaric acid (a highly common organic acid, also found in our teeth). In fact, while studying this substance in 1848 [117], Pasteur noticed the presence of two different types of crystals, one being the mirror image of the other (what would later be defined as enantiomers). He was the first to manually separate the two crystallized enantiomers using only an optical microscope and tweezers, achieving what can be considered the first artificial chiral resolution in the history of science. Subsequently, he analyzed the solutions of the two separated enantiomers with a polarimeter and observed the following effect: the passage of light through the two enantiopure mixtures of tartaric acid resulted in the dextrorotatory or levorotatory rotation of the polarization plane of the outgoing radiation with respect to the incoming radiation, depending on which solution was used as a “filter”. This ability to rotate the plane of polarization of light is called optical activity and constitutes the first observed experimental manifestation of chirality.

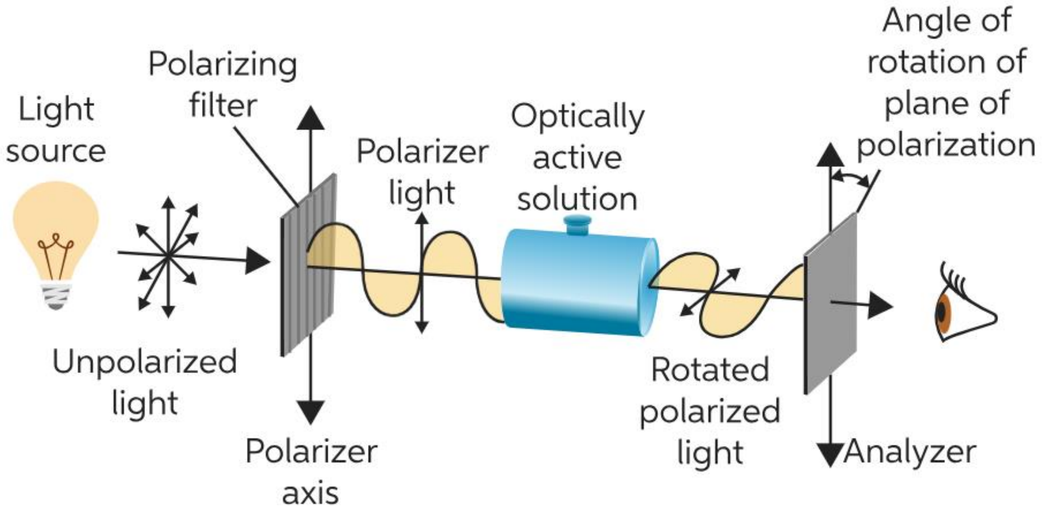

Figure 21 Schematic representation of a polarimeter, an instrument which can be used to measure the rotation of polarized light when it passes through an optically active (chiral) substance (the optical activity). The process starts with a light source (a LED, for example) generating regular light, which is then polarized by passing it through a polarizer. This polarized light travels through the sample, and if the substance is optically active, it causes the polarization plane to rotate. Finally, the light with the altered polarization plane passes through an analyzer, which is another polarization filter. Reprinted with permission from ref [47].

Aways Pasteur, in 1857 [118], published a study in which he observed the preferential consumption of (+)-tartaric acid over (-)-tartaric acid in the fermentation of ammonium paratartaric acid under the influence of microscopic fungi. This example of asymmetry can be considered the earliest known form of "chiral recognition," which refers to the preferential interaction of an analyte with one enantiomer of a chiral substance (the selector) [119].

These discoveries led to the formulation of the first definition of chirality by Kelvin in 1905 “any geometrical figure, or group of points,” is chiral and has chirality “if its image in a plane mirror, ideally realized, cannot be brought to coincide with itself ” [120]. Therefore, chirality was first defined as a situation of geometrical broken symmetry: a molecule is chiral if it is not superimposable on its mirror image by any combination of rotations, translations, or some conformational changes. The presence of a symmetry element of reflection (such as a point or plane of symmetry) guarantees the achirality of an object. Consequently, chiral objects lack reflective symmetry elements (though they might possess rotational symmetry axes) [121]. A common stereogenic element that defines the chirality of a molecule is a chiral center, which refers to an atom with four distinct groups bonded to it in a way that its mirror image cannot be superimposed. The most typical example is that of the so-called asymmetric carbon atom. Two stereoisomers that are mirror images of each other are called enantiomers and they are often distinguished as either "right-handed" or "left-handed" by their absolute configuration. The two enantiomers have the same chemical properties, except when interacting with other chiral compounds (i.e. chiral recognition). They also have the same physical properties, except that they exhibit opposite optical activities (i.e. opposite interaction with linearly polarized photons) [122].

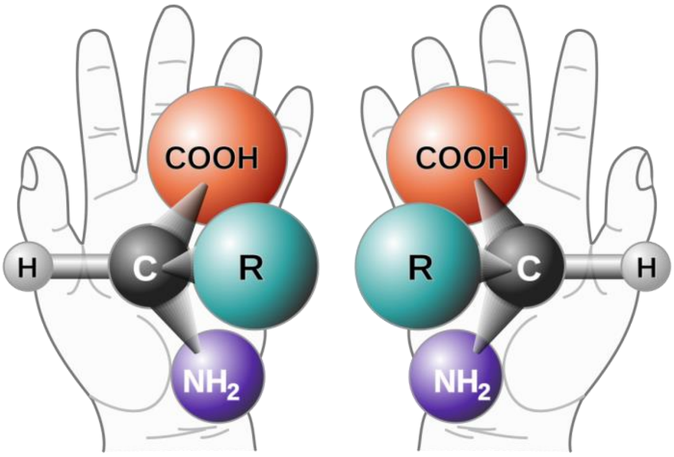

Figure 22 Chirality is derived from the Greek word χειρ (kheir) that stands for "hand". In fact, hands serve as instances of non-superimposable mirror images. However, the concept of chirality (along with its ensuing implications) is significantly more expansive. This conventional portrayal involving hands runs the risk of becoming overly simplified and reductionist.

The discussion presented so far about chirality involves a predominantly geometric approach to the issue. This is the most "basic" definition, which has been used extensively in chemistry. However, delving deeper into the matter, such a perspective proves to be significantly incomplete and constraining. Furthermore, when contemplating how nature evolved life on Earth, it becomes evident how crucial and intricated chirality's implications are: the vast majority of amino acids, proteins, and various bio-related molecular structures are chiral and exhibit a single handedness in the natural world. For instance, proteins typically possess a right-handed configuration, while amino acids are only found in nature in their L-configuration [36]. RNA and DNA also exhibit supramolecular right-handed chirality, because of the compositional asymmetry of sugars forming their backbones [39]. This phenomenon is referred to as the "homochirality of life" and extends to macroscopic reality as well; in fact, living organisms generally display a preferred handedness even on a larger scale. For example, body snail shells can be right-turning or left-turning helices, but one form or the other is strongly preferred in a given species; even more simply, the human heart is typically located on the left side of the body. Biological organisms easily discriminate between molecules with different chiralities, even though the mechanism underlying this recognition process remains unclear to this day [119]. Given this complexity, it becomes essential to look beyond the "right-left hand typical cartoon used to explain chirality at-a-glance" (i.e. Figure 22), and consider the implications that chirality, as a pervasive and intrinsic phenomenon in all life as we know it, has on all interactions of matter.

For instance, it's necessary to distinguish between the chirality arising from a stereogenic center and the so-called inherent chirality, which is caused from the twisting of a molecule in 3-D space. The term "inherent chirality" was first introduced by Volker Boehmer in a 1994 review [123] to describe the chirality of calixarenes resulting from their non-planar structure in three-dimensional space. Numerous studies in the literature report the use of molecules possessing this kind of "tailored torsion" chirality, leading to remarkable results in the discrimination of enantiomers of chiral probes [124], [124]–[127].

Furthermore, while the "geometric" approach to chirality can effectively describe rigid molecules, it may not provide a complete understanding for flexible or partially flexible molecules. This Erica Flapan to introduce the concept of "topological chirality," which treats all molecules as if they were entirely flexible and employs distinct mathematical techniques to demonstrate a molecule's topological chirality [128].

The classifications of chirality mentioned so far, whether they are "classical", intrinsic, chemical, or topological chirality, all involve assigning a dichotomous character: the molecule (or the ion or the molecular complex) is either chiral or not. However, in his 2000 paper Patrick Le Guennec has very elegantly shown that this discrete view of chirality coexists with a continuous description of how achiral symmetry is broken in the case of square-integrable ($L^2$) wavefunctions of non-relativistic quantum mechanics [129]. His results are presented in the case of two spatial dimensions and then generalized to three and higher dimensions and to the whole nonrelativistic quantum description of matter, leading to the identification of two complementary forms of chirality: absolute and relative As a result, chirality can be conceptually described both in a dichotomous manner (in accordance with Kelvin's definition), like an open/closed door, and simultaneously in a continuous manner: molecules are more or less chiral just as a door can be more or less open. These two interpretations, whose coexistence may seem paradoxical, are hierarchically related since the geometrical toolbox in which chirality is understood as discrete, i.e., Euclidean geometry, is included within the geometrical toolbox in which it is understood as continuous (the “post-Euclidean” operations associated with radial canonical groups).

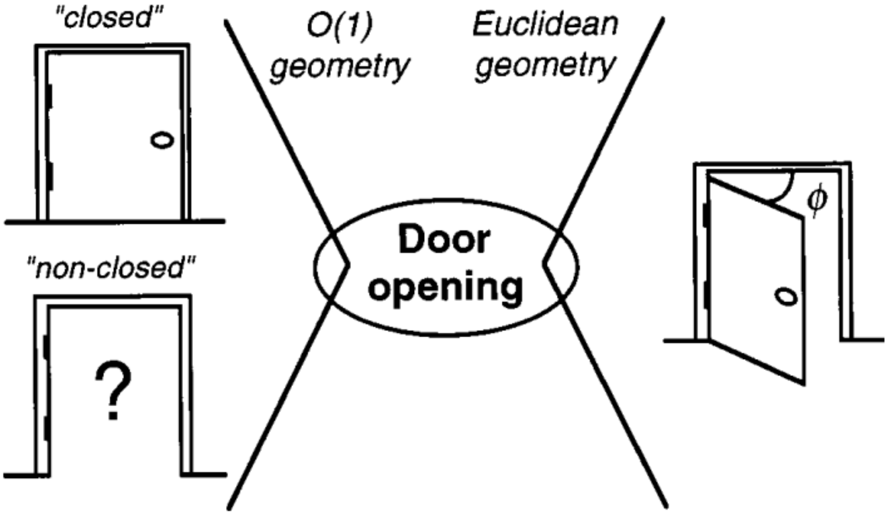

Figure 23 The phenomenon of door opening can be perceived through two distinct geometric "lenses" (in this example, O(1) geometry and Euclidean geometry). On the left, a simplified toolbox employing only two operations, “id” and “σ”, forming the O(1) group. O(1) definition of door opening: “I call any door non-closed (open), and say it has opening, if its σ image cannot be brought to coincide with itself. This definition confines our perception to the closed arrangement's associated symmetry property. On the right, the broader Euclidean toolbox empowers us to consider the rotational aspect of the door/wall system. This approach provides a continuous framework for describing how the previous symmetry is disrupted during door opening. O(1) and Euclidean operations can be likened to optical and electronic microscopes, offering varying levels of detail about the same surface. This continuous interpretation of chirality evolves in a similar manner. Reprinted with permission from ref [129]

Within the realm of defining chirality, it's also crucial to emphasize that its meaning is not interchangeable with that of handedness: despite often being used as synonyms, these terms indeed hold distinct implications in specific systems, such as in the context of magneto-chiral dichroism [8], [130]. The magneto-chiral dichroism was experimentally established in 1997 through luminescence measurements in a magnetic field by Rikken and Raupach. Two years later, in 1999, K. Ray, P. Ananthavel, D. Waldeck and R. Naaman definitively unveiled the complementary Chiral Induced Spin Selectivity effect (CISS effect) [6] following the earlier experimental confirmations by Mayer and Kessler [7]. These two discoveries added crucial pieces to the scientific puzzle of establishing a definitive connection between magnetism, spin, handedness, and chirality; quantities that have been suggested to be closely intertwined since Pasteur's early insights.

The essence of the CISS effect lies in experimental evidence that charge transport and transmission through a chiral molecule is spin dependent. The CISS effect can be quantified by defining a polarization for a measurable property and its dependence on the electron spin direction [40]. Commonly, the polarization P is defined as

$$P(\%) = \frac{A_{UP} - A_{DOWN}}{A_{UP} + A_{DOWN}} \cdot 100 \qquad (61)$$

Where $A_{UP}$ and $A_{DOWN}$ are measurable properties of the system that depend on the spin direction ($UP$ versus $DOWN$). Properties for which polarizations have been measured include current, electron transfer rate, and yield of electrons.

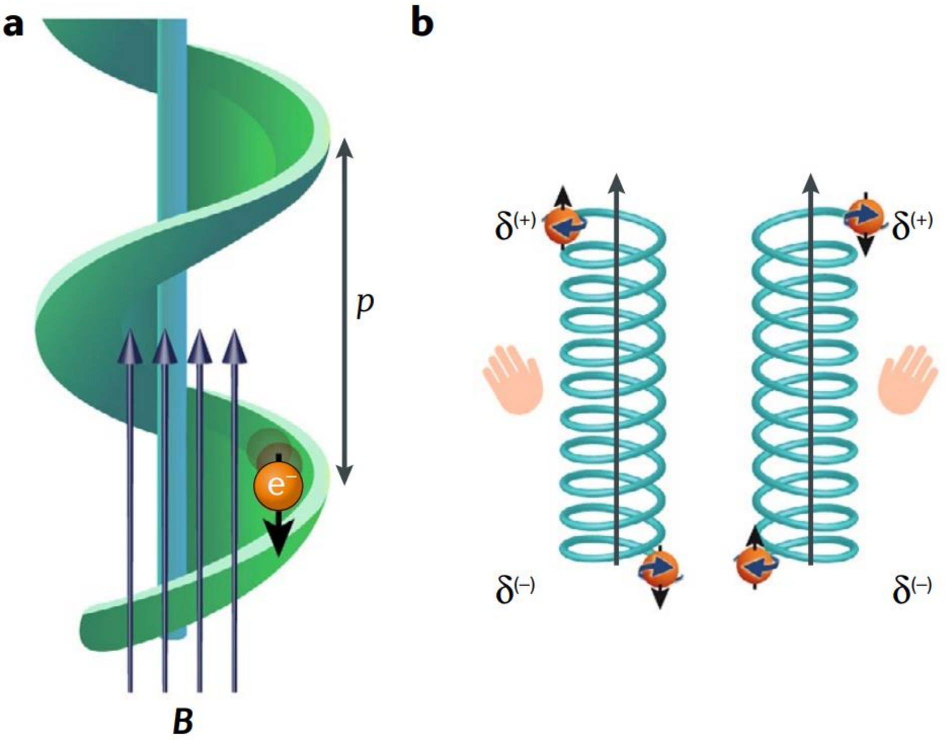

Figure 24 **a)** illustrative representation of electron transmission through a chiral potential with a given pitch, denoted as "p". The electron is symbolized as a sphere, with its spin direction indicated by an arrow. As the electron navigates within the potential, it experiences a constant force modeled as a classical centripetal force ($F_{CEN}$), acting perpendicularly to its velocity. This force is analogous to a Lorentz force "F" generated by an applied magnetic field "B" along the molecule's axis. The effective spin-orbit coupling is expressed as $(\vec{\mu} \cdot B)$, where $\vec{\mu}$ represents the spin magnetic moment. **b)** schematic depiction of the charge and spin polarization within chiral molecules when subjected to an electric field directed along their axes (as indicated by the black arrows). The electric field induces a spin-selective electron displacement that results in temporary spin polarization at the electric poles (designated as $\delta^{(+)}$ and $\delta^{(-)}$, positioned at the helices' ends). The spin associated with each pole depends on the handedness of the molecule (SDCR effect). Reprinted with permission from ref [2].

In general, experiments studying CISS effect manifestations can be classified into three main categories: the first one involves the transmission of unbound electrons (often photoexcited from an underlying substrate) through a chiral medium into vacuum (this was the first experimental evidence recorded even at a historical level, precisely through the measurements conducted by Meyer and Kessler). The second category, where most research has been focused, involves the transport of bound electrons between electrode leads through a chiral medium. The third and more recent category revolves around the interplay between electron spin and chemical reactions.

Regardless of the type of experiment, a common element that emerges from many measurements involving CISS is the connection between spin polarization and the optical activity of a chiral molecule (as defined at the beginning of this section) [18], [30], [131]. These observations imply that the magnitude of spin polarization is influenced by the interaction between the moving electron and the electron cloud of the chiral molecule. Furthermore, this interaction is itself affected by the motion of the moving electron. This reciprocal influence leads to another important manifestation of the CISS effect, known as spin-dependent charge reorganization (SDCR) [42]. So, even when dealing with closed-shell molecules (total spin equal to 0), exposure to the electric field associated with the passing electron, due to the reorganization of molecular charges, generates a spin dipole whose orientation depends on the handedness of the molecule. This spin polarization, which goes with charge redistribution in chiral molecules, has been experimentally confirmed for the first time through Hall effect measurements by Anup Kumar et al. [42] and has significant consequences for all molecular interactions. In fact, the SDCR effect results in spin-dependent forces that impact charge transfer capability, but also reactivity and interactions with ferromagnetic surfaces (as will be discussed shortly), as well as effects related to enantio-recognition and enantio-separation [40]. In this regard, this thesis work specifically focuses on transport experiments across chiral interfaces and the investigation of the implications of CISS on reactivity (within the second and third categories previously mentioned). In particular, one of the aspects we have investigated the most is the mechanism underlying enantio-recognition and the rationale it finds when considered as a manifestation of the CISS effect. Indeed, chiral recognition, intended as the preferential, non-isotropic interaction between a pure chiral selector and one of the two enantiomers of an analyte, is one of the most important issues in the natural world. Biological molecules exhibit this type of behavior naturally and continuously, making them much more efficient than synthetic chiral receptors [132]. To this day, as stated in an important paper by one of the leading pioneers in the field in 2006, Alain Berthod [119], a complete understanding of the chiral recognition mechanism has not been realized, despite its utmost scientific and technological urgency (considering that a complete description of the phenomenon would allow researchers to predict which selector would best separate the enantiomers of chiral compounds, with all the associated implications). Current models, such as the three-point interaction or the lock and key mechanism, are based on assumptions of mere molecular geometry, providing a superficial and inadequate description of chirality (as discussed at the beginning of this section). Consequently, these models on their own are incapable of explaining numerous experimental findings involving phenomena that do not exclusively involve "simple" molecules (like enantiomerism based on a stereogenic center) or “simple” interactions.

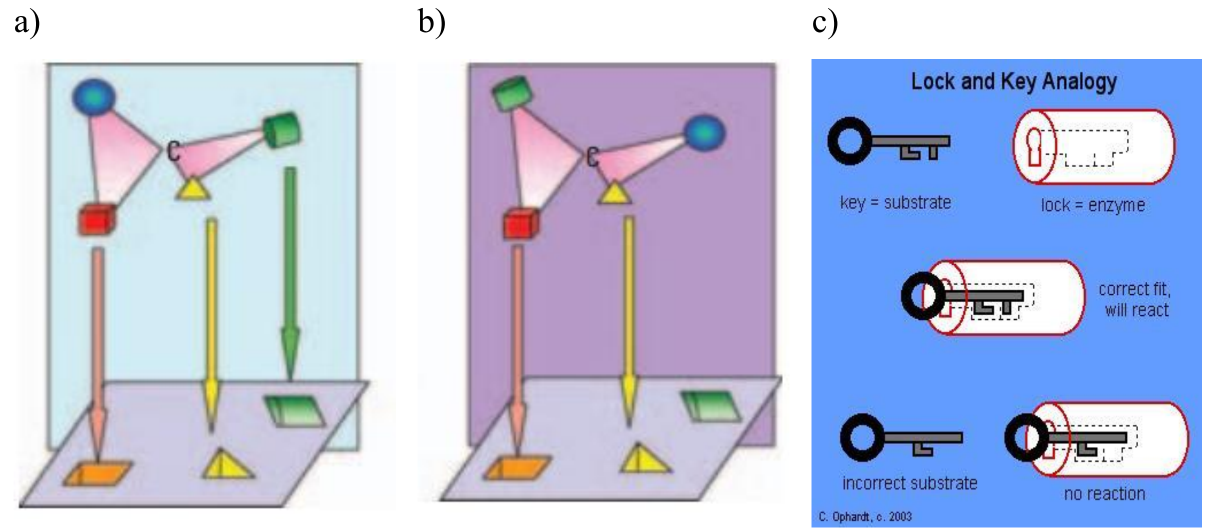

Figure 25 Panels **a)** and **b)**: three-point model interaction (different binding constants between two enantiomers for a specific selector handedness). The enantiomer in panel a) can present three substituents to match the selector's three-point site; no matter how its mirror image rotates (panel b), the enantiomer can match a maximum of only two sites [119]. Panel **c)**: lock and key model. An over simplistic interpretation of natural asymmetric synthesis [133].

Evidence in the study of SDCR, which highlights its consequences in the study of interactions between a molecule and ferromagnets[41], [134] as well as between two chiral molecules[42], suggests that enantioselectivity should depend on both a three-dimensional spatial or steric shape effect (the lock and key effect) and a spin-dependent electronic term (in which CISS plays a fundamental role).

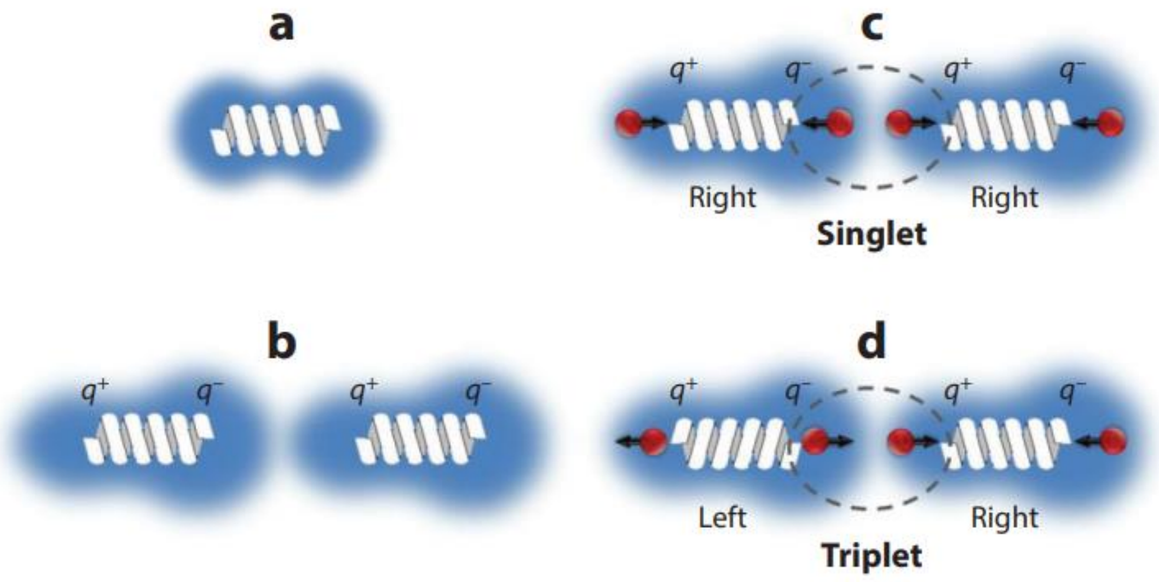

Figure 26 The impact of spin-dependent charge reorganization (SDCR) when two chiral molecules approach each other and interact. **a)**: the electron distribution (blue cloud) within a molecule without a dipole moment before it engages with another molecule. In this scenario,

the distribution is symmetrical. **b)** two molecules interact. The interaction term is the spin-exchange interaction, the same term that causes the splitting between singlet and triplet states in molecules and atoms. When the two molecules interact, the electron density distribution generates charge polarization, specifically, an induced dipole-induced dipole interaction. **c)** the described interaction occurs between same handedness molecules: as charge q shifts from one side of the molecule to the other, it generates a spin polarization (red ball and black arrow) of the same spin in the two molecules. The residual electron density exhibits the opposite spin polarization; as a result, the interaction between the molecules is marked by two opposing spins, as illustrated by the singlet region in the dotted circle. **d)**: on the contrary, when the two interacting molecules have opposite chirality, the interaction is characterized by two parallel spins (within the triplet region in the dotted circle). Reprinted with permission from ref [42].

In order to investigate these subtle phenomena through transport measurements, various types of techniques are employed in the literature. Certainly, one of the crucial aspects is to establish appropriate contact between the chiral medium and the metallic electrodes used to inject current or impose a voltage difference. In this regard, one solution is to exploit the formation of Self-Assembled Monolayers (SAMs) on noble metals. Many studies have particularly utilized the chemisorption of thiol groups (-SH), which are often included in the structure of the chiral molecule of interest during synthesis for the purpose of anchoring to the substrate, given their strong binding energies. This approach is used for a variety of purposes, including both chiral molecules with aliphatic backbones [135] and double-stranded DNA chains [10], as well as aromatic systems [136]. The scientific path involving the use of thiophenes ($-C_4H_4S$) as anchoring groups to obtain Self-Assembled Monolayers (SAMs) on electrode materials is much less explored, and the SAM growth process of monomer thiophene is still yet to be clarified. This is despite the fact that thiophenes consist of π-conjugated groups and, in principle, could exhibit charge transport behavior with higher carrier mobilities compared to thiols under equivalent conditions. The primary reasons for the lower success of thiophenes, when it comes to adsorption, lie in the greater difficulty in achieving an ordered packing of the film and the possibility of dissociation phenomena during adsorption, especially when using transition metals [137]. In the case of noble metals, the results are still not entirely clear, as there have been numerous examples of efficient SAM formation with a good degree of order [138]–[140].

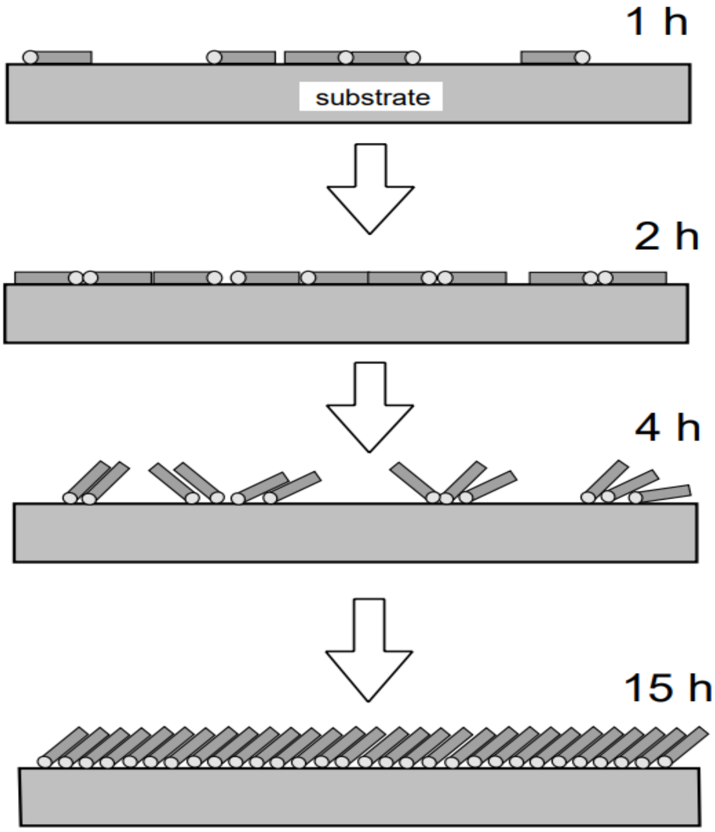

Figure 27 Pictorial diagrams of a mono-layer growth of thiophene from ethanol solution on a gold substrate, forming a well-ordered SAM. Reprinted with permission from ref [139].

In this thesis, both thiophenes and tetrathiafulvalenes (TTF) have been successfully employed to create hybrid interfaces between noble metals and monolayers of chiral molecules. The resulting architectures were meticulously characterized, and the functionalization procedures were accurately described, expanding the focus not only on the manifestation of the CISS itself but also on the preparation of a "clean" setup to ensure the quality of the contacts.

Once the system has been carefully contacted, transport measurements in the context of the CISS can be carried out using two main paradigms: in the solid state and in electrochemical systems. In the former case, two of the most relevant techniques employed are magnetic conductive AFM (mc-AFM) and magnetoresistance. In the first case, spin injection is achieved either by utilizing a ferromagnetic substrate (to which the molecules are adsorbed) and closing the circuit with the conductive tip of the AFM [141], or conversely, by using a ferromagnetic tip (usually made of nickel) that contacts a metal|molecule hybrid system [21]. The system is, of course, placed within a static magnetic field. Several studies have reported current imbalances in the resonance region of I-V curves depending on the handedness of the chiral medium and the orientation of the magnetic field, with observed spin polarization ranging between 30% and 50% [142]–[144], with particularly impressive exceptions of 85% values. An example of this is found in the multilayer configuration of hybrid 2D layers of perovskites, where a presumed "multiple chiral tunneling process" effect has been hypothesized [21]. Regarding magnetoresistance, given that spin injection requires one of the two terminals to be ferromagnetic, experimental setups with both two and four contacts are used, with a cross or inline arrangement. Current polarization is measured as a function of the magnetic field orientation, with reported spin-polarization values ranging from 6% to 90% for self-assembled monolayers (SAMs) of chiral molecules [136], [141], [143], [145]–[150].

In the field of electrochemistry, over the last two decades, a specific branch of spintronics based on the study of spin-polarized transport and spin-detection has emerged and developed: spin-dependent electrochemistry [151]. This technique involves the use of a chiral spin-filtering medium coupled to a ferromagnet that acts as the working electrode of an electrochemical cell. The ferromagnetic material is magnetized by a permanent magnet and allows to introduce charge carriers with a particular spin orientation [144]. This effect is known as spin injection and is the exact same phenomenon utilized in the previously discussed solid-state techniques within the field of spintronics. To briefly explain the physics: the "majority" spin electrons become stabilized relative to the "minority" spin electrons. Consequently, the spin sublevels of the ferromagnetic electrode become populated to varying degrees (there is an imbalance in the population of the "$DOWN$" and "$UP$" spin sublevels, also referred to as "$\alpha$" and "$\beta$"). When we examine the electronic states just below the Fermi level ($\varepsilon_F$), the density of states is higher for the “majority” spins, causing that most of the spins ejected from the electrode have the “spin orientation” of the “majority” spins (relevant to an electrochemical driven reduction process) [152]. On the other hand, when we look at electronic states above the Fermi level, we observe that the highest density of states corresponds to minority spins; as a result, electrons with this spin orientation will be more effectively injected into the electrode (electrochemical oxidation process). Such a theoretical based picture yields for a spin polarized current to flow through the chiral medium coupled to the ferromagnetic surface. Thus, the spin polarization (SP) induced by the chiral systems can be calculated by measuring the current as a function of the magnet orientation

$$SP = \frac{I_{UP} - I_{DOWN}}{I_{UP} + I_{DOWN}} \qquad (62)$$

It's worth noting that the terms "$UP$" and "$DOWN$" are used for convenience in various experiments, but they don't necessarily reflect the actual orientation of the spin.

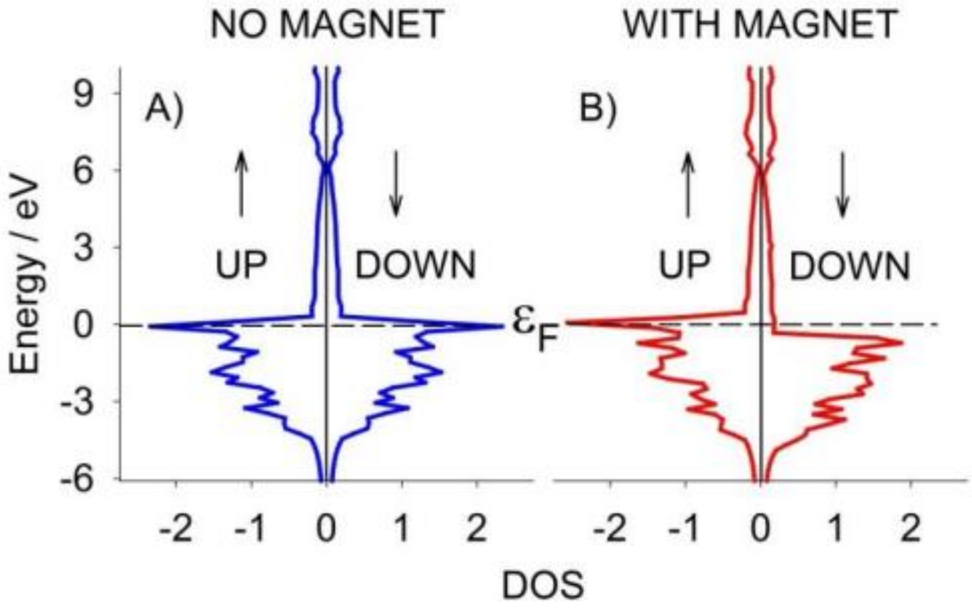

Figure 28 Theoretical VASP based calculations: spin polarized energy vs Density of State (DOS) pattern for metallic Nickel: without (blue curves) and with application of a magnetic field (blue and red curves, respectively). Reprinted with permission from ref [152].

Spin-dependent electrochemistry can be utilized for conducting spin-dependent electrochemical measurements at both the monomer level (by electrode functionalization with a self-assembled monolayer) [153] and for complex systems such as chiral polymers (usually deposited or electro-polymerized on the electrode )[154], [155]. In either case, the chiral medium serves as an analyzer of the spins injected through the ferromagnet, as a function of the direction of the magnetic field. An alternative approach involves embedding a Hall probe inside the working electrode and measuring magnetization resulting from the spin current through the Hall voltage [156]. In the most classical configuration of a Working Electrode (WE) consisting of a spin-selective interface within a magnetic field (within the context of an electrochemical setup with a 3-electrode cell), the faradaic current signal that is measured to probe the charge transfer is typically obtained through the oxidation-reduction of a redox probe. This probe can be present in the bulk solution [13] or covalently bound to the electrode [28]. In the field of electrochemistry, there has recently been significant attention on a second-order effect that can still be attributed to the CISS phenomenon. This effect pertains to the influence that the use of spin-selective interfaces can have in guiding enantioselective chemical reactions or promoting/inhibiting the production of byproducts. While these processes still involve charge transport through a chiral medium, this research area is typically considered separately. The emphasis is placed on the "chemical" effects of spin-selectivity, treating the electron's spin as a genuine enantioselective chemical reagent [33]. The origins of this field can be traced back to the work of Rosenberg et al. [157]: they demonstrated that the use of low-energy spin-polarized secondary electrons, initially obtained through irradiation of a ferromagnet and later achieved through a nonmagnetic substrate with a chiral DNA overlayer acting as a spin filter [158] (exploiting the CISS effect), leads to different bond cleavage rates for R and S enantiomers. The chiral bias produced by the electron helicity of spin-polarized electrons (which results in the discussed SDCR effect) has subsequently been employed in numerous other experiments. These include guiding enantioselective electrochemical reactions (both oxidation and reduction) and explaining the enantiospecific interaction of various enantiomers with magnetized substrates [69], [72], [74], [159]–[161].

Among the examples of utilizing spin as a chemical reagent, this thesis primarily focuses on its influence on a highly relevant technological process: hydrogen production ($H_2$) through electrochemical water splitting (WS). The overall water electrolysis reaction involves the transfer of four protons and four electrons and can be simply written as [162]:

$$2H_2O_{(l)} \rightarrow 2H_{2(g)} + O_{2(g)} \tag{63}$$

This reaction is the result of two semi-reactions that must occur, one at the cathode and the other at the anode, leading to the splitting of water molecules. These are known as the hydrogen evolution reaction (HER) and the oxygen evolution reaction (OER), respectively. As just mentioned, both semi-reactions can occur under both acidic and alkaline solution conditions, but their mechanisms and efficiency strongly depend on the pH. Of the two semi-reactions, the OER exhibits the most technological challenges and is often the rate-determining step in hydrogen production from water. Consequently, nowadays the tendency is to adopt alkaline electrolyte solutions, which strongly favor the OER over a neutral or acidic environment [163]. Explaining the difficulties associated with the OER is not straightforward and has been the subject of extensive research efforts over the past 20 years. It is a multi-step reaction involving the exchange of 4 electrons (one at each step) to achieve the oxidation of 4 hydroxyl groups (in the case of a basic environment).

$$4OH^- \rightarrow 2H_2O_{(l)} + O_{2(g)}4e^- \tag{64}$$

The primary obstacle is the sluggish kinetics of this complex reaction. At each elementary step, energy accumulates, necessitating the application of significant overpotential compared to the theoretical thermodynamic potential (which is 1.23 V at 25°C), resulting in strong process inefficiency. Additionally, devices based on water splitting, such as fuel cells or metal-air batteries, suffer from the production of unwanted byproducts, such as peroxides and superoxide radicals [164]. These byproducts further reduce overall efficiency and can adsorb to electrode materials, causing damage or inhibiting reaction sites. For these reasons, it is crucial that the anode serves as an electrocatalyst with characteristics that promote OER kinetics, thus reducing overpotential, while limiting the formation of byproducts, all while remaining stable in a strongly alkaline environment.

Initially, a common approach for finding the ideal catalyst involved using electrodes based on noble metals like Pt, Pd, Ru, Ir, and Rh. However, this path became impractical due to their cost and availability. An increasing understanding of the OER reaction mechanism has led to the development of more efficient materials, such as transition metal (oxy)hydroxides and oxides (in particular Fe- Co- and Ni- based), doped 2D materials, perovskites, etc. [165] These electrode materials are particularly attractive due to their electronic structure, which theoretical simulations have identified as a fundamental parameter for reducing overpotential. The prevailing interpretation in the literature to explain the catalyst's action is based on the assumption that the main active sites for OER are the surface metal cations (M). During the reaction, numerous reaction intermediates form M-O bonds, and high catalytic activity is achieved when adsorbed species bind neither too strongly nor too weakly to the surface (Sabatier's principle) [166], [167]. The relationship between OER activity and M-O bond strength exhibits a volcano shape [168], with the catalyst having the optimal M-O bond strength at the top, while catalysts with excessively strong or weak M-O bond strength are located on the left and right sides of the volcano plot [169].

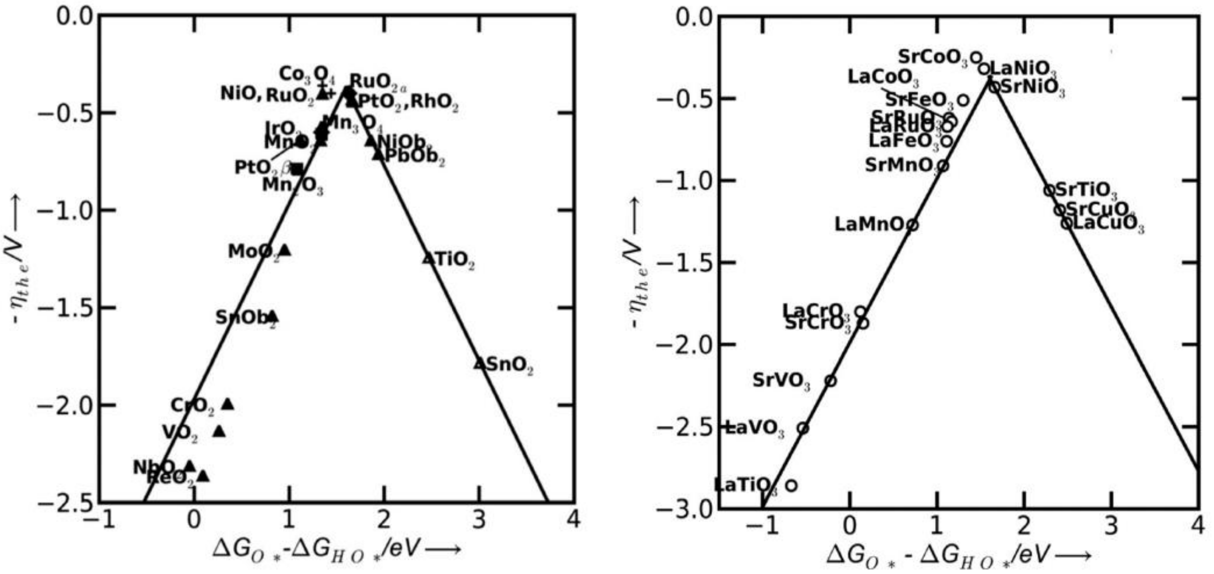

Figure 29 Volcano plots: theoretical overpotential for oxygen evolution ( $\eta_{the}$ ) vs. the difference between the standard free energy of two subsequent intermediates ( $\Delta G^0_{O^*} - \Delta G^0_{HO^*}$ )

for various binary oxides (left) and perovskite oxide (right). Reprinted with permission from ref [162].

In the last decade, this traditional view regarding the fundamental parameters influencing the anodic material for the OER has been complemented and enriched by the study of spin effects on oxygen evolution. This line of research draws inspiration from natural biological processes, particularly the study of how electron-spin correlation impacts the generation of $O_2$ in photosynthesis. This development naturally arises when considering that the OER involves the transition from reactants in a ground spin state of singlet ($OH^-$ / $H_2O$), where all electrons are paired, to the diatomic oxygen product, whose ground state is a triplet with the frontier $\pi^*$ orbitals occupied by two electrons in parallel alignment. In general, transitions from a singlet species to a triplet one are very complicated and require specific perturbations such as spin-orbit coupling, which often involves the use of high-atomic-number (heavy) atoms [72]. This observation has led to the hypothesis that one of the reasons for the high overpotential required for the OER is an unfavorable reaction pathway: a high percentage of $O_2$ is actually produced in an excited singlet state (rather than the ground state triplet), which is over 1 eV higher in energy, leading to a much greater activation barrier [170]. Additionally, the primary byproduct of the reaction, hydrogen peroxide ($H_2O_2$), is also in a singlet state. Therefore, its production competes strongly with the desired oxygen production. The natural implication of these considerations is the recognition that the role played by the spin polarization of the radical intermediates in the reaction is crucial for achieving high OER efficiency. In this regard, starting twenty years ago, numerous theoretical works have highlighted the centrality of a magnetic anode in the catalysis process. Magnetic anodes that were already experimentally used (Nickel, Iron, Cobalt-based oxides) led to good results which were attributed almost entirely to their adsorbate binding energy performance (again, the Sabatier principle). In fact, Chretien S. et al. (2008) [171] as well as Torum E. et al. (2013) [172] have highlighted the possibility of obtaining a kinetic benefit in the oxygen evolution reaction by using magnetic anodes since they add the necessary degree of freedom to produce oxygen directly in the ground state triplet without violating angular momentum conservation. Since then, numerous experimental results have transformed the field of electrochemical and photoelectrochemical water splitting thanks to the benefits of spin control.

Two complementary approaches have emerged to form the two main streams: the use of magnetic transition metal oxides in a static magnetic field and the use of chiral catalysts. Two major proponents of the first approach are Garces-Pineda et al. (2019, Nature Energy) [173], who demonstrated increases of up to 100% in the oxygen oxidation current in a weak static magnetic field (0.45 T) with a $NiZnFe_4O_x$ anode and Xiao Ren et al. (2021, Nature Communications) [174], who used ordered ferromagnetic $CoFe_2O_4$ catalysts in a static magnetic field to achieve reductions in the overpotential required for the reaction. In particular, they showed that spin selection crucially enters the reaction mechanism at the first step (first electron transfer between the ferromagnetic catalyst and the adsorbed reactant at the anode). The imposed spin alignment is then spontaneously maintained in the next 3 steps by the adsorbed oxygen species: the electrons involved in the oxygen evolution reaction need to follow the Hund rule and the Pauli principle ultimately resulting in the generation of the triplet state $O_2$. It's important to highlight that, in this case, the effects of applying a magnetic field on the OER are not attributable to indirect influences on performance such as improved gas/liquid diffusion or increased local temperature (as seen in previous studies focusing on the effects of Lorentzian movement on diffusion) [175]–[177]. The results presented in this thesis (Section 4.4) belong to the second approach: utilizing chiral catalysts capable of inducing spin polarization through the CISS effect. Significant improvements have been reported using various anodes (Zn-porphyrins [70], $TiO_2$ nanoparticles CdSe terminated [71], $Fe_3O_4$ nanoparticles [178]) combined with a chemisorbed layer of chiral molecules (typically amino acids, peptides, or DNA chains). The charge transfer through the homochiral layer aligns the spins of the intermediate radicals adsorbed on the electrode surface, promoting the production of ground state triplet $O_2$ molecules and suppressing the formation of singlet $H_2O_2$.

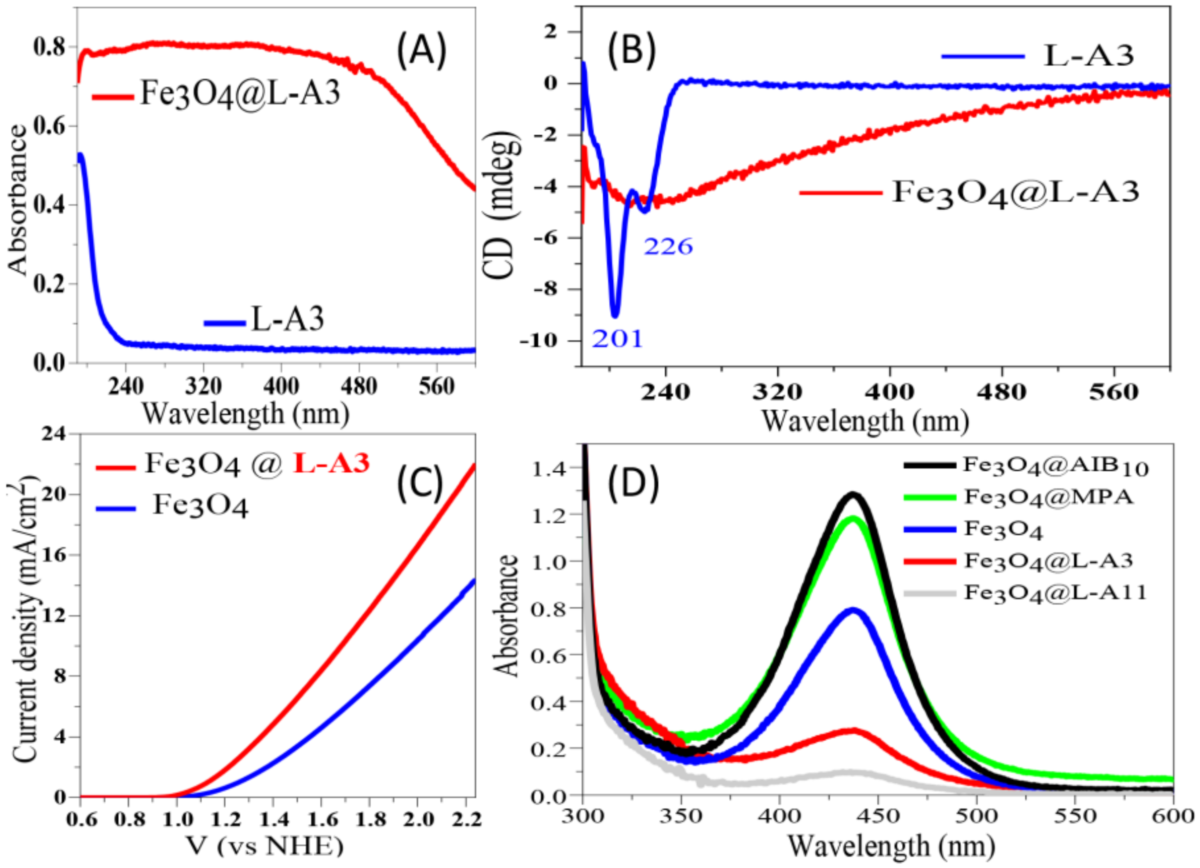

Figure 30 Spin-controlled water splitting performed using regular magnetite nanoparticles ($Fe_3O_4$) and magnetite nanoparticles capped with chiral and achiral molecules: $Fe_3O_4$@L-A11 (chiral), $Fe_3O_4$@L-A3 (chiral), $Fe_3O_4$@MPA (achiral), and $Fe_3O_4$@AIB10 (achiral). **(A)** Absorption spectra of a 1 mM L-A3 solution (blue line) and $Fe_3O_4$@L-A3 (red line); **(B)** panel (A) correspondent CD spectra **(C)** Current density of $Fe_3O_4$ NPs linked with L-A3 (chiral) and pure $Fe_3O_4$ NPs. **(D)** Visible absorption spectra from the titration of the electrolyte used (0.1 M $Na_2SO_4$) with o-tolidine. Displayed trace colors are associated with different measurements in which the respective different working electrodes were used to perform the OER. A higher absorption peak (attributed to reacted o-tolidine with $H_2O_2$) corresponds to a higher $H_2O_2$ presence in solution (developed during the OER). Reprinted with permission from ref [178].

On the other hand, a much less explored approach consists of using modified inorganic electrodes, where a chiral agent is introduced in bulk (rather than solely at the interface as in previous cited works) to induce chirality. This is the case of the so-called "chiral imprinting" practice, which has been brilliantly utilized by Gosh, Bloom, et al. to create homochiral $CuO_x$ films that significantly enhance the efficiency of the OER when compared to the corresponding meso-$CoO_x$ analogs [170]. Over the past two decades, chiral imprinting has received increasing attention due to its potential to create new materials (organic and metal-organic hybrids) with enantio-selective responses. In this case, the introduction of a chiral catalyst is not aimed at guiding a synthesis to favor the formation of one enantiomer over another (in a reaction that can potentially produce a racemic mixture) or at separating a racemic mixture of two enantiomers (common practices in organic chemistry) [179]. Instead, it's focused on inducing chiral properties within the bulk of a typically achiral material, thereby generating a chiral superstructure [19]. This "chiral imprinting" has been successfully employed in the field of organic polymers (experimentally demonstrated in this work, Section 4.2.2) [19], [180]–[182] and, more notably, in the inorganic domain to synthesize chiral metals [161], [183]–[190]. While the mechanism behind the symmetry breaking by the chiral catalyst is still debated, the effects of superstructural imprinting have been observed both at a geometrical and electronic level. This suggests that the induction of chiral properties in the system (resulting in different photoemission of electrons upon excitation by clockwise (cw) and anticlockwise (acw) circularly polarized light, stereo-selective responses to chiral analytes, circular dichroism in the UV-vis and near-UV range, optical activity, etc.) [191]–[194] may be due to a synergistic combination of both effects. In this work, the effects of chiral imprinting are investigated through spin-controlled OER catalysis using an inorganic Nickel electrode [195], building upon the foundations laid by the article by Mishra et al. on chiral nickel [73] (of which I have briefly observed the genesis during my academic journey at the University of Modena and Reggio Emilia).

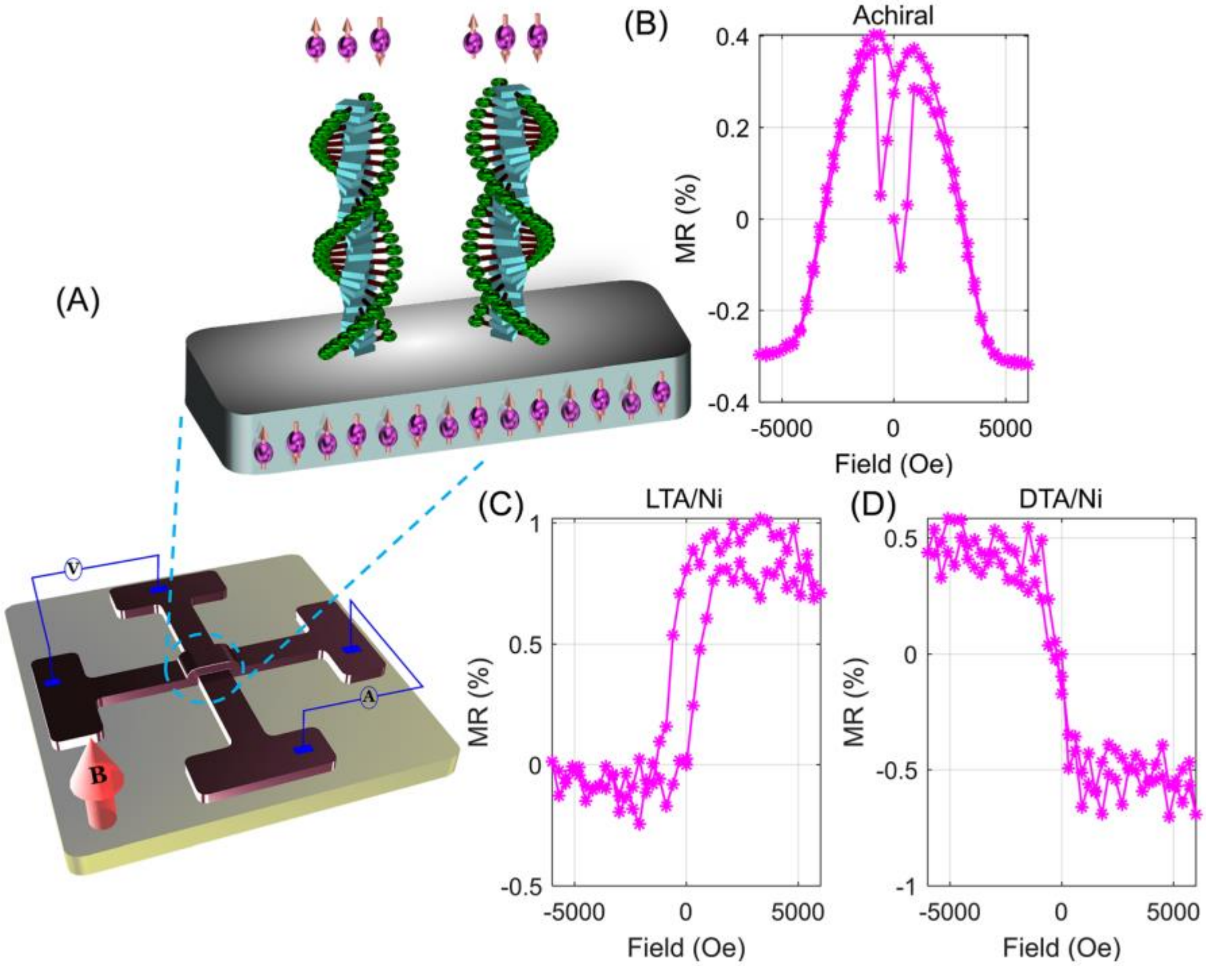

Figure 31 Characterization of chiral Nickel (cNickel): magnetoresistance (MR) measurements were conducted using a cross device (panel (a)) in a 4-probe configuration. b) MR plot with a magnetic field measured on achiral Ni as a cross-check experiment. (c) and (d) on chiral Ni L-TA (electrodeposited with a bulk presence of L-tartaric acid) and D-TA (electrodeposited with a bulk presence of D-tartaric acid), respectively. Reprinted with permission from ref [73].

# 3. Results and discussion: monomer SAM

This Section compiles the first part of the results presented in this work, focusing particularly on investigating electrochemical and solid-state interfaces which are mapped and controlled to the monomer molecule level.

Three subsections are presented (3.1, 3.2, 3.3), each dedicated to distinct but interrelated research directions, characterized by the charge-transfer through different chiral molecules. The common experimental archetype between these three sections can be summarized as it follows: hybrid chiral interfaces are produced through the adsorption onto metallic surfaces of both thiophene and TTF derivatives. Eventually this leads to the formation of Self-Assembled Monolayers (SAMs) on both noble (Au and Ag) and ferromagnetic (Ni) surfaces. These systems are thoroughly characterized and subsequently employed as electrodes to investigate charge transport across the metal|SAM interface by using various experimental setups and techniques. This depending on the specific research topic under investigation.

Unless otherwise stated, all experimental procedures (including nanoparticles synthesis, electrodes fabrication, evaporation, surface functionalization, electrochemistry-probing, SDE, enantio-recognition, adsorption/desorption, XPS, synchrotron radiation measurements, SEM, Raman spectroscopy) and all the presented calculations have been carried out by the author of this thesis.

## 3.1. Enantiopure chiral oligothiophene derivative: 2T3N

### *3.1.1. Introduction and motivation*

The chiral oligothiophene derivative N,N'-bis-[2,2';5',2"]tert-thiophene-5-yl methylcyclohexane-1,2-diamine (2T3N), synthesized by Bandini et al. [196] at Bologna CNR, consists of two terthiophene branches attached to a central cyclohexane through nitrogen atoms (chiral centers). Firstly, the study of this molecule focuses on a preliminary aspect: the reactivity of the thiophene groups towards noble metals such as gold and silver. In fact, while gold surfaces functionalization via thiol chemisorption is a thoroughly studied topic [197]–[200], thiophenes adsorbed on gold are by far a less explored route. As elaborated in Section 2.3 of the theoretical background, experimental research regarding the attainment of dense and well-ordered monolayers of thiophene-derivative molecules through "wet functionalization" is still ongoing [139], [201]. Given the strong technological interest in surface modification of solid surfaces with π-conjugated systems (in contrast to thiols), with all the implications for transport efficiency that can be achieved in the field of organic semiconductor electronics [202], [203], this research path remains highly relevant [204], [205].

Therefore, the adsorption of the chiral 2T3N on gold is experimentally studied, together with the calculated optimized structure on an Au(111) cluster of 57 atoms.

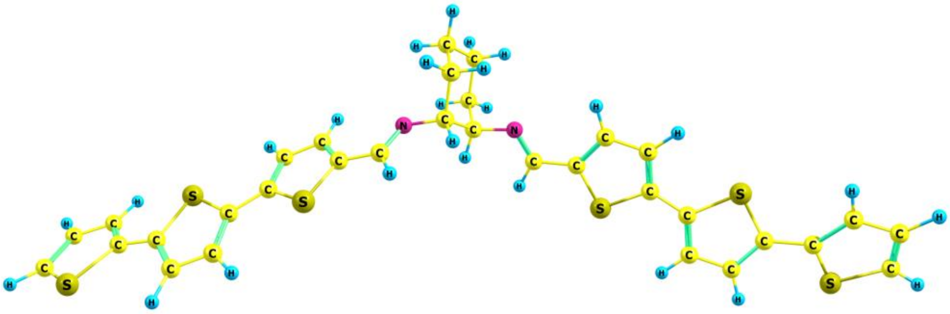

Figure 32 Ball and stick molecular structure of the 2T3N molecule.

Secondly, the obtained Au|R-2T3N interface is meticulously characterized using synchrotron radiation. XPS and PECD measurements were conducted at the CiPo beamline of Elettra (Trieste, proposal number 20210018) to investigate the achieved SAM in terms of reproducibility, interaction strength, and substrate "chiralization" (chiral induction in the electronic properties of the substrate) [206]. Furthermore, the interface is employed in enantio-recognition measurements. This electrochemical technique holds fundamental importance on a technological level, as it constitutes one of the primary sensing methods for enantio-discrimination [207]–[209]. In this experimental domain, enantiorecognition is still presented as an electrode characterization measure. However, one of the major focal points of this thesis work is to establish the connection between enantiorecognition and spin-dependent transport. This aspect will be treated in much more detail in the following sections, particularly in paragraph 3.2, where the use of an inherently chiral molecular filter (devoid of chiral centers) will further enhance the theory's generality. Beyond the fundamental scientific interest related to the 2T3N adsorption and the Au|R-2T3N dichroic signal, the major interest in this study relies on the anomalous, quite large charge transmission ability exhibited by the Au|R-2T3N interface (as evidenced by the high value obtained for the charge transfer rate constant $k^o$). The charge transfer is probed via electrochemical methods and in the solid-state (magneto-conductive AFM), as a function of the spin-injection [210].

The electrode preparation and functionalization procedures, as well as the experimental techniques and setups used, are thoroughly described in Section 5 (Experimental).

### 3.1.2. Au|2T3N cluster: theoretical results

The Au|2T3N interaction is calculated within the embedded cluster approach, that is: considering a slab of gold (102 atoms) with fixed geometry coordinates (corresponding to the experimental coordinates of the gold crystal) and placing a molecule of adsorbate in contact with the surface (in this case having 111 symmetry). Then the coordinates of 2T3N are full optimized (the relevant optimized geometry is shown below, Figure 33).

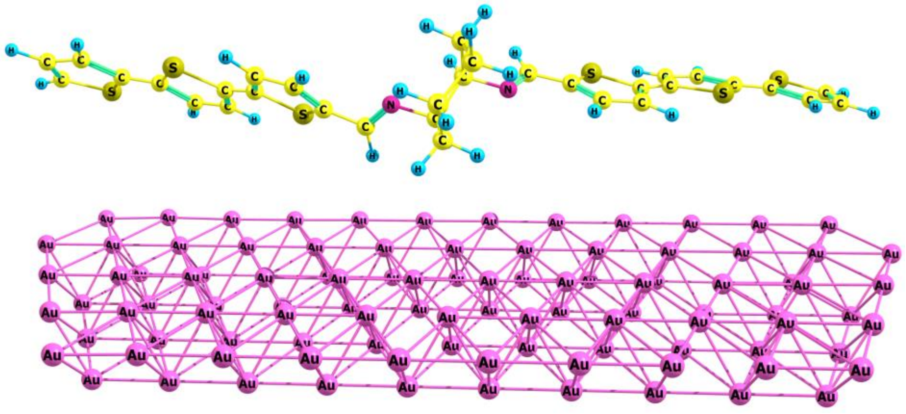

Figure 33 PM7 optimized 2T3N geometry on a fixed coordinates Au(111) 57 atoms slab.

Geometry optimization of the Au(111)|2T3N cluster is carried out using the semiempirical PM7 Hamiltonian, needed to handle the large 102 atoms Au cluster. The adsorption energy is calculated as the difference between the Au|2T3N cluster electronic energy minus that one of the Au(111) slab and adsorbate molecule:

$$E_{ads} = E_{Au_{57}|2T3N} - \left(E_{Au_{102}} + E_{2T3N}\right) \qquad (65)$$

Where: $E_{ads}$, $E_{Au_{57}|2T3N}$, $E_{Au_{102}}$ and $E_{2T3N}$ are the molecular electronic energies of adsorption, Au|2T3N cluster, Au102 slab and 2T3N, respectively. The adsorption energy is found to be $-140\ kcal\ mol^{-1}$, with a rather small charge transfer of about 0.0110 electrons from the 2T3N to the gold cluster, i.e. the 2T3N is slightly positive, polythiophenes are indeed typical electron-donor compounds. The HOMO-LUMO energy difference is of 1.74 eV in the Au|2T3N cluster, 7.3 eV for the neutral 2T3N, 2.15 eV is the Au102 slab HOMO/LUMO gap. Also, the decrease in energy of 0.41 eV, obtained comparing the gap of the Au102 slab with that of the Au|2T3N cluster suggests a strong interaction between gold and 2T3N.

### *3.1.3. Experimental results: Au|R-2T3N interface UHV characterization*

Given the promising absorption theoretical results, Au(111) surfaces are functionalized with the chiral R-2T3N (compare Section 5, Experimental).

Fig. 34 shows XPS data acquired for the Au|R-2T3N interface. In particular, Fig. 34 a, b, c, d show the S 2p, C 1s, N 1s and Au 4f core level energy regions, respectively.

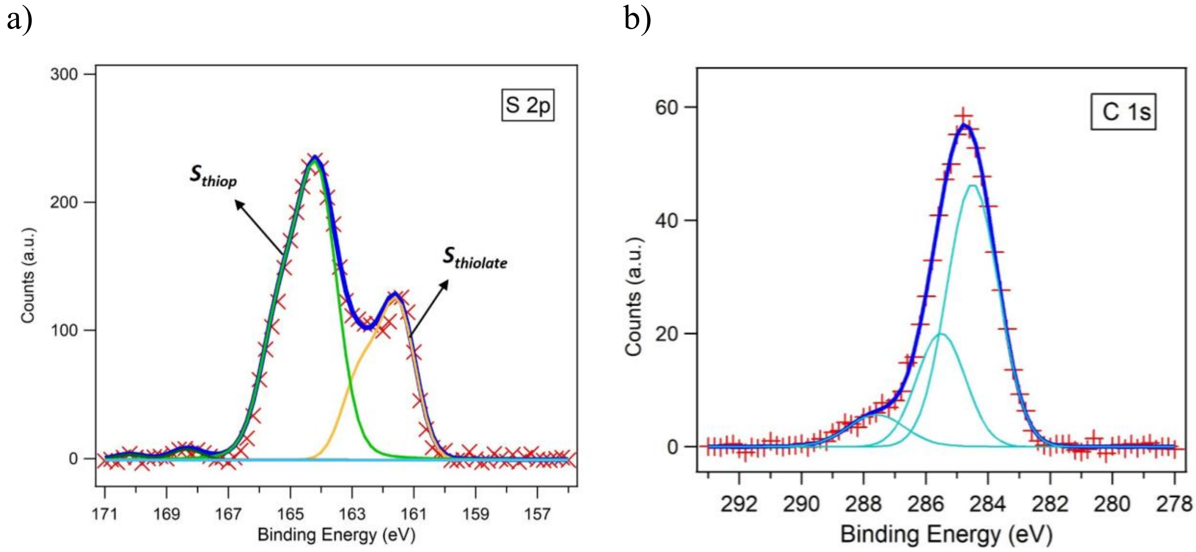

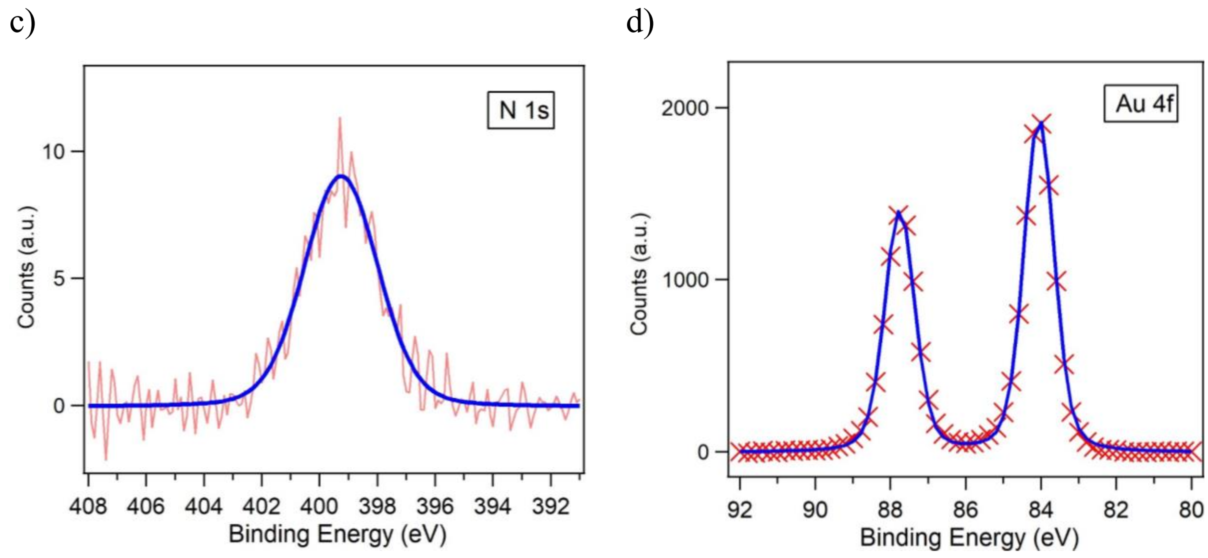

Figure 34 Au|R-2T3N interface synchrotron radiation XPS measurements. **a)** S 2p spectrum (300 eV exciting photon energy), **b)** C 1s spectrum (650 eV exciting photon energy), **c)** N 1s spectrum (650 eV exciting photon energy), **d)** Au 4f spectrum (300 eV exciting photon energy). Red crosses are the experimental spectra, solid blue line the overall fit. Thin green, yellow and light blue lines are the single Voigt fitting individual components. The Au $4f_{7/2}$ peak is used as reference for the binding energy scale calculation.

The S 2p region is of particular interest in the case of sulfur-based SAMs since it can be analyzed to gain insight into the interaction between the organic molecules and the substrate. The S 2p spectrum, reported in Fig 34a, shows two different main structures centered at 163.8 and 161.5 eV (fitted by two Voigt doublets, green trace and yellow trace, respectively). According to the literature, the component at 163.8 eV can be ascribed to the free, not-chemically-bound sulfur of thiophene, while the lower binding energy peak at 161.5 eV is associated to the S atoms of the 2T3N chemisorbed on the Au surface. A shallow shoulder of extremely low intensity is evident at 168.5 eV, which is due to extremely low traces of oxidized sulfur. The extremely low concentration of oxidized sulfur is a further indication of an optimal 2T3N adsorption on the Au surface, without any fragmentation of the 2T3N.

Fig. 34b shows the C 1s spectrum. An effective fit can be obtained combining three different components (light blue curves in Fig. 34b): the 284.4 eV component can be assigned to C-C and C=C ($sp^2$ hybridization) chemical bonds, the 285.5 eV component stems from C-N and C-O ($sp^3$) chemical bonds, while the higher binding energy signals (> 286 eV of rather low intensity) arise from more oxidized carbon (i.e. C=O and O-C=O groups). The N 1s and Au 4f core level spectra reported in Fig. 34 c and d, respectively, show results consistent with data in the literature [211], [212].

Fig. 35 shows Au|2T3N interface valence band (VB) measurements and calculations.

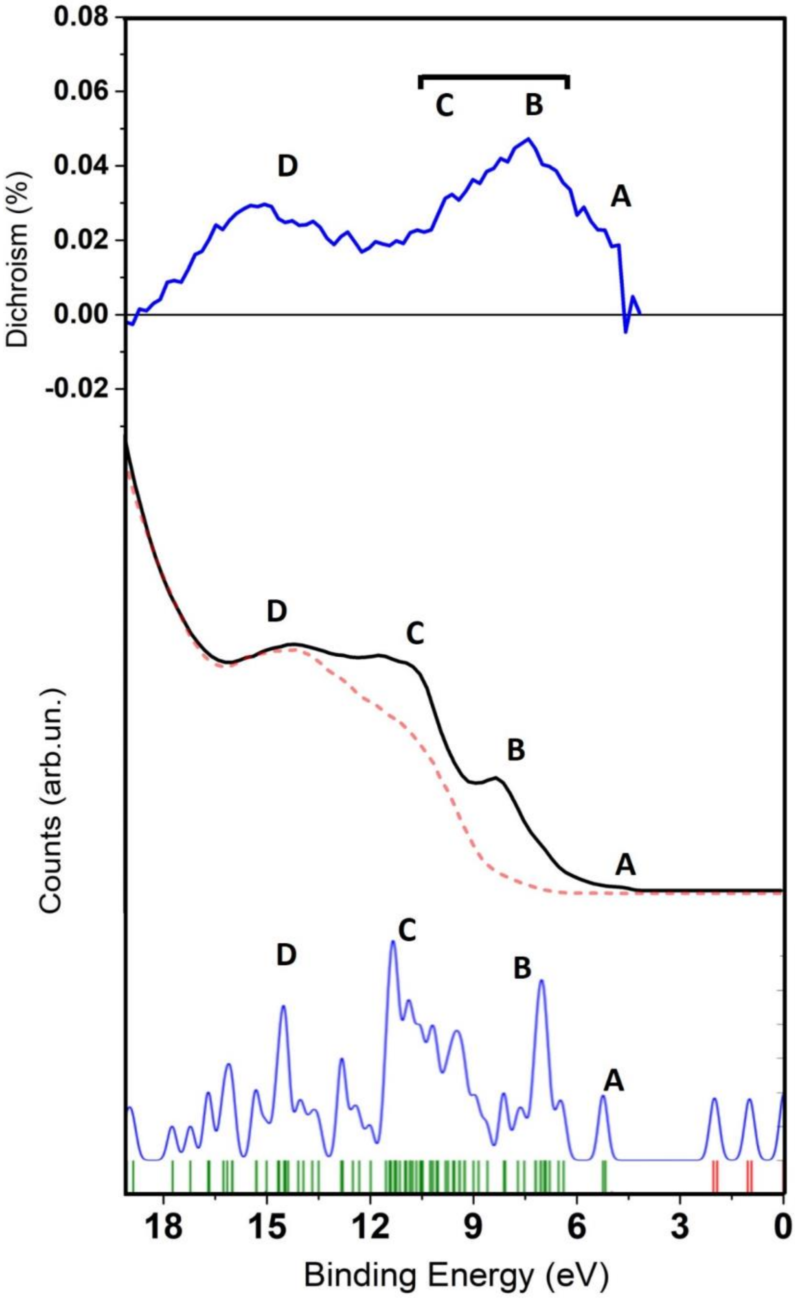

Figure 35 Valence band (VB) synchrotron radiation measurements acquired at the Au|2T3N interface. Upper panel: Au|R-2T3N VB dichroic signal, calculated as the difference between right-handed and left-handed circularly polarized spectra. Central panel: photoemission VB spectrum for the Au|R-2T3N interface (black line) and for the bare Au substrate (red dashed line); the spectra were obtained with 25 eV exciting photon energy in Normal Incidence Monochromator (NIM) configuration. Lower panel: the calculated density of states (DOS) of the isolated 2T3N molecule, reported for comparison purposes.

In the central panel, experimental synchrotron radiation photoemission spectra of the Au|2T3N (black line) and bare Au substrate (red dashed line) VBs are reported. In the Au|2T3N VB spectrum, tight comparison with the bare Au one, allows to appreciate the presence of additional structures (labeled A-D) in the interval between 4 and 15 eV below the Fermi level, which stem as a result of the 2T3N interaction with the substrate. In addition, a good agreement is found between the experimental VB spectrum (black line in Fig. 35) and the calculated density of states (DOS) reported in the lower panel of Figure 35: the A (4 eV), B (7.5 eV), C (10.5 eV) and D (15 eV) structures are clearly evident in the Au|2T3N spectrum and in the 2T3N DOS. The Au|2T3N VB is investigated by means of circularly polarized synchrotron radiation and the dichroism results are reported at the top of Figure 35 (blue trace). Multiple VB spectra recorded with photons of opposite helicity lead to a clear-cut dichroic signal, whose 4 to 18 eV energy interval is consistent with the 2T3N DOS: the A, B, C, D structures marked in the DOS reported at the bottom of Fig. 35 (details concerning PECD spectra calculation are reported in appendix A.2). The dichroic signal reported in Fig. 35 shows that the presence of molecular chiral domains induces asymmetry in the interaction with the substrate and locally transfers the chiral character to the underlying gold atoms participating in the adsorption process; adsorbed chiral molecule effects are large for the molecular states that in the adsorption process gives rise to hybrid interface states and render the surface chiral [213], [214].

### 3.1.4. *Magneto-conductive AFM*

In the solid-state, the spin-polarized transport through the R-2T3N SAM is investigated by means of magneto-conductive atomic force microscopy (mc-AFM). These measurements were performed at the Pritzker School of Molecular Engineering, University of Chicago, and results are reported in Figure 36. The current between the Au|R-2T3N interface and the Ni AFM tip is recorded as a function of the magnetic field direction, in the -3.0 ÷ 3.0 V voltage interval. The ferromagnetic Ni tip is placed in tight contact with a permanent magnet, in a direction orthogonal to the FM electrode surface. Changing the orientation of the magnet, i.e. swapping the north and south poles (MagDOWN, MagUP) allows to control the spin injection within the chiral Au|R-2T3N interface. The resulting I-V plot (Fig. 36) shows visible differences in the resonant conditions region (i.e. voltage ≥ |1.8| V) between the two magnet orientations. The quantitative analysis of the current vs. potential pattern yields a substantial maximum spin-polarization value of about 28% at 3.0 V bias. SP% is calculated as:

$$SP\% = \frac{\left(I_{MagUP} - I_{MagDOWN}\right)}{\left(I_{MagUP} + I_{MagDOWN}\right)} \times 100 \qquad (66)$$

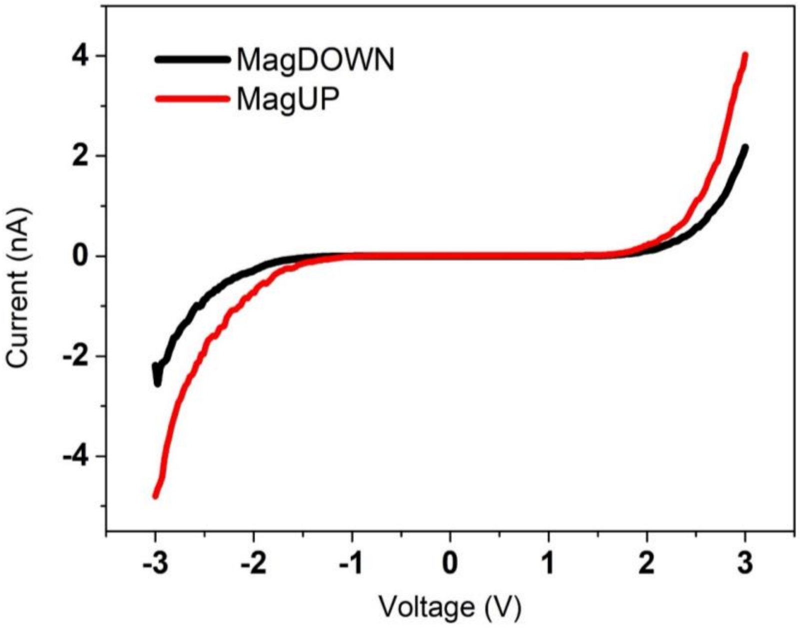

Figure 36 mc-AFM measurements recorded at the Au|(R)-2T3N interface with a Ni ferromagnetic tip placed in contact with a permanent magnet. Red solid line MagUP, black solid line MagDOWN.

Figure 37 shows AFM images of the bare Au substrate and of the Au|R-2T3N, respectively panel a) and panel b). The organic molecules are visible as white dots in the relevant sample.

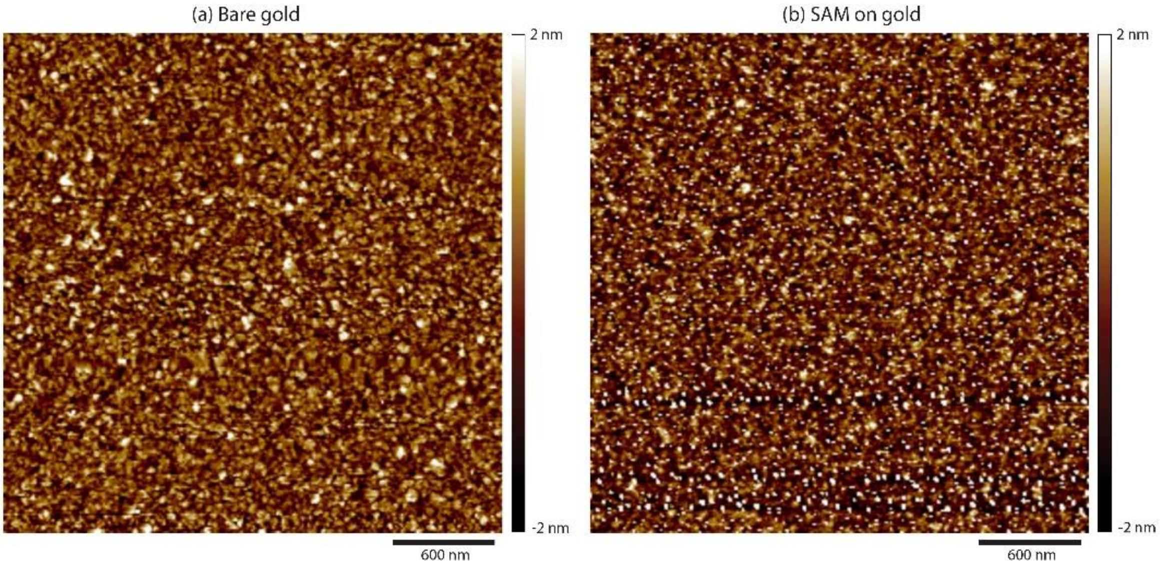

Figure 37 Bare (left panel) and SAM on gold (right panel) surface measured using dynamic mode (peak force QNM) for both the surfaces.

As a further cross-check, Figure 38 panel a) (on the left) displays mc-AFM measurements performed on the “blank” sample, i.e. bare gold substrate. Comparison of the I-V patterns shows that there is no significant current difference between magnet orientation Up (black points) and Down (red points), i.e. no mc-AFM artifacts are detected due to changing the location of the tip on the sample and/or flipping the magnet field direction. Figure 38 b) and c) panels just show the mc-AFM raw data (over 100 scans for both MagUP and MagDOWN orientation) for the Au|R-2T3N interface. The averaging of all the recorded curves leads to figure 36 main result.

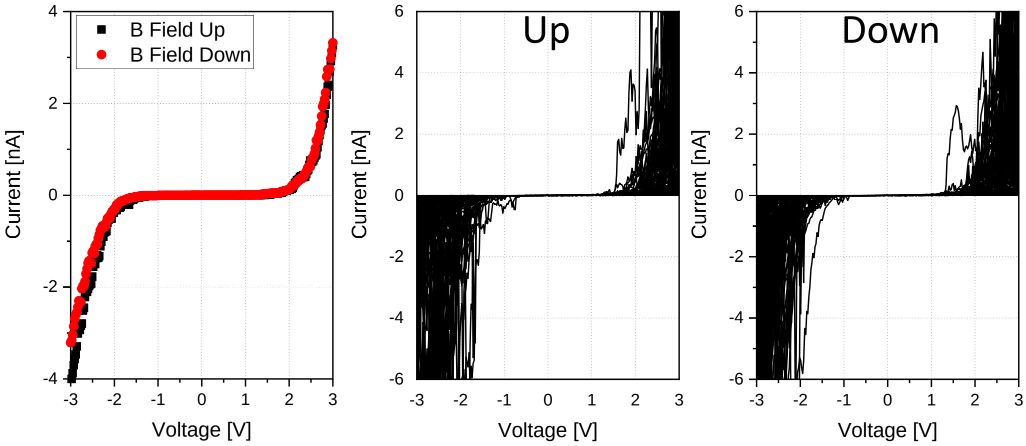

Figure 38 mc-AFM bare gold surface. **Left panel**: average I-V curves: black curve magnetic field Up, red curve magnet field Down. **Center and right panels**: raw data, for a total of 5000 points mapped on the Au surface.

Since the investigated system can be schematized as a molecular junction, where the 2T3N acts as the molecular bridge between the two metals (Au and Ni, as schematized in Figure 39a), the Figure 36 experimental I-V curves can be fitted with the Landauer formula in the single-level resonant tunneling approximation (compare Section 2.1, theoretical background, equation 33). As exhaustively discussed in the theoretical section, the SLRT model enables the fitting of experimental curves based on only three parameters: the position of the transmission mode ($\varepsilon_0$) and the molecule's coupling to the metallic reservoirs ($\Gamma_L$ and $\Gamma_R$). Consequently, this approach does not allow for rationalizing the differences between the two curves (UP and DOWN magnet orientations) based on the CISS and relative spin-dependent transport. However, the fitting procedure is still useful for assessing the order of magnitude of the interaction with the two metallic reservoirs (which in this case are different: asymmetric interface) and the energy of the main transport channel (LUMO).

The relevant fittings are shown in Figure 39 b and c panels and feature the following values:

MagDOWN (panel b): $\varepsilon_0 = 1.41\ eV$, $\Gamma_R = 0.263$ (Au) and $\Gamma_L = 0.178$ (Ni)

MagUP (panel c): $\varepsilon_0 = 1.26\ eV$, $\Gamma_R = 0.270$ (Au) and $\Gamma_L = 0.175$ (Ni)

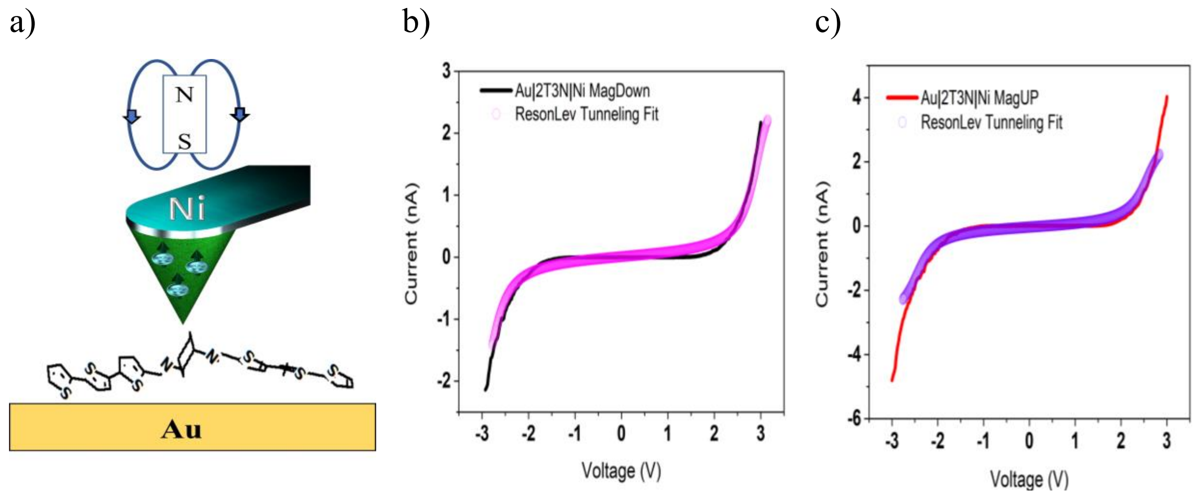

Figure 39 **a)** schematic representation of the experimental setup for mc-AFM measurements. **b)** and **c)** Single-level resonant tunneling fitting of the experimental I-V characteristics (the black and red lines display the same measured curves from Figure 36, previously discussed in the text). Fitting parameters for panel **b)** curve (MagDOWN): $\varepsilon_0 = 1.41\ eV$, $\Gamma_R = 0.263$ (Au) and $\Gamma_L = 0.178$ (Ni). Fitting parameters for panel **c)** curve (MagUP): $\varepsilon_0 = 1.26\ eV$, $\Gamma_R = 0.270$ (Au) and $\Gamma_L = 0.175$ (Ni).

comparing the two fits, it can be observed that the coupling values to the two metals are constant changing the orientation of the magnetic field, as expected. In particular, the ratio of the coupling strengths is $^{\Gamma_R}/_{\Gamma_L} \cong 1.5$ This is consistent with the semiempirical PM7 calculation results, which provide 2T3N interaction energies of $-140.01\ \text{kcal mol}^{-1}$ and $-84.64\ \text{kcal mol}^{-1}$ with Au and Ni respectively, the ratio between these values being $\frac{-140.01\ \text{kcal mol}^{-1}}{-84.64\ \text{kcal mol}^{-1}} = 1.65$ indeed.

### *3.1.5. Electrochemistry*

Fig. 40 sets out CV curves recorded at the Au|2T3N interface in a Fe(III)|Fe(II) aqueous solution. In particular, Fig. 40a shows the comparison between the CV recorded at the bare (black curve) and at the 2T3N functionalized Au surface (red curve). For the bare Au, the typical shape expected for diffusion-controlled reversible redox processes is observed: the peak-to-peak separation between the oxidation (positive) and the reduction (negative) current peaks is 68 mV and the relevant CV fitting yields a charge transfer rate constant ($k°$) of $1 \times 10^{-1}$ cm s$^{-1}$. In the case of noble metals $k°$ is found ranging between 0.01 and 0.1 cm s$^{-1}$ [215]. The CV pattern is different when the Au|2T3N interface acts as working electrode (red line in Fig. 40a and 40b): the current peaks transform into broad shoulders and there is about a 40% decrease in the current, with respect to the bare Au (black line in Figs. 40a and 40b). The peak-to-peak separation increases from 68 mV to 325 mV, the CV fitting allows to estimate a significant decrease of $k°$ to $3.3 \times 10^{-2}$ cm s$^{-1}$. Thus, the voltametric response clearly indicates the effective chemisorption of 2T3N on the Au surface.

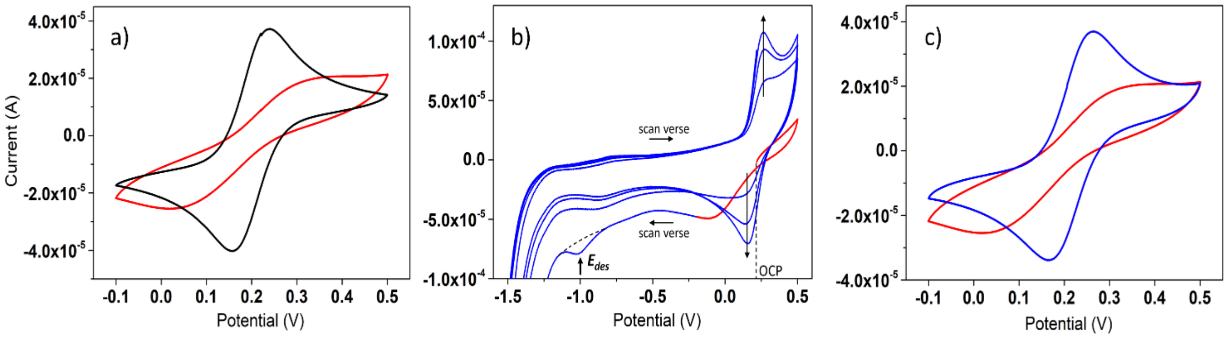

Figure 40 CV curves of a 5 mM Fe(III)|Fe(II), 0.1 M KCl aqueous solution **a)** 0.1 V s$^{-1}$ potential scan rate: black line is the bare Au WE, red line is the Au|2T3N interface acting as the WE **b)** CV curves recorded at 0.5 V s$^{-1}$ potential scan rate: red line is the CV forward scan recorded before electro-desorption, the blue curves features a peak (labelled as Edes in Fig. 40b) in the very first reductive scan (due to the electro-desorption of 2T3N): the first CV forward scan starts from OCP to 0.5 V, then the potential is scanned from 0.5 to -1.7 V, the successive CV scans are carried out in the -1.7 to 0.5 V potential range **c)** CVs of Au|2T3N WE: before red line, and after, blue line, the electro-desorption procedure, recorded at a 0.1 V s$^{-1}$ potential scan rate.

The 2T3N adsorption on the Au surface is further investigated by an electro-desorption experiment: the Au|2T3N interface is used as working electrode and the potential scanned in the reduction potential domain up to -1.7 V. Remarkably, in the very first scan toward negative potentials (marked by the change in color from red to blue in the CV curve), a clear-cut current peak is evident at $-1.0$ V, due to the 2T3N irreversible electrodesorption. The latter peak is indicated by an arrow ($E_{des}$) in Fig. 40b, and it is not present in the successive CV scans. Remarkably, the current in the -0.2 to -1.2 potential domain decreases after the first cycle: the current is simply due to the double-layer charging/discharging process (no faradaic process are active in the -0.2 to -1.2 potential domain window). This result agrees with the capacity drop associated to 2T3N desorption. Reaction (67) is the redox reaction underlying the $E_{des}$ current peak:

$$Au|2T3N + e^{-} \rightarrow Au + 2T3N^{-}_{bulk\ solution} \qquad (67)$$

Focusing the attention on the potential range between -0.25 V and 0.5 V, after the first potential scan up to -1.7 V, we note that the CV pattern closely resembles that of the reversible $[Fe(CN)_6]^{3-/4-}$ redox couple. Which is eventually consistent with the CV recorded in the case of the pristine Au surface. Thus, the $E_{des}$ current peak marks the boundary between the Au|2T3N and the bare Au surface. Overall, these results provide a consistent indication that the incubation of gold in the 2T3N ethanolic solution effectively yields a functionalization of the Au surface by 2T3N. Moreover, integration of the peak current at $E_{des}$ allows to estimate the area occupied by a 2T3N molecule adsorbed on the Au surface, which is found to be about 200 $\text{Å}^2$ (details of the relevant calculation procedure can be found in Appendix A.1). This value is consistent with the formation of a monolayer, obtained for the disposition of 2T3N molecules laying "flat" on the electrode surface, as shown in Fig. 33. This result is due to the chemical interaction between sulfur atoms of the oligothiophene backbone and the gold surface. For the sake of completeness, the same complete functionalization procedure and electrochemical analysis is carried out incubating the Au surface with the 11-mercaptoundecanoic acid (C11). This approach allows for a comparison with a widely studied thiol in the literature, both in terms of the area occupied by each molecule of the SAM on the electrode and the charge transfer constant $k°$ measured using the Fe(III)|Fe(II) redox probe in solution. Figure 41 displays CV curves recorded on the Au|C11 interface in a Fe(III)|Fe(II) aqueous solution before (Fig. 41a) and after (Fig. 41b, black line) the C11 electrodesorption procedure. It is evident that the $Fe^{2+}/Fe^{3+}$ redox signals are almost indiscernible in the CV when the C11 is adsorbed on the Au substrate (Fig. 41a): no peak-to-peak separation can be determined, and the current values are extremely low (order of magnitude of 1 μA). The Au|C11 interface CV can be fitted by a charge transfer rate constant ($k°$) of $1 \times 10^{-6}$ cm $s^{-1}$.

a)

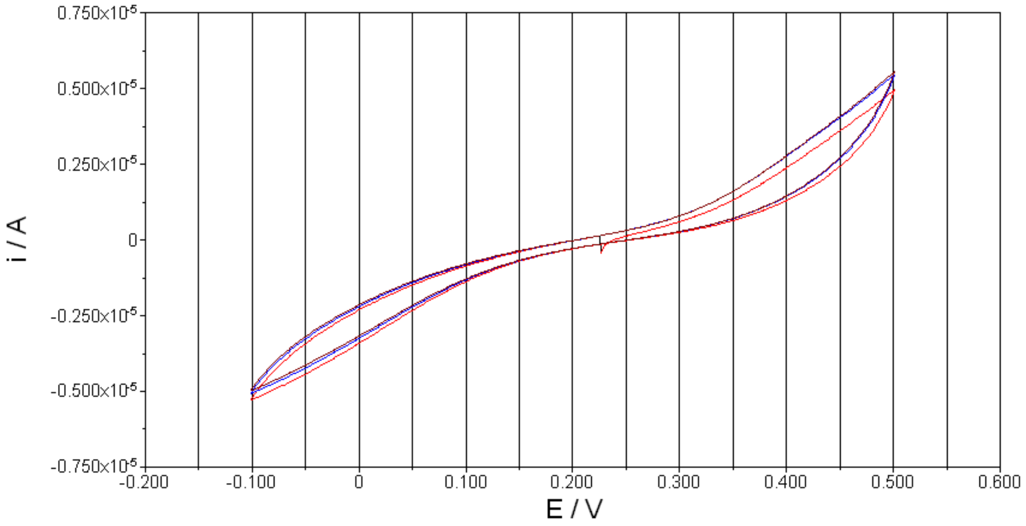

b)

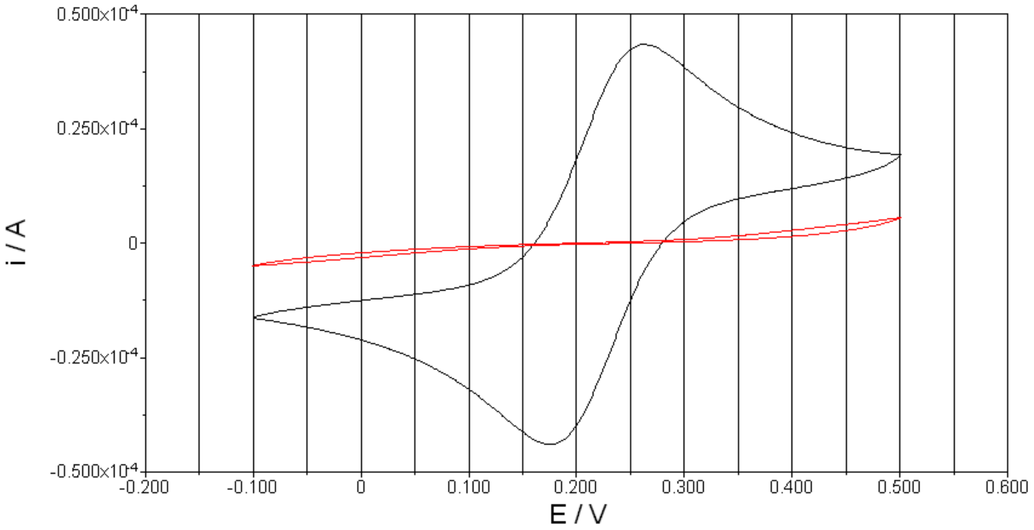

Figure 41 CV curves of a 5 mM Fe(III)|Fe(II), 0.1 M KCl aqueous solution, 0.1 V s$^{-1}$ potential scan rate. **a)** Au|C11 interface acts as the WE, red line is the first scan, blue line is the second scan **b)** Au|C11 WE: comparison between before (red line) and after (black line) the electrodesorption procedure.

Following the exact same electrodesorption procedure as for the Au|2T3N interface (which can be found in Appendix A.1) the mean surface area occupied by the adsorbed C11 molecule on the electrode is estimated to be $A_{molC11} \cong 13\ \text{Å}^2/molecule.$ This value is consistent with a well-ordered SAM with the C11 adsorbed with a perpendicular orientation with respect to the electrode surface, by and large the projected area of a methyl group. After the electrodesorption procedure, the CV shape is back to the one expected for a diffusion-controlled reversible redox process (figure 41b, black trace) and current values increase by one order of magnitude. This comparison demonstrates that the charge transfer efficiency of 2T3N is over four orders of magnitude higher than that of C11.

To further probe the effective "chiralization" (induced surface handedness obtained *via* chemisorption of a chiral compound) of the gold surface, the Au|R-2T3N interface is exploited as WE in typical enantio-recognition electrochemical measurements. Figure 42a shows CVs obtained by using ferrocene derivatives bearing a chiral center, namely S-FC and R-FC. The relevant CV responses recorded at Au|R-2T3N interface show a difference of about 70 mV (the S-FC is shifted towards more positive potentials) in the redox peak potential of the two enantiomers, whereas CV curves of the two chiral ferrocene enantiomers are coincident when recorded on pristine Au surface. The electrochemical behavior observed for the Au|R-2T3N interface agrees with the results obtained with electrode surfaces functionalized with chiral polythiophene derivatives [216], [217]. Fig. 42b and 42c show a further enantio-recognition voltammetric experiment still using Au|R-2T3N interface as the WE: the oxidation responses due to D-Tyrosine (red curve) occurs at a potential value slightly higher than the oxidation of L-Tyrosine (black curve) indicating the enantioselectivity of the functionalized Au surface obtained [218].

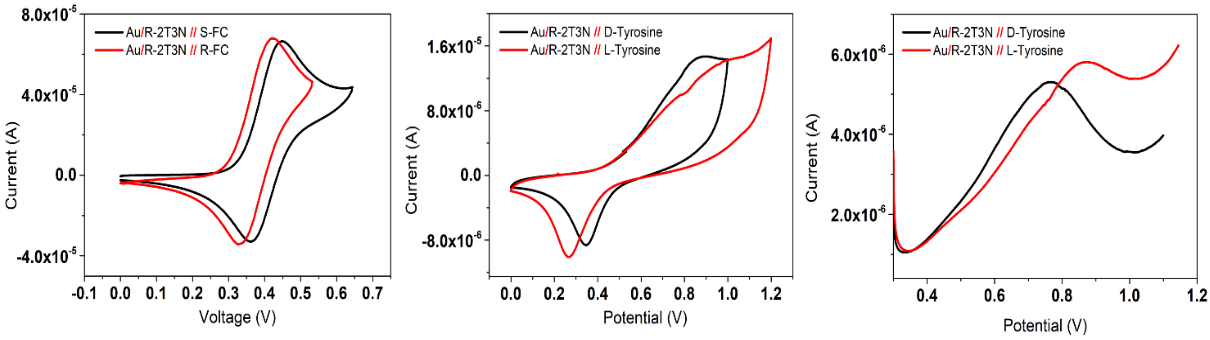

Figure 42 Voltammetric measurements recorded using Au|R-2T3N as the WE. **a)** CV curves in 5 mM R-FC (red curve) or S-FC (black curve), 0.1 M TBATFB in ACN solution, 50 mV $s^{-1}$ is the potential scan rate **b)** CVs curves in 2 mM D-Tyrosine (red curve) or L-Tyrosine (black curve), 0.1 M TBATFB in ACN solution, 50 mV $s^{-1}$ is the potential scan rate. **c)** DPV curves performed on the same solutions of panel **b)**, 1 mV is the step-potential, 50 mV is the modulation amplitude and 0.05 s is the modulation time.

The 2T3N interaction with the gold surface is also probed exploiting a complex multilayered interface: the Au|2T3N electrode is furtherly functionalized with Ag nanoparticles, adsorbed on the 2T3N SAM and thus the Au|2T3N|AgNPs electrode is obtained (surface preparation details are reported in Section 5, Experimental). This experiment aims to further investigate the charge transmission characteristics of the 2T3N monolayer, which is now “sandwiched” between two metals. The system obtained was electrochemically investigated by recording the CV response in KCl aqueous solution (see Fig. 43). Indeed, a couple of well-defined current peaks are evident at +0.04 and –0.06 V.

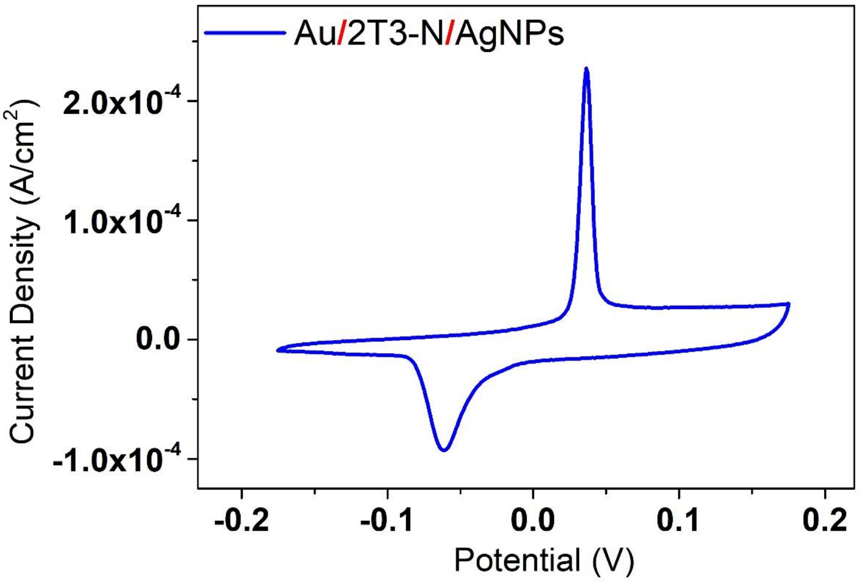

Figure 43 CV curve: Au|2T3N|AgNPs interface is the WE, in 0.1 M KCl; 0.1 V s$^{-1}$ potential scan rate.

At +0.04 V AgNPs adsorbed on the 2T3N SAM are oxidized to AgCl, the latter is formed on the surface of the AgNPs due to the presence of chloride anions in solution. At -0.06 V the reverse reaction occurs (reduction of AgCl to Ag and chloride redissolution), resulting in an overall reversible electrochemical process. The difference in shape between the oxidation and reduction current peaks is due to the asymmetry of the redox process: the oxidation process is diffusion controlled and chloride ions diffuse from bulk solution to the surface, the reduction process occurs on the surface of the AgNPs.

On the whole, the electrochemical results obtained by using the Au|2T3N|AgNPs interface as the working electrode, are in agreement with voltametric results shown in the previous section. A further indication that the charge-transfer through the 2T3N SAM adsorbed on Au is rather efficient, implying that the 2T3N acts as a good channel for conduction despite its thickness and irregular molecular conformation.

### *3.1.6. Conclusions*

The experimental outcome reported in this section relates on one side to the preparation and characterization of an enantiopure chiral oligothiophene on gold: the Au|2T3N metal|organic hybrid interface. On the other side, the role of chirality on such hybrid interface has been addressed, focusing in particular on optical and charge transmission physical properties. The physical state and structure of the Au|2T3N hybrid interface was characterized by using XPS, PECD and voltametric techniques, and the relevant experimental data are compared with theoretical calculations referring to a “Au(111) 102 atoms slab”|2T3N cluster (PM7 Hamiltonian).

Three main points are worth to be emphasized:

- The effective gold functionalization is achieved via 2T3N, a chiral oligothiophene derivative, chemisorbed by overnight incubation, with the formation of an enantiopure monolayer (somehow an unexpected result). The chiral nature of the surface is consistent with CV responses in presence of enantiomers, allowing for “chiral recognition” of chiral compounds in bulk solution.
- PECD results indicate that gold on top of the surface is “chiralized”, i.e. PECD spectrum exhibits a dichroic signal in the typical gold energy range as discussed in the par 3.1.3. Chiral induction in the substrate electronic properties is indeed a result already observed in the literature (please compare Section 2.3, Theoretical Background).
- The charge transmission through the enantiopure chiral 2T3N monolayer is quite efficient, if compared to alkyl long chain compound (spin assisted transmission), and it is spin polarized, as revealed by the analysis of mc-AFM and voltammetric results.

Remarkably, all of the peculiar three main achievements outlined in this work find their natural rationalization within the chiral-induced spin selectivity (CISS) effect. These results lay the foundations for further investigating the connection between high transport efficiency, spin-polarized transport and enantiomeric recognition, which are further explored in the subsequent Sections 3.2 and 3.3.

## 3.2. Enantiopure inherently chiral oligothiophene: $BT_2T_4$

### 3.2.1. Introduction

In this section, inspired by the Stefani et al. paper[87], it is experimentally demonstrated that the electron-spin/molecular-handedness interaction plays a fundamental role in the chiral recognition process. In this context, the conclusions regarding the connection between CISS and chiral recognition that were suggested in the previous paragraphs are reiterated and bolstered by additional experimental evidence. These conclusions are inferred comparing current vs potential (I-V) curves recorded using chiral electrode surfaces, which are obtained via chemisorption of an enantiopure intrinsically chiral thiophene derivative: 3,3’-bibenzothiophene core functionalized with 2,2’-bithiophene wings ($BT_2T_4$). The chiral recognition capability of these chiral electrodes is probed via cyclic voltammetry (CV) measurements, where Ag nanoparticles (AgNPs) capped with enantiopure $BT_2T_4$ ($BT_2T_4$@AgNP) are used as the chiral redox probe (Experiment I). Then, the interface handedness is explored by recording spin-polarized I-V curves in spin-dependent electrochemistry (SDE, Experiment II) and magnetic-conductive atomic force microscopy (mc-AFM) measurements (Experiment III). The architecture of this research is thus aimed at achieving three separate experiments (Experiment I, II, III), which are conceived to probe independently the interplay between chirality, molecular handedness and spin selectivity. The three different experimental configurations, are summarized in Fig. 44B, C and D.

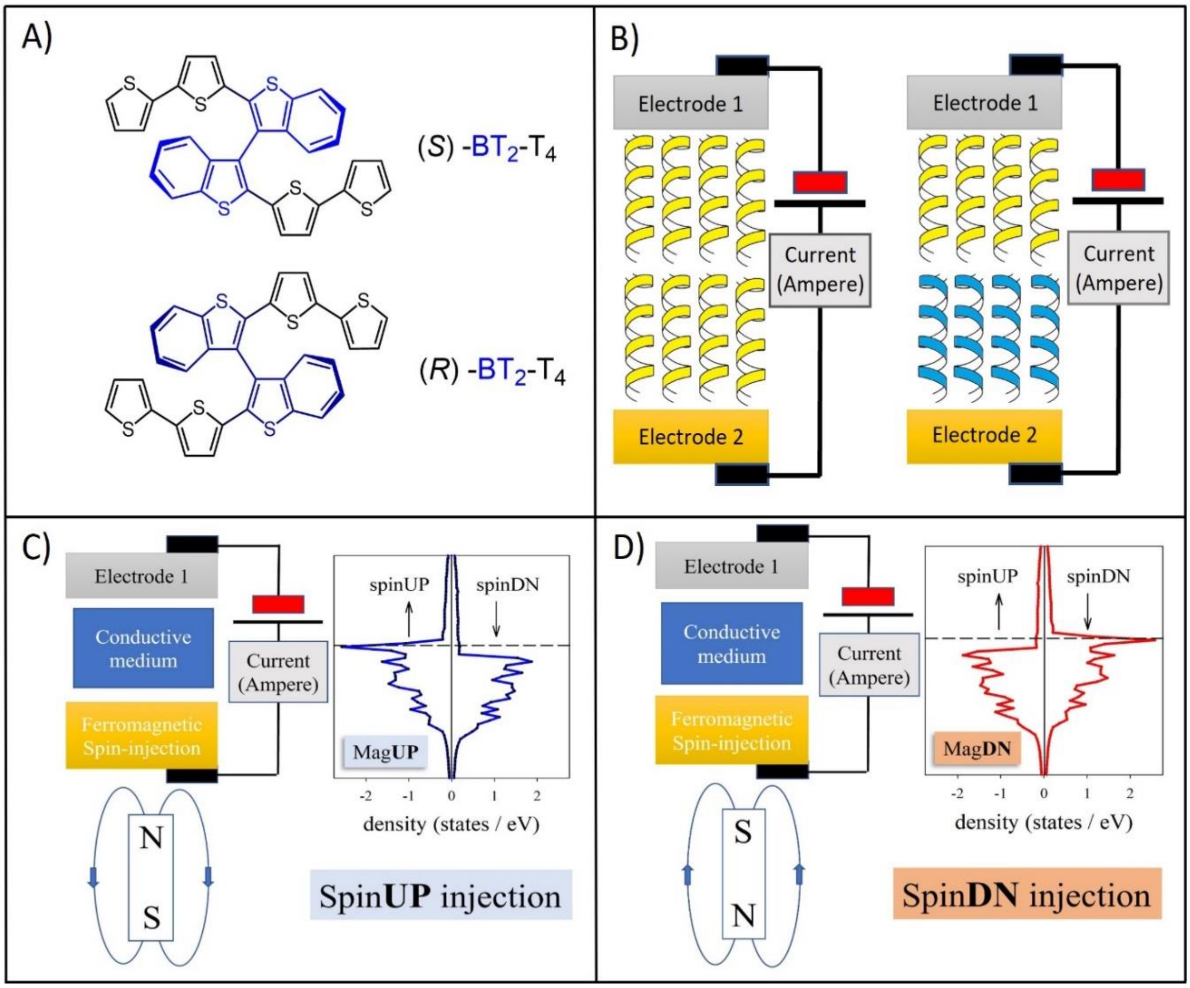

Figure 44 **A)** $BT_2T_4$ molecular structure both the (S)- and (R) – enantiomers are shown. **B)** experimental set up for the "true" chiral recognition experiment: two $BT_2T_4$ SAMs are placed in tight contact with the two possible handedness combinations. On the left: same handedness (symmetric interface); on the right: the two SAMs feature opposite handedness (dissymmetric interface). **C)** and **D)** Spin-injecting/spin-probing device. The energy vs density of state (DOS) pattern of the ferromagnetic electrode is shown as a function of the magnetic field orientation, the horizontal black dotted line is the Fermi energy. Blue curves DOS for magnetic field up. Red curves DOS for magnetic field down [219].

In the first experiment, a current is transmitted through a "sandwich" of two molecular layers on gold, either of the same (symmetric) or opposed (dissymmetric) handedness, electric contact is provided via grafted AgNPs. These measurements exploit the same mechanism as the chiral-recognition tests described in the previous Section 3.1.5. However, in this case, the chiral probe in solution is represented by the same molecule that is adsorbed on the electrode ($BT_2T_4$): an *intrinsically* chiral oligothiophene. Therefore, it's important to note that the "lock and key" and "Three-Point Interaction" rudimental models, which still represent the state of the art in explaining the mechanism of chiral recognition, cannot be applied (see Theoretical Background, Section 2.3). In the second experiment, in a typical SDE set up [144], [152], a spin-polarized current is measured through molecular layers of different helicities, yet AgNPs are used as terminal contact. The third experiment is conceptually similar to the second, except that the contact to the film is provided through an AFM magnetized tip. Note that, handedness in these experiments relies on the use of two enantiopure stereoisomers of the same chemical species (R- and S- $BT_2T_4$), thus variations observed in I-V curves are exclusively due to handedness discrimination, i.e. chiral recognition.

### *3.2.2. Main results*

#### 3.2.2.1. Probing molecular handedness

***Experiment I:*** *chiral recognition.* CV curves are recorded for the four possible combinations Au|(S)-$BT_2T_4$|(R)-$BT_2T_4$@AgNP, Au|(S)-$BT_2T_4$|(S)-$BT_2T_4$@AgNP, Au|(R)-$BT_2T_4$|(R)-$BT_2T_4$@AgNP and Au|(R)-$BT_2T_4$|(S)-$BT_2T_4$@AgNP, interfaces, *i.e.* probing the charge transmission of interfaces of symmetric *vs* dissymmetric handedness, a typical way to investigate chiral recognition [220], [221]. Figure 45A shows the relevant actual experimental implementation.

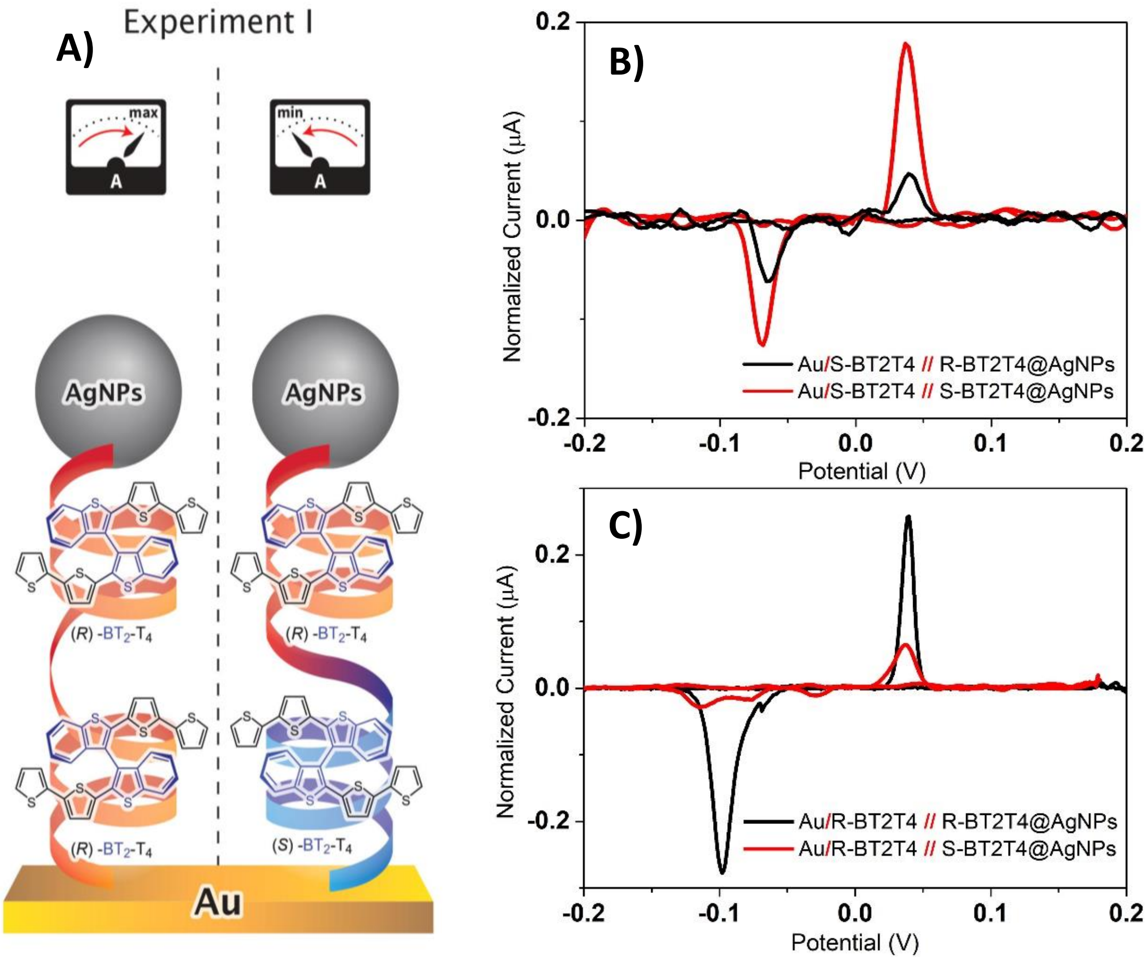

Figure 45 **A)** Actual experimental implementation of Experiment I: chiral recognition electrochemistry. CVs are recorded for all the possible handedness combinations: **B)** black Au|(S)-BT2T4|(R)-BT2T4@AgNPs, red Au|(S)-BT2T4|(S)-BT2T4@AgNPs. **C)** black Au|(R)-BT2T4|(R)-BT2T4@AgNPs, red Au|(R)-BT2T4|(S)-BT2T4@AgNPs. 0.1 M KCl in aqueous solution is the base electrolyte.

Remarkably, the peak current (at -0.1 and 0.05 V) is larger for the "symmetric" combination, i.e. when the two facing interfaces feature the same handedness. Red curve in Figure 45B (S)-BT$_2$T$_4$|(S)-BT$_2$T$_4$, while the black curve in Figure 45C has the largest current corresponding to the (R)-BT$_2$T$_4$|(R)-BT$_2$T$_4$ combination. Details concerning AgNPs preparation (and capping) and the chemisorption on Au are reported in Section 3.2.3 ("Further in-depth characterization") and in Section 5.3 (Experimental, preparations).

#### 3.2.2.2. Spin-dependent electrochemistry (SDE)

***Experiment II:*** *spin-dependent electrochemistry*. The charge transmission through the enantiopure Ni|(S)-BT$_2$T$_4$@AgNPs and Ni|(R)-BT$_2$T$_4$@AgNPs interfaces is probed by recording CV curves (SDE) as a function of spin-injection: i.e. by application of a magnetic field UP vs magnetic field DOWN orientation (a permanent magnet is placed just under the WE surface, 0.5 mm away from the actual contact between the solution and the ferromagnetic WE surface). Figures 44C and 44D represent schematically the physics underlying Experiment II, while Figure 46A shows the actual experimental implementation, the relevant experimental CV curves are presented in Figures 46B and 46C.

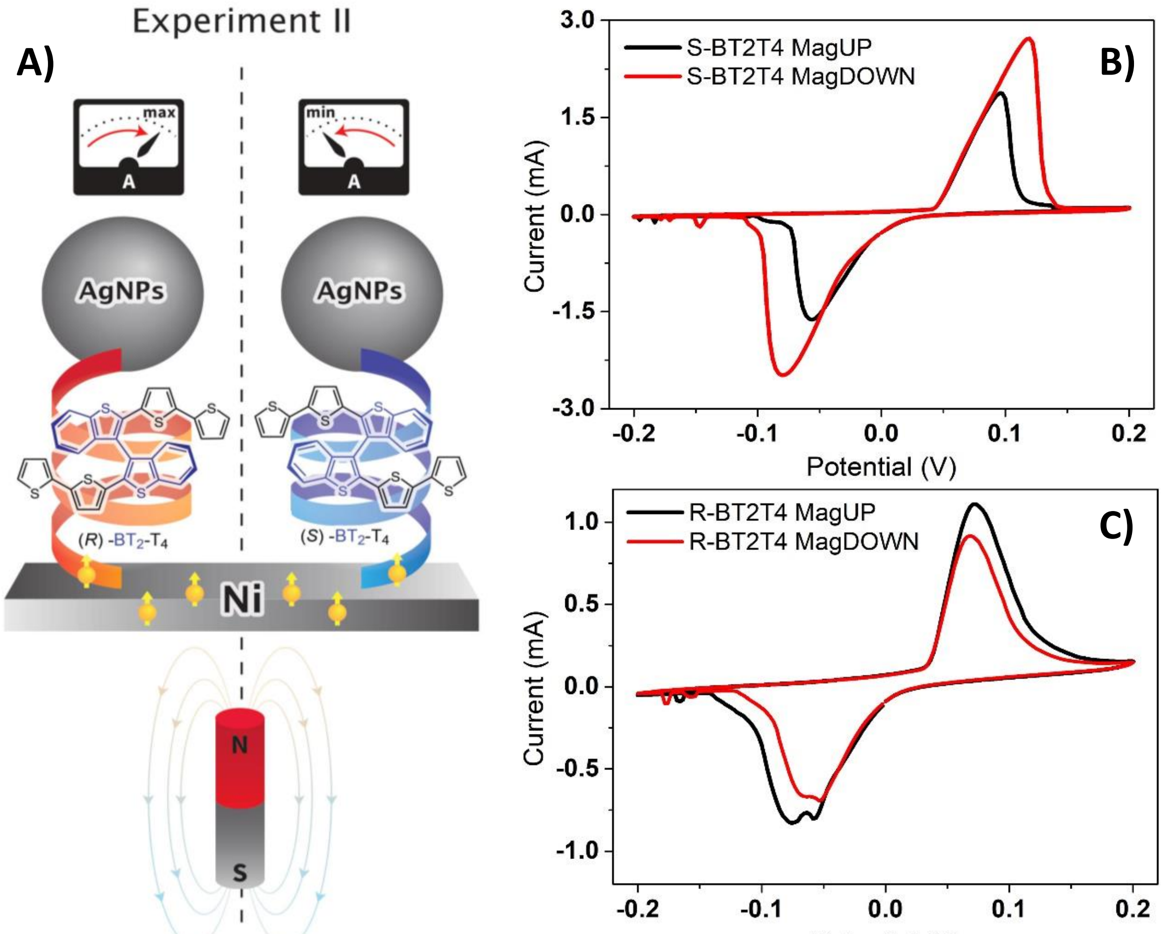

Figure 46 Experiment II: spin-dependent CVs. **A)** Schematic representation of Experiment II set up. **B)** Ni|(S)-$BT_2T_4$@AgNPs: black line MagUP, red curve MagDOWN. **C)** Ni|(R)-$BT_2T_4$@AgNPs: black line MagUP, red curve MagDOWN.

Remarkably, the I vs E pattern is found to be a function of the magnet orientation. What is more, for the Ni|(S)-$BT_2T_4$@AgNP interface the largest current peaks (at about 0.1 V and -0.075 V) in the CV are found for spin-injection corresponding to magnet DOWN orientation, Figure 46B red curve. The opposite result (the largest current is relevant to the magnet UP orientation) is found for the Au|(R)-$BT_2T_4$@AgNP interface, Figure 46C black curve. Comparison of differences in current peak values Fig. 46C and D as a function of magnet orientation allow to determine a spin polarization (SP%) value ranging between 13% and 15%. Spin polarization is defined as:

$$SP\% = \frac{(I_{MagUP} - I_{MagDOWN})}{(I_{MagUP} + I_{MagDOWN})} \times 100 \qquad (68)$$

Where: $I_{MagUP}$ and $I_{MagDOWN}$ are the peak current values recorded with the magnet orientation UP and DOWN, respectively. The quantitative assessment of the spin-chirality interaction energy can be addressed, by considering the potential difference in between the current peaks in the CVs shown in Figures 46B and 46C, the potential shift is ranging between 50 and 100 $mV$. The Nernst equation $\widetilde{\Delta\mu} = -nFE$ ($\widetilde{\Delta\mu}$ is the Gibbs energy involved in the spin-chirality interaction process, $n$ is considered one transferred electron, $F$ is the Faraday and $E$ in our case the peak potential shift due to magnet orientation) allows for a crude estimation of 5 to 10 $kJ\ mol^{-1}$ as the range of spin-"molecular-handedness" interaction energy. Details concerning the $BT_2T_4$ chemisorption on Ni, the fabrication procedure of the hybrid Ni|$BT_2T_4$@AgNP interface and relevant characterizations are reported in Section 3.2.3 ("Further in-depth characterization").

#### 3.2.2.3. Magnetic conductive probe AFM

***Experiment III:*** *magnetic conductive probe AFM.* The charge transmission through the enantiopure Au|(S)-$BT_2T_4$ and Au|(R)-$BT_2T_4$ interfaces is determined by recording I-V curves as a function of spin-injection (i.e. magnetic field UP vs magnetic field DOWN). Figures 44C and 44D represent the physics underlying Experiment III (it is the same of the Experiment II), Figure 47A shows the experimental set up. The relevant I-V curves are presented in Figures 47B and 47C, which are recorded using a magneto-conductive contact probe atomic force microscopy (mc-AFM). In this experiment the current between the AFM tip and the surface is recorded as a function of the magnetic field direction: spin-injection occurs via the ferromagnetic Ni tip. In Figure 47B, (R)-$BT_2T_4$ adsorbed on gold (Au|(R)-$BT_2T_4$ interface), the largest current is found for the magnet UP orientation; while in Figure 47C the opposite is observed: the largest current is found for the (S)-$BT_2T_4$ enantiomer adsorbed on gold (Au|(S)-$BT_2T_4$ interface).

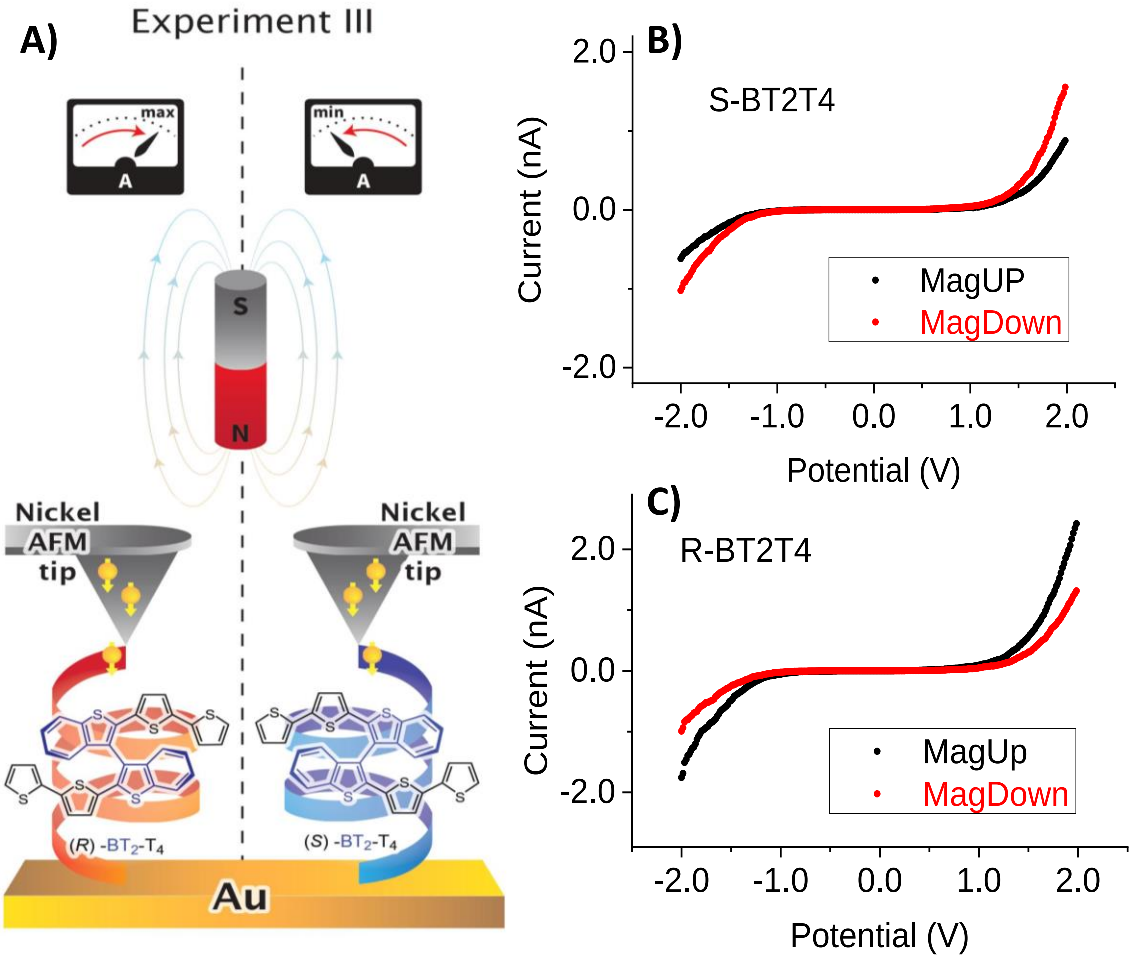

Figure 47 **A)** Schematic representation of Experiment III set up: magnetic conductive probe AFM. Au substrate and Ni ferromagnetic tip: black line MagUP orientation, red line MagDOWN orientation. **B)** Au|(S)-BT$_2$T$_4$ interface. **C)** Au|(S)-BT$_2$T$_4$ interface.

The quantitative analysis of mc-AFM I-V curves as a function of magnet orientation, Figures 47B and 47C, allows to determine a maximum spin-polarization value, which is found ranging between 28% to 30%, obtained for a ± 2 V bias.

### 3.2.2.4. XPS S 2p

Figure 48 shows XPS S 2p spectra recorded for the interfaces used in the Experiments I, II and III. Fig. 48a sets out S 2p spectra of the BT$_2$T$_4$@AgNPs interface, the peak found in the 168 to 158 eV range is due to three different components: sulfur involved in a strong chemical interaction at 161.4 eV, free not-bound thiophene sulfur at 163.6 eV and oxidized sulfur at 166 eV, these components are indicated in Fig. 48a as $S_{bound}$ , $S_{thioph}$ and $S_{ox}$ , respectively. The prominent S 2p 161.4 eV component stems from the strong S-Ag interaction (bound sulfur) giving due reason to the effective AgNPs capping. Figure 53 in Section 3.2.3 shows the

$BT_2T_4$@AgNPs XPS survey, C 1s and Ag 3d spectra, together with the relevant Voight doublets components fitting (compare Section 5.2 for details concerning the fitting procedure). Fig 48b shows XPS S 2p spectra for the Au|$BT_2T_4$ interface, the peak in the170 to 158 eV can be effectively fitted by two components centered at 163.6 (due to the free, not-chemically-bound thiophene) and 161.4 eV (associated to the S atoms of the $BT_2T_4$ adsorbed to the Au surface) [204], [222]–[225]. The absence of any signal for energy values larger than 166.5 eV further supports the effective gold surface functionalization (signals at energies larger than 166.5 eV are typical of oxidized sulphur) [205], [226]. The component relevant to chemisorbed sulphur appears more intense than the free thiophene one, this suggests a disposition of the $BT_2T_4$ which maximizes the number of sulphur atoms interacting with the gold surface [227]–[229].The inset in Fig. 48b sets out the S 2p core level spectrum using a 260 eV probing photon energy (Elettra synchrotron facility, 0.1 eV of resolution). Fig. 48b inset analysis allows to appreciate a neat separation between the two components of the doublet, the relative intensity of the two main components at 163.6 eV and 161.4 eV is reversed, with respect to Fig. 48b main spectrum, acquired at 1253.6 V of photon energy. Remarkably, a lower energy of the probing photon implies a higher surface sensitivity, this allows for a more sensitive detection of electrons ejected from sulfur atoms dangling towards the vacuum, i.e. far (not-bonded) from the gold surface. All in all, both high- and low-energy XPS results suggest that a monolayer of $BT_2T_4$ is chemisorbed on gold maximizing the interactions between sulfur and gold. A picture which is consistent also with theoretical results relating to the optimization of the $BT_2T_4$ on a gold slab (as described in Section 3.2.3). Fig 48c shows XPS S 2p spectra for the Au|$BT_2T_4$@AgNPs, note that the spectrum is rather noisy, but this result is consistent with sulfur of thiophene buried in between the gold and silver. The two components at 161.4 (orange solid curve) and 163.9 eV (green solid curve) are attributed to bound ($S_{bound}$) and free ($S_{thioph}$) sulfur atoms, respectively, their difference in energy, 1.5 eV, is consistent with results present in the literature [230]. The component at 168.1 (black solid curve) eV is assigned to oxidized sulfur [230]. Fig. 48d and 48e show XPS S 2p spectra for the Ni|$BT_2T_4$ and Ni|$BT_2T_4$@AgNPs interfaces, respectively. Spectrum in Figure 48d features a well-defined peak, which has the typical line-shape of thiols and thiophene-based SAMs: in fact, both the 161.4 eV (free S atoms) and the 163.6 eV (bound S atoms) are present, indicated as $S_{thioph}$ and $S_{bound}$, respectively (in agreement with the results of Fig. 48b). No components of energy larger than 166.5 eV are present, indicating a negligible amount of oxidized sulfur. Ni|$BT_2T_4$@AgNPs interface, Fig 48e: the S 2p spectrum analysis shows a very close agreement between Au-based and Ni-based systems. Also, the pattern of the spectrum is noisier with respect to the Ni|BT$_2$T$_4$ interface, Fig. 48d, again in tight agreement with the results obtained on gold.

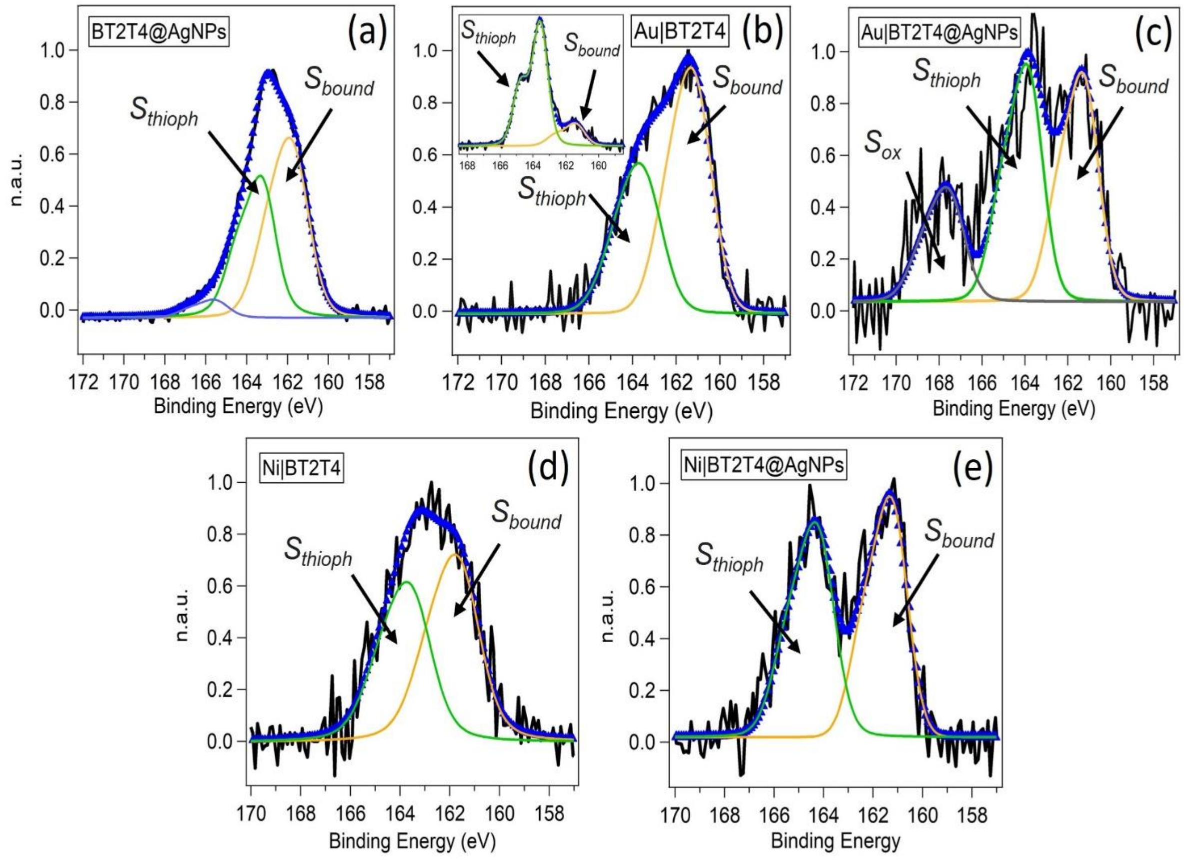

Figure 48 S 2p XPS spectra. **A)** BT$_2$T$_4$@AgNPs capped nanoparticles. **B)** Au|BT$_2$T$_4$ interface. **C)** Au|BT$_2$T$_4$@AgNPs interface. **D)** Ni|BT$_2$T$_4$ interface. **E)** Ni|BT$_2$T$_4$@AgNPs interface. The black curve represents the experimental spectra, the thick blue line curve are the overall fitted data. Individual components: thin orange line is the bound sulfur, thin green line the unbound sulfur, thin sky-blue line the oxidized sulfur.

#### 3.2.2.5. Electrodesorption

Fig. 49 sets out cyclic voltammetry curves of a ferrocyanide 5 mM, ferricyanide 5 mM (Fe(III)|Fe(II) redox couple) KCl 0.1 M aqueous solution, the Au|BT$_2$T$_4$ interface serves as the WE. The red curve in Fig. 49a shows the CV recorded using a bare Au surface WE as a reference. A peak-to-peak potential separation of about 70 mV is obtained, and the relevant fitting yields a charge transfer rate constant $k^0$ of 0.1 cm s$^{-1}$. The black curve in Figure 49a shows the CV recorded using a Au|BT$_2$T$_4$ WE, please note a decrease (about 50%) in the redox current peaks, with respect to the bare gold. Moreover, a larger peak-to-peak potential difference, between the forward and backward redox peaks (about 0.350 V) is found, typical of a slower electron transfer kinetics. The relevant curve fitting yields a $k^0$ charge transfer constant of about $5 \times 10^{-4}$ cm s$^{-1}$. Indeed, also the CV measured after the BT$_2$T$_4$ electro-desorption procedure, Fig. 49b CVs, is reported in Figure 49a, but it overlaps exactly with the CV obtained for the bare Au surface. A further clear-cut indication of the effective BT$_2$T$_4$ chemisorption on gold.

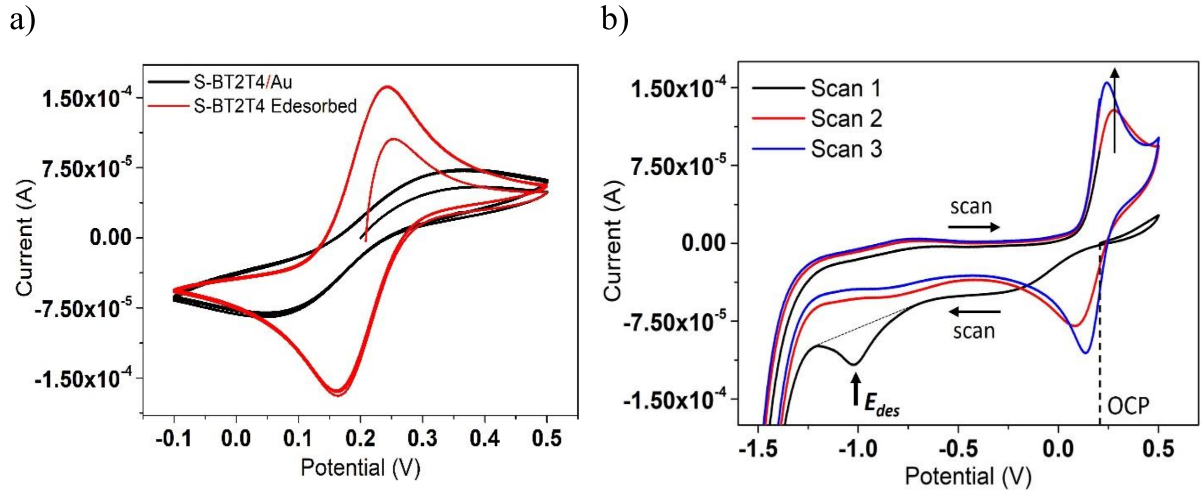

Figure 49 CV curves 5 mM Fe(III)|Fe(II) redox couple in 0.1 M KCl aqueous solution, recorded at 0.1 V s$^{-1}$ potential scan rate. Pt and Ag/AgCl/KCl$_{sat}$ are the CE and RE, respectively. **a)** Solid black line Au|BT$_2$T$_4$ WE. Solid red line CV recorded after the BT$_2$T$_4$ electrodesorption. **b)** CV curves for the electrodesorption procedure, 0.5 V s$^{-1}$ potential scan rate. Solid black line: first CV cycle, starting from OCP to 0.5 V, then the potential is scanned from 0.5 to -1.5 V. Solid red curve is the second scan -1.5 to 0.5 V potential range. Solid blue lines: subsequent cycles, carried out in the -1.5 to 0.5 V potential range.

Such considerations are also supported by a quantitative assessment of electrodesorption CVs. Compare the CV curves reported in Fig. 49b: in the anodic part of the first CV scan, from OCP (*i.e.* +0.24 V) to 0.5 V (black line), much lower currents are observed with respect to the bare Au surface (subsequent scans, as well as comparison with Fig. 49a bare Au CV). The cathodic part of the first scan features a broad shoulder at about -0.39 V with a $-5 \times 10^{-5}$ A current (this current value compares well with the backward current recorded on the modified electrode, i.e. the Fig. 49a black curve). Scanning more negative, a neat current peak is present in the first scan at $-1.05$ V (which can be related to BT$_2$T$_4$ electro-desorption), indicated by an arrow ($E_{des}$) in Fig. 49b. The latter peak is absent in the successive CV cycles (red and blue curves). The redox reaction underlying the $E_{des}$ current peak can be assumed as follows (69):

$$Au|BT_2T_4 + e^- \rightarrow Au + BT_2{T_4}^-_{bulk\ solution} \qquad (69)$$

Focusing the attention on the potential range between -0.1 and 0.5 V, after the first potential scan up to -1.5 V which means after the electrodesorption, the CV becomes coincident to that measured on the bare Au. Thus, the $BT_2T_4$ electro-desorption peak potential, $E_{des}$ marks the boundary between the functionalized Au|$BT_2T_4$ (Figure 49a, black line) and the bare Au behavior (Figure 49a, red line). Taken together, all these results provide a consistent indication that the incubation of gold in the $BT_2T_4$ solution yields a functionalized surface by a $BT_2T_4$ self-assembled monolayer (SAM). Moreover, integration of the peak current at the $E_{des}$ potential value, Fig. 49b black curve, allows to estimate the area of $BT_2T_4$ adsorbed on the Au surface, which is found to be about 50 $Å^2$. The latter value is consistent with a surface coverage in the one to two monolayers range, with a $BT_2T_4$ disposition allowing for the closest contact between sulfur atoms of the $BT_2T_4$ thiophene backbone and the gold surface (please compare the theoretical results Section 3.2.3.5).

Fig. 50 displays CV measurements concerning the $BT_2T_4$ electrodesorption: Ni|$BT_2T_4$, interface. CVs were recorded before (Fig. 50a black curve) and after the electrodesorption experiment (Fig. 50b red curve), 5 mM Fe(III)|Fe(II) in 0.1 M KCl aqueous solution. Fig. 50b shows the $BT_2T_4$ electrodesorption experiment CVs. The $BT_2T_4$ electrodesorption underlies the current peak, $E_{des}$ , in the solid red curve Fig. 50b. Overall, the electrodesorption experiment yields results in tight comparison with the electrodesorption experiment carried out in the case of the Au substrate. The peak-to-peak potential difference decreases after $BT_2T_4$ electrodesorption: compare black and red CV curves in Fig. 50b.

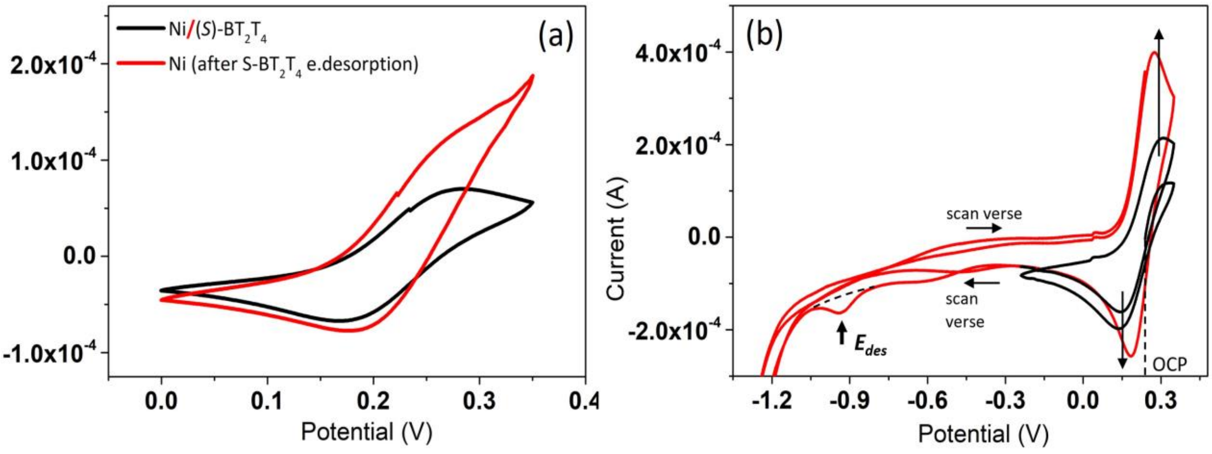

Figure 50 CV curves 5 mM Fe(III)/Fe(II) redox couple in 0.1 M KCl aqueous solution. Pt and Ag/AgCl/$KCl_{sat}$ are the CE and RE, respectively. **a)** Solid black line Ni|$BT_2T_4$ WE. Solid red line CV recorded after the $BT_2T_4$ electrodesorption, 0.1 V $s^{-1}$ is the potential scan rate. **b)** CV curves for the electrodesorption procedure, 0.5 V $s^{-1}$ potential scan rate. Solid black line: first CV forward cycle, starting from OCP to 0.5 V, then the potential is scanned from 0.5 and reversed at -0.2 V. Solid red lines: subsequent cycles, carried out in the -1.5 to 0.5 V potential range. Upward and downward arrows indicate the CV oxidation and reduction peaks before the electrodesorption.

### *3.2.3. Further in-depth characterization*

The conclusions presented in paragraph 3.2.2 rely on the accurate fabrication of complex hybrid multilayered molecular architectures, a quite complex and crucial task. A substantial effort was devoted to the characterization of such interfaces. The physical arrangement of the interfaces was investigated in depth, by cross-checking results obtained using independent surface sensitive techniques: XPS, Raman, electro-desorption. Experiments have been replicated a number of times (at least five times), eventually proving that the current vs. potential curves are affected by an overall confidence interval of ±1%.

#### 3.2.3.1 Silver Nanoparticles (AgNPs)

$BT_2T_4$ capped AgNPs ($BT_2T_4$@AgNP) serve as the redox couple to probe charge transmission in electrochemical experiments, i.e. Experiment I and II in Section 3.2.2. In view of the main role played in this work by $BT_2T_4$@AgNPs, a section is here devoted to show the XPS and electrochemical characterization results.

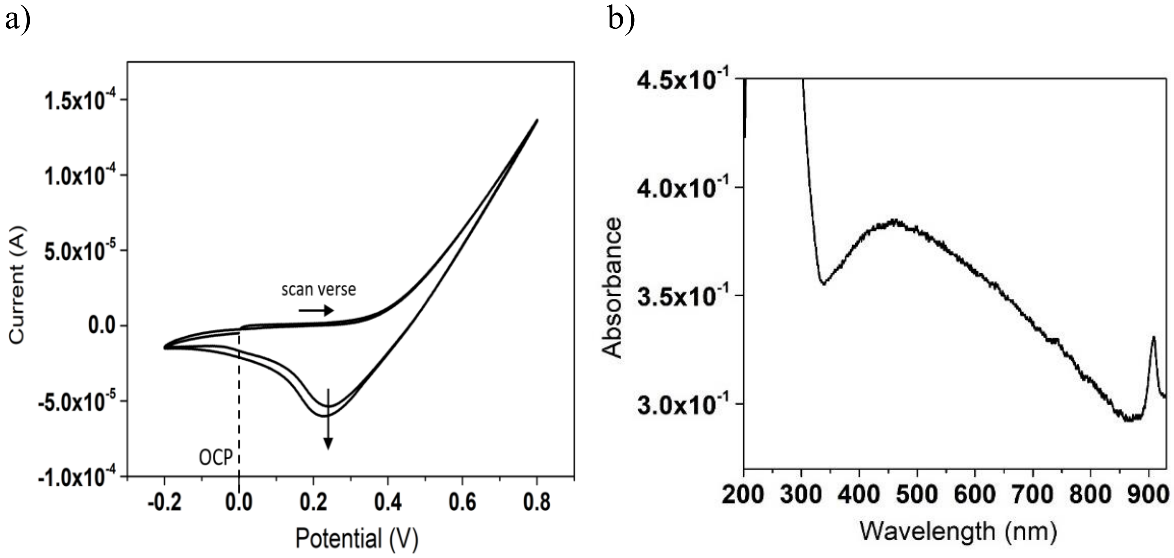

Figure 51 **a)** CV relevant to the AgNPs electrochemical synthesis. A silver wire serves as the WE in a 0.02 M $NaNO_3$ ethanol solution, 0.1 V $s^{-1}$ is the potential scan rate. Pt and Ag/AgCl/$KCl_{sat}$ served as the (CE) and (RE) electrodes respectively. **b)** UV-Vis absorption spectrum of the solution after electrochemical AgNPs production [231].

Silver nanoparticles were electrochemically synthesized following the method of Starowicz *et al.* [232]. Fig. 51a shows the preliminary cross-check cyclic voltammetry, performed on the electrochemical system in a $NaNO_3$ 0.02 M ethanol solution, just before starting the proper AgNPs synthesis. Both the oxidation onset potential (0.35 V) and the reduction peak potential

(0.22 V) are in tight agreement with the results reported in the literature [232], [233]. The actual AgNPs synthesis was carried out under galvanostatic control, for 30 minutes with a constant current of 0.14 mA (which corresponds to the current at 0.8 V potential, compare the CV in Fig. 51a). Then, the freshly prepared AgNPs suspension was characterized via UV-Vis spectroscopy, the relevant spectra are reported in Figure 51b. The spectrum shows a broad and shallow peak centered at 420 nm, an outcome consistent with literature data, suggesting a AgNPs size distribution in the 20 to 50 nm range [232], [233]. The presence of the nanoparticles in suspension was also cross-checked via a simple laser scattering experiment, Fig. 52. The cuvette closer to the laser contains the solution before the electrochemical production of AgNPs (blank solution), the cuvette closer to the white screen contains the solution after AgNPs electrochemical synthesis. The AgNPs presence is clearly seen in the AgNPs suspension due to scattering (allowing to "see" the green laser ray passing "within" the AgNPs suspension).

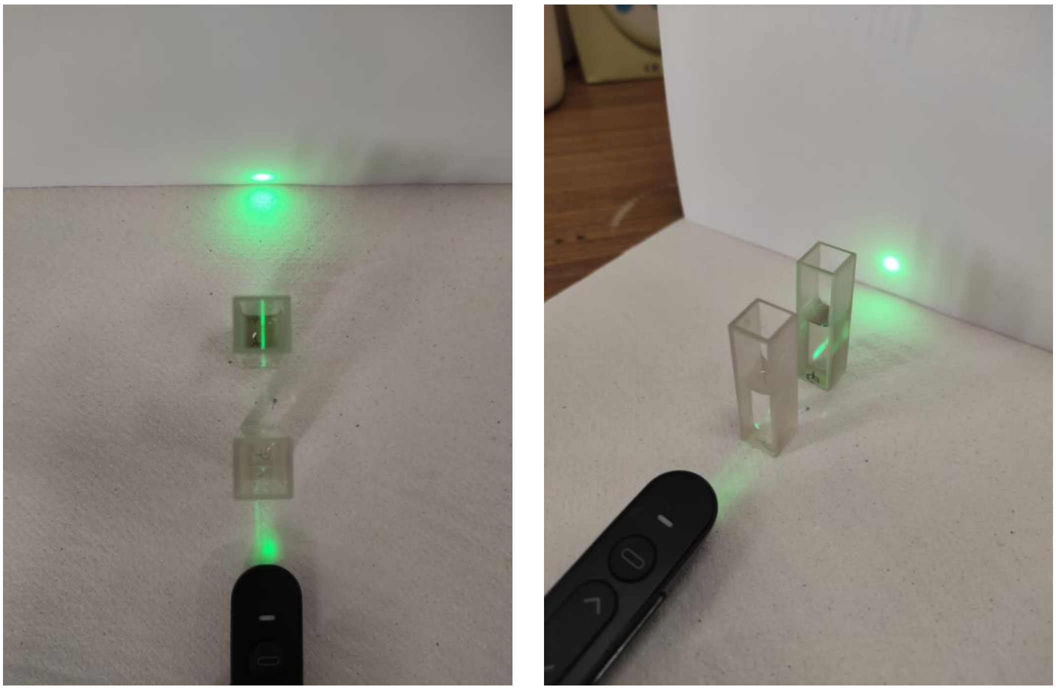

Figure 52 Laser scattering experiment, two cuvettes: the cuvette closer to the laser source contains the ethanolic solution prior AgNPs synthesis, while the cuvette closer to the screen is the AgNPs suspension after electrosynthesis.

###### *3.2.3.1.1 BT2T4 capped AgNPs (BT2T4@AgNPs)*

The electrochemically synthesized AgNPs are then chiralized by capping with enantiopure $BT_2T_4$ molecules (please refer to Section 5.3.5). XPS spectra have been recorded for $BT_2T_4$@AgNPs, to cross-check the effective functionalization. To this purpose, the most critical aspect of the XPS characterization is the investigation of the S 2p core level, which was included in the Main Results Section (3.2.2). Figure 53 presents all the supplementary details concerning the XPS investigation of the $BT_2T_4$@AgNPs interface. Freshly synthesized $BT_2T_4$@AgNPs suspension was drop-casted on a glassy carbon substrate, and then dried under a nitrogen stream. The nanoparticles suspension was drop-casted on a glassy carbon surface in order to minimize any complication due to possible chemisorption on the substrate.

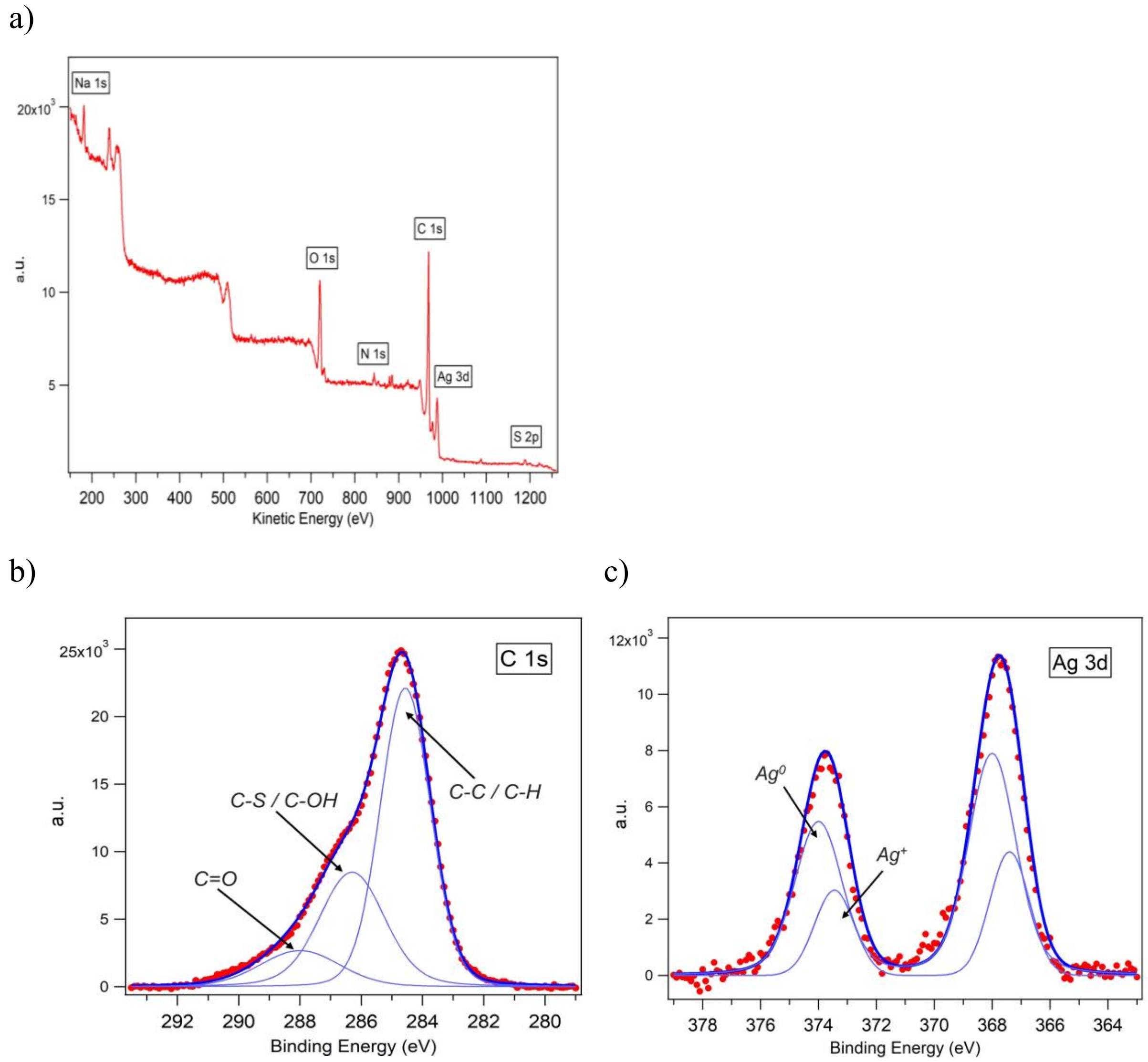

Figure 53 XPS spectra of a $BT_2T_4$@AgNPs suspension drop-casted on a glassy carbon surface, probed with Mg Kα X-ray source, 1.254 keV of photon energy. **a)** Survey spectrum. **b)** C 1s. **c)** Ag 3d. The dotted red curve represents the experimental spectra. The thick blue line curve are the overall fitted data (thin blue line curves are the individual components).

The survey scan (Fig. 53a) shows prominent peaks associated with silver and sulfur (as expected). The Ag 3d spectrum shown in Fig. 53c features two components with a very small energy splitting, of about 0.5 eV. The higher binding energy structure, 368.3 eV (Ag $3d_{5/2}$ peak), is assigned to metallic silver, while the lower energy structure, 367.7 eV, is due to silver cation, Ag$^+$. The presence of Ag$^+$ is possibly due to silver not reduced by ethanol, following the electrochemical oxidation.

#### *3.2.3.1.2 Au|BT$_2$T$_4$|AgNPs*

AgNPs were exploited as a reversible redox couple to probe the charge transmission properties of the Au|BT$_2$T$_4$ interface. To this end, an Au|BT$_2$T$_4$|AgNPs multi-layered interface has been prepared via overnight incubation of Au|BT$_2$T$_4$ into the AgNPs suspension (details are reported in Experimental Section 5.3.4). It is expedient to assume that a strong chemical interaction occurs between Au|BT$_2$T$_4$ and AgNPs, via the dangling thiophene sulfur atoms oriented towards the solution. An assumption consistent with XPS, Raman and theoretical results.

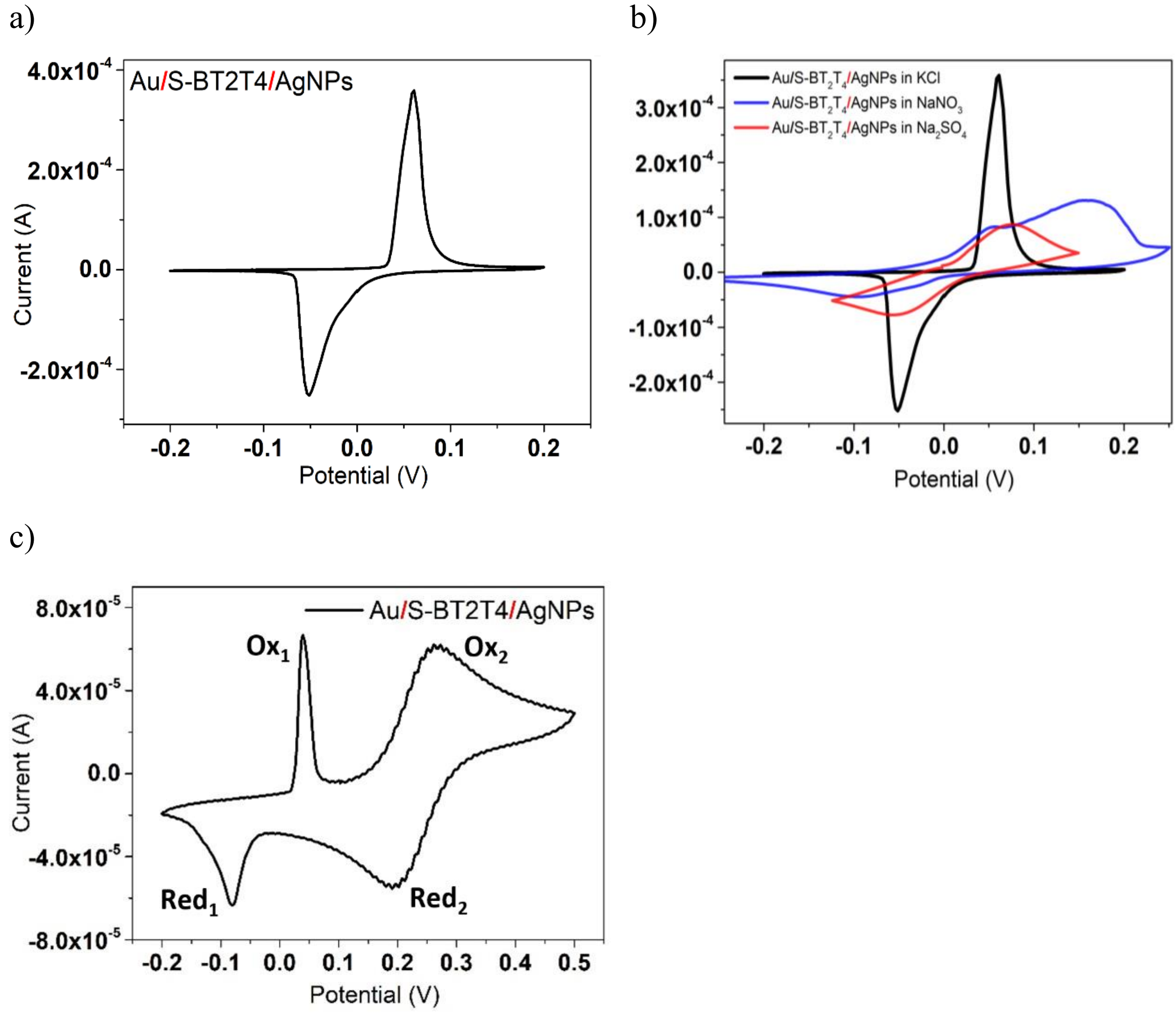

Figure 54 CV curves of the Au|BT$_2$T$_4$|AgNPs interface serving as the WE. **a)** 0.1 M KCl aqueous solution, 0.05 V s$^{-1}$ potential scan rate. The potential is cycled in the -0.2 V to 0.2 V range, i.e. around the redox couple Ag/Ag$^+$ standard potential window. **b)** Comparison of the AgNPs redox signal using KCl as the supporting electrolyte (black line, same plot as panel a)

and other electrolytes (blue line $NaNO_3$ 0.1 M, red line $Na_2SO_4$ 0.1 M) **c)** 5 mM Fe(III)|Fe(II) redox couple in 0.1 M KCl aqueous solution, 0.1 V $s^{-1}$ potential scan rate.

Figure 54 shows cross-check CVs of the Au|S-$BT_2T_4$|AgNPs hybrid-interface, which serves as the WE. In particular, Figure 54a is recorded in a 0.1 M KCl aqueous solution, at a 50 mV $s^{-1}$ potential scan rate, two quasi-reversible current peaks are present in the CV, centered at about +0.075 V (oxidation regime, labelled as $E_{ox}$ in Fig. 54a) and -0.075 V (reduction regime, labelled as $E_{red}$ in Fig. 54a). The oxidation of silver with formation of silver chloride is the redox reaction underlying the oxidation peak, compare reaction (70). This result is confirmed by cross-check of CV measurements carried out in 0.1 M $Na_2SO_4$ and 0.1 M $NaNO_3$ water solutions (Fig. 54b): the current peaks are almost absent, in agreement with results in the literature [234], [235].

$$\mathrm{AgNPs_{adsorbed}} + \mathrm{Cl^-} \rightleftharpoons \mathrm{AgNPs_{adsorbed}} - \mathrm{Cl} + \mathrm{e^-} \qquad (70)$$

Figure 54c shows a CV curve where the Au|S-$BT_2T_4$|AgNPs interface serves as the WE, with the presence in solution of a 5 mM Fe(III)|Fe(II) redox couple, in a 0.1 M KCl aqueous solution, at 100 mV $s^{-1}$ potential scan rate. In this case, both the Ag/$Ag^+$ ($Ox_1$ and $Red_1$ current peaks) and the $Fe^{3+}$/$Fe^{2+}$ ($Ox_2$ and $Red_2$ current peaks) one-electron reversible electrochemical processes are present, and they show clear-cut current peaks. The redox processes underlying the presence of the current peaks are shown below:

**Ox₁**: $Ag + Cl^- \rightarrow AgCl + e^-$ **Ox₂**: $Fe^{2+} \rightarrow Fe^{3+} + e^-$.

**Red₁**: $AgCl + e^- \rightarrow Ag + Cl^-$ **Red₂**: $Fe^{3+} + e^- \rightarrow Fe^{2+}$

Chemisorption of $BT_2T_4$ on AgNPs has been characterized recording XPS spectra of the Au|$BT_2T_4$@AgNPs interface. The survey scan and the relevant core levels are displayed in Figure 55, except for the critical S 2p domain, which is included and largely discussed in the Main Results Section (3.2.2).

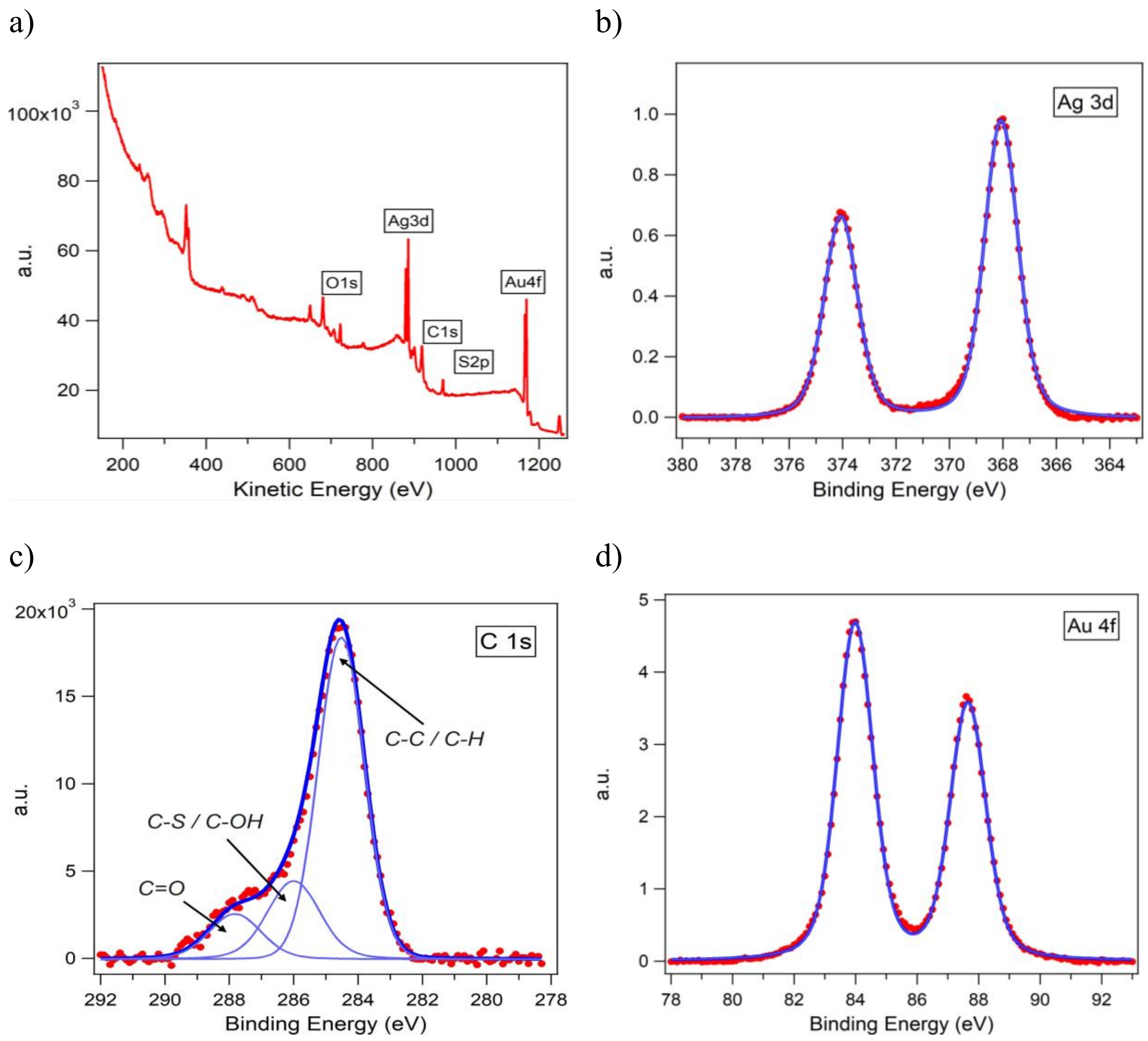

Figure 55 XPS spectra of the Au|BT$_2$T$_4$@AgNPs interface, Mg Kα photons, 1.254 keV photon energy. **a)** Survey spectrum **b)** Ag 3d **c)** C 1s **d)** Au 4f. The dotted red curve represents the experimental spectra. The thick blue line curve are the overall fitted data (thin blue line curves are the individual components).

### 3.2.3.2 Gold surfaces: Au|BT$_2$T$_4$

Overnight incubation of gold surfaces in a freshly prepared enantiopure BT$_2$T$_4$ ethanolic solution allowed to obtain gold functionalized WE, see above the Experimental Section 5.3 for details. As it is well known, this is exactly the same procedure usually exploited to functionalize gold surfaces with thiol derivatives [197], [236]. To gain a well-defined picture of the gold functionalization, the theoretical calculations were followed by an in-depth experimental characterization of the post-incubation surface.

#### *3.2.3.2.1 Au|BT2T4 XPS results*

Fig. 56 shows XPS spectra of the Au|BT$_2$T$_4$ interface. Fig. 56 a, b, c show the survey scan, the C 1s and the Au 4f core levels, respectively. S 2p data are reported in the Main Results Section (3.2.2).

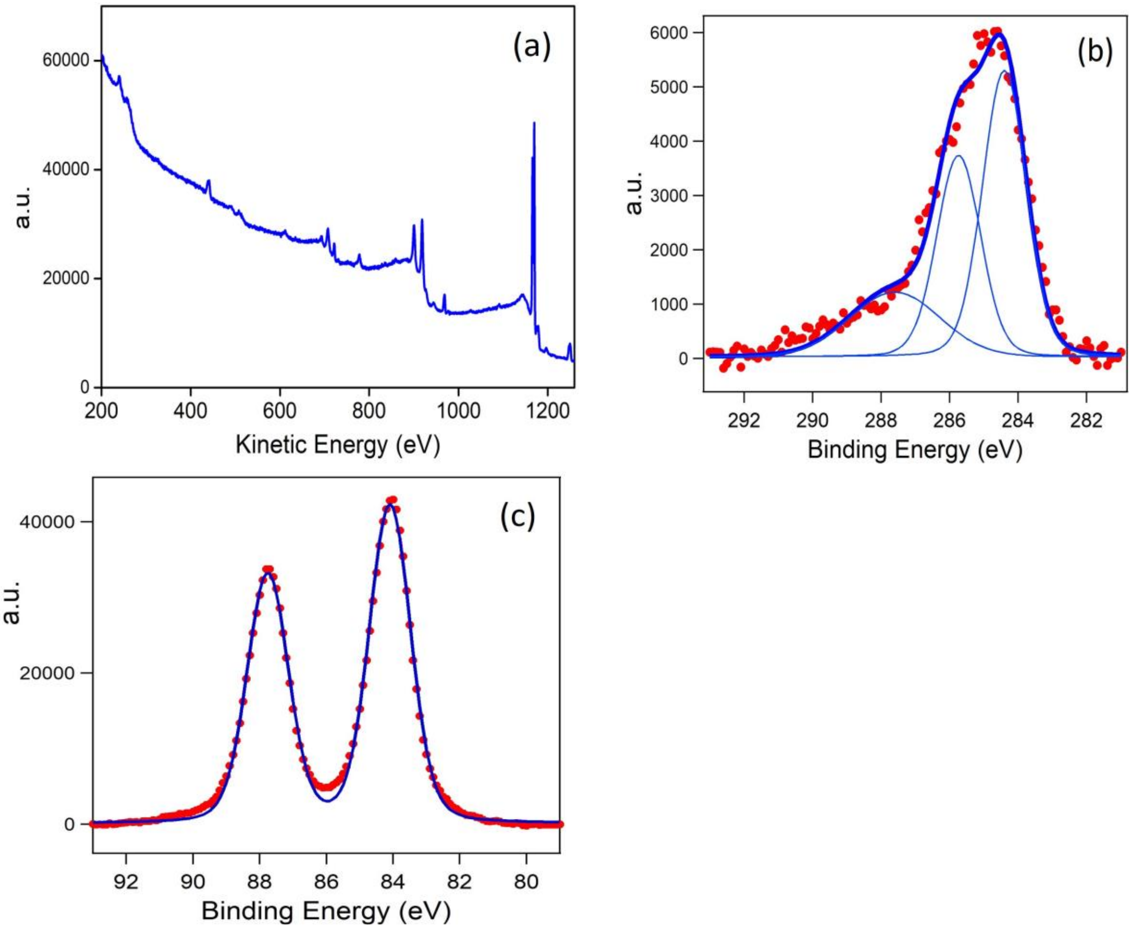

Figure 56 XPS spectra of the Au|BT$_2$T$_4$interface, Mg Kα photons, 1.254 keV photon energy. **a)** Survey spectrum **b)** C 1s **c)** Au 4f. Dotted red curves are the experimental spectra. Thick blue line overall fit, thin blue line the fitted data individual components.

In the Main Results Section, the S 2p domain is investigated with two different probing photons (Fig. 48b). The main spectrum is acquired with Mg Kα photons (1.254 keV); the inset spectrum is probed with 260 eV synchrotron light photons. Based on the Mg Kα XPS results, it is possible to estimate the effective film thickness from optical absorption of the BT$_2$T$_4$. Accounting also for the reflectivity of the gold surface, i.e. quantitative comparison, Au 4f spectra, of the bare and functionalized surface [235], [237]. In fact, a 1.254 keV energy, of probing photons, corresponds to a high inelastic mean free path in the organic film: a value of $\Lambda$=30 Å ± 2 Å is expected for organic chemisorbed molecules [228], [238]. Eq. (71) allows to determine the effective interface film thickness ($d$), for an estimated value of $\Lambda \sim 30$ Å [217], [234], [238].

$$d \approx \Lambda \, ln\left(I_{Au_0}/I_{Au_d}\right) \qquad (71)$$

where $I_{Au_0}$ is the Au $4f_{7/2}$ bare gold surface intensity, $I_{Au_d}$ is the intensity of the Au $4f_{7/2}$ photoelectrons attenuated by a homogeneous film of effective thickness d, and Λ is the inelastic mean free path of the photoelectrons within this layer. The estimated thickness of the $BT_2T_4$ SAM is 50 Å. This value is consistent with a surface coverage ranging between 1 and 1.5 monolayers.

#### *3.2.3.2.2 Au|BT2T4|BT2T4@AgNPs enantio-recognition (Exp I reproducibility)*

Figure 57 shows three physically different experiments which are the replica of Experiment I, this to assess the reproducibility of the whole synthesis and measurement procedure, from sample (interfaces) preparation to CV measurements concerning the electrochemical based chiral(enantio) recognition.

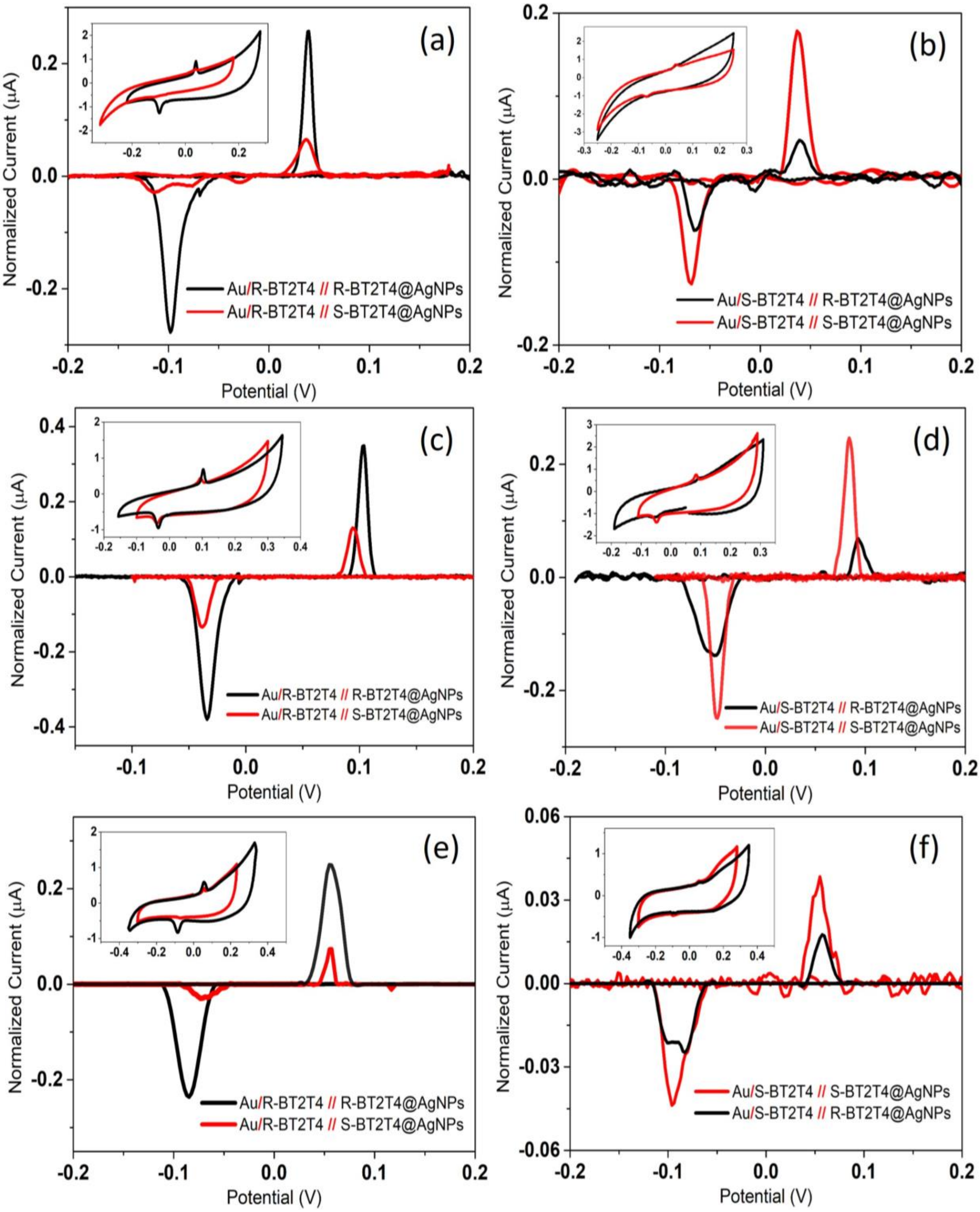

Figure 57 Physically different replica of the CVs of the Main Results Section (3.2.2): Experiment I (chiral recognition electrochemistry). CVs are recorded for all the possible handedness combinations using different WEs (for the same preparation procedure). Main panels show the normalized current vs potential curves (baseline subtraction) while the insets display the raw data.

Based on the results shown in Figure 45 and Figure 57, we can conclude that CVs data relevant to Experiment I allow for a certain enantio recognition of the surface handedness exploiting the "chiralized" AgNPs. From a quantitative point of view the degree of uncertainty in both potential shift and peak current are around 5 %.

#### *3.2.3.2.3 TD-DFT Raman spectra, single BT2T4 species*

To account for Raman spectroscopy results collected by using two excitation laser energies (514.5 nm and 785 nm excitation light sources), electronic spectra (TD-DFT) have been calculated. Fig. 58 shows $BT_2T_4$ TD-DFT spectra calculated at the B3LYP/cc-pVTZ level of the theory, for both the neutral (Fig. 58a) and cation (Fig. 58b) species. The lowest energy of absorption for the neutral form corresponds to 440 nm wavelength, whilst the cation has its maximum absorption in the 550 to 850 nm range. This is relevant to the results observed both for $BT_2T_4$ chemisorbed on Au and in *"in-situ"/"in-operando"* Raman spectra of $BT_2T_4$ chemisorbed on Ni (*vide infra*, Sections 3.2.3.2.5 and 3.2.3.3.2).

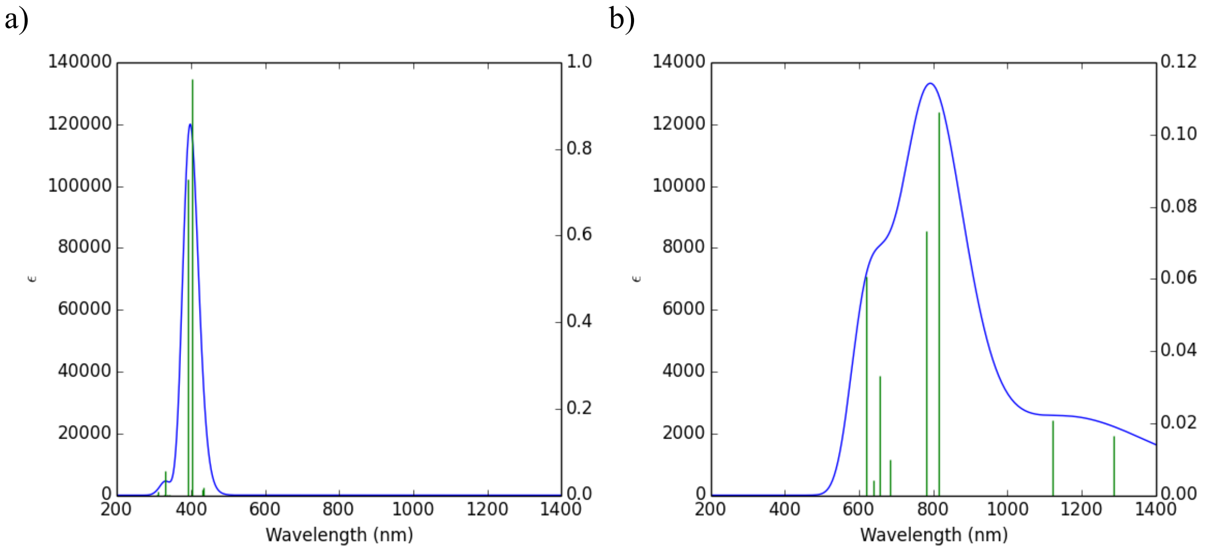

Figure 58 DFT UV-Vis spectra calculated at the $BT_2T_4$, B3LYP/cc-pVTZ level of the theory. **a)** neutral singlet. **b)** cation doublet.

Fig. 59 shows Raman spectra calculated at the B3LYP/cc-pVTZ level of the theory. Theoretical Raman spectra feature a significative large intensity peak centered at around 1500 $cm^{-1}$ and the two largest intensity peaks in the 1300 to 1400 and $cm^{-1}$ range.

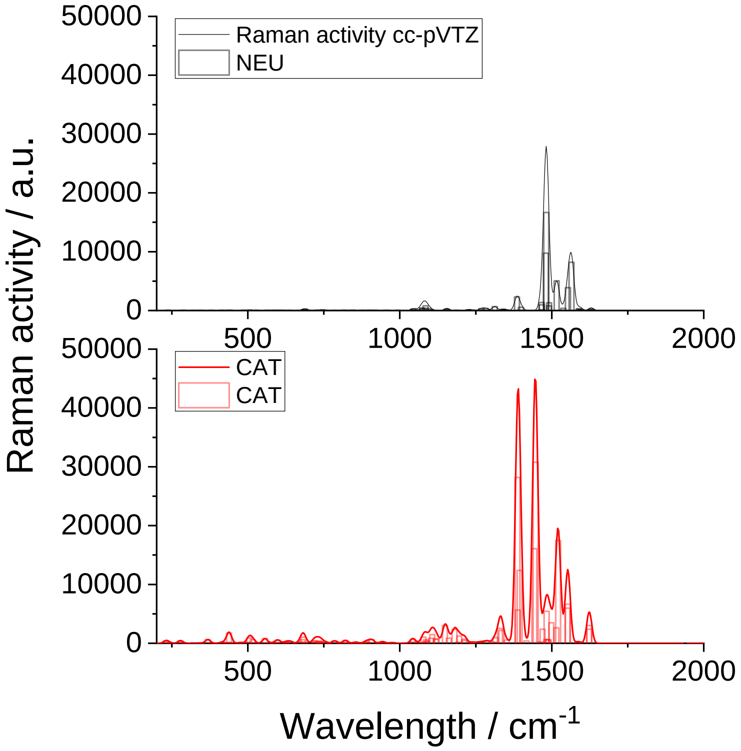

Figure 59 DFT Raman intensity calculated for the $BT_2T_4$, B3LYP/cc-pVTZ level of the theory. Black bars and curve neutral (NEU) species. Red bars and curves refer to the cation (CAT) species.

#### *3.2.3.2.4 PM6 Au|BT2T4 Raman spectrum*

Fig. 60 shows the Raman spectrum calculated for the $BT_2T_4$/Au57 cluster, three Au atoms in direct contact with the $BT_2T_4$ molecule are allowed to relax (the geometry optimization has been performed according to the PM6 semiempirical method, please compare Section 5.2.12). Both satellite peaks at around 750 $cm^{-1}$ and the prominent peaks at 1250 $cm^{-1}$ are also found in the experimental spectrum of the Au|$BT_2T_4$ interface (vide infra, Section 3.2.3.2.5), they are not evident in the neutral molecule (Fig 59). The calculated Mulliken net charges yield a value of 1.3 electrons transferred from the chemisorbed $BT_2T_4$ to the gold cluster.

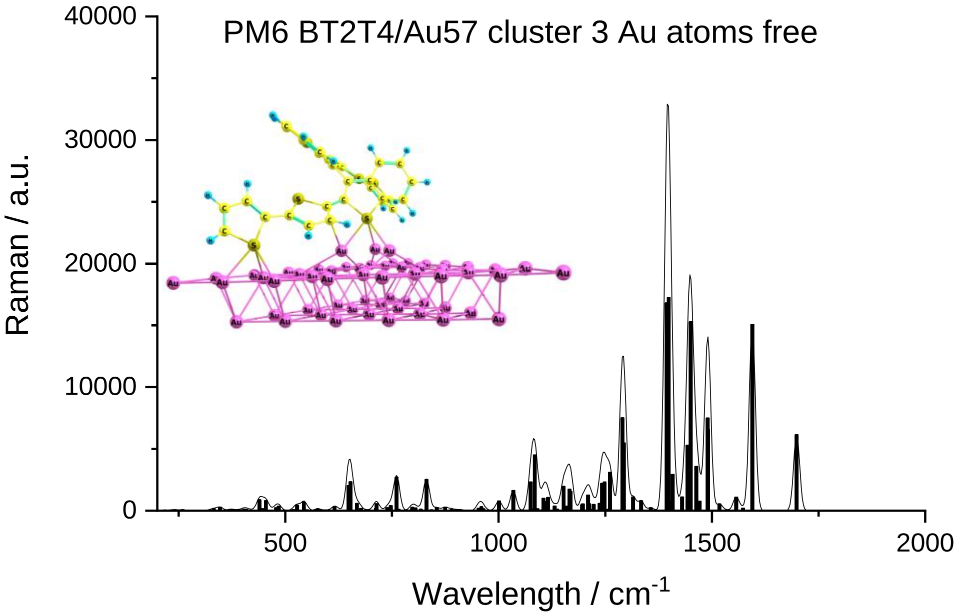

Figure 60 Theoretical Raman spectrum for the $BT_2T_4$/Au57 cluster, PM6 level of theory.

#### ***3.2.3.2.5 Au|BT2T4 experimental Raman results***

Fig. 61 shows experimental Raman spectra of the Au|$BT_2T_4$ and Au|$BT_2T_4$@AgNPs interfaces. Remarkably, a neat difference is found in the spectra as a function of the excitation energy. The use of the 514.5 nm excitation yields a rather noisy spectrum. On the contrary, spectra recorded by using a 785 nm excitation energy, Fig. 61a, feature a much better signal to noise ratio (this peculiar behavior is related to the charge transfer between $BT_2T_4$ and gold, *vide supra* theoretical results Sections 3.2.3.2.3 and 3.2.3.2.4). The intensity of the latter spectra is higher if compared with that of the $BT_2T_4$ powder. The observation of SERS effect suggests a strong chemisorption of $BT_2T_4$ on Au, Fig. 61a, and the subsequent chemisorption of AgNPs on top in Fig. 61b. All in all, Raman spectra suggest a strong interaction with both the gold substrate and AgNPs, as well, and that the $BT_2T_4$ chemisorption is accompanied by a strong charge transfer. In fact, comparison of the absorption spectrum of $BT_2T_4$ neutral and cation species gives due reason to the difference observed when using the 514.5 nm and 785 nm excitation light sources. Theoretical spectra show that the neutral species absorbs at wavelengths smaller than 450 nm, while the cation has maximum absorption in the 550 to 820 nm range. Thus the absorption of the cation species matches the 785 nm laser excitation energy, which is able to yield good quality Raman spectra.

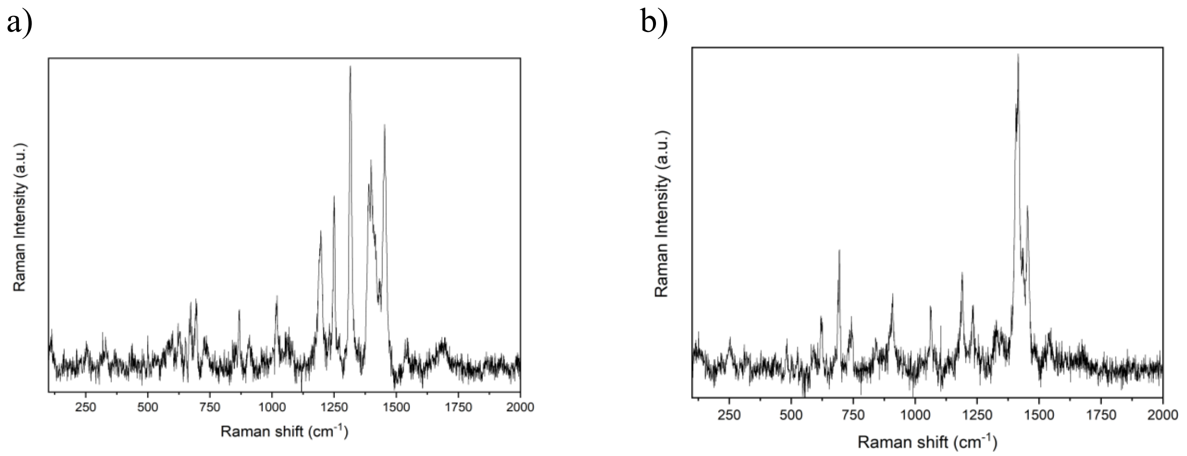

Figure 61 Raman spectra recorded with a 785 nm excitation energy wavelength. **a)** Au|$BT_2T_4$ interface. **b)** Au|$BT_2T_4$@AgNPs.

### 3.2.3.3 Nickel surfaces: Ni|$BT_2T_4$

Ni|$BT_2T_4$ and Ni|$BT_2T_4$@AgNPs interfaces were produced with a strategy developed to minimize the Ni oxidation (compare the Experimental Section, 5.3.7) [217].

#### *3.2.3.3.1 Chiral Ni|BT2T4 interface: XPS surface characterization*

Figure 62 shows XPS spectra of the Ni|$BT_2T_4$ interface: the survey scan as well as the C 1s, and Ni 2p core level regions. The S 2p photoemission spectrum is shown and discussed in the Main Results Section (3.2.2).

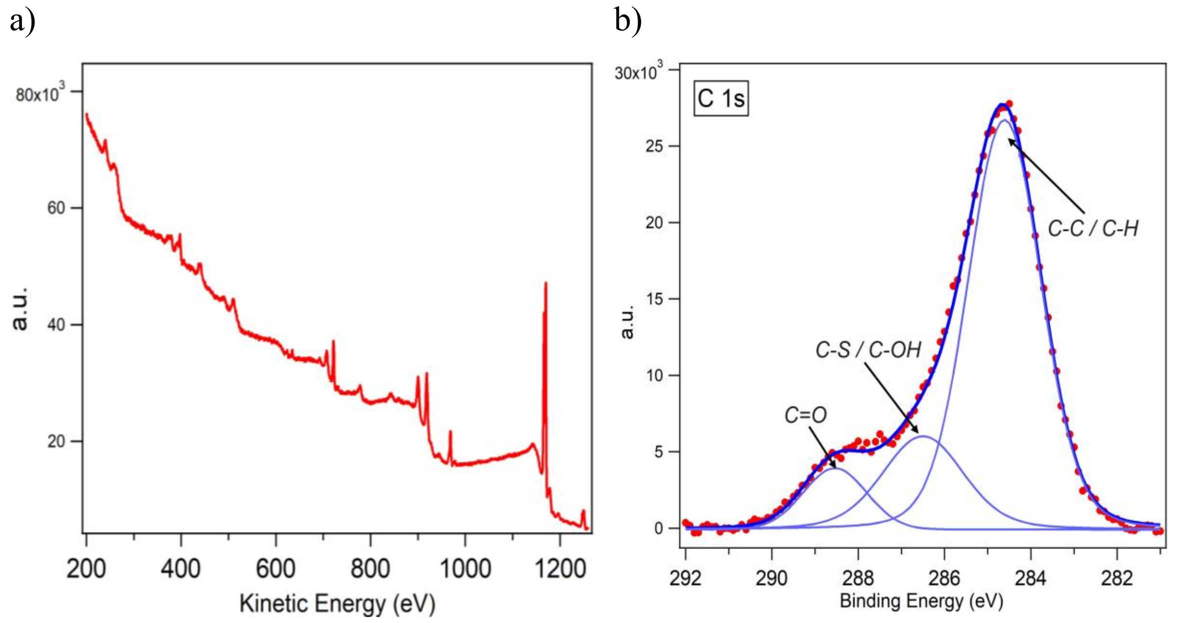

c)

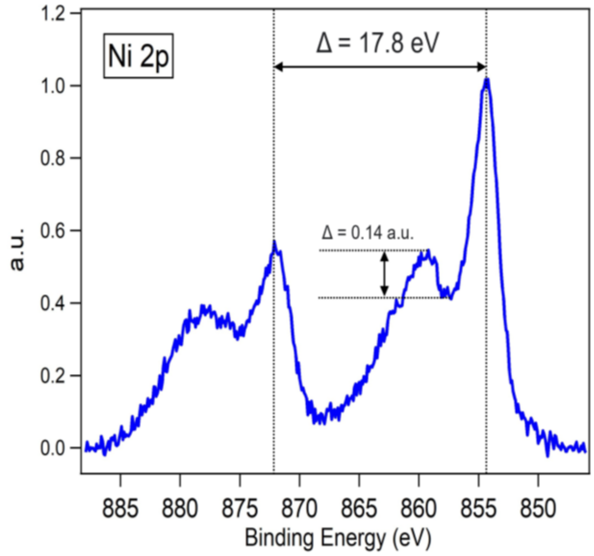

Figure 62 XPS spectra of the Ni|$BT_2T_4$interface, Mg Kα photons, 1.254 keV photon energy. **a)** Survey spectrum **b)** C 1s **c)** Ni 2p. Panel b): the dotted red curve is the experimental spectrum. Thick blue line overall fit. Thin blue lines are the individual components contribution.

Fig. 62c sets out the XPS spectrum of the Ni 2p core level region, showing a difference in energy between the Ni $2p_{1/2}$ and Ni $2p_{3/2}$ components of 17.8 eV. Suggesting the presence of nickel oxide traces, due to air contamination during the transfer between the electrochemical cell (where the Ni functionalization occurs at a constant reduction potential, i.e. metallic Ni) and the XPS chamber.

#### *3.2.3.3.2 Chiral Ni|BT2T4 interface: In-situ electrochemical-Raman characterization*

Fig. 63 sets out *in-operando* Raman spectra, recorded in-situ with the laser focus on the WE in the electrochemical cell of the Ni|$BT_2T_4$ interface collected as a function of time, while the Ni|$BT_2T_4$ interface is under potentiostatic reduction regime. Raman spectra were recorded as a function of time at a constant potential of $-0.5\ V$, to maintain Ni in its neutral metallic state (compare the Experimental Section 5.2.10 for details concerning the relevant experimental set-up) [217]. Fig. 63 shows the Raman spectrum recorded in a wide wavenumber range. Fig. 63b sets out a narrower wavenumber region, which shows a remarkable time evolution. Fig. 63b allows to appreciate a clear-cut increase in two Raman peaks found at 1517 and 1537 $cm^{-1}$, vertical dashed line, although they are quite close to a prominent peak of acetonitrile solvent (centered at 1420 $cm^{-1}$). Remarkably the 1517 and 1537 $cm^{-1}$ peaks increase in intensity at increasing time, whilst the 1420 $cm^{-1}$ is decreasing as the $BT_2T_4$ increases its surface coverage.

Two prominent Raman peaks are found in the theoretical spectrum of the $BT_2T_4$ cation, vide supra the theoretical results section (Fig. 59 lower panel, cation species, the two peaks at 1519 and 1551 $cm^{-1}$).

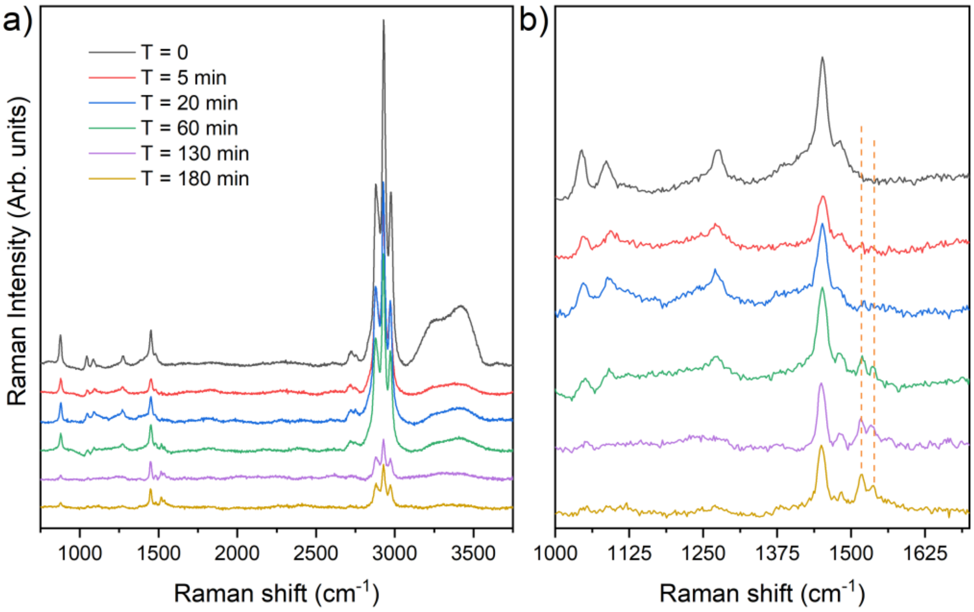

Figure 63 In-situ Raman spectra of the Ni|$BT_2T_4$ interface, in-operando conditions. The Ni substrate (WE) is maintained at -0.5 V under reduction potentiostatic regime. **a)** wide wavelength domain **b)** zoomed region in the 500 – 1800 cm$^{-1}$ wavelength domain.

#### *3.2.3.3.3 Chiral Ni|BT2T4@AgNPs interface: XPS characterization*

The Ni|$BT_2T_4$@AgNPs interface, which is the WE in the Spin-Dependent Electrochemistry measurements in the Main Results Section (Experiment II: Fig. 46B, C) has been characterized via XPS spectroscopy measurements, reported in Fig. 64.

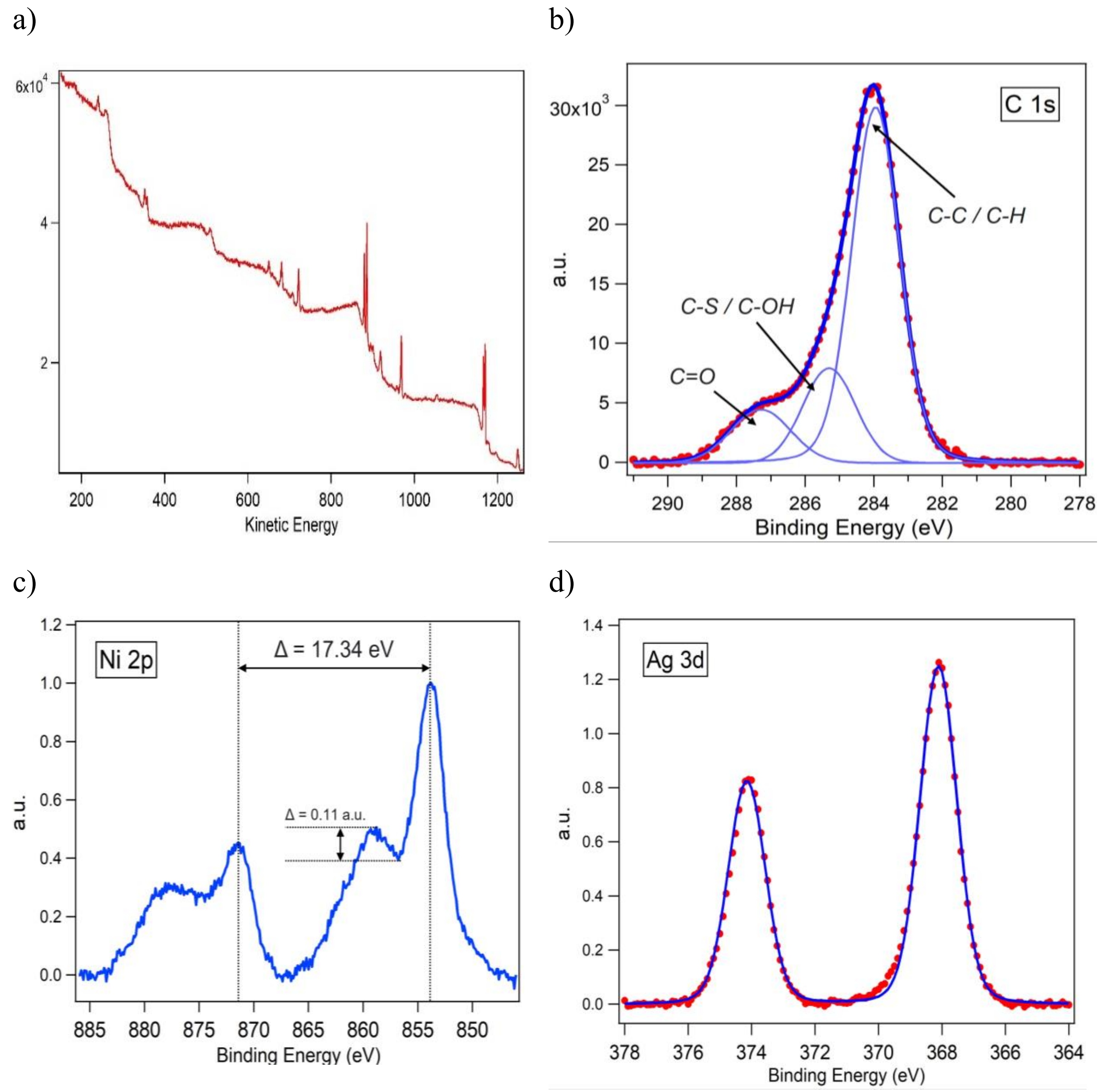

Figure 64 XPS spectra of the Ni|BT$_2$T$_4$@AgNPs interface, Mg Kα photons, 1.254 keV photon energy. **a)** Survey spectrum **b)** C 1s **c)** Ni 2p **d)** Ag 3d. Panel b) and d): the red dot curve is the experimental spectrum, the blue line is the fitted data.

The survey scan and the C 1s, Ni 2p and Ag 3d core levels are displayed in figure 64a, b, c, d, respectively. The S 2p core level measurements are included and discussed in the Main Results Section (3.2.2). In the Nickel 2p spectrum (panel c), a difference in energy between the Ni 2p$_{1/2}$ and Ni 2p$_{3/2}$ components of 17.34 eV is shown, which is slightly lower with respect to the Ni|BT$_2$T$_4$ interface (figure 64c). This is an indication of a smaller amount of Nickel oxide.

### 3.2.3.4 mc-AFM

We investigated the spin selective transport properties through conducting probe AFM where $BT_2T_4$ molecules of either chirality was self-assembled on gold substrate (Au/Ti/Si: 50nm/10nm/500mm, fabricated by e-beam evaporation). We used a Bruker Scan Analyst system with Co/Cr MESP tips with a spring constant of 0.8nN. We applied Peak Force TUNA mode with a peak force of 20 nN and a gain of 10 during IV sweeps with a current sensitivity of 100 pA. We found significant differences in the IV curves depending on the direction of the magnetic field and the chirality of the $BT_2T_4$ molecules, indicating spin filtering effects. The spin polarization was estimated to be about 30% at room temperature, Fig. 65 (a) to (d) panels. Fig. 65 shows also AFM images of the bare (panel g) and of the functionalized ($Au|BT_2T_4$, panel h) surfaces. The surface morphology is quite similar between bare and functionalized gold surface.

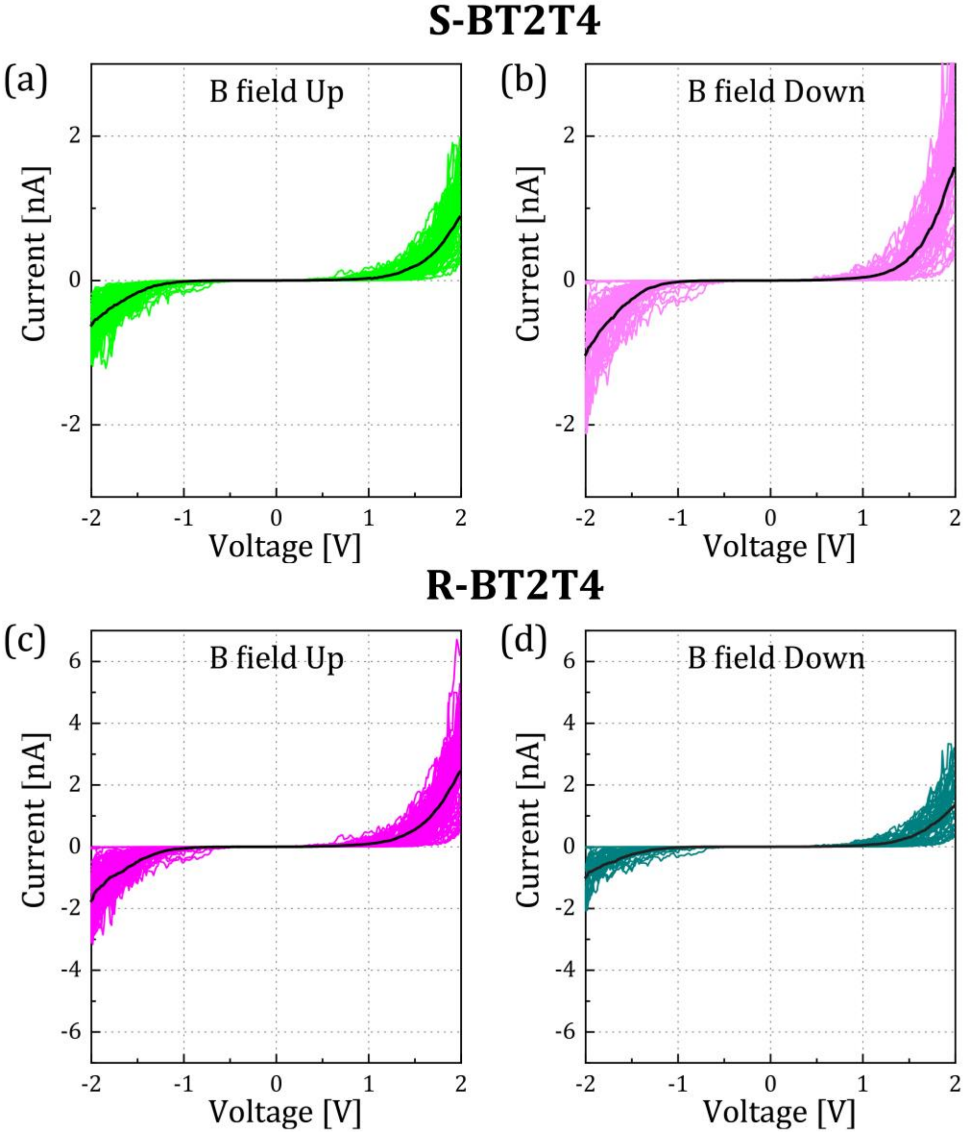

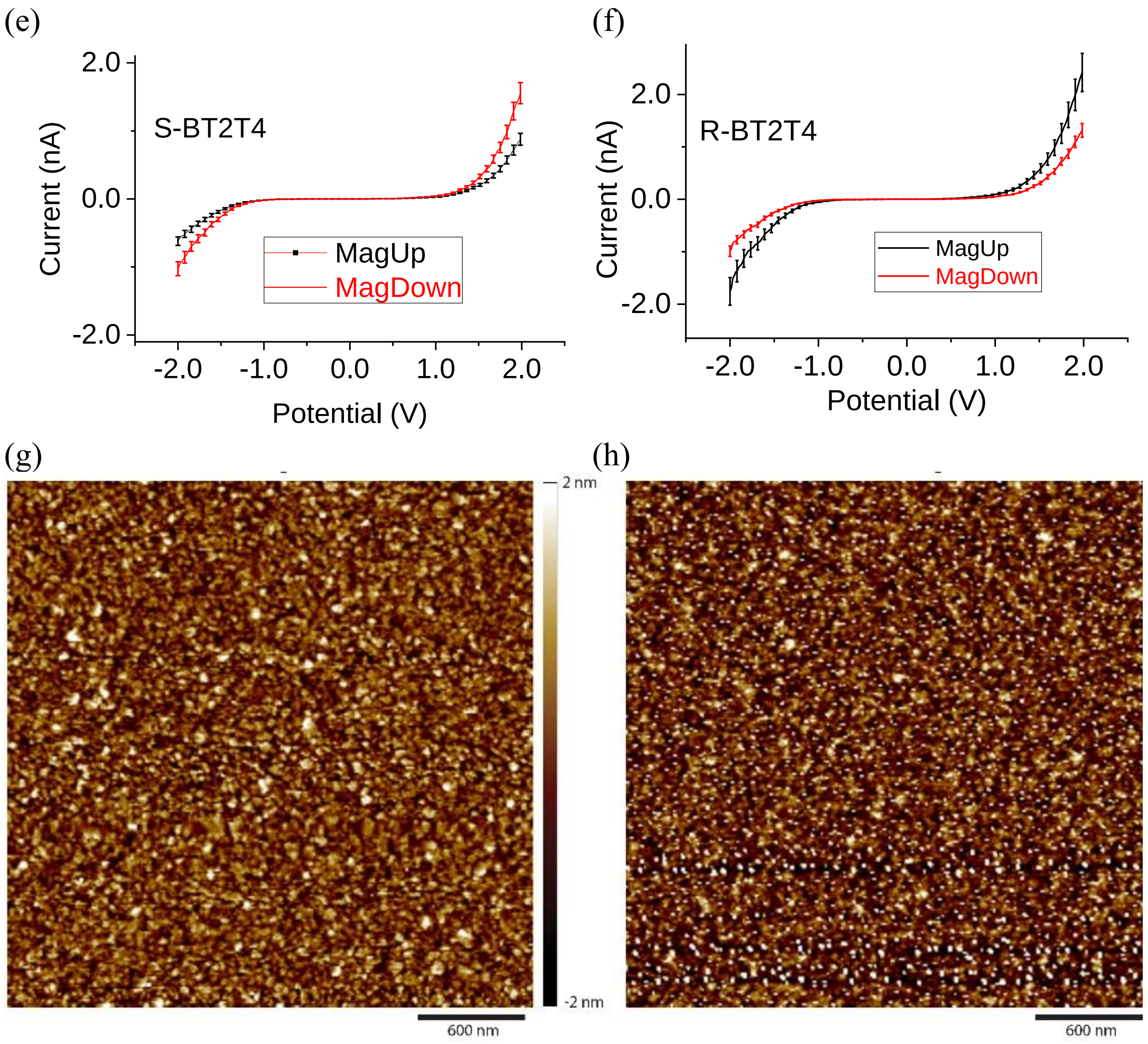

Figure 65 **(a)** to **(d)** Multiple I-V curves recorded on various location of the sample presented in the colored graphs where black lines showing the corresponding average I-V response. Conditions indicated within the figure. **(e)** and **(f)** I-V curves with a 15% error bar. **(g)** and **(h)** bare gold and $BT_2T_4$ SAM on gold surface measured using dynamic mode (peak force QNM) for both the surfaces

Statistical elaboration of the multiple I-V curves indicate a standard deviation just below 5%, which is the sensitivity associated to circle dimensions in the Main Results, Figure 47. Figure 65 (e) and (f) show I-V curves with a 15% error bar, which is a crude overestimation of the sensitivity error. Nonetheless, I-V curves recorded as a function of magnet orientation are still neatly discernible.

### 3.2.3.5 Theoretical results

Theoretical calculations are exploited to provide a molecular based description of the interaction between $BT_2T_4$ and the Au and Ni surfaces (chemisorption) as well as electronic and spectroscopic properties to be related to the experimental Raman spectroscopy measurements. To this end, both isolated $BT_2T_4$ theoretical spectra and $BT_2T_4$ interacting with gold and nickel small clusters have been considered.

#### 3.2.3.5.1 *$BT_2T_4$|metal cluster*

Gold substrate, PM6 semiempirical calculations have been carried out within a cluster embedded approximation to gain a molecular insight on the $BT_2T_4$ interaction with gold. The gold surface was simulated by considering a slab of 57 gold atoms, organized in two layers, with a (111) surface orientation. For the sake of comparison two initial guess geometries have been created:

- Parallel, or flat, $BT_2T_4$ disposition with respect to the gold surface, Fig.66.
- Perpendicular, or vertical, $BT_2T_4$ disposition with respect to the gold surface, Fig.67.

Geometry optimization of the Au|$BT_2T_4$ cluster shows that $BT_2T_4$ adsorbs with a “flat” (the $BT_2T_4$ C2 symmetry axis is parallel to the Au cluster surface) disposition on the surface, maximizing the gold/sulfur interaction, compare Fig. 66b.

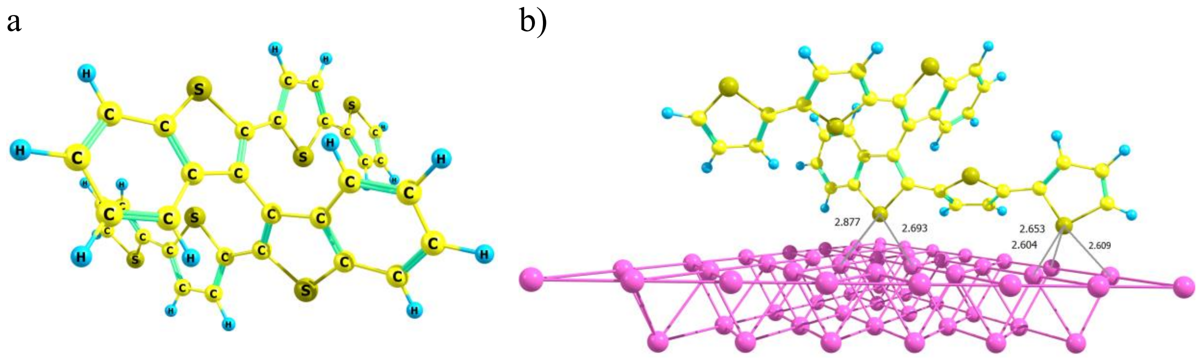

Figure 66 **a)** (R)-$BT_2T_4$ molecular structure. **b)** PM6 semiempirical method-based optimization of the $BT_2T_4$ geometry on a fixed-geometry Au (111) 57 atoms slab. Parallel orientation

Then, the adsorption energy has been calculated as the difference between the Au|$BT_2T_4$ cluster electronic energy minus that one of the Au(111) slab and adsorbate molecule:

$$E_{ads} = E_{Au_{57}|BT_2T_4} - \left(E_{Au_{57}} + E_{BT_2T_4}\right)$$

Where: $E_{ads}$, $E_{Au_{57}|BT_2T_4}$, $E_{Au_{57}}$ and $E_{BT_2T_4}$ are the molecular electronic energies of adsorption, Au/$BT_2T_4$ cluster, Au57 slab and $BT_2T_4$, respectively. The geometry of the Au(111) slab is kept fixed to that of the experimental crystal [237], while the geometry of the free isolated $BT_2T_4$ (relevant to the calculation of $E_{BT2T4}$) have been fully optimized. In the case of the Au(111)| $BT_2T_4$ the geometry of the adsorbed thiophene has been fully optimized, while keeping the geometry of the Au(111) slab fixed. The theoretical adsorption energy results $-120.1$ $\mathrm{kcal\,mol^{-1}}$ for the Au(111)| $BT_2T_4$ cluster for the parallel (Fig. 66b). The optimized perpendicular orientation geometry, Fig. 67, is found 53 $\mathrm{kcal\,mol^{-1}}$ less stable than the parallel orientation, with an adsorption energy of about 67 $\mathrm{kcal\,mol^{-1}}$.

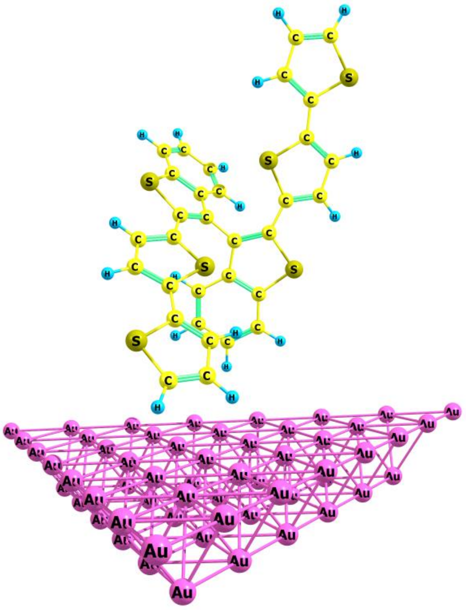

Figure 67 PM6 semiempirical method-optimized $BT_2T_4$ vertical geometry on a fixed-geometry Au (111) 57 atoms slab.

The adsorption process is driven by the tight interaction, i.e. a short interatomic distance, between the sulfur and Au atoms, with the sulfur “trying” to occupy a hollow adsorption site. A strong charge transfer occurs between the adsorbed molecule and the Au, with a positive Mulliken net charge of 0.4 on the $BT_2T_4$. Indeed, the MOs ordering in energy, of the Au cluster with respect to that of the $BT_2T_4$ free molecule, shows that the LUMO of the Au cluster is lower in energy with respect to the HOMO of $BT_2T_4$, Fig. 67. Theoretical facts and figures give strong indication of a chemisorption rather than a pure physisorption. In tight agreement with the experimental outcome: both XPS and Raman results. In particular, a large charge transfer between $BT_2T_4$ and the Au slab is in agreement with the SERS observed measurements of the $BT_2T_4$ adsorbed on the Au (vide supra).

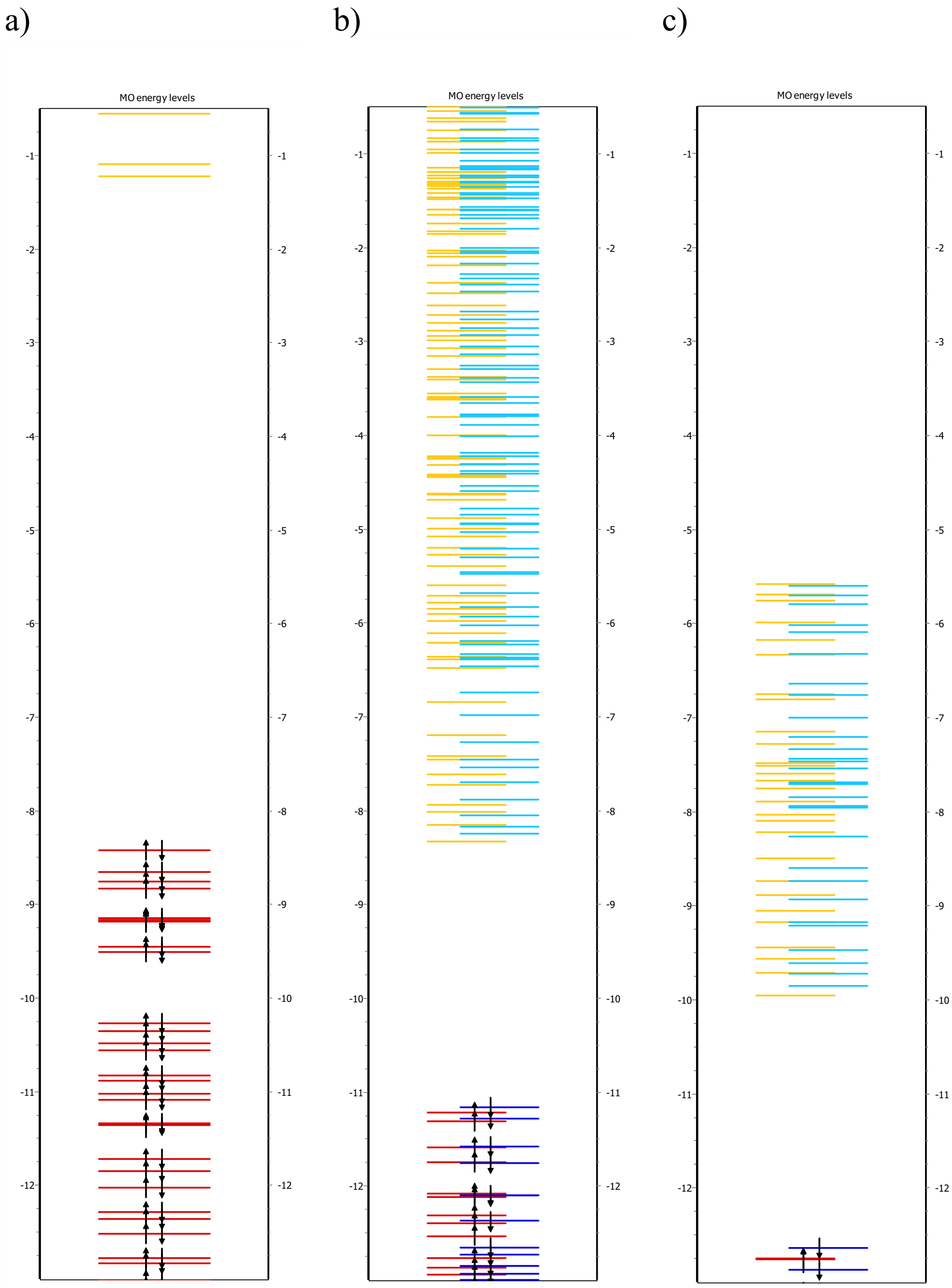

Figure 68 Correlation diagram MO energies, PM6: **a)** $BT_2T_4$ **b)** Au57(111)|$BT_2T_4$ **c)** Au57(111) slab

Regarding the Nickel substrate: the theoretical adsorption of $BT_2T_4$ on Ni was modelled following the same approach developed for the Au. The theoretical adsorption energy on Ni results $-77.8$ kcal $mol^{-1}$ for the Ni(111)| $BT_2T_4$ cluster, with a charge transfer of 1.4 electrons from $BT_2T_4$ to Ni. Thus, the adsorption energy of $BT_2T_4$ on Ni is smaller than for Au. This result is consistent with the bond dissociation energies of sulfur with Au and Ni, 104.2 and 87.5 kcal $mol^{-1}$ respectively [239].

### *3.2.4 Conclusions*

This work relies upon the idea to exploit the charge transmission process (which is made quantitative recording I-V curves) to gain quantitative insight on the conductive/blocking properties of chiral interfaces. The results can be summarized in three different achievements.

- Current peak maxima of the I-V curves in Exp I are found to depend on the symmetric and dissymmetric nature of the chiral interface, in a classical chiral-recognition electrochemical experimental arrangement. Where the handedness of the electrode surface is probed exploiting a chiral redox couple [220]. In our case handedness is imparted by exploiting enantiomers of the same chiral compound, thus differences in the I-V curves are only due to chiral-recognition as the chemical nature of the molecules is the same. Remarkably, I-V curves in Exp II and III are found to be spin-injection dependent. As a consequence, the difference in current of I-V curves controlled by chiral-recognition can be explained on the basis of the CISS effect: handedness S is conducting the UP spin, which yields "high" conduction if the subsequent facing layer handedness is S (symmetric interface), but yield "low" if conduction if the subsequent facing layer handedness is R (dissymmetric interface), swapping S and R handedness yields exactly the mirror-opposite situation. This explanation is inferred by the ability of spin-injection to yield I-V curves (SDE and mc-AFM experiments) whose charge transmission efficiency depends on the interface handedness. We can conclude that spin is a hidden driving force in chiral recognition. Indeed, the paradigm of chiral-recognition as a spin-driven process falls in line with experimental results observed in the case of ultra-high vacuum experiments of polarized-electrons scattering with chiral molecules [240]–[242] and the so-called chiral-induced spin selectivity (CISS) effect [6]. Furthermore, the spin-based chiral recognition model here proposed fits theoretical results showing the crucial role of spin-orbit coupling in the charge transmission of chiral molecular architectures, as proposed by Cuniberti, Herrmann and Mujica [4], [20], [243].
- Furthermore, chemisorption of the thiophene based $BT_2T_4$ on Au, Ni and Ag allows to prepare (tunable) robust and reproducible chiralized interfaces, via facile wet chemistry preparation. Thus, chiral thiophene based oligomers appear a promising class of compounds to be exploited in organic electronics and spintronics (a SP% of about 30% is found in mc-AFM measurements) applications.

- Chiral-capped AgNPs have been used as reversible redox probe, proving to be of facile preparation and robust electrochemical behavior. The properties of chiral-capped AgNPs can be easily tuned by selection of suitable chiral oligothiophenes. Moreover, the standard reversible potential is much more negative (about 0 V with respect to Ag/AgCl/KCl reference electrode) compared to both the Fe(III)/Fe(II) and ferrocene based chiral organics redox couples (about 0.24 V). This makes chiral-capped AgNPs well suited to be exploited in the case of electrodes which can be easily oxidized.

## 3.3. Chiral tetrathiafulvalenes (TTF) derivatives

### *3.3.1. Introduction and motivation*

In this third work presented, results regarding enantio-discrimination and spin-dependent electrochemistry (SDE) are reaffirmed as manifestations of the chiral induced spin selectivity effect. In this case, the focus is shifted from thiophene-derivatives to another significant family of sulfur-rich electroactive molecular precursors for chiral crystalline conductors: chiral tetrathiafulvalenes (TTF) [244], which considerably developed within the last decade [245], very much motivated by the observation of direct or indirect chirality triggered effects in the electrical conductivity, such as the electrical magnetochiral anisotropy (eMChA) effect [246] for the former or the modulation of the crystalline packing for the latter[247], [248]. Some of the most popular chiral TTFs are the methylated BEDT-TTF [BEDT = bis(ethylenedithio)] derivatives, such as DM-BEDT-TTF (DM = dimethyl) "**1**" and TM-BEDT-TTF (TM = tetramethyl) "**2**" [249], [250], which provided important series of chiral conductors with peculiar properties and structures [251]–[255], not encountered in the achiral homologue BEDT-TTF (Fig. 70).

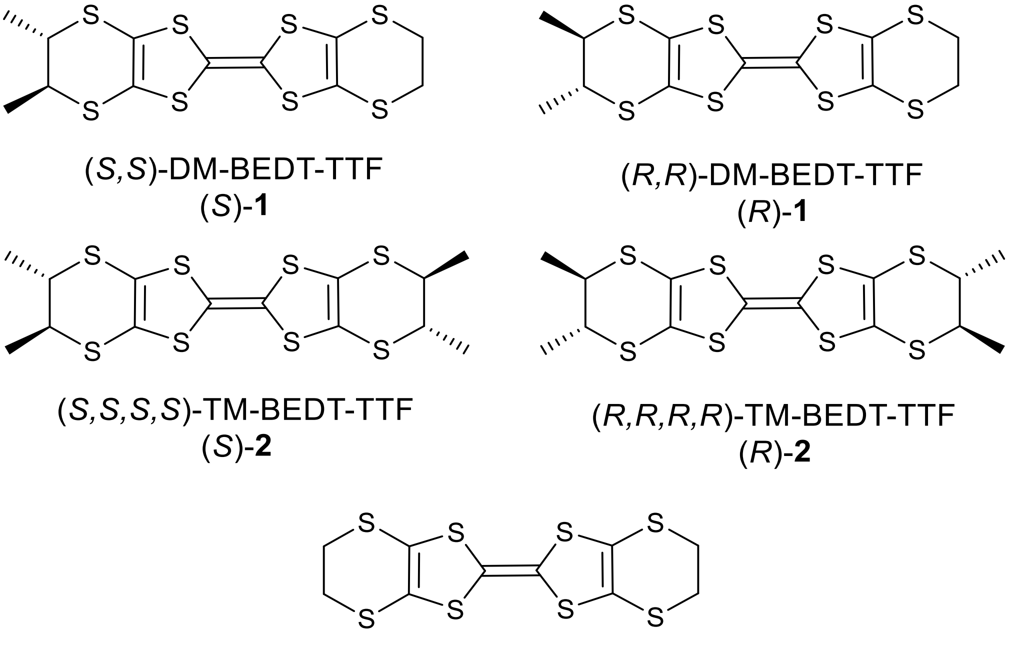
(*S*,*S*)-DM-BEDT-TTF
(*S*)-**1**

(*R*,*R*)-DM-BEDT-TTF
(*R*)-**1**

(*S*,*S*,*S*,*S*)-TM-BEDT-TTF
(*S*)-**2**

(*R*,*R*,*R*,*R*)-TM-BEDT-TTF
(*R*)-**2**

BEDT-TTF

Figure 69 Chiral TTF derivatives **1** and **2** investigated in this section by means of SDE, and their achiral homologue BEDT-TTF.

However, neither CISS investigations nor electrochemical enantio-discrimination have been reported so far with chiral TTF precursors, despite of the propensity of TTF to self-assemble on Au surfaces [256]. Following the same experimental framework as in the previously presented works in Sections 3.1 and 3.2, we prepared chiralized surfaces of gold and nickel to serve as working electrodes. This was achieved through the effective chemisorption of enantiopure dimethyl-bis(ethylenedithio)-tetrathiafulvalene (DM-BEDT-TTF), referred as “**1”**, tetramethyl-bis(ethylenedithio)-tetrathiafulvalene (TM-BEDT-TTF), referred as “**2**” (structure formulas shown in Figure 70), as well as their capped silver nanoparticles (AgNPs) aggregates. The relationship between electron spin and molecular handedness is then investigated. The Au|**1** and Au|**2** chiral electrodes are used in enantio-recognition cyclic voltammetry (CV) experiments, where CVs are conducted in bulk with the presence of chiral redox probes. In addition, the hybrid interfaces Ni|enantiopure **1** or **2**|AgNPs serve as working electrodes in spin-dependent electrochemistry (SDE) experiments, where the current is measured as a function of the spin-injection by the ferromagnetic substrate in the presence of an external magnetic field.

### *3.3.2. Experimental results: Au electrodesorption experiments*

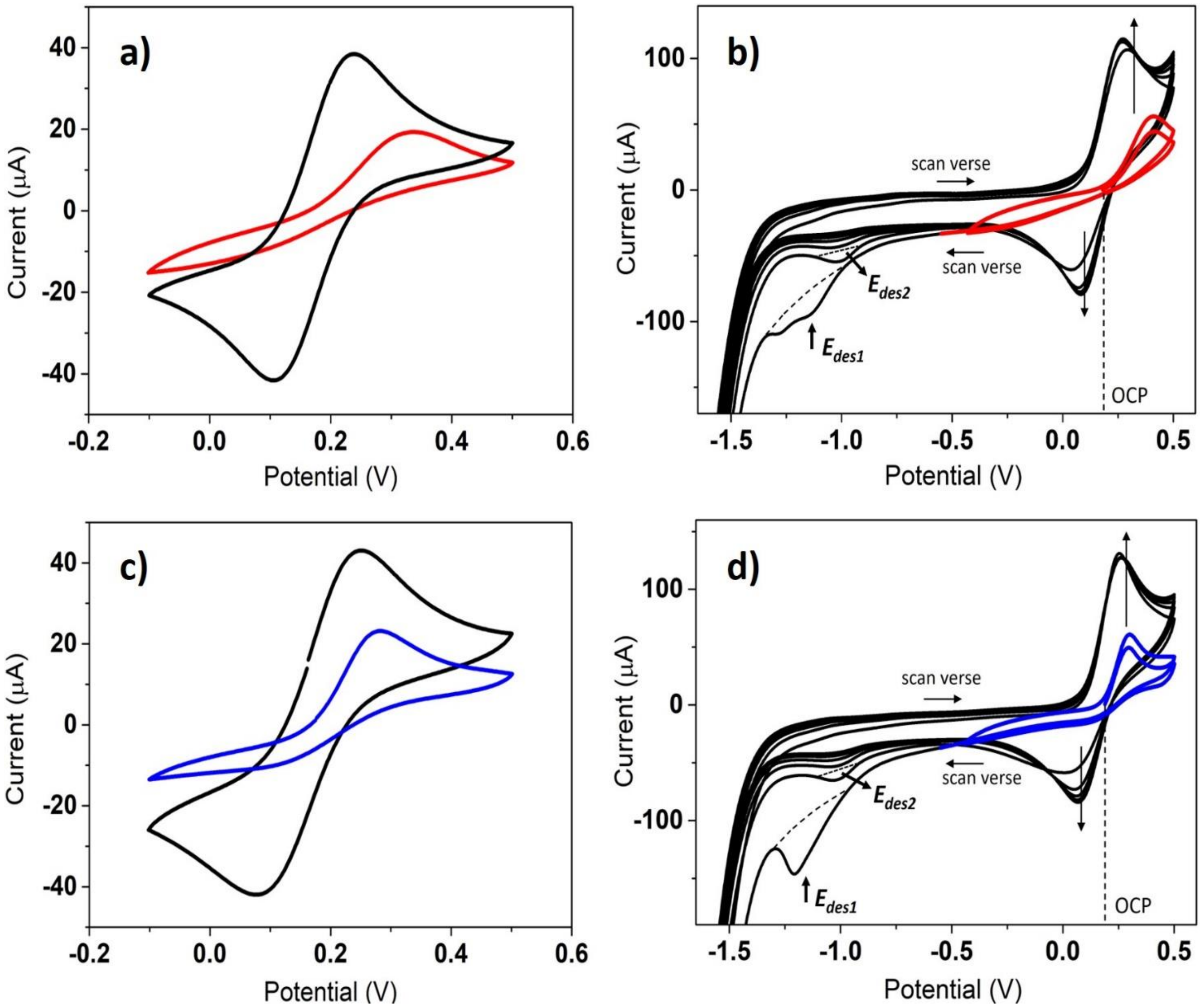

Figure 70 CV curves of a 5 mM Fe(III)|Fe(II), 0.1 M KCl aqueous solution, recorded at the Au|(S)-**2** (a and b panels) and at the Au|(S)-**1** (c and d panels) in a three-electrodes electrochemical cell (Ag/AgCl is the Ref, a Pt sheet the Counter Electrode). **(a)** 0.1 V $s^{-1}$ potential scan rate: the red line is the Au|(S)-**2** interface acting as the WE, the black line is the same Au|(S)-**2** WE after the electro-desorption procedure; **(b)** 0.5 V $s^{-1}$ potential scan rate: the red line is the CV forward 2 scans recorded before electro-desorption, the black curves feature a main peak (labelled as Edes1 in Fig. 71b) in the first reductive scan and a small peak (Edes2) in the second scan (due to the electro-desorption of (S)-**2**): the first CV forward scan starts from OCP to 0.5 V, then the potential is scanned from 0.5 to -1.7 V; the successive 6 CV scans are carried out in the -1.7 to 0.5 V potential range; **(c)** 0.1 V $s^{-1}$ potential scan rate: the blue line is the Au|(S)-1 interface acting as the WE, the black line is the same Au|(S)-**1** WE after the electro-desorption procedure; **(d)** 0.5 V $s^{-1}$ potential scan rate: the blue line is the CV forward 2 scans recorded before electro-desorption, the black curves feature a main peak (labelled as Edes1 in Fig. 71d) in the first reductive scan and a small peak (Edes2) in the second scan (due to the electro-desorption of (S)-**1**): the first CV forward scan starts from OCP to 0.5 V, then the potential is scanned from 0.5 to -1.7 V; the successive 6 CV scans are carried out in the -1.7 to 0.5 V potential range.

Figure 71 shows CVs relevant to the electro-desorption experiments of enantiopure (*S*)-**1** and (*S*)-**2** SAMs chemisorbed on Au, after overnight incubation in ethanol solution. CVs were recorded in a 5 mM Fe(III)|Fe(II), 0.1 M KCl aqueous solution, Fig. 71a black line shows the reference CV recorded on a bare and freshly cleaned gold surface, the red line curve is the CV recorded on the Au functionalized with (*S*)-**2**; please note the substantial decrease in the current and the absence of neat peaks, replaced by two "shoulders" featuring a potential difference of about 300 mV. Fig. 71b shows the electro-desorption CVs for the Au|(*S*)-**2** interface, which acts as the WE: the first two scans are carried out in the -0.1 to 0.5 V potential window (red line) then the potential scan window is widened to -1.6 V (black line). In the first scan in the negative potential range two peaks (reduction current, negative in sign) are evident in the -1.0 to -1.4 V potential range (labelled as Edes1); in the following potential scans the current is definitively lower showing a much weaker peak at -1.0 V (labelled Edes2). Figs. 71c and 71d show exactly the same type of experiment carried out for the Au functionalized with (*S*)-**1**. The blue curves in Figs. 71c and 71d refer to the functionalized surface, for which a similar behavior is observed compared to Figs. 71a and 71b, excepting the Edes1 pattern. Indeed, the latter is much neater and more defined with respect to the result observed for (*S*)-**2**. Thus, the SAM formed by (*S*)-**1** is very likely a little more ordered with respect to the SAM formed by (*S*)-**2**. In addition, the charge calculated by integration of the Edes1 peaks yields a surface area of 0.55 and 0.80 nm$^2$ for the SAMs of **1** and **2**, respectively, suggesting an orientation of **1** a little more tilted with respect to the electrode surface, while **2** should be adsorbed almost "flat" on the surface (calculations of the estimated surface coverage, based on the integration of the desorption peak, can be found in Appendix A.1.3). Indeed, the latter values of surface coverage match reasonably well with the theoretical projected area of (*S*)-**1** and (*S*)-**2** disposed almost flat on the electrode surface, considering the Van der Waals radii. In fact, assuming a flat disposition on the surface, both **1** and **2** occupy a rectangular area of about 0.55 by 1.6 nm (about 0.90 nm$^2$, Fig. 72 panels a, b). Alternatively, in a "perpendicular disposition (compare Fig. 72c) the occupied area is about 0.55 (width) by 0.9 (height) nm (about 0.3 nm$^2$)

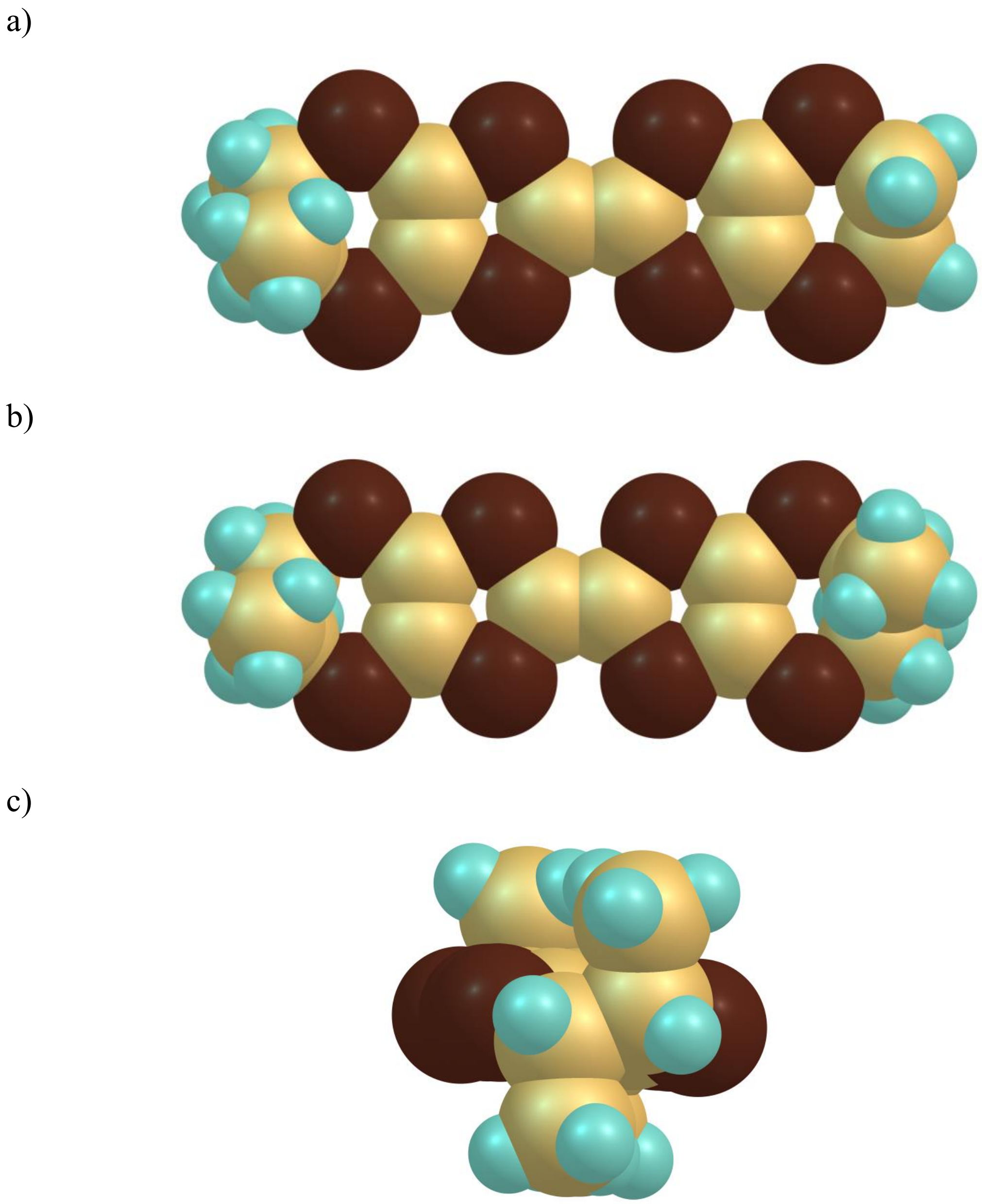

Figure 71 Van der Waals radii representation. a) “flat” disposition of **1** b) “flat” disposition of **2** c) side view of **2** (to appreciate the molecular minimum thickness.

### *3.3.3. XPS analysis*

Fig. 73 shows the S2p XPS spectra relevant to the Au, Ni and Ag surfaces functionalized with the **1** and **2** SAMs: red dots are the experimental data, blue thick line the overall fit of the experimental curve, thin lines represent single Voigt doublets. Au and Ni functionalized surfaces have been produced by incubation of clean surfaces in solution (details of the functionalization procedure are reported in the Experimental Section, 5.3), whilst functionalized Ag nanoparticles have been directly dropcasted on a clean glassy carbon flat surface.

Figs. 73a and 73b show XPS S 2p spectra for the Au|(*R*)-**1** and Au|(*R*)-**2** interfaces. The peak in the 166 to 160 eV range can be effectively fitted by two main components centered at 164.1 (due to the free, not chemically-bound sulfur) and 162.2 eV (associated to S atoms chemisorbed onto the Au surface [222], [223], [225], [257]). The absence of any signal for energy values larger than 166.5 eV further supports the effective gold surface functionalization (signals at energies larger than 166.5 eV are typical of oxidized sulfur) [205], [226]. All in all, XPS results concerning the Au|(*R*)-**1** and Au|(*R*)-**2** interfaces suggest bonding between the metal and the chiral molecules.

Figs. 73c and 73d show XPS S 2p spectra for the Ni|(*R*)-**1** and Ni|(*R*)-**2** interfaces, a rather neat difference being observed between them. Spectra in Figs. 73c and 73d feature a prominent peak at 164 eV which has the typical line-shape of thiophene-based SAMs. Both interfaces present the two components related to bound and free thia-heterocycles, with Ni|(*R*)-**2** showing a slightly larger chemisorbed/unbound component ratio with respect to Ni|(*R*)-**1**, suggesting a stronger bonding for Ni|(*R*)-**2**. Also, a prominent component is found for Ni|(*R*)-**1** at binding energies larger 166.5 eV, indicating a not negligible amount of oxidized sulfur, whilst for the Ni|(*R*)-**2** interface this peak is significantly smaller.

Figs. 73e and 73f show XPS S 2p spectra for the Ag|(*R*)-**1** and Ag|(*R*)-**2** interfaces. All in all the outcome of the XPS spectra parallel the results obtained for the Ni interface, with a slightly larger oxidized sulfur contribution for the Ag|(*R*)-**1** interface with respect to the Ag|(*R*)-**2** one, and a larger contribution from bounded sulfur for the Ag|(*R*)-**2** system, in any case giving strong evidence for the effective AgNPs capping by the chiral TTFs **1** and **2**.

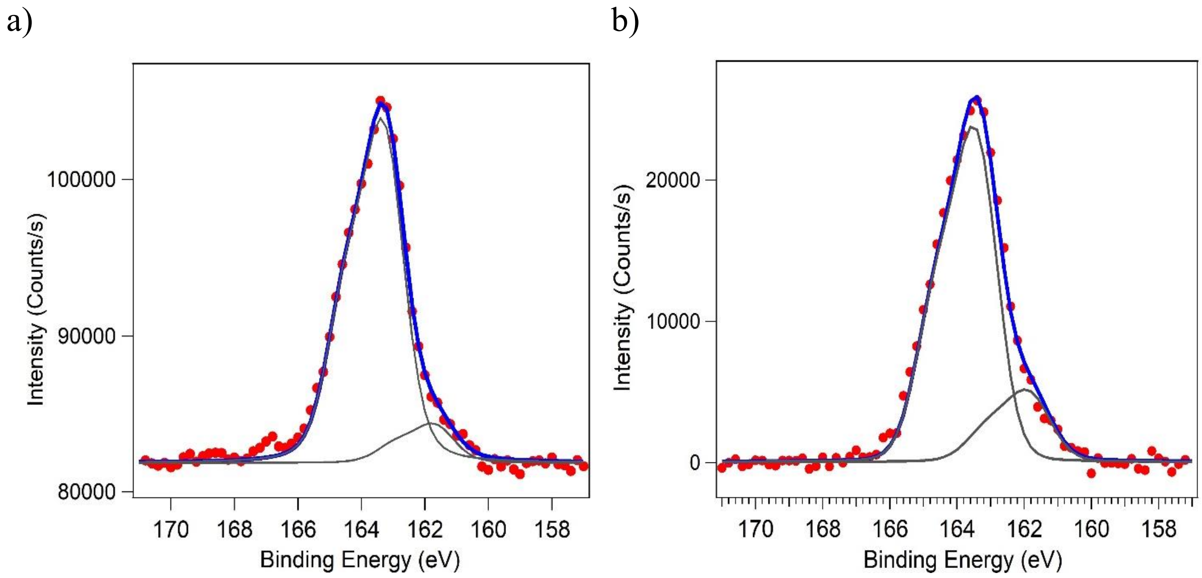

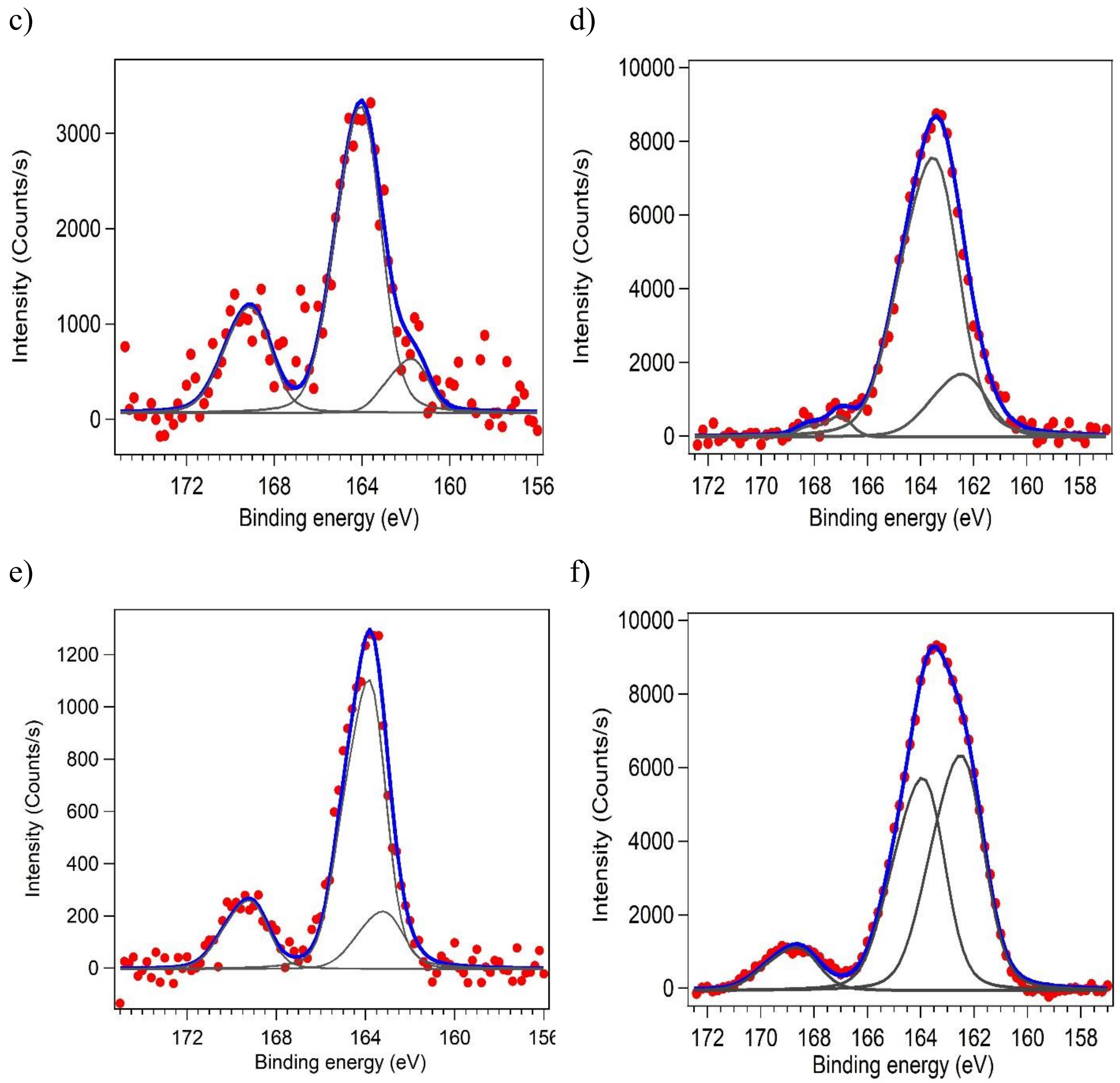

Figure 72 S 2p core-level XPS spectra, Mg Kα photons, 1.254 keV photon energy. **(a)** Au|(R)-**1** interface; **(b)** Au|(R)-**2** interface; **(c)** Ni|(R)-**1** interface; **(d)** Ni|(R)-**2** interface; **(e)** (R)-**1**@AgNPs suspension drop-casted on Glassy Carbon; **(f)** (R)-**2**@AgNPs suspension drop-casted on Glassy Carbon.

Following the presented XPS results, it is possible to estimate the effective SAM film thickness from optical absorption. This accounting for the reflectivity of the gold surface, i.e. quantitative comparison of the bare and functionalized surface [235], [237]. Indeed, 1.254 keV probing photons feature a high inelastic mean free path in the organic film: $\Lambda$=30 Å ± 2 Å is a reasonable expected value for SAMs due to organic chemisorbed molecules [227], [228]. All in all, using eq. (72) it is possible to determine the interfacial film thickness ($d$), for $\Lambda \sim 30$ Å [217], [234], [238]:

$$d \approx \Lambda\, ln\left(I_{Au_0}/I_{Au_d}\right) \qquad (72)$$

where $I_{Au_0}$ is the Au 4f$_{7/2}$ bare gold surface intensity, $I_{Au_d}$ is the intensity of the Au 4f$_{7/2}$ photoelectrons attenuated by a homogeneous film of effective thickness $d$, and $\Lambda$ is the inelastic mean free path of the photoelectrons within the SAM (as defined above). Eventually, the estimated thickness of **1** and **2** SAMs is just less than 10 Å. This value is consistent with a surface coverage of one monolayer.

### *3.3.4. Enantiorecognition with chiral electrodes*

Electrochemical enantiomer discrimination in both analytical and preparative contexts is of great fundamental and applicative interest [221], [258]. This technique most commonly involves the occurrence of a diastereomeric relation between a chirally modified electrode surface, serving as working electrode (WE), and a chiral analyte. Accordingly, chiral modifiers such as tartaric acid [161], chiral PEDOT (poly-3,4-ethylenedioxythiophene) derivatives [66], oligomers of the axially chiral 2,2'-bis[2-(5,2-bithienyl)]-3,3'-bi-thianaphthene ($BT_2T_4$) [29], Cu(II) cysteine complexes [259], thiahelicenes [127], have been deposited on Ni, Au or glassy carbon electrodes for the enantio-recognition of a large variety of analytes including the commercially available N,N-dimethyl-1-ferrocenylethylamine (S-FC and R-FC hereafter for the (*S*) and (*R*) enantiomers), provided with planar chirality thanks to the electroactive ferrocene unit, or the L-dopamine (L-Dopa hereafter) [127], [220]. In the present work we have evaluated the enantio-discrimination ability of our Au/**1** and Au/**2** chiral interfaces as working electrodes (WE) towards N,N-dimethyl-1-ferrocenylethylamine and L-dopamine. As can be observed from Figs. 74a, 74b, 74e and 74f, excellent enantio-recognition is obtained with S-FC and R-FC for both platforms, as evidenced by the large differences in the peak potential values, i.e. average values of 150 mV for the system Au/**1**//FC (compare Fig. 74a and 74b) and of 90 mV for the system Au/**2**//FC (compare Fig. 74e and 74f). It can be thus hypothesized that the interaction between the chiral TTFs **1**-**2** and FC involves the chiral group of the ferrocene unit, possibly through hydrogen bonding interactions that can establish between the $NMe_2$ group attached to the stereogenic center of FC and H atoms of the ethylene groups [260]. Note that for both systems the oxidation of FC is perfectly reversible.

Table 1 Average peak potential difference for the electrochemical enantio-recognition.

| Reference | Working electrode (WE) | Chiral analyte | ΔE (mV) |
|---|---|---|---|
| [161] | Ni/tartaric acid | glucose | 120 |
| [66] | GC/PEDOT | Dopa | 50 |
| [261] | GC/oligo-($BT_2T_4$) | ferrocenes | 20 - 120 |
| [127] | GC/[7]thiahelicene | FC | 250 |
| [127] | GC/[7]thiahelicene | Dopa | 350 |
| this work | Au/**1** and Au/**2** | FC | 150 and 90 |
| this work | Au/**1** and Au/**2** | Dopa | 50 and 120 |

For comparison sake we report in Table 1 the peak potential values reported for closely related systems, i.e. Au, Ni or glassy carbon (GC) electrodes and various chiral analytes, including N,N-dimethyl-1-ferrocenylethylamine (FC) and L-Dopa as in the present study.

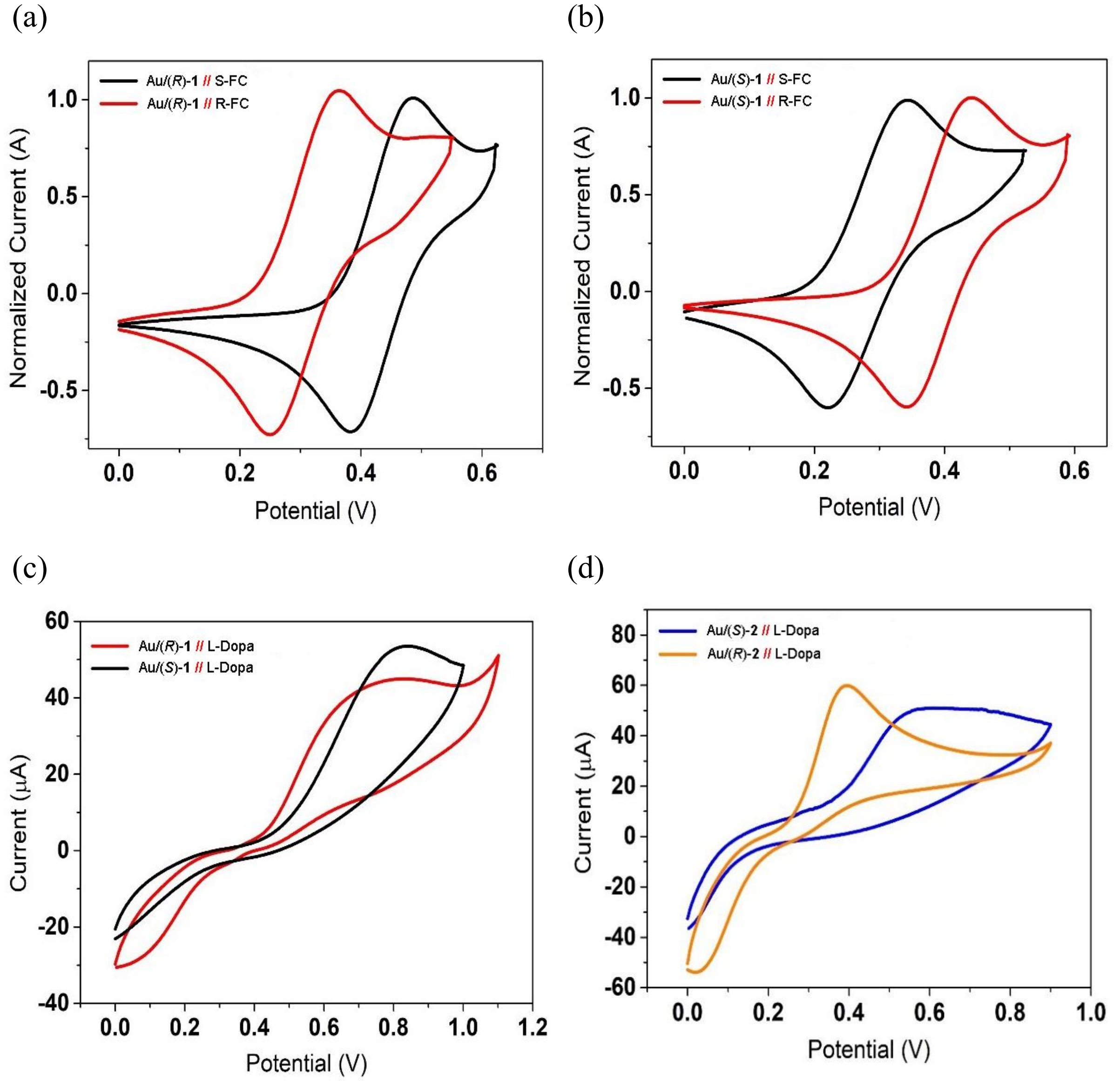

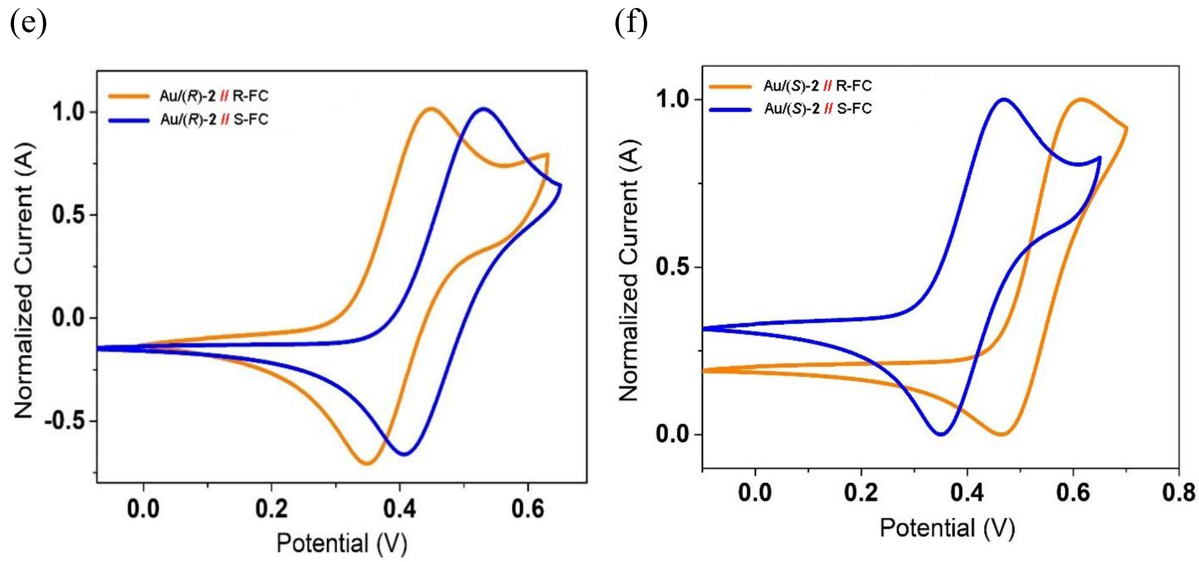

Figure 73 Voltammetric measurement of the Au|(R)-**1** & Au|(S)-**1** interfaces (panels a, b, c) and of the Au|(S)-**2** & Au|(R)-**2** interfaces (panels d, e, f), acting as the WE. CVs were recorded with a 0.05 V s-1 potential scan rate and the support electrolyte is 0.1 M tetrabutylammonium tetrafluoroborate (TBATFB) in ACN solution. **(a)** CV curves in 5 mM S-FC (black curve) or R-FC (red curve); the WE is the Au|(R)-**1** interface; **(b)** CV curves in 5 mM S-FC (black curve) or R-FC (red curve); the WE is the Au|(S)-**1** interface; **(c)** CVs curves in 2 mM L-Dopa recorded at the Au|(R)-**1** (red curve) and at the Au|(S)-**1** interface (black curve); **(d)** CVs curves in 2 mM L-Dopa recorded at the Au|(S)-**2** (blue curve) and at the Au|(R)-**2** interface (orange curve); **(e)** CV curves in 5 mM R-FC (orange curve) or S-FC (blue curve); the WE is the Au|(R)-**2** interface; **(f)** CV curves in 5 mM S-FC (orange curve) or R-FC (blue curve); the WE is the Au|(S)-**2**.

The enantio-discrimination of our platforms with L-Dopa is comparatively less efficient, but still not negligible, as highlighted in Figs. 74c and 74d. As usually observed for this analyte, its oxidation is irreversible [127], therefore only the oxidation peak potentials are considered in order to determine the diastereomeric potential differences, which are just larger than 50 mV for Au/**1**/L-Dopa (compare Fig. 74c, indeed referred to the onset potential, peaks are rather broad) and 120 mV for Au/**2**/L-Dopa (compare Fig. 74d) with an oxidation at lower potentials for the (*R*) enantiomers of **1** and **2**. Different competing intermolecular interactions could take place between L-Dopa and the TTFs **1** and **2**, such as: *i*) hydrogen bonding involving the H atoms of the ethylene bridges of **1** and **2**, as mentioned above, and the *ortho*-dihydroxy group of L-Dopa, which would not provide an efficient discrimination as this group is remote from the stereogenic center, *ii*) π-π interactions between the two π frameworks, which would probably afford a better chiral recognition for **2** which possesses stereogenic centers on both sides of the π system, and, finally, *iii*) hydrogen bonding involving the chiral α-amino-acid group of L-Dopa and the H atoms of the TTF ethylene groups. All in all, the enantio-discrimination towards L-Dopa is more efficient for **2**, containing four stereogenic centers, than for **1**, with two stereogenic centers.

### *3.3.5. Spin-dependent electrochemistry (SDE)*

The ultimate goal of our investigations with the chiral TTF precursors **1** and **2** was the demonstration of the CISS effect through spin dependent electrochemistry experiments. To reach this goal, we have prepared ferromagnetic nickel electrodes coated with enantiopure **1** and **2**, according to previous reports on such chiral working electrodes [13]. Functionalized Ni|TTF@AgNPs surfaces were obtained by overnight incubation of the compounds **1** and **2** capped with AgNPs (see Experimental Section, Preparations, 5.3). Although our chiral precursors are redox active themselves, their first oxidation potentials occur at 0.50-0.53 V *vs* SCE (saturated calomel electrode). Unfortunately, these oxidation values are more positive than the oxidation potential of the nickel surface. We have therefore decided to use as redox mediator AgNPs [233], which oxidize at lower potential than Ni. Figures 75a and 75b show SDE results for surfaces chiralized with **1,** the results being consistent with swapping the spin-injection (i.e. flipping the magnet under the Ni WE). In Fig. 75 b, S-surface, the current is larger for the Mag DOWN disposition, while the opposite is found for the R-surface (Fig. 75a) in the reduction peak, but not in the oxidation current.

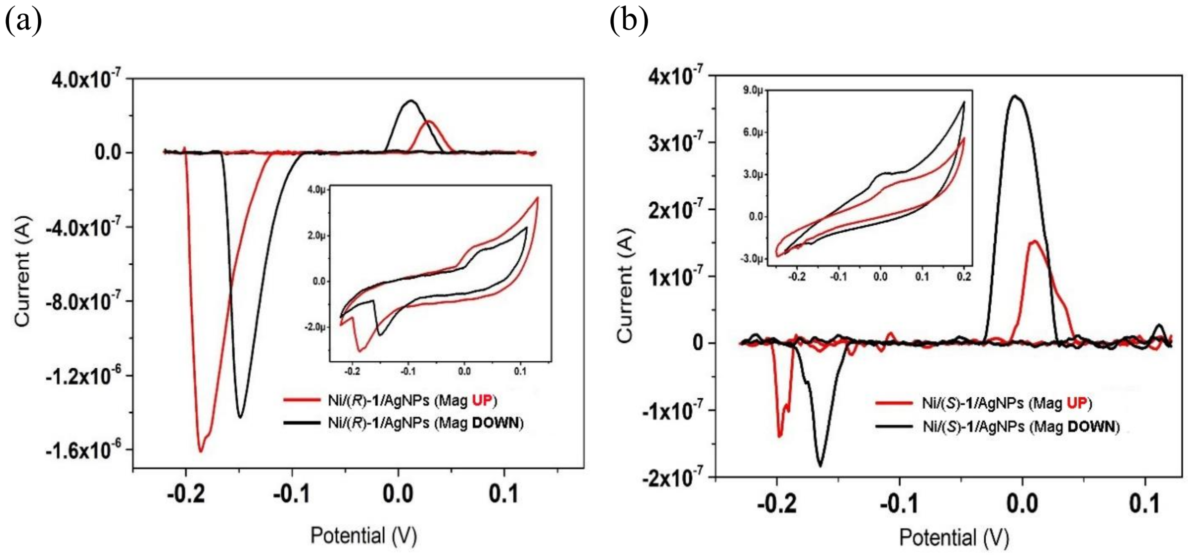

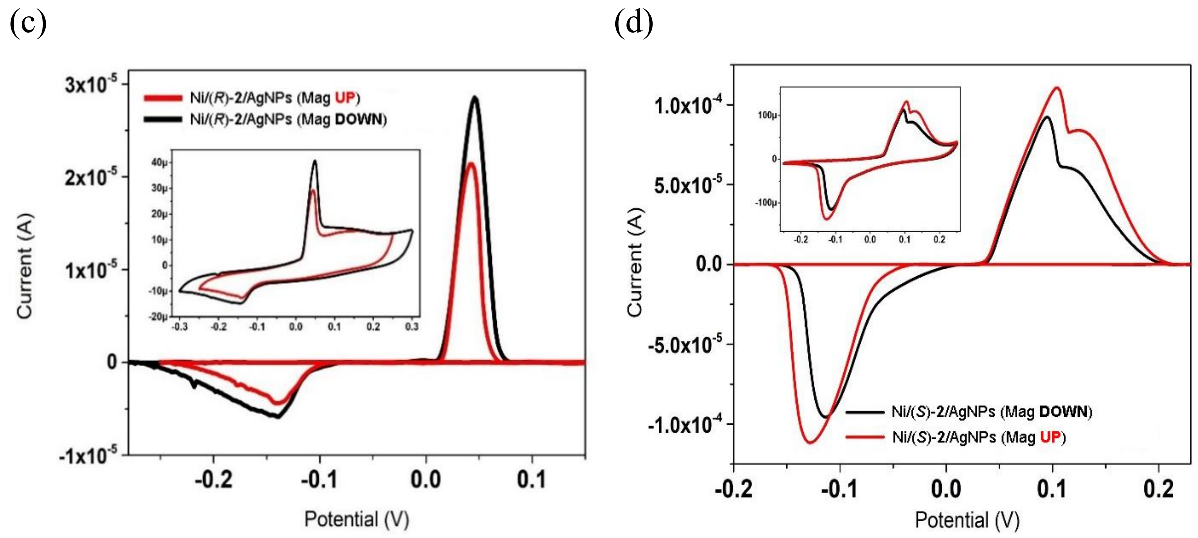

Figure 74 Spin-dependent electrochemistry CVs: a Pt sheet and Ag/AgCl/KCl$_{sat}$ are used as the CE and RE, respectively. CVs were recorded with a 0.05 V s-1 potential scan rate in a 0.1 M KCl aqueous solution. **(a)** Ni|(R)-**1**|AgNPs interface acts as WE; **(b)** Ni|(S)-**1**|AgNPs interface acts as WE; **(c)** Ni|(R)-**2**|AgNPs interface acts as WE; **(d)** Ni|(S)-**2**|AgNPs interface acts as WE. Black solid curve magnet DOWN orientation. Red solid curve magnet UP orientation. The main panels display the data after background subtraction (removal of the double layer contribution), while the insets show the raw data from the corresponding measurements.

The calculated spin polarization values are 6% for (*R*)-**1** and 13% for (*S*)-**1**, spin polarization being defined as:

$$SP\% = \frac{(I_{MagUP} - I_{MagDOWN})}{(I_{MagUP} + I_{MagDOWN})} \times 100 \qquad (73)$$

$I_{MagUP}$ and $I_{MagDOWN}$ are the peak current values recorded with the magnet orientation UP and DOWN, respectively.

Figures 75(c) and 5(d), related to (*R*)-**2** and (*S*)-**2**, respectively, show much more consistent SDE behavior, i.e. the R-surface shows magnet DOWN spin selectivity, while the S-surface shows magnet UP spin selectivity, with spin polarization values on the average just below 15%, as calculated from the maximum value of current at the peaks in the cyclic voltammograms, which are values in the usual range observed for different combinations of chiral/redox couples (mediators) in the area of spin-dependent electrochemistry [144], [152], [262]. However, the present system is very easy to implement since the chiral mediator consists in the simplest chiral TTF precursors for which the synthesis is straightforward. Going into details: the SDE results for **2** compared to **1** appear a bit more robust (this at variance of enantio-recognition results, please compare Figure 74 CVs and the relevant discussion in the previous section 3.3.4). This could be most likely related to the different Ni-TTF interaction: spin-injection efficiency depends also on the reciprocal spatial disposition – geometry of adsorption on the electrode – of the chiral molecule on the electrode surface. Indeed, precursor **1** contains a more accessible side, without methyl substituents, which is prone to interact stronger with the surface (although possibly leading to a twisted adsorbed disposition). In addition, **2** possesses stereogenic centers on both sides of the TTF framework, thus having a chiral space more pronounced than in **1**. These results point out the importance of the proper selection of the chiral mediators and their interaction with the electrode in order to maximize the chiral induction. From the analysis of different SDE experiments involving the investigated Ni|TTF@AgNPs surfaces it is found that from a quantitative point of view the degree of uncertainty in both potential shift and peak current is around 6 %. Therefore, the curves in Figure 75 have been reprocessed and are presented in Figure 76 using a 10% standard deviation error bar. It's clear that the I-V signal extracted from the CVs remains distinctly discernible.

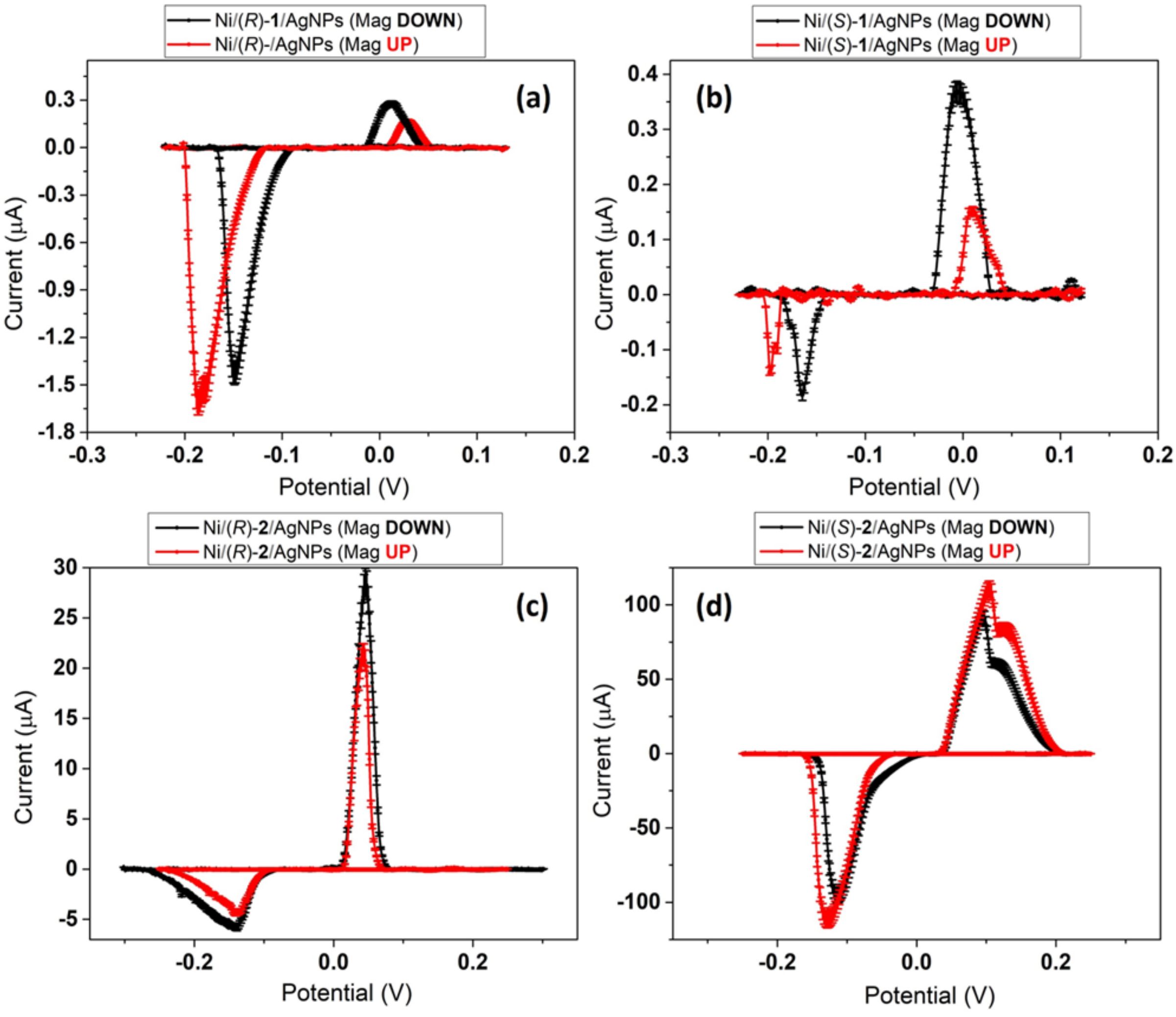

Figure 75 Spin-dependent electrochemistry CVs from Figure 75, elaborated featuring a 10% standard deviation error bars.

### *3.3.6. Conclusions*

We have demonstrated the efficiency of two chiral methylated TTF derivatives for electrochemical chiral enantio-discrimination and for chirality induced spin selectivity through spin dependent electrochemistry measurements. The chiral precursors are suitable for the functionalization of gold and nickel surfaces which show very good stability in a wide range of potential. Excellent enantio-recognition was achieved with both Au|TTF platforms towards N,N-dimethyl-1-ferrocenylethylamine, with potential differences between the two enantiomers of 90 – 150 mV, while the recognition of L-Dopa is more effective with compound **2**. The CISS effect is clearly more robust for the latter as well, with average spin polarization values of ±15%, very likely thanks to the more chiral environment created at the interface between the chiral TTF and the nickel surface and thus correlating with the higher ratio of bound *vs* unbound sulfurs as observed by XPS in compound **2** with respect to **1**. These results are a clear proof-of-concept concerning the use of chiral TTFs for electrochemical enantio-discrimination and for the spin polarization and open up numerous perspectives. The electrochemical recognition of redox inactive substrates can be envisaged when taking into account that TTFs are redox active all the more since their redox potentials can be finely tuned by changing the substitution scheme. To comply with the relatively low oxidation potential of metallic Ni, chiral metal bis(dithiolene) complexes can be used as spin polarizers in SDE experiments as they possess much lower oxidation potentials and have accessible reduction stable states [263], [264].

# 4. Results and discussion: complex systems

In this section, the second part of the results presented in this thesis work is compiled. This division reflects the shift in the underlying transport mechanism of the investigated phenomena. In fact, we transition from a focus on the single monomeric species (where carriers flow through a monolayer, therefore coherent transport is the dominant regime, Section 3) to more extensive systems, orders of magnitude larger, characterized by incoherent charge carrier transport. Beyond the intrinsic research interest, this section contains the results that are likely to be closest to actual industrial applications. This includes the development of catalyst electrodes for more efficient water electrolysis (hydrogen production) and the electrochemical organic transistor (for which we have indeed applied for a patent). In some of these research projects, definitive conclusions have not yet been completely reached. However, if preliminary results have shown promise, they have still been included in this thesis and will be further explored after the completion of my doctoral research. As in the previous paragraph, unless stated otherwise, all the presented experimental procedures and theoretical calculations were conducted by the author of this thesis.

## 4.1. Chiral thiophenic polymer: p-2T3N

### *4.1.1. Introduction and motivation*

Following the convincing results regarding the charge transport capabilities of a monolayer of the chiral oligothiophene derivative 2T3N (Section 3.1), a natural experimental development consists of studying the associated polymer (p-2T3N) resulting from the electropolymerization of the monomer. Thiophenic derivatives typically exhibit excellent electropolymerization capacity driven by the oxidation of monomers to form intermediate radical cations, immediately followed by the formation of oligomers and/or deposition near the surface of the anode [265]–[267]. Moreover, chiral electrode surfaces are widely used to distinguish enantiomers of different chiral probes (enantiorecognition) based on variations in both potential and current peak values [268]–[271]. Through this operation, it's indeed possible to recognize the enantiomers of the analyte without preliminary separation steps, which is a fundamental practice in chiral electrochemistry. Consequently, the perspective of obtaining a modified electrode through a chiral coating of p-2T3N, directly grafted onto the electroactive surface, is investigated and its sensor performance in terms of enantiomer recognition is characterized. Given the extensive study of the individual 2T3N molecule, the investigation of p-2T3N allows for a stringent comparison on numerous aspects.

In primis, the charge transfer capacity of the resulting conjugated polymer and its doping mechanism. In the case of so-called "conductive polymers", the induction of conductivity in an essentially insulating organic architecture relies on a redox reaction, typically referred to as a "doping process" (drawing a loose analogy with the doping phenomenon in inorganic semiconductors). However, this analogy can be misleading. In inorganic systems, dopants are integrated into the crystal structure. In contrast, the doping concept in organic compounds is realized through a "net charge transfer process", which can involve a donor and an acceptor species, or the external modulation of the system's potential leading to the formation of charge carriers along the conjugated polymer backbone (as in the electrochemical doping case). The presence of net charges along polymeric chains involves a complex interplay between electronic and structural properties. This interplay is typically explored through the concept of the polaron quasiparticle, which can be probed spectroscopically.

Secondly, the comparison is conducted in terms of enantioselective performance. If the electrode modified with the homochiral SAM of 2T3N exhibited enantioselective capabilities towards an analyte in solution, it is not guaranteed that this sensory property is retained by the p-2T3N film. The preservation of chirality can be verified through measurements of optical activity (CD spectrum), and its interaction with the same chiral compound in solution, as utilized in section 3.1.5 (S-FC and R-FC).

### *4.1.2. Experimental results*

#### 4.1.2.1. Spectroelectrochemical polymerization

Charge-transfer at the organic/electrode interface is characterized by studying the process of polymerization of enantiopure 2T3N and the electrochemical behavior of the polymer coating obtained (p-2T3N). In Figure 77, the polymerization of R-2T3N on an ITO electrode is illustrated. In the first anodic scan, two distinct peaks appear at potentials around +1.15 V and +1.20 V, respectively. However, in the reverse scan, only a cathodic peak at approximately +0.90 V is observed, and this peak grows in subsequent scans. Since the oxidation process of the monomer leading to polymer formation is irreversible, the reduction signal can be attributed to the de-doping of the polymer film, which gradually thickens scan after scan, and returns to its neutral state at around +0.90 V. The increase in the signal even during the scan towards positive potentials clearly indicates that a film is being deposited on the electrode. Therefore, the two distinct oxidation peaks observed in the first scan can be attributed to two successive oxidations of the R-2T3N monomer.

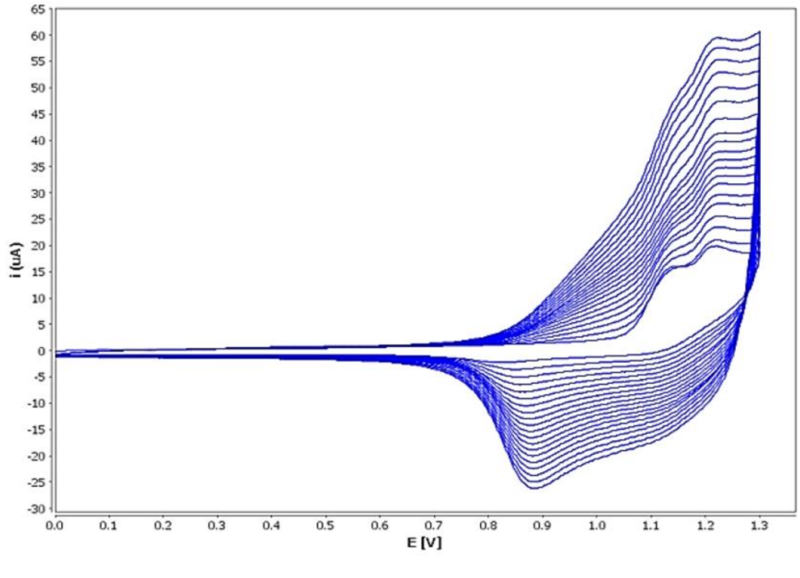

Figure 76 R-2T3N potentiodynamic electropolymerization. 3-electrodes electrochemical cell, with ITO as the working electrode (WE), Pt as the counter electrode (CE), and Ag/AgCl as the reference electrode (Ref). The electrolyte solution consists of 5 mM R-2T3N and 0.1 M TBATFB (supporting electrolyte) in ACN (acetonitrile). The electropolymerization process involves 20 cycles from 0.0 V to 1.3 V, with a scan rate of 50 mV s$^{-1}$.

Once the most efficient electrochemical parameters for stable electropolymerization were identified, the deposition was conducted simultaneously with the acquisition of the UV-Vis spectrum of the sample (in-situ/in-operando). This spectroelectrochemical approach allowed us to monitor the real-time formation of the p-2T3N coating and the relevant results are reported in Figure 78 below. These investigations were conducted using an ITO-coated glass as the working electrode (WE), scanning the potential between 0.5 V and 1.5 V twenty times while monitoring absorption at a constant wavelength of 680 nm. This wavelength corresponds to a characteristic band of the p-doped polymer, as confirmed by theoretical calculations (vide infra, section 4.1.3).

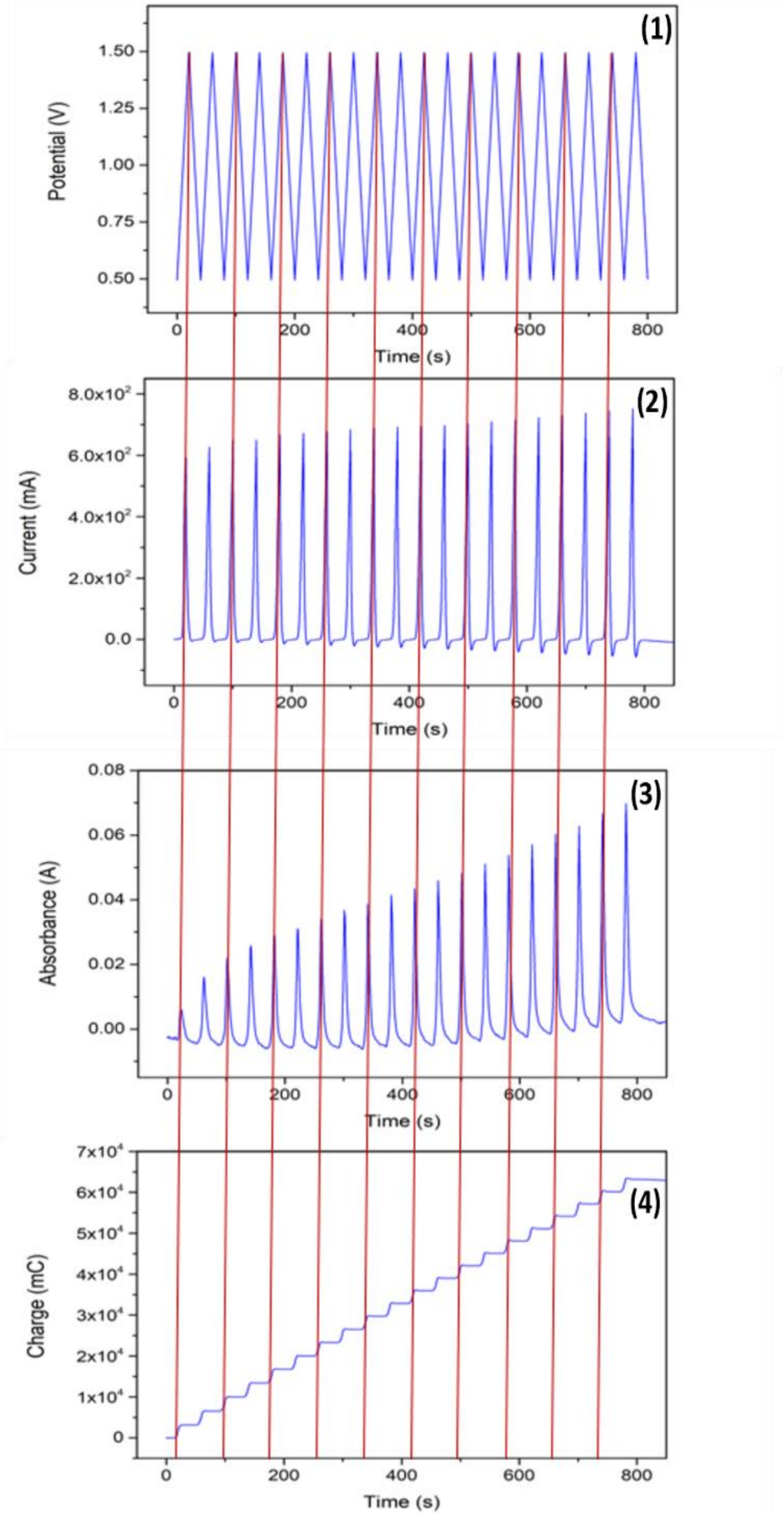

Figure 77 Spectroelectrochemical polymerization of 5 mM R-2T3N in 0.1 M TBATFB, ACN solution. An ITO coated glass acts as WE in a 3-electrode electrochemical cell also containing Pt as CE and Ag/AgCl/KCl$_{sat}$ as RE. The potential is scanned between 0.5 and 1.5 V at 0.05 V s$^{-1}$ for 20 cycles, allowing the R-2T3N polymerization. Panels (1), (2) and (4) display the potential, current and charge vs time, respectively. Adsorption recorded at 680 nm measured during the electro-polymerization procedure is reported in panel (3).

It is evident the synchronization between the oxidation of R-2T3N in the CV experiment at approaching the potentials of 1.5 V and the monotonic increase in the absorbance signal, represented with a vertical red line. The absorption is clearly related to the increasing thickness of the p-2T3N on the ITO surface. At the end of the electro-polymerization process, a dark yellow deposit is obtained on the ITO electrode.

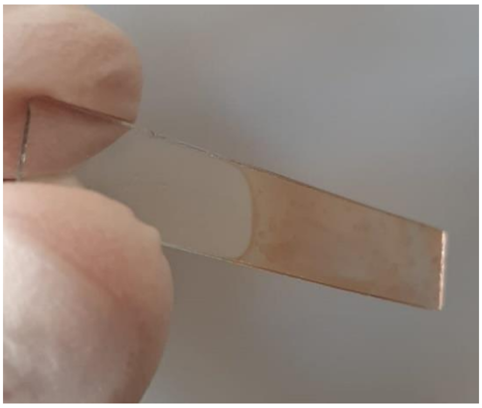

Figure 78 Homochiral p-2T3N coating deposited on a ITO electrode after the electropolymerization procedure

#### 4.1.2.2. Spectroelectrochemical p-doping

The synthetized p-2T3N coating was studied again by combining electrochemistry and UV-Vis spectroscopy, and the results are reported in Figure 80. The polymer was progressively oxidized (*p-doping*) by application of a constant positive potential, while registering the spectrum of the coating in the 300 – 1400 nm wavelength range. The results finally reported in the figure are the variation of the absorption recorded at the different wavelength with respect to the spectra collected at 0.0 V, whereas the raw absorption data are reported in the inset. The black solid line in the inset corresponds to the spectrum of p-2T3N in the neutral state (obtained at E = 0.0 V), showing a prominent adsorption centered at about 400 nm. Remarkably, as potential was increased, the p-doping process advances as shown by the arising of two broad peaks at about 680 nm and 1200 nm, while the adsorption at about 400 nm consistency decreases.

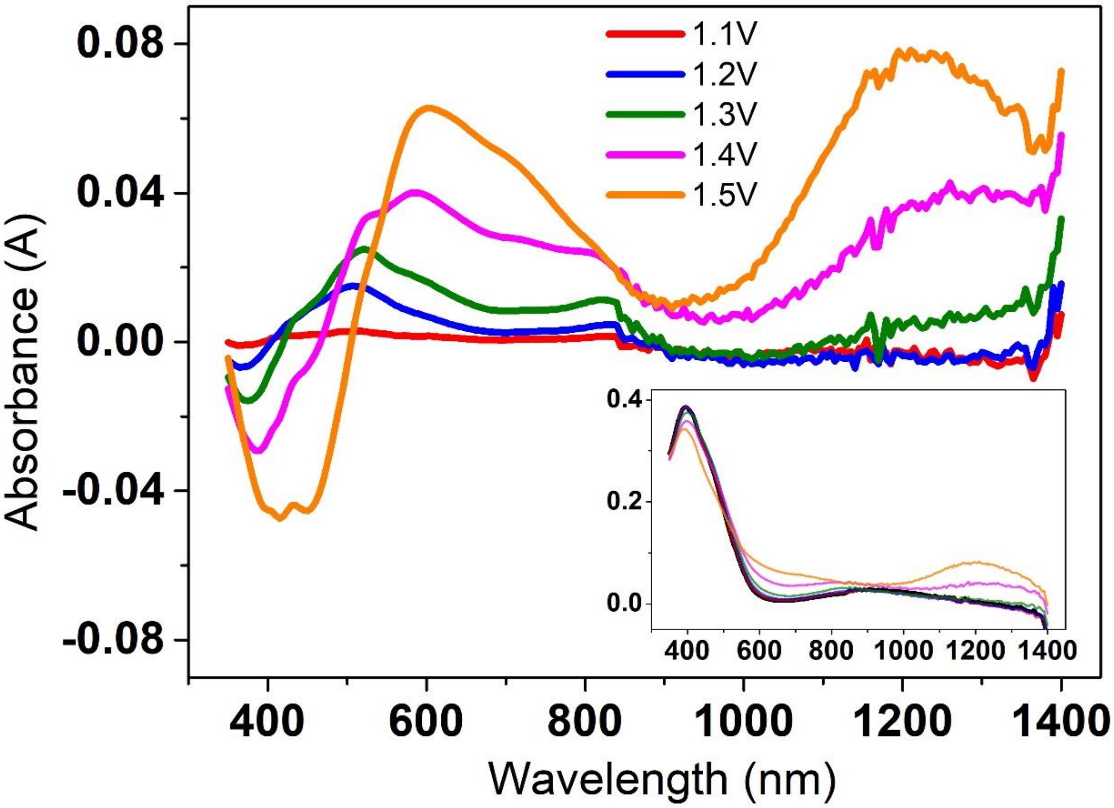

Figure 79 *Spectroelectrochemical characterization of the p-2T3N coating deposited on ITO electrode, using Pt as CE and Ag/AgCl/KCl$_{sat}$ as RE. The electrolytic solution is 0.1 M TBATFB in ACN. A constant positive potential (from 1.0 to 1.5 V) is imposed to the system while in-situ UV-Vis/NIR spectrum is measured at the same time. The spectra obtained are reported in the inset, in comparison to the undoped p-2T3N coating recorded at 0.0 V (**black line**). In the main panel, the results are shown as variation of the absorption with respect to the species spectrum recorded at 0.0 V.*

The characteristic bands of the p-2T3N cation, located at 680 nm and 1200 nm, are then individually examined in figures SEC3.a and SEC3.b. The absorbance is continuously recorded at a constant wavelength over time for the ITO|p-2T3N electrode, which was produced following the electrochemical procedure outlined in Figure SEC1. Remarkably, the maximum absorbance value, again observed at 1.5 V, remains constant, confirming the stability of the film on the electrode surface. The presence of the p-2T3N polaron is evidenced by the absorption peak centered at approximately 1200 nm. This aspect will be extensively discussed in the theoretical section (*vide infra,* Theoretical Results Section, 4.1.3).

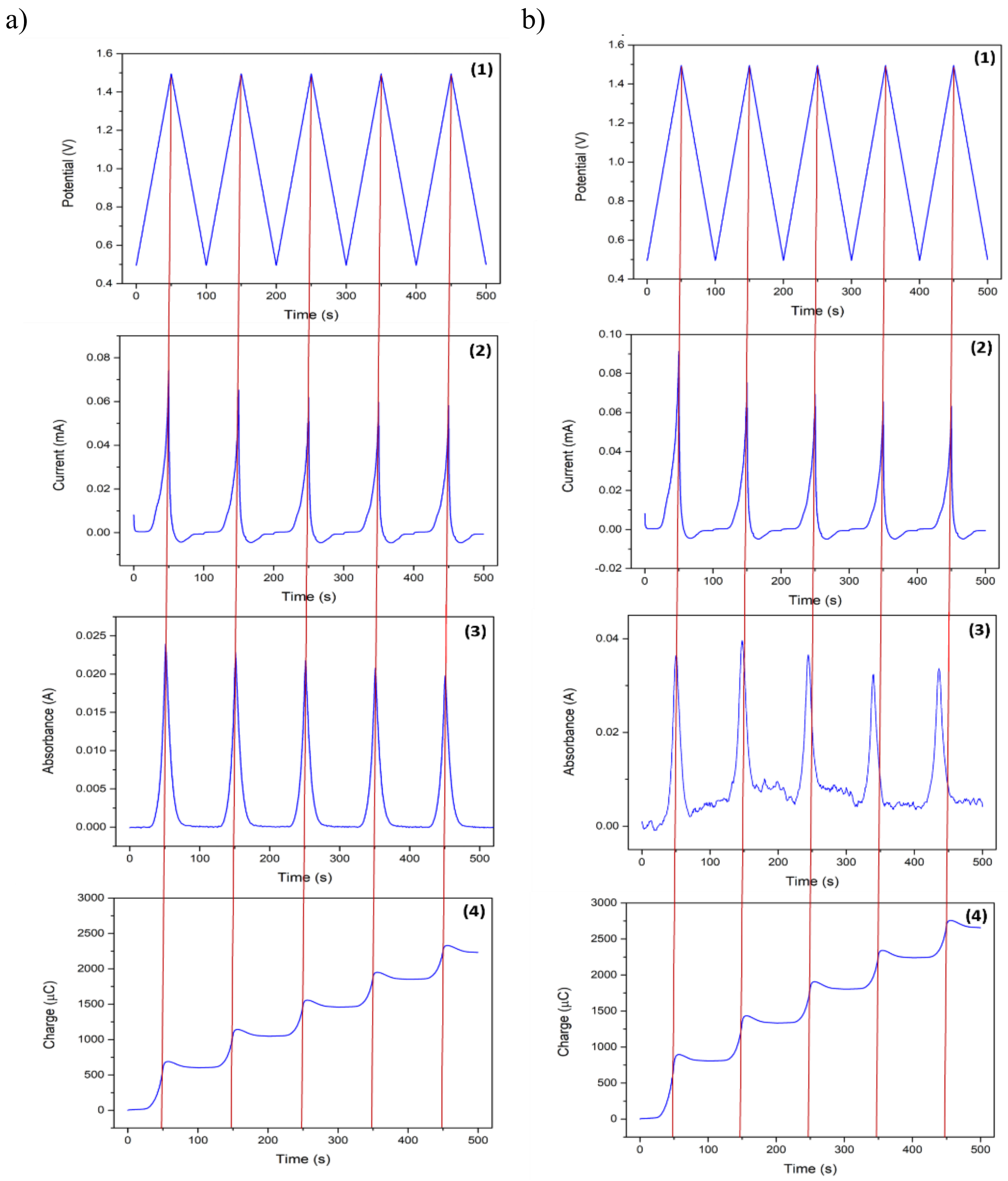

Figure 80 Spectroelectrochemical characterization of the p-2T3N coating on ITO electrode, using Pt as CE and Ag/AgCl/KCl$_{sat}$ as Ref. The potential is varied between 0.5 and 1.5 V at 0.05 V s$^{-1}$ (as shown in panes 1) while recording the spectrum at 680 nm **(a)** and at 1200 nm **(b)**. The correspondent variation of current, charge and adsorbance are reported in panels (2), (4) and (3), respectively.

#### 4.1.2.3. Circular Dichoism

Figure 82 shows the absorption and CD spectra recorded in the 300 to 600 nm wavelength range for the ITO|p-2T3N interface. The absorption spectrum exhibits a broad peak centered at

450 nm. The corresponding CD spectrum reveals two prominent optical activity peaks centered at approximately 350 and 550 nm.

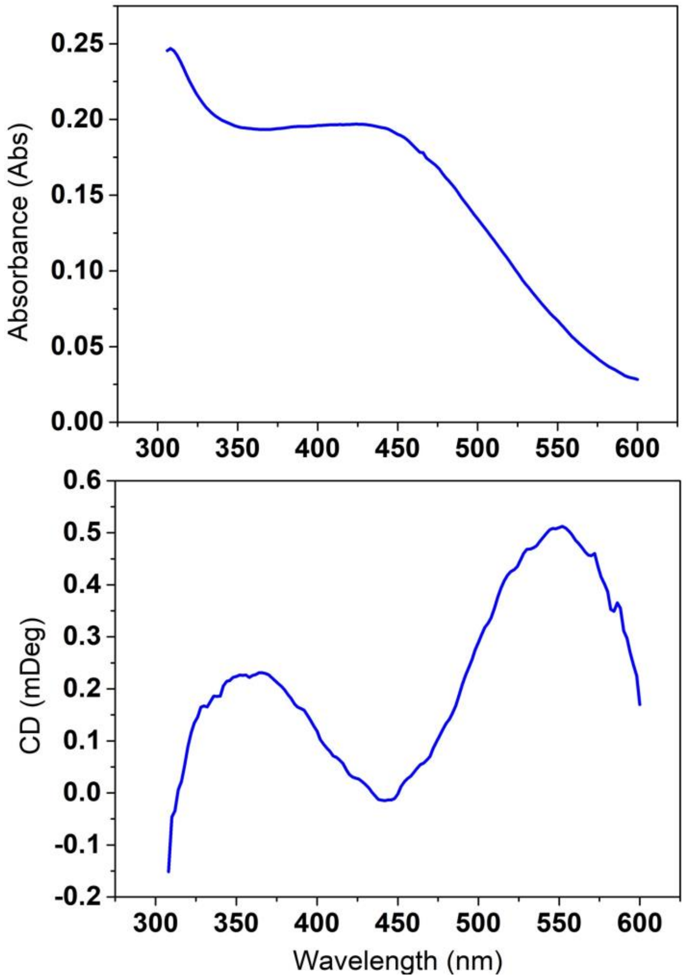

Figure 81 Absorption and CD spectra of the ITO|p-2T3N interface

#### 4.1.2.4. Enantiorecognition

The enantioselective ability of p-2T3N was assessed concerning the R-FC and S-FC pair in bulk solution (the same experiment of section 3.1.5). The GC|p-2T3N interface is produced according to the electropolymerization procedure described in Figure 78 and is then used in a classic enantiorecognition measurement. The results are cross-checked by conducting the same test with the bare glassy carbon electrode before the electropolymerization of p-2T3N. Figure 83 shows that the homopolymeric GC|p-2T3N interface, unlike the initial GC electrode, provides two distinct voltammograms for the two enantiomeric species in solution (R-FC, green trace, and S-FC, orange trace). Clear differences are evident both in terms of potential ($\Delta E \sim 45\ mV$) and current ($\Delta I \sim 35\ \mu A$) for the reversible redox process of ferrocene, with the S-FC shifted towards more positive potential and exhibiting higher current magnitude (the oxidation peak is used as a reference for Δ$I$). It's possible to observe that in the case of the GC|p-2T3N electrode, both redox signals of the probe (R-FC and S-FC) are shifted to a higher potential compared to the bare electrode. This shift is due to the nature of the polymer, which becomes conductive only after the p-doping process occurs. This effect is also reflected in the current values, which are lower on the modified electrode compared to the bare one.

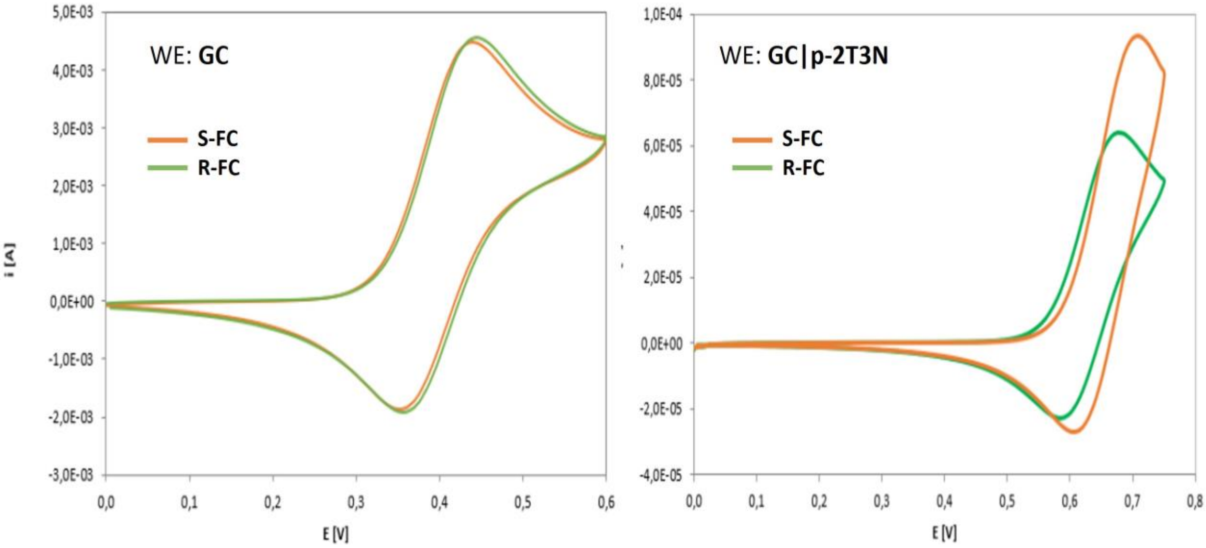

Figure 82 Enantiorecognition voltammetric measurements. CVs are recorded in 5 mM R-FC (green curve) or S-FC (orange curve), 0.1 M TBATFB in ACN solution, 50 mV $s^{-1}$ is the potential scan rate. **a)** a clean Glassy Carbon acts as the WE. **b)** The GC|p-2T3N interface acts as the WE.

### *4.1.3. Theoretical results*

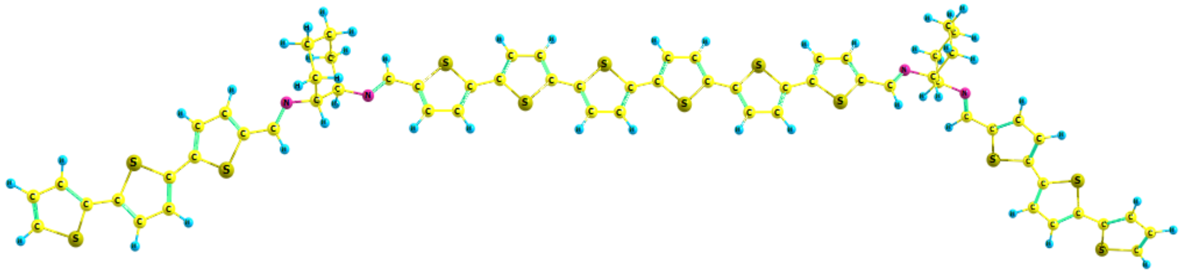

Figure 83 The full optimized geometry of the p-2T3N dimer species, obtained using density functional theory (DFT) with the CAM-B3LYP functional and the 6-31G* basis set.

Figure 84 depicts the minimum energy geometry (full optimization) calculated for the p-2T3N dimer. The polymerization of thiophenes is extensively studied in the literature. Many theoretical and experimental studies have indicated that the monomer units are incorporated into the polymer chain dominantly through the α-α linkages due to the much higher reactivity at the α-position compared to the β-position in the monomer [272]–[274]. This trend is confirmed in the case of p-2T3N, as in our calculations, a minimum energy geometry is achieved after a small number of SCF iterations, resulting in the reported geometry: the bonding occurs between the two terthiophenic regions as a consequence of electrochemical oxidation (required to obtain the radical cations).

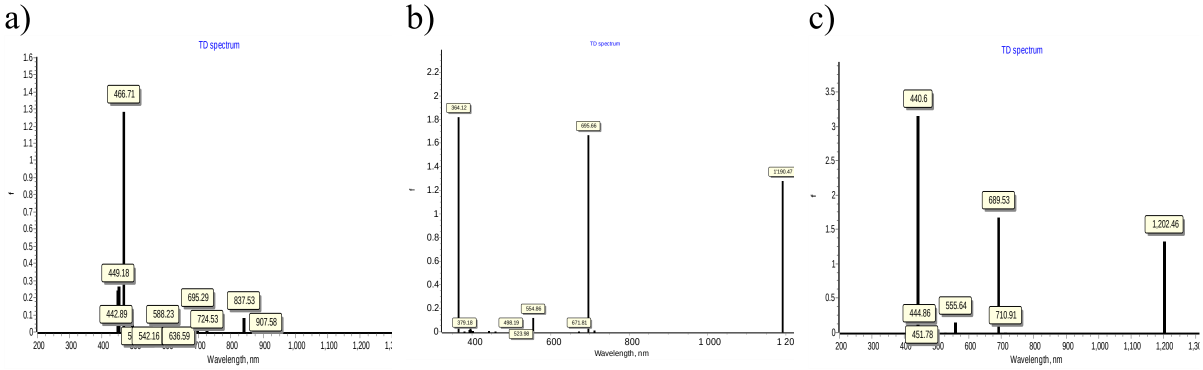

Figure 84 TDDFT CAM-B3LYP 631-G* electronic spectrum of the 2T3N radical cation **a)** monomer **b)** dimer **c)** trimer

Figure 85 a, b, and c depict the theoretical spectra of the radical cation species for the monomer (2T3N) and the polymer (p-2T3N: dimer in panel b, trimer in panel c). These spectra were calculated using the time-dependent density functional theory (TDDFT) method with the hybrid functional CAM-B3LYP / 6-31G* level of theory. The electronic spectrum of the monomer, Fig. 85a, is dominated by an absorption peak at 466 nm, while the spectra of the polymer (panels b and c) exhibit the appearance of two distinct bands at 690 nm and 1200 nm (the latter assigned to the electronic polaron). These theoretical spectra show consistent agreement with the experimental spectroelectrochemical data (compare Fig. 80). Furthermore, it is noteworthy that the electronic spectra of the dimer and trimer (as well as the tetramer, although not presented here) are essentially identical. This outcome (coupled with the robust consistency of the experimental data, where spectroscopic investigations probed chains that are considerably longer than a trimer or tetramer in the case of p-2T3N electropolymerized on ITO) implies that the electronic spectrum of p-2T3N remains unaltered regardless of its length. The electronic spectrum transitions in focus are of low energy, primarily the HOMO-LUMO (in this case, SOMO-LUMO, as the spectra depict radical cationic species), and these transitions are predominantly governed by electronic configuration. Given the sharp discontinuity in spectral results between monomer and dimer species (followed by nearly identical spectra regardless of length), it is reasonable to conclude that the spectroscopic signature of the polymer is predominantly dictated by the six thiophene rings formed during polymerization, enclosed within the six carbons aliphatic ring. Thus, these cyclohexane ring structures effectively serve as “conjugation switches”.

Figure 86 shows theoretical IR spectra, which give a clear-cut view of the giant signature of the vibrational polaron (which always accompanies the electronic one). The giant IMV peak is centered at about 1000 $cm^{-1}$. Maximum intensities are 17000 km $mol^{-1}$ and 100000 km $mol^{-1}$ for the monomer and dimer (trimer as well) species, respectively. The peculiar result is the almost constant value of the peak maximum for the dimer and trimer species. In general, in conjugated doped polymers the intensity of the polaron IMV mode is monotonically related to the geometrical length, physical extension of the conjugated π system. The same intensity found in this case is related to the switch-off role of the bridging six carbons aliphatic ring, thus the maximum length in the polymer remains of 6 thiophene units π-conjugated.

a)

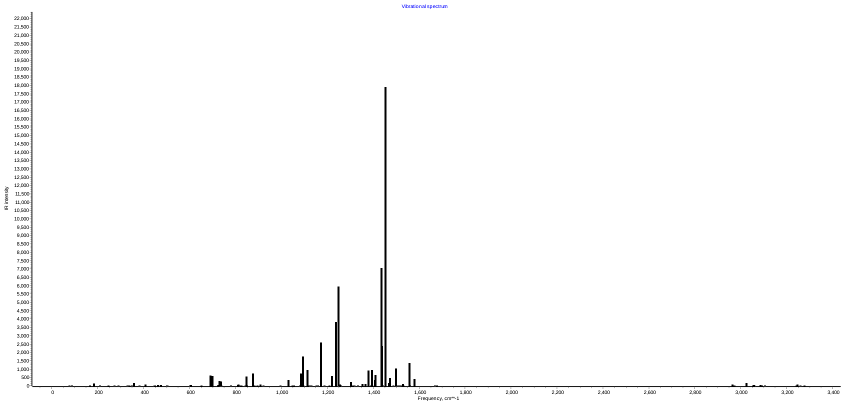

b)

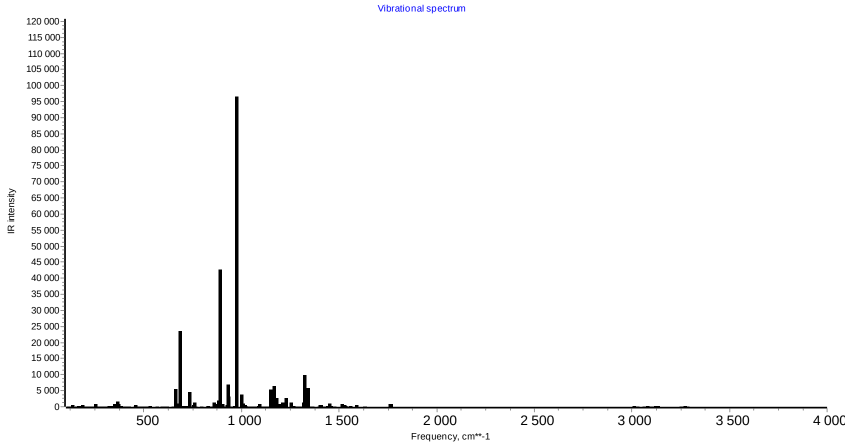

c)

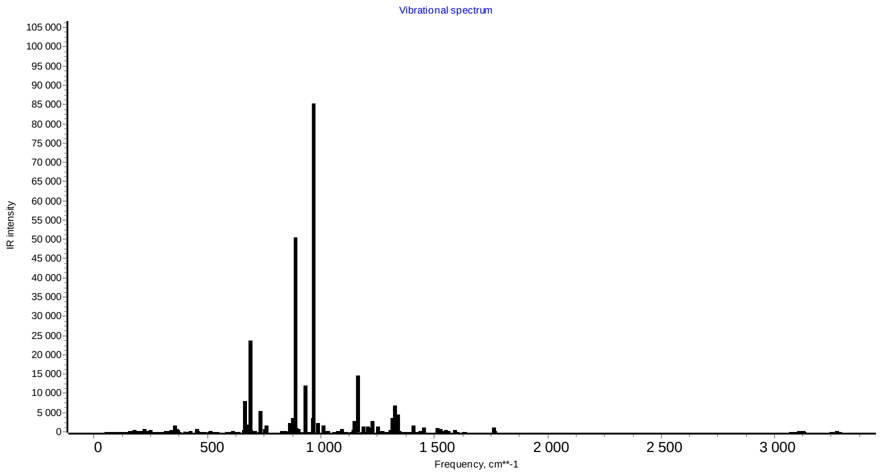

Figure 85 Calculated TDDFT CAM-B3LYP 631-G* vibrational spectrum of the 2T3N radical cation **a)** monomer **b)** dimer **c)** trimer

### *4.1.4 Conclusions*

In this section, we presented the results regarding the polymerization of the chiral molecule R-2T3N, which was previously studied in Section 3.1. we synthesized a chiral polymer (p-2T3N) by spectrophotometrically monitoring the real-time polymerization process (in-situ/in-operando spectroelectrochemistry) and subsequently tracking its characteristic absorption bands during electrochemical p-doping. In this context, we spectroscopically probed the signature of the electronic polaron at 1200 nm. The optical power of the obtained polymer was confirmed through CD spectroscopy, and its enantioselective properties were measured via charge transfer at the electrode|solution interface using the chiral ferrocene redox probe. Theoretical calculations closely mirror the experimental results, providing a confident understanding of the polymerization mechanism and the crucial role played by the conjugation switch that separates the thiophenic regions within the polymer structure.

## 4.2. Polyaniline

In the previous section, charge transfer through the chiral polymer p-2T3N was studied in relation to the electrochemical p-doping of the organic semiconductor (spectroscopically probing the electronic polaron signature) and its enantioselective performance towards a chiral probe in solution. Our experimental research continues with one of the most studied and utilized conducting polymers of the last century: polyaniline (PANI )[275]. The success of PANI is attributed to its unique switching, optical, conductive, and solubility properties that distinguish it from other conducting polymer s[276]. The technological importance of PANI is highly significant since it has been used in various applications, including solar cells [277], lithium batteries [278], supercapacitor s[279], fuel cells [280], flexible electrodes [281], corrosion-resistant coatings [282], water pollutant removal [283], screen printing [284], and sensors[285]. In this extensive scientific literature scenario, this work contributes to two specific aspects:

- PANI electropolymerization (preliminary step, Section 4.2.1): we investigated the electropolymerization of PANI as a function of the pH of the electrolyte solution and created hybrid (metal-organic) interfaces with ferromagnetic materials through electrodeposition.
- Introduction of asymmetry in PANI electropolymerization (end-goal, Section 4.2.2): we explored the induction of supramolecular chirality in polyaniline by introducing a chiral agent into the reaction environment during the electropolymerization process.

### *4.2.1. PANI-based stacked ferromagnetic systems. Electrochemical preparation and characterization*

Unlike other CPs, polyaniline can exist in different forms, depending on the degree of oxidation. Polyaniline is formed by monomer units built from reduced (y) and oxidized (1-y) groups, with $0 \leq y \leq 1$ (compare with Figure 87b) [286]. The redox state of the polymer is determined by the value of y: at y = 0, polyaniline is in the form of pernigraniline, the fully oxidized form; if y = 0.5, polyaniline is the form of emeraldine while y = 1 corresponds to the form of leucoemeraldine (the fully reduced form).

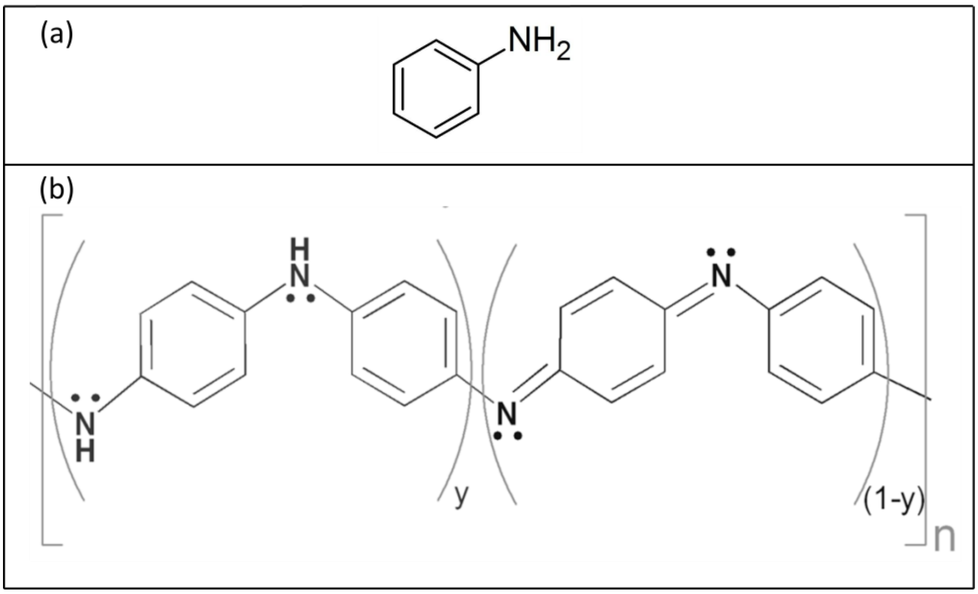

Figure 86. **a)** Aniline structural formula. **b)** Polyaniline structure as a repetition of y and (1-y) units.

In addition, the transitions between different polyaniline forms (and consequently different oxidations levels) are characterised by changes in many physical properties, such as colour and conductivity. The maximal conductivity of polyaniline is achieved at the doping degree of 50%, which corresponds to polyaniline in the form of emeraldine salt [287]. For higher doping degrees some of the amine sites (-NH-) are protonated, while lower doping degrees mean that some of the imine (=NH-) sites were left unprotonated [288]. Therefore, reduction of emeraldine salt to leucoemeraldine and oxidation to pernigraniline states decrease the conductivity (accordingly to the polaron conductivity model) [289]. The order of magnitude for conductivity varies from $10^{-2}$ S cm$^{-1}$ for undoped emeraldine, up to $10^{3}$ S cm$^{-1}$ for doped emeraldine salt [290].

The mechanism and the kinetics of the electrochemical polymerization of aniline were intensively studied [290]–[298]. Nevertheless, in the context of applications, aniline polymerization is typically performed only in acidic environment, since higher pH results in short and conjugated bonds as the protonation is favoured [288].

In this section, the electrochemical polymerization of PANI was investigated with particular attention to the interaction possibility with ferromagnetic materials and magneto-responsive devices, in the context of an electrochemical simple production [152], [161], [299]–[302]. Galvanostatic and potentiodynamic electropolymerization of aniline has been explored as a function of the pH of the electrolytic solution, allowing to produce stacked systems with ferromagnetic layers.

#### 4.2.1.1 PANI electropolymerization from acidic solution

The standard conditions for PANI electropolymerization include an acidic environment, typically provided by sulfuric acid or perchloric acid in aqueous solution [19], [303]. In our study, potentiostatic and galvanostatic PANI depositions were performed on an Au substrate from a $H_2SO_4$ (1 M) and aniline (0.1 M) electrolytic solution (please see Figure 95 of the following Section 4.2.1.3 for the CV method electropolymerization). Figure 88 displays the potential (V) vs time (t) trend for a PANI galvanostatic deposition. The polymer coating is grown by applying a constant current of 0.25 mA.

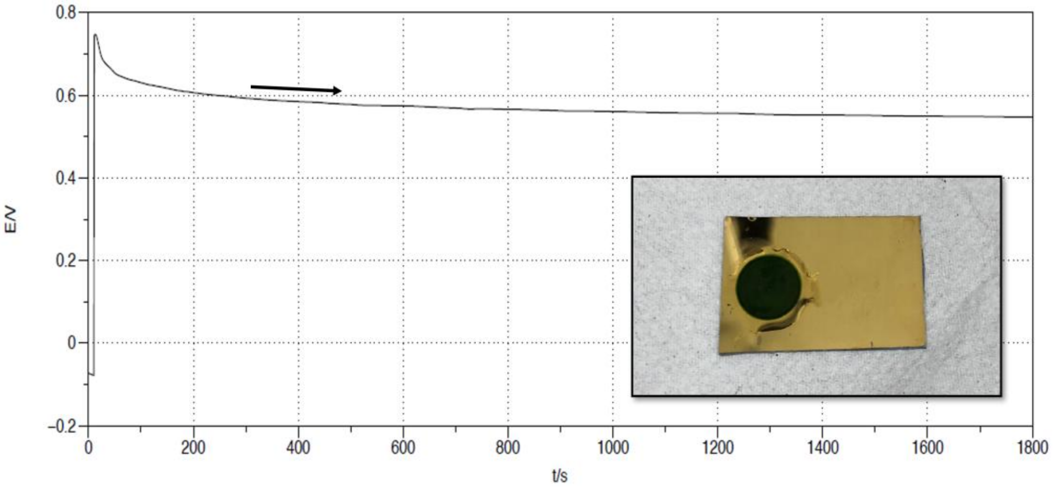

Figure 87 PANI galvanostatic electropolymerization on a Au/Si WE, in a 3-electrodes cell. Pt was used as CE, Ag/AgCl/KCl$_{sat}$ as Ref. The electrolyte consists of aniline (0.1 M) in a $H_2SO_4$ (1 M) aqueous solution. 0.25 mA of current was imposed for 1800 seconds. The inset displays the produced surface.

Figure 88 evidences an initial transient where the potential reaches up to 0.75 V, to match with the imposed current. During these first seconds, the double layer charging process is occurring; then, after the correspondent value of potential is set, the diffusion dynamics take over and the potential is approximately constant for the rest of the time. The trend of the curve is slightly decreasing because new conductive surface is growing on the electrode as PANI is polymerized, and so a lower potential is needed to maintain the imposed value of current. The PANI coating obtained in the described procedure is illustrated in figure 88 inset. The deposit is uniform, firmly adherent to the substrate, and shows a dark green colour (further evidence that PANI in the form of emeraldine has been synthetized, as expected by using acidic medium).

The relation between PANI thickness and the imposed current during the galvanostatic electropolymerization has been investigated by means of CV both in bare support electrolyte (KCl) and in a ferrocyanide/ferricyanide $[Fe(III)(CN)_6]^{3-}$/ $[Fe(II)(CN)_6]^{4-}$ (referred as Fe(III)/Fe(II) in the text) redox probe electrolytic solution. Results are presented in Figure 89 and Figure 90, respectively.

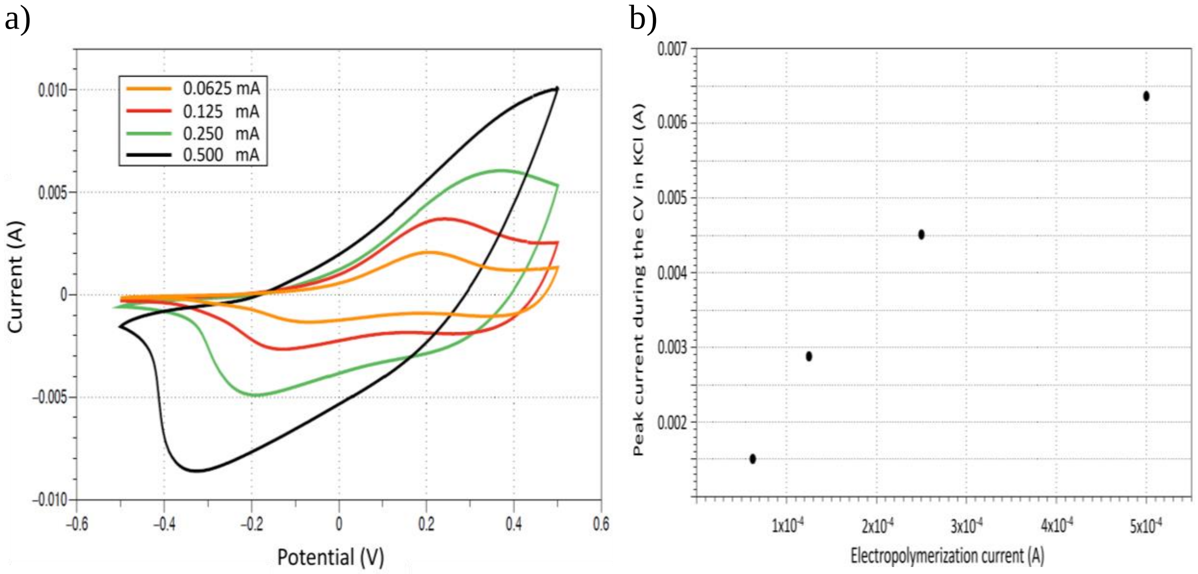

Figure 88 **a)** Cyclic voltammetry (CV) curves recorded on PANI/Au WEs. The several colours are associated with separate samples which underwent different currents of electropolymerization, leaving unaltered all the other parameters (electrochemical bath, electropolymerization time of 900 seconds, substrate, electrode area…). **Orange curve**: PANI electropolymerization at 0.0625 mA for 900 s; **red curve**: PANI electropolymerization at 0.125 mA for 900 s; **green curve**: PANI electropolymerization at 0.25 mA for 900 s; **black curve**: PANI electropolymerization at 0.5 mA for 900 s. These samples were tested by CV between -0.5 V and 0.5 V vs Ag/AgCl/$KCl_{sat}$; Pt was the counter electrode. The solution only consists of the support electrolyte: KCl (0.1 M). 0.1 V/s is the scan-rate. **b)** relation between the peak oxidation current recorded in the CVs from panel (a) and the value of the imposed current during the electropolymerization of the samples.

Figure 89 features CV curves in the same potential window (-0.5 V ÷ 0.5 V) for different PANI coatings, which were deposited in the same conditions previously described (please compare Figure 88) but with different values of constant current. Since the electrolytic solution only consists of support electrolyte, the observed current is associated with the PANI electrode reversible redox activity (oxidation peak between 0.2 V and 0.4 V, correspondent reduction peak between -0.2 V and -0.4 V). As the polymerization current increases (at constant time, in this case 900 seconds), the thickness of the produced surface grows as well. The greater amount of conductive surface (for higher PANI thicknesses) results in the larger number of sites for the electrons exchange, and correspondent higher currents displayed in the CVs. In Figure 89b it can be observed that it exists a rough semiquantitative monotonic pattern between the current for the PANI electro polymerization (galvanostatic regime) and the currents obtained in the KCl CVs. These results are cross-checked adding the Fe(II)/Fe(III) redox probe in the KCl solution (Figure 90): the obtained curves confirm the trend emerged from Fig. 89 measurements.

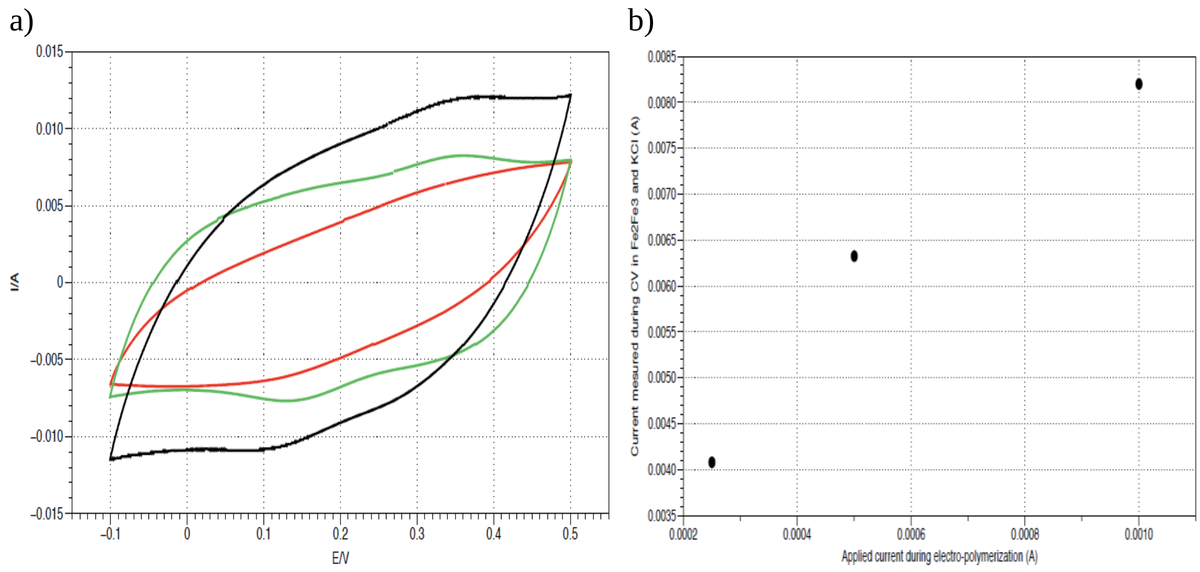

Figure 89 **a)** Cyclic voltammetry (CV) curves recorded on PANI/Au WEs. The several colours are associated with separate samples which underwent different currents of electropolymerization, leaving unaltered all the other parameters (electrochemical bath, electropolymerization time of 900 seconds, substrate, electrode area…). **Red curve**: PANI electropolymerization at 0.25 mA for 900 s; **green curve**: PANI electropolymerization at 0.5 mA for 900 s; **black curve**: PANI electropolymerization at 1.0 mA for 900 s. These samples were tested by CV between -0.1 V and 0.5 V vs Ag/AgCl/KCl$_{sat}$; Pt was the counter electrode. The solution consisted of the Fe2$^{+}$/Fe$^{3+}$ redox probe (K$_3$Fe(CN)$_6$ and K$_4$FeCN)$_6$ 2mM) in support electrolyte (KCl 0.1 M). 0.1 V/s is the scan rate. **b)** Relation between the oxidation peak current of Fe$^{2+}$ recorded in the CVs from panel (a) and the value of the imposed current during the electropolymerization of the samples.

The characterization CVs on the Au|PANI electrodes suggest that the doubling of the electropolymerization current translates to a thickness increase by a coefficient between 1.4 (for higher thicknesses i.e lower curve gradient) and 1.9 (small thicknesses, higher gradient of the quadratic curve). This result is confirmed by the PANI thickness measurements: two distinct samples of PANI were synthetized from the acidic solution, adhering to the previously outlined procedure, employing currents of 0.25 mA and 0.5 mA over a duration of 900 seconds, respectively (while maintaining all other parameters unaltered). The thickness of the initial sample (0.25 mA, 900 seconds) underwent measurement using profilometry (depicted in Figure 91a), yielding a thickness of 4.1 µm. The thickness of the second sample (0.5 mA, 900 seconds) was estimated through Monte Carlo simulations, drawing from EDS microanalysis data [304], and it was determined to be 7.3 µm Figure 91b).

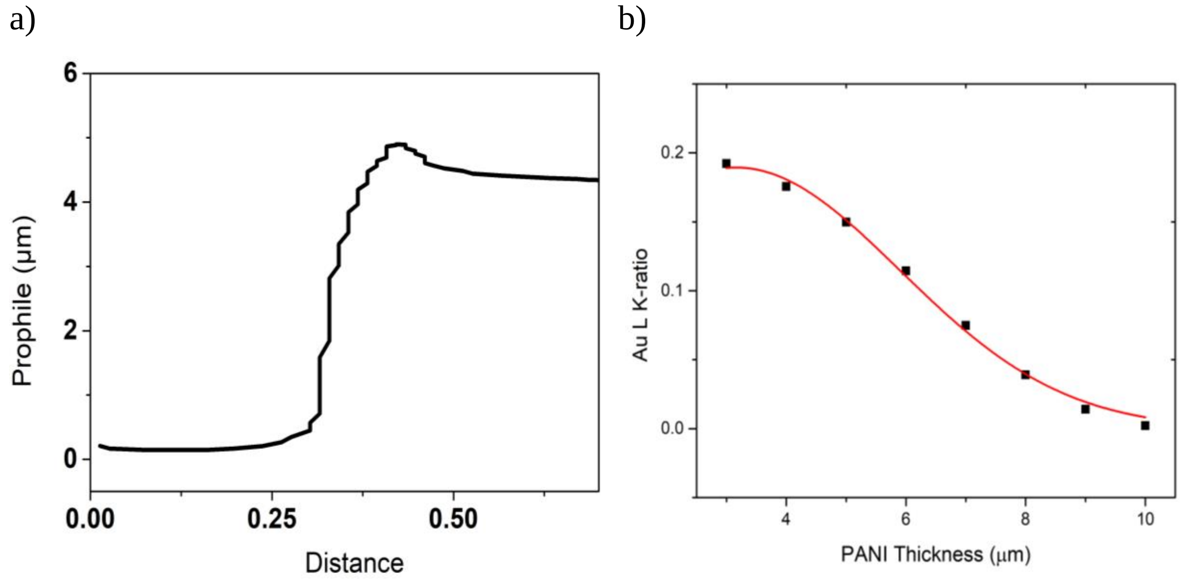

Figure 90 **a)** Profilometry analysis performed on a Au|PANI interface. The PANI was electropolymerized on the Au substrate by galvanostatic electrochemical procedure: 0.25 mA applied for 900 seconds. **b)** Au K-ratio based calibration curve, for the calculation of the overlying PANI coating. The curve is calculated after simulating multiple Au|PANI specimens, with different PANI thicknesses (ranging from 1 µm to 10 µm) with DTSA-|| software [305]. Au K-ratio values were then calculated, considering that the substrate signal's drop is proportional to the PANI coating thickness.

Further data about the thickness of the PANI coatings can be extrapolated by the SEM top view and cross-section imaging, *vide infra*, Section 4.2.1.2, Figure 93 and Figure 94. All the performed measurements show consistent results with the electrochemical data.

### 4.2.1.2 Nickel electrodeposition on top of PANI

Nickel electrodepositions on top of the Au|PANI interface have been carried out as the conclusion of this simple 2-step process, allowing for producing an hybrid layered electronic device (PANI-Nickel systems are extensively used in multiple applications [306]–[308]).

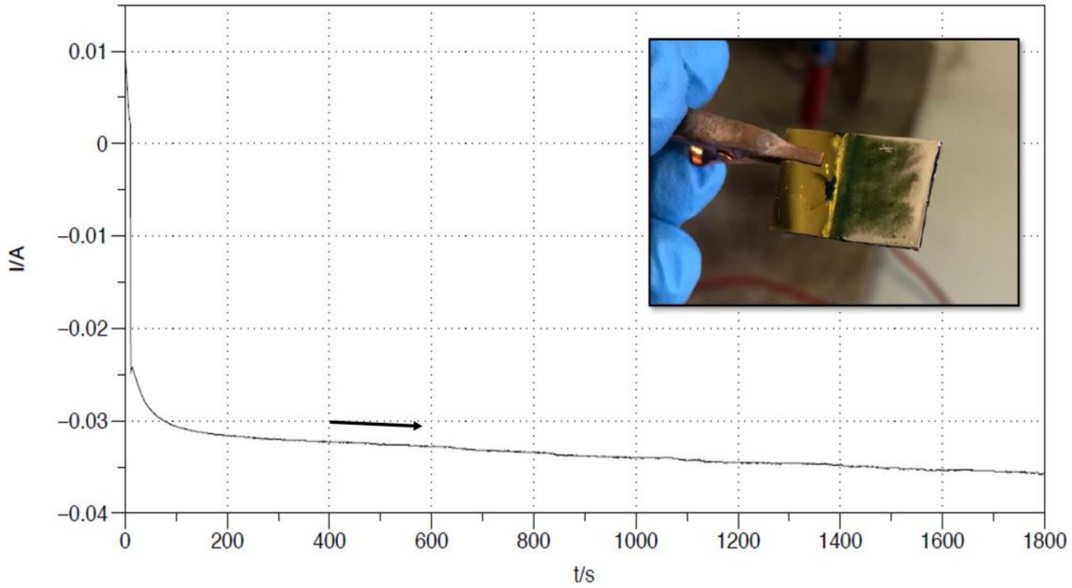

Figure 91 Nickel potentiostatic electrodeposition on a PANI/Au WE, in a 3-electrodes cell. Pt was used as CE, Ag/AgCl/KCl$_{sat}$ as Ref. The Watt's Bath was used as electrolyte: nickel sulphate $NiSO_4$ (1 M), nickel chloride $NiCl_2$ (0.25 M), boric acid $H_3BO_3$ (0.6 M), pH = 5. The imposed potential was -1.4 V for 1800 seconds. The inset displays the produced surface.

Figure 92 reports a potentiostatic Ni deposition performed on an Au|PANI Working Electrode for 1800 seconds, at a constant reduction potential of -1.4 V vs Ag/AgCl. The underlying Au|PANI interface was previously produced by 900 seconds, 0.125 mA constant current electrodeposition, following the exact same procedure described in Section 4.2.1.1. In the inset, a picture of the electrode after only 300 seconds of electrochemical Ni deposition is reported. Since the process is not complete yet, it is possible to appreciate the metallic layer growing on the green PANI surface, starting from the edges of the electrode as expected (stronger electric field force lines). In fact, the electrode does not even need to be disassembled from the electrochemical cell in-between the two depositions. The only middle step required is vacuum drying for 30 minutes approximatively, in order for the Nickel layer to adhere properly to the PANI surface.

Figure 93 presents the SEM top-view of the fabricated device. The acquisition is performed with secondary electrons at 200x and 1000x magnification. The metallic Ni layer exhibits a compact morphology with globular-like crystallites, proving a good adhesion on the PANI substrate. The presence of micro-cracking may be due to $H_2$ evolution during the cathodic electrodeposition or to internal tensions releasing.

Figure 94 shows a SEM cross-section image of the produced specimen, with relative EDS microanalysis, where all the different elements of the layered structure can be appreciated. The acidic PANI mid-layer (0.125 mA for 900 s) is about 2.4 μm thick and follows the thin Au substrate (100 nm, evaporated on top of a Silicon wafer with an in-between 10 nm Ti adhesion layer) very closely, suggesting a good adhesion. The Ni top coating is mainly metallic, with very weak Oxygen signal in the bulk region (typical of galvanic metallization).

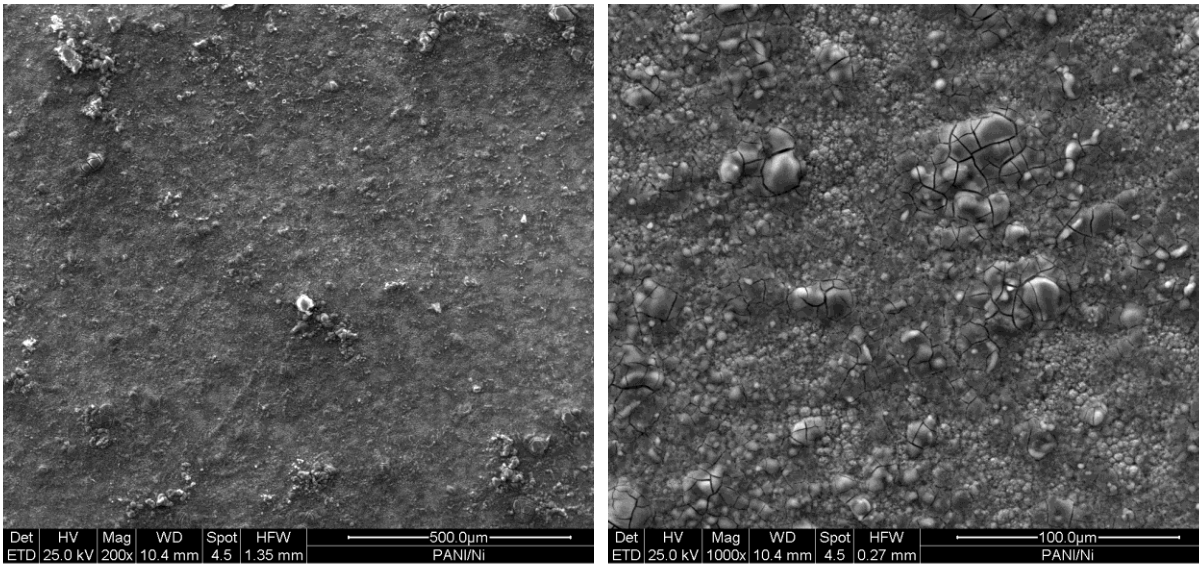

Figure 92 SEM micrographs (top-view) of the layered Au|PANI|Ni specimen

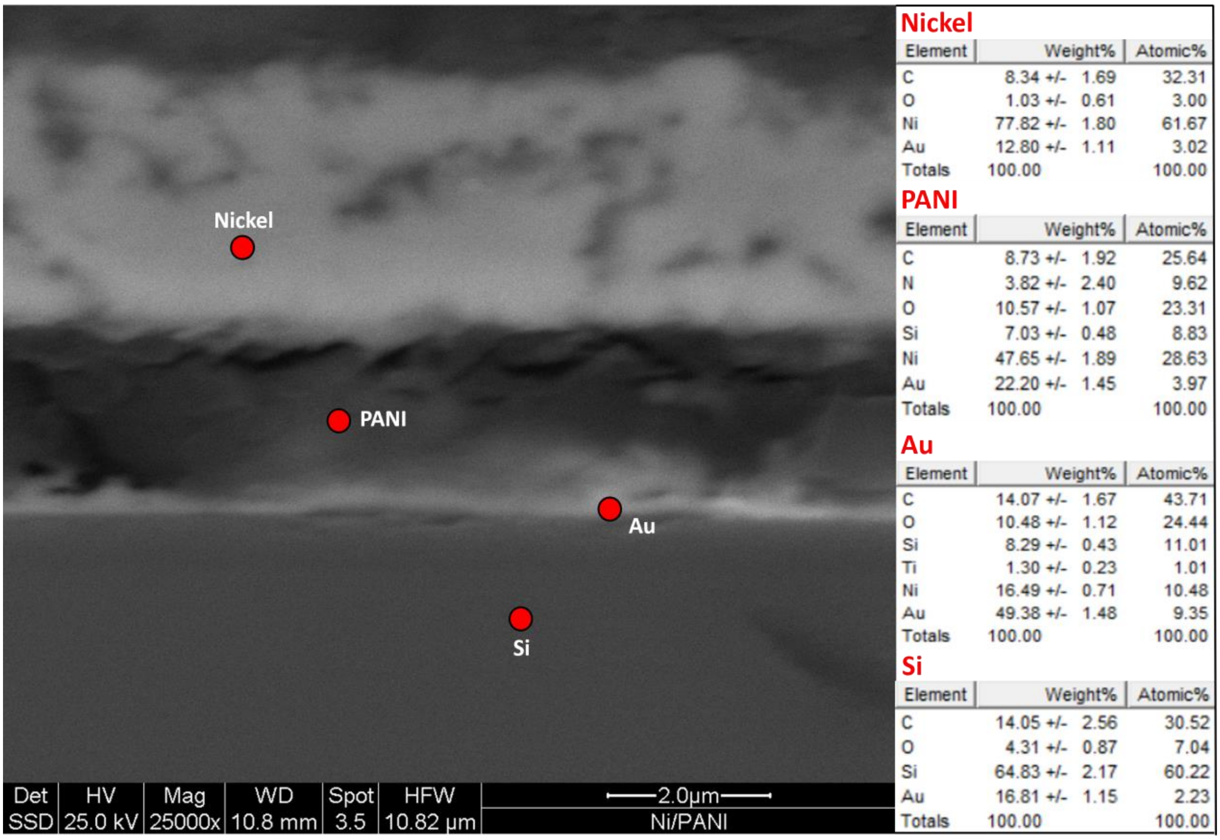

**Nickel**

| Element | Weight% | Atomic% |
|---|---|---|
| C | 8.34 +/- 1.69 | 32.31 |
| O | 1.03 +/- 0.61 | 3.00 |
| Ni | 77.82 +/- 1.80 | 61.67 |
| Au | 12.80 +/- 1.11 | 3.02 |
| Totals | 100.00 | 100.00 |

**PANI**

| Element | Weight% | Atomic% |
|---|---|---|
| C | 8.73 +/- 1.92 | 25.64 |
| N | 3.82 +/- 2.40 | 9.62 |
| O | 10.57 +/- 1.07 | 23.31 |
| Si | 7.03 +/- 0.48 | 8.83 |
| Ni | 47.65 +/- 1.89 | 28.63 |
| Au | 22.20 +/- 1.45 | 3.97 |
| Totals | 100.00 | 100.00 |

**Au**

| Element | Weight% | Atomic% |
|---|---|---|
| C | 14.07 +/- 1.67 | 43.71 |
| O | 10.48 +/- 1.12 | 24.44 |
| Si | 8.29 +/- 0.43 | 11.01 |
| Ti | 1.30 +/- 0.23 | 1.01 |
| Ni | 16.49 +/- 0.71 | 10.48 |
| Au | 49.38 +/- 1.48 | 9.35 |
| Totals | 100.00 | 100.00 |

**Si**

| Element | Weight% | Atomic% |
|---|---|---|
| C | 14.05 +/- 2.56 | 30.52 |
| O | 4.31 +/- 0.87 | 7.04 |
| Si | 64.83 +/- 2.17 | 60.22 |
| Au | 16.81 +/- 1.15 | 2.23 |
| Totals | 100.00 | 100.00 |

Figure 93 SEM micrographs (cross-section) of the layered Au|PANI|Ni specimen

#### 4.2.1.3 PANI electropolymerization at different pH

The study of different PANI structures as a function of the pH of the electropolymerization solution arises from the need to coat with PANI an electrodeposited layer of Magnetite ($Fe_3O_4$). In fact, while the above-mentioned Nickel is deposited from an acidic bath, Magnetite quickly dissolves in $H_2SO_4$ [309], therefore it is not possible to expose a $Fe_3O_4$ surface directly to the acidic aniline solution. Consequently, a systematic investigation is carried out electropolymerizing aniline from three further electrolytic baths:

- weakly acidic solution ($CH_3COOH$ (40 mM), aniline (0.1 M), pH=3)
- neutral solution (NaCl (0.1M), aniline (0.1 M), pH=7)
- basic solution (NaOH (0.1 M), aniline (0.1 M), pH=13)

The electropolymerization in these 3 additional environments is performed through a CV procedure and it is compared to the $H_2SO_4$ electrolyte one. All these depositions are carried out on Au substrates (MetrOhm Au electrodes) and results are listed in figure 95.

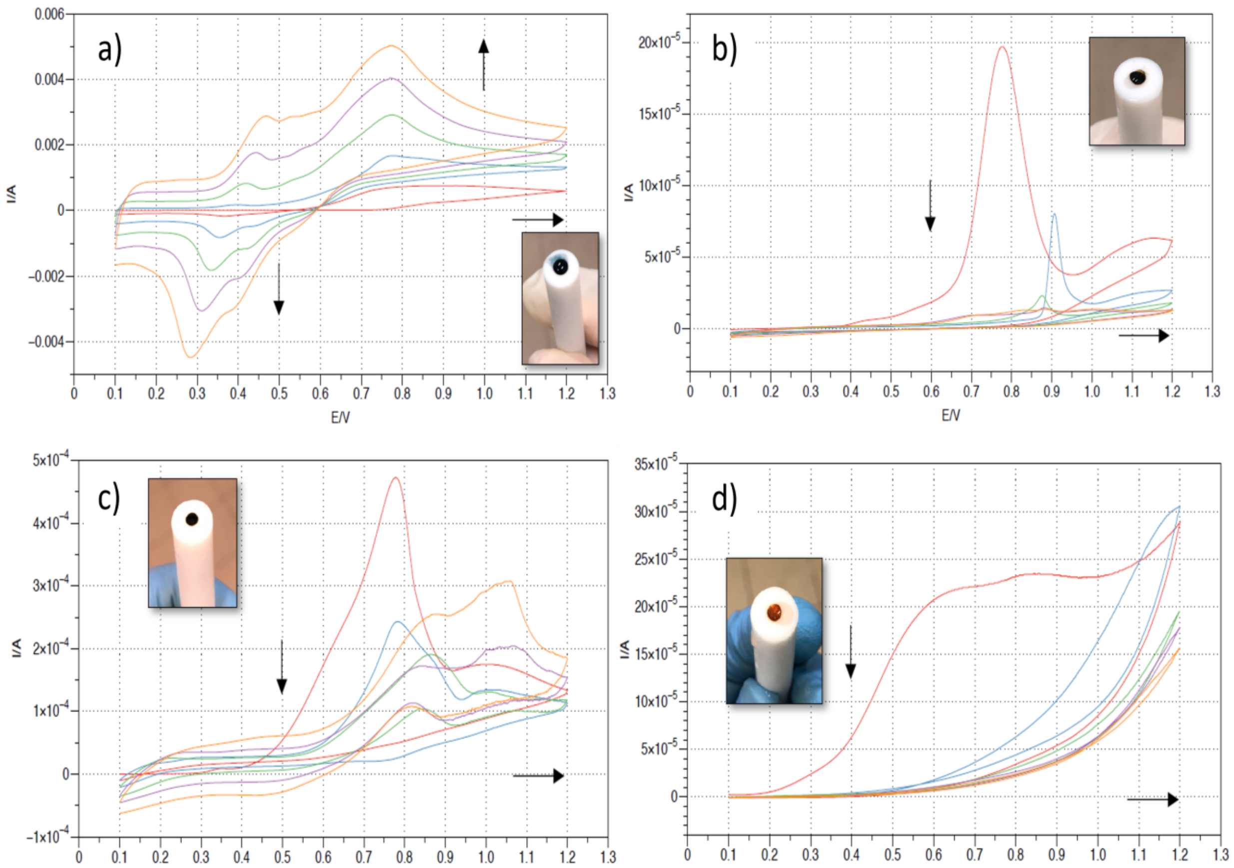

Figure 94 PANI potentiodynamic electropolymerization as a function of the electrolytic solution. Different electrolytes have been used to perform aniline electropolymerization, while all the other experimental parameters have been kept constant: electrochemical setup (Pt as CE, Ag/AgCl as Ref), electrochemical settings (0.1 V ÷ 1.2 V potential window, 0.1 V/s scan-rate), substrate (Metrohm Au rod electrode). **(a)** electrolyte consists of $H_2SO_4$ (1 M), aniline (0.1 M). **(b)** electrolyte: $CH_3COOH$ (40mM), aniline (0.1 M). **(c)** electrolyte: NaCl (0.1 M), aniline (0.1 M). **(d)** electrolyte: NaOH (0.1 M), aniline (0.1 M).

Figure 95a shows a potentiodynamic PANI polymerization in the standard $H_2SO_4$ medium (the system investigated in Section 4.2.1.1). The CV shows that the current increases at every successive cycle, which confirms the electrodeposition of the PANI film. In the forwards scans, the positive current peaks at 0.45 V and 0.75 V can be related to the leucoemeraldine base transition to emeraldine and to the following emeraldine oxidation to pernigraniline, respectively [310]. In the backwards scans, two corresponding reduction peaks are evidenced at about 0.4 V and 0.3 V, showing good reversibility. As the number of cycles increases, the oxidation peaks shift to higher potential values and the reduction peaks shift to lower potential values. The electropolymerized polyaniline is green (as shown in the related inset), as expected for PANI in the form of emeraldine.

Figures 95b, 95c and 95d represent the PANI electropolymerization in the $CH_3COOH$, NaCl and NaOH electrolyte respectively. In all the three CVs, it is still recognizable the oxidation peak between 0.7 V and 0.8 V, related to the aniline oxidation (thus allowing the polymerization). Nonetheless, the current decreases at every successive cycle (in contrast to Figure 95a) and the full-scale value for the current is more than one order of magnitude lower. The reduction peaks between 0.25 V and 0.35 V associated to the leucoemeraldine-emeraldine transformation are absent. The colour of the deposited film switches from very dark green (almost black) in Figure 95 panels b and c, to dark orange in the basic solution case (Figure 95d).

#### 4.2.1.4 PANI electropolymerization on top of Magnetite

The basic aniline solution is used to electropolymerize PANI on a $Fe_3O_4$ electrode. $Fe_3O_4$ was previously electrodeposited on an Au substrate following a standard procedure [311]: the electrolytic solution consisted of Na(OH) (2 M), $Fe_2(SO_4)_3$ (50 mM) and TEA (0.1 M). The Au WE underwent a potentiostatic electrodeposition at -1.3 V vs Ag/AgCl for 1800 seconds. In the PANI electropolymerization on top of magnetite, the same recipe from figure 95d (consisting of Na(OH) (0.1 M), aniline (0.1 M), pH=13) acts as the electrolyte and the Au|$Fe_3O_4$ interface as the WE. Figure 96 displays the galvanostatic PANI deposition, which was performed imposing 0.6 mA of constant current.

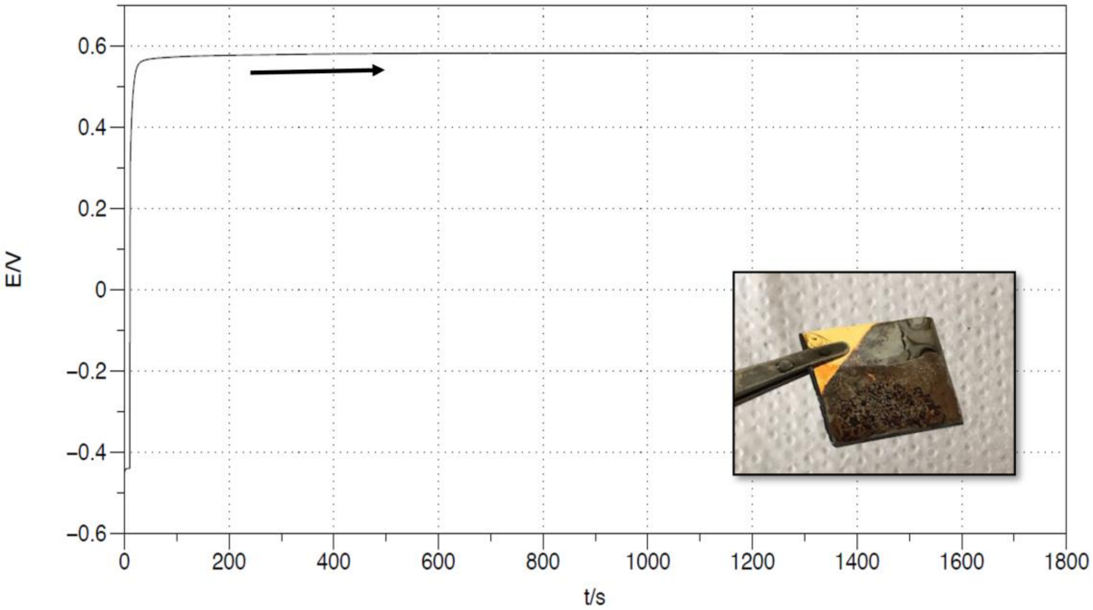

Figure 95 PANI galvanostatic electropolymerization on a $Fe_3O_4$/Au WE, in a 3-electrodes cell. Pt was used as CE, Ag/AgCl/$KCl_{sat}$ as Ref. The electrolyte consisted in the basic aniline solution (pH=13) previously studied in Figure 95: Na(OH) (0.1 M) and aniline (0.1 M). A constant current of 0.6 mA was applied for 1800 seconds. The inset displays the produced surface.

As expected, the conductivity of the basic PANI is much lower than the emeraldine, described in Section 4.2.1.1, since the protonation of the imine sites is largely prevented due to the basic environment. As a result, the obtainable thicknesses with an electrochemical polymerization are much thinner, at most 500 nm according to our experiments. In fact, thicker coatings act as insulator and break the contact with the electrode, making the continuation of the electrochemical procedure impossible. Figure 97 displays the SEM top-view of the $Fe_3O_4$|PANI device. The acquisition is performed with secondary electrons at 200x and 1000x magnification. In particular, in the left image (200x magnification), the interface between the substrate (Au), magnetite and PANI can be distinguished, since the different coatings have been deposited with a stepped structure. The 1000x magnification picture (right panel) presents the basic PANI top-layer in detail and evidences the organic coating's uniformity.  Figure 98 shows a SEM cross-section image of the produced Au|$Fe_3O_4$|PANI interface specimen, with relative EDS microanalysis. A columnar morphology of the metallic ferromagnetic mid-layer can be observed, while the PANI top layer proves to be around 400 nm thick.

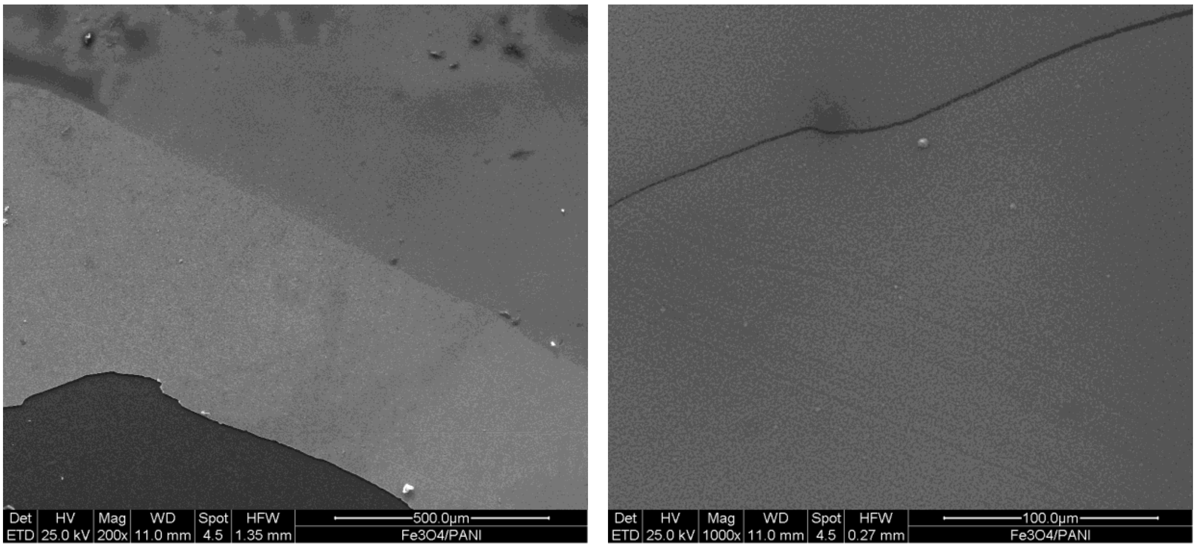

Figure 96 SEM micrographs (top-view) of the layered Au|$Fe_3O_4$|PANI specimen

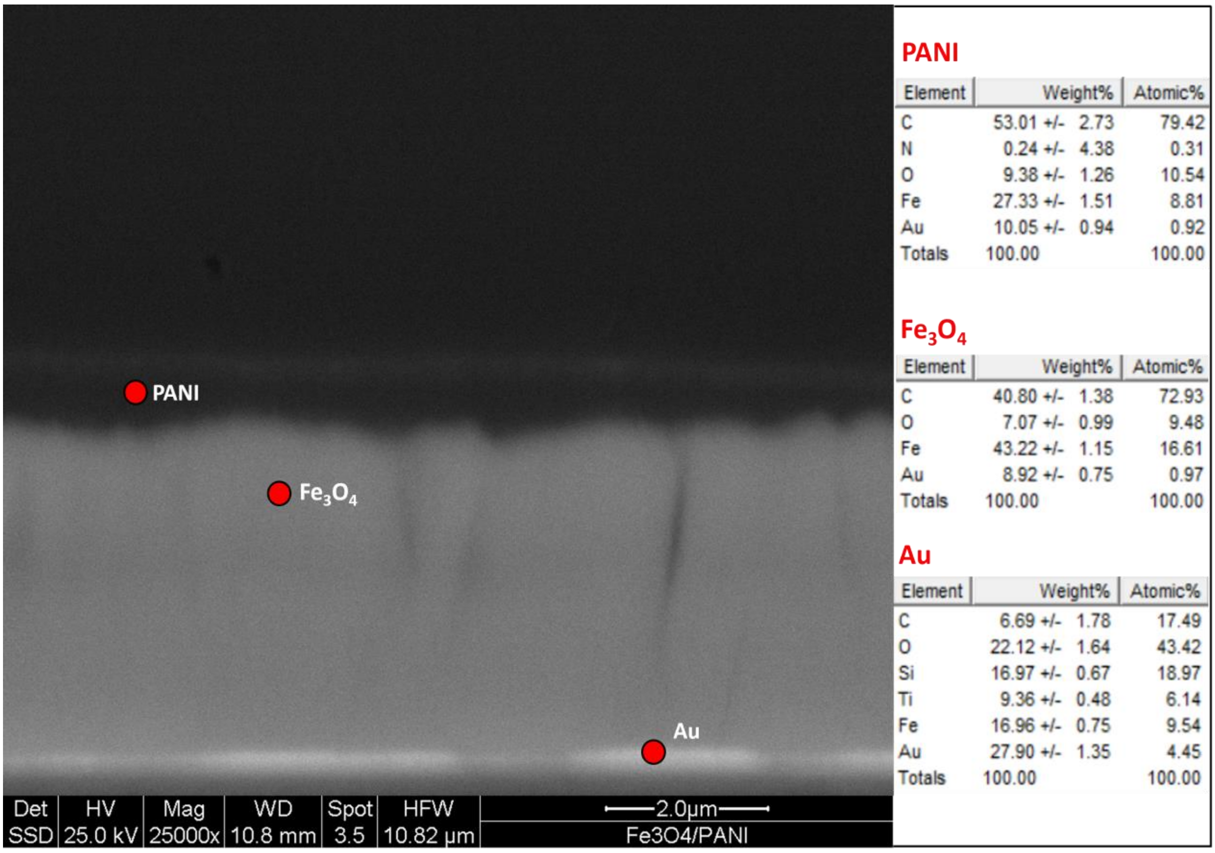

**PANI**

| Element | Weight% | Atomic% |
|---|---|---|
| C | 53.01 +/- 2.73 | 79.42 |
| N | 0.24 +/- 4.38 | 0.31 |
| O | 9.38 +/- 1.26 | 10.54 |
| Fe | 27.33 +/- 1.51 | 8.81 |
| Au | 10.05 +/- 0.94 | 0.92 |
| Totals | 100.00 | 100.00 |

**$Fe_3O_4$**

| Element | Weight% | Atomic% |
|---|---|---|
| C | 40.80 +/- 1.38 | 72.93 |
| O | 7.07 +/- 0.99 | 9.48 |
| Fe | 43.22 +/- 1.15 | 16.61 |
| Au | 8.92 +/- 0.75 | 0.97 |
| Totals | 100.00 | 100.00 |

**Au**

| Element | Weight% | Atomic% |
|---|---|---|
| C | 6.69 +/- 1.78 | 17.49 |
| O | 22.12 +/- 1.64 | 43.42 |
| Si | 16.97 +/- 0.67 | 18.97 |
| Ti | 9.36 +/- 0.48 | 6.14 |
| Fe | 16.96 +/- 0.75 | 9.54 |
| Au | 27.90 +/- 1.35 | 4.45 |
| Totals | 100.00 | 100.00 |

Figure 97 SEM micrographs (cross-section) of the layered Au|$Fe_3O_4$|PANI specimen

#### 4.2.1.5 Conclusions

In this section, the aniline electropolymerization has been studied with the prospect of coupling the PANI organic layer with a ferromagnetic material, producing a stacked hybrid system. In particular, the pH of the electropolymerization bath has been optimized for a suitable co-electrodeposition of Nickel (Ni) and Magnetite ($Fe_3O_4$), thus allowing for an easy and flexible way to manufacture the entire sample by electrochemical methods. Different electrochemical regimes have been explored, and an extensive characterization has been performed on the obtained systems. Electrochemical data, SEM surface and cross-section analysis, EDS microanalysis data and simulations and profilometry measurements define a consistent comparison between the different PANI organic coatings.

### *4.2.2. Supramolecular chiral induction in Polyaniline (chiral PANI)*

The polymerization of aniline in the presence of enantiopure 10-camphor sulfonic acid (CSA) represents a well-established example of a chiral supramolecular system [19], [32], [312]. The first instances of optically active polyanilines were reported in 1994. These involved CSA-doped emeraldine salts, which were synthesized using two distinct approaches: electropolymerization of aniline in the presence of enantiomeric HCSA acids, or the acid doping of pre-formed emeraldine base. The remarkable chemical and physical properties of PANI, including its high conductivity and stability, along with the ease of electrochemically synthesizing chiral films of this polymer, make it a promising candidate for applications in the field of spintronics [153]. This raises the prospect of developing PANI-based CISS devices. In this section, the production and characterization of chiral PANI films (cPANI) are conducted with the aim of using them as the active material in the electrochemical transistor configuration, which will be presented in the following results Section (4.4).

#### 4.2.2.1 Circular Dichroism

PANI electrodeposition is performed using exactly the same procedure described in the previous paragraph, Section 4.2.1.1, which features the extensive study and characterization of PANI electropolymerization. The electrolytic solution consists of aniline (0.1 M) in a $H_2SO_4$ (1 M) aqueous solution. A current of 0.1 mA cm$^{-2}$ is applied for 600 seconds to an ITO electrode, which acts as the working electrode (WE) in a 3-electrode electrochemical cell (Pt wire as the CE and Ag/AgCl/KCl$_{sat}$ as the Ref). In the case of cPANI samples, 50 mM of R-CSA or S-CSA is alternately added to the electrolyte solution. Figure 99 displays the absorption and CD spectra of PANI and cPANI deposits (R-CSA PANI and S-CSA PANI) electropolymerized on ITO, spanning an energy range of 350 - 700 nm.

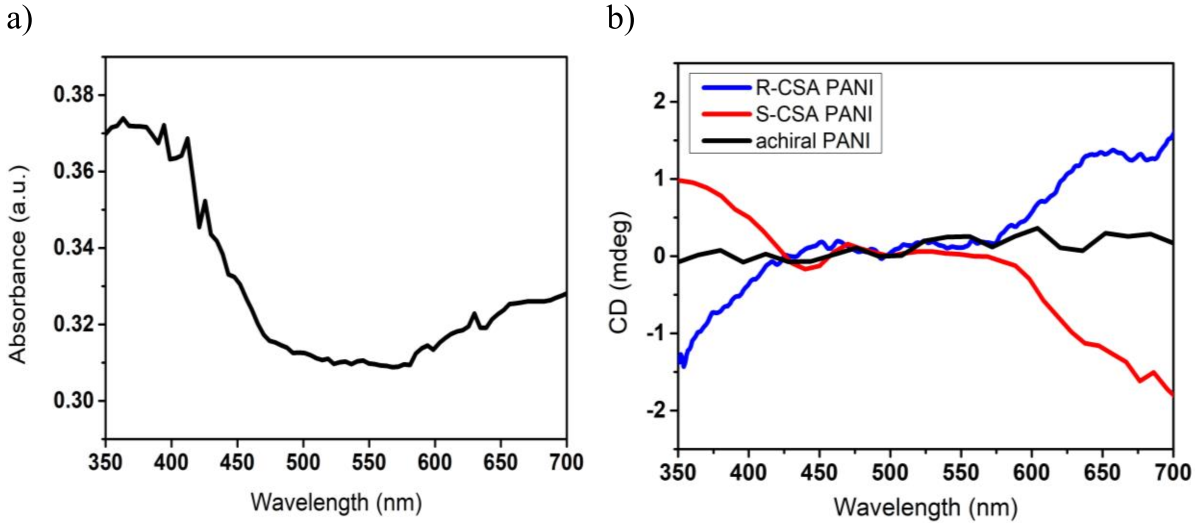

Figure 98 UV-vis and CD spectra of PANI (black trace) and cPANI films (blue trace for R-CSA PANI, red trace for S-CSA PANI), electropolymerized on ITO glass. The absorption spectra overlap of the three samples overlap, so only one curve is shown (panel a).

The absorption spectrum, as shown in Fig. 99a, exhibits a prominent peak in the high-energy region, spanning from 350 to 420 nm, along with a lower-energy absorption tail extending from 600 nm. No significant differences are observed in the absorption spectra between the two enantiomers of cPANI (i.e., doped with R-CSA and S-CSA, as expected), or between these samples and regular PANI, which lacks CSA. This suggests the absence of any cross-linked CSA/aniline chemical reaction, with the possible formation of any covalent bond between the CSA and aniline [19]. Conversely, noticeable differences among the three spectra emerge in the CD signal (Fig. 99b). While the PANI sample, electropolymerized without CSA in bulk solution, demonstrates no optical activity (Fig. 99b, black trace), the CD signals from the two cPANI deposits exhibit a symmetrical pattern with respect to the baseline (red trace and blue trace). Their signs differ according to the handedness of the enantiopure camphor sulfonic acid introduced during electropolymerization. Two regions of optical activity can be distinguished within the spectrum, one spanning from 350 to 450 nm and the other from 600 to 700 nm. This preliminary measurement, conducted on ITO substrates, intends to replicate the findings of the Mishra et al. study (although a slightly different one-step spectroelectrochemical approach was employed in the reference) [19] in order to investigate the actual imprinting of supramolecular chirality on cPANI deposits. The results obtained are in complete accordance with those reported in the reference work and other scientific literature on the induction of chirality in polyaniline [182], [313]–[315]. The spectroscopic analysis of specular optical activity signals within the UV-vis range, occurring at typical PANI absorption energies (an energy range in which the chiral inducer CSA does not absorb, as it is indeed a colorless substance), affirms the effective electrochemical synthesis of chiral PANI layers.

#### 4.2.2.2 Solid-state resistance measurements

The same electropolymerization procedure described in the previous Section 4.2.2.1 was then carried out to deposit the two enantiomers of cPANI on custom substrates (Fig. 100a), designed to accommodate resistance measurements as a function of temperature and applied magnetic field. To exclude the possibility of any substrate contribution to PANI conductivity, the custom substrates consist of two gold pads separated by a 750 μm channel, evaporated on glass (dielectric).

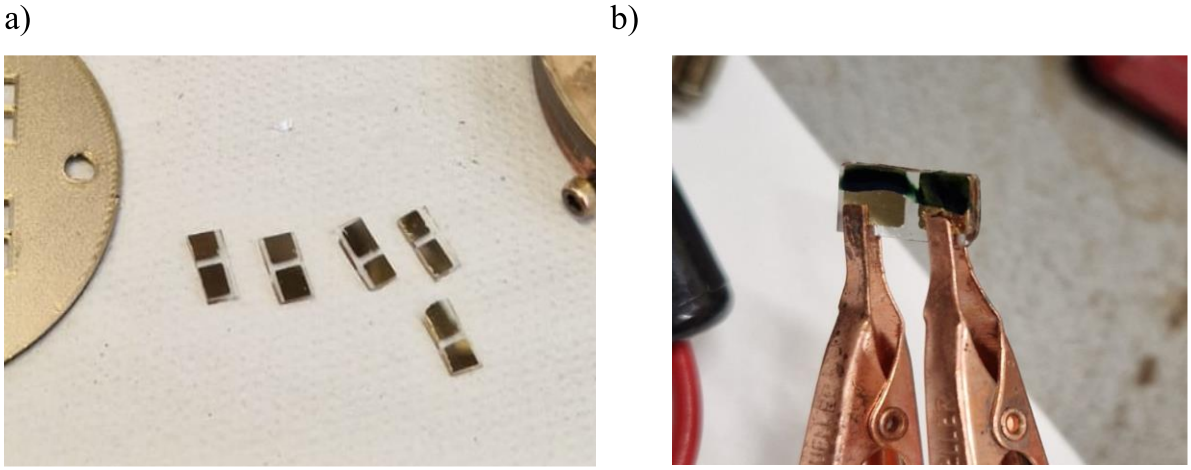

Figure 99 **a)** two-Au pads substrates for the preparation of Au|PANI samples suitable for transport measurements (electrical characterization in a 4-point configuration) **b)** sample obtained at the end of the electropolymerization process.

PANI is then electropolymerized using a dual working electrode electrochemical approach: both pads are simultaneously contacted as the working electrode (WE) and subjected to the same oxidation potential. This allows the progressive growth of the polymer film on both pads. As the electropolymerized thickness increases, the film tends to grow more at the edges of the deposit (due to a higher electric field intensity at the tips), spreading into the non-conductive glass channel until the polymer completely covers the gap between the two gold pads, closing the circuit with a single continuous layer of PANI (Fig. 100b).

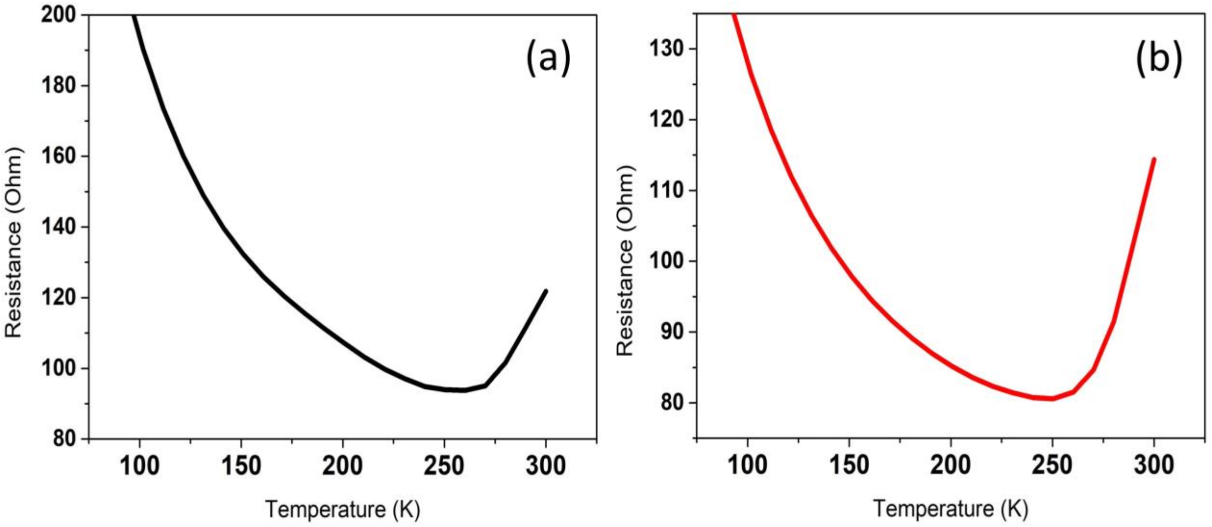

Figure 100 Resistivity vs. temperature curves for the Au|PANI (a) and Au|cPANI (b) interface

Figure 101 shows the change in electrical resistance with temperature for PANI (Fig. 101a, black trace) and cPANI (Fig. 101b, red trace) specimens within the 300 - 120 K interval. Considering the temperature range of 250–300 K, both curves exhibit a positive temperature coefficient of resistivity (TCR), meaning their resistivity decreases with decreasing temperature (metallic region). Subsequently, they reach a minimum point where the slope reverses, leading to a negative TCR at lower temperatures (non-metallic or semi-conductive region). Such a trend is in accordance with scientific literature regarding PANI doped with protonic acids [316]–[319]. The positive TCR typically results from carriers scattering predominantly along the polymer chains by high-energy phonons. This leads to quasi-1D conduction, resulting in low resistivity values, provided that the high-energy phonons are thermally excited [320]. As a result, the resistance decreases as thermal energy $k_B T$ approaches the energy of the backscattering phonons $\hbar\omega_b$, while it remains high at low temperatures. In the negative TCR interval, the dominant model is that of 3D variable-range hopping (VRH) conduction in disordered regions [321]. An expression that accounts for both of these mechanisms (3D-VRH in disordered regions with quasi-1D metallic conduction in ordered regions) and allows for fitting the temperature dependence of resistivity of protonated PANI across the entire temperature range, including the transition from negative to positive TCR, has been proposed by Long et al. [322], equation (74):

$$\rho(T) = a\,\rho_m \exp\left(\frac{-T_m}{T}\right) + b\,\rho_0 \exp\left(\frac{T_0}{T}\right)^{1/4} \qquad (74)$$

with $\rho_m$, $T_m$, $\rho_0$ and $T_0$ being intrinsic constants.

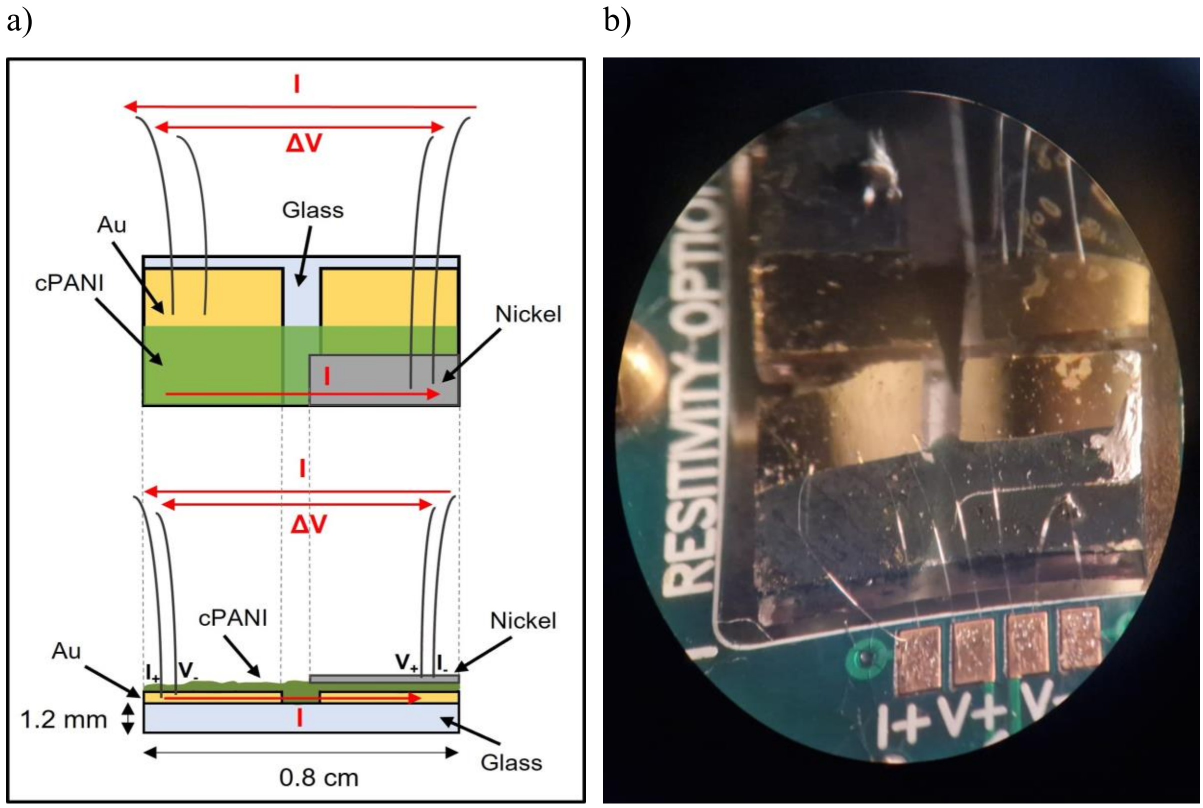

Figure 101 **a)** Schematic representation of the custom-built setup for magnetoresistance measurements. In a standard 4-point configuration, the contacts for measuring the resistivity of cPANI as a function of the magnetic field are taken from the left Au pad and the top Nickel layer on the right. b) Actual photograph of the sample taken under an optical microscope.

cPANI samples, including both R-CSA and S-CSA PANI, are electrochemically produced on the custom substrates described earlier for magnetoresistance measurements. Once PANI is electropolymerized onto the substrate, a Physical Vapor Deposition (PVD) process is employed, exploiting an additional mask to create a thin layer of Nickel (80 nm) on one of the two terminals of the device. A schematic representation of the final sample for magnetoresistance is depicted in Figure 102a. The Nickel, in the presence of an external magnetic field, serves as the spin injector. The "homemade" device is then connected in a classic 4-probe configuration, utilizing the micro-bonding technique with aluminum wire and a small amount of silver paste, between the Au pad without the ferromagnet and the Ni top-layer on the opposite side. Figure 102b illustrates the device connected to the sample holder terminals. Magnetoresistance measurements are conducted at room temperature by scanning the external magnetic field from +10’000 to -10’000 Oersted. The results are presented in Figure 103.

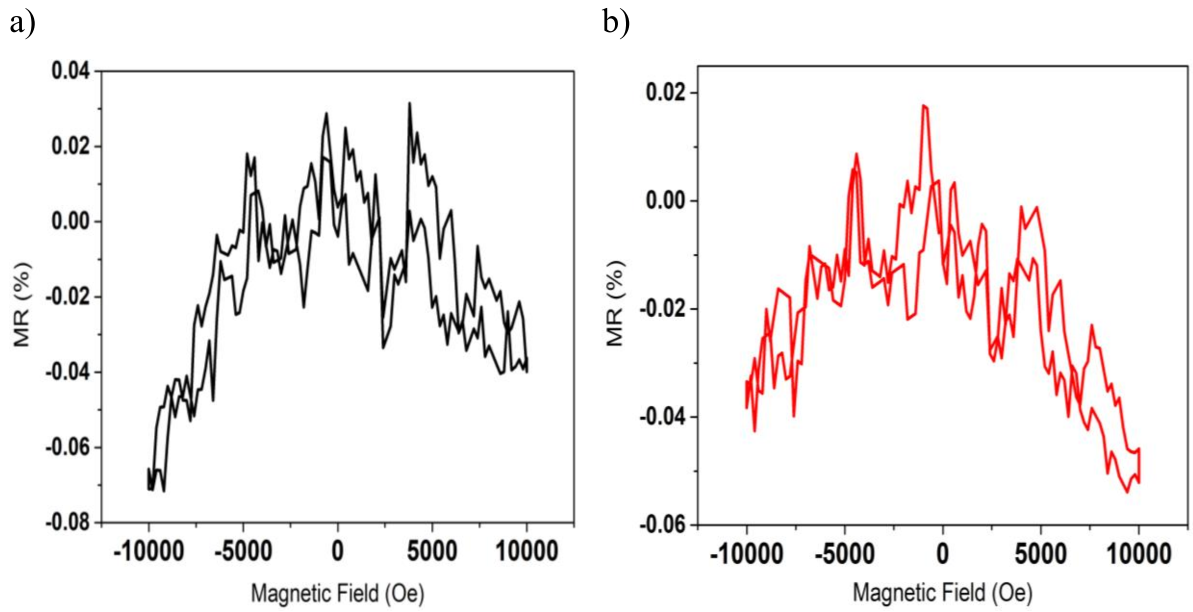

Figure 102 Magnetoresistance measurements carried out on the samples of cPANI: **a)** R-CSA doped PANI and **b)** S-CSA doped PANI.

The sample of cPANI doped with R-CSA (black trace, panel a) exhibits an asymmetric resistance trend as a function of the magnetic field. A saturation value of -0.07% is observed at the maximum negative magnetic field intensity, while a value of 0.03% is measured at the highest positive field intensity. A similar but reversed trend is seen in the cPANI S-CSA doped sample (red trace, panel b). In this case, the effect is less pronounced but still present, with values of -0.04% at a magnetic field of -10 kOe and a saturation of 0.55% when reversing the field. This behaviour of resistance as a function of the magnetic field is not straightforward to interpret. In the literature, typical examples of magnetoresistance in chiral systems of this kind exhibit a qualitative "S" shaped trend, with resistance increasing for positive field values and decreasing when the field is reversed (or vice versa), with the opposite situation for the other enantiomer [18], [323], [324]. In this case, an effect is certainly evident and well-distinguished given the mirror symmetry of the two curves. Specifically, the resistance decreases for both directions of the magnetic field (but to a lesser extent depending on the measured enantiomer).

#### 4.2.2.3 Conclusions

Based on the data and experience with the electropolymerization of PANI (as discussed in the previous Section, 4.2.1), this Section introduces an additional complexity to the system. PANI is electropolymerized in the bulk presence of a chiral inducer (enantiopure 10-camphor sulfonic acid). The supramolecular induction of chirality on the polymer chains has been successfully achieved, as evidenced by circular dichroism measurements, which show optical activity that is dependent on the enantiomer of the doping CSA used. Home-made devices were fabricated for characterizing the charge transport of the synthesized cPANI. The resistivity curves as a function of temperature closely match literature data, highlighting the transition from positive to negative temperature coefficient of resistance (TCR) as the temperature decreases. Lastly, the cPANI enantiomers are coupled with a ferromagnetic spin injector (Nickel) and subjected to magnetoresistance measurements at room temperature under an external magnetic field of up to 10,000 Oe in intensity. The behavior of resistivity as a function of the direction of the external magnetic field reveals a specular asymmetry for the two cPANI enantiomers, with different saturation values at +10 and -10 kOe. A more precise interpretation of the physics behind this effect is still under development. The immediate prospect is to use the cPANI described in this section as the "gate" electrode in the electrochemical transistor architecture (presented in the next section, 4.3). This is done to compare the performance of this chiral polymer with that of an achiral polymer (PCPDT-BT, *vide infra*).

## 4.3 Electrochemical transistor

### 4.3.1 Introduction

Bioelectronics is fuelling significant scientific endeavours in the development of enhanced biomedical devices, heralding innovative solutions for disease diagnostics and therapeutics [325], [326]. This transformative field is paving the way for groundbreaking innovations that bridge the gap between biology and electronics, offering new possibilities for healthcare solutions [327]. This advancement is primarily driven by the utilization of organic electrochemical transistor (OECT) sensors [328]. While a wide array of bioelectronic devices and architectures have been devised in recent decades, they share a fundamental concept based on the utilization of organic mixed ionic-electronic conductors (OMIECs). In contrast to conventional organic semiconductors, OMIECs can conduct both traditional electronic charge carriers, such as holes and electrons, and ionic ones, like cations and anions [329]. This unique property positions OMIECs as ideal materials to bridge the interface between the ionic signals produced in biological systems and the electronic outputs common in electronic circuits. Additionally, OMIECs offer several advantageous properties, including their synthesis from readily available elements, inherent mechanical flexibility, compatibility for operation in aqueous environments, and biocompatibility [330]. Consequently, OMIECs have found applications in various technologies, including electrophysiological recorders[331]–[333], metabolite sensors [334], [335], pathogen detectors [336], [337], actuators relevant to drug delivery systems and artificial muscles [338]–[341], and next-generation energy storage devices [342]–[344]. The concept of an electrochemical transistor (ECT) dates back to 1984 [345]. Since then, growing scientific interest in the ion sensing capabilities of these devices, as well as their potential for biocompatibility, has led to the proposal of numerous versions. However, the basic architecture almost always follows a well-defined and standardized design with three terminals: a source, a drain, and a gate electrode [346]. The channel material, an OMIEC, is situated between the source and drain electrodes and facilitates the transport of both electronic and ionic charges. Gold is commonly used for the source and drain electrodes due to its low work function of ≈5 eV, which results in a good energy level match for both hole and electron injection, as well as providing excellent ambient stability [347], [348]. The gate electrode can also be made of gold or other polarizable materials, such as conjugated polymers [349]. However, this necessitates a large gate electrode area to maximize the capacitance at the gate and ensure that the primary voltage drop occurs across the channel-electrolyte interface rather than at the gate-electrolyte interface. During the operation of an OECT, a voltage bias is applied between the source and drain electrodes ($V_{DS}$), which drives an electronic current through the active channel (source-to-drain current, $I_{DS}$) [350]. The magnitude of this current is modulated by an input voltage at the gate electrode ($V_G$), which controls the extraction or injection of ions from the electrolyte into the channel, thereby regulating the doping level of the channel material. Broadly, channel materials are categorized based on their ability to transport either holes (p-type) or electrons (n-type) as electronic charge carriers. The doping level of this material at zero gate bias results in a further classification of accumulation mode and depletion mode devices. In accumulation mode operation, the semiconductor remains undoped at zero gate bias (its OFF state), while applying a gate bias switches the device ON. The opposite is true for depletion mode devices. Our approach introduces a substantial modification to the typical experimental layout of the OECT. In the presented case, the organic semiconductor serves as the gate, whereas, in the traditional OECT layout, the electrolyte solution functions as the "gate". Therefore, the concept presented in this section is distinctly different, with the most apparent advantage being related to the organic semiconductor. Its nature and functionalization can be tailored to match different application fields. A key feature of our geometrical layout is the ability to conduct capacitive measurements as a function of the applied electrochemical bias, making use of the organic semiconductor acting as both the "gate" and "working electrode”. In our measurements, this dual role is fulfilled by the organic semiconductor PCPDT-BT. Its conductivity is probed through electrochemical impedance spectroscopy measurements and is tuned by electrochemical p-type doping. Specifically, positive charges are introduced into the polymer by applying an electrochemical oxidation potential, leading to the formation of "cation" PCPDT-BT units within the polymer structure, and therefore inducing a polaronic state. The connection between the enhanced conductivity of PCPDT-BT and its polaron state in the oxidative regime is demonstrated by in-situ and in-operando vibrational IR spectra recorded using an ATR configuration, which reveals significant IRAV vibrational responses, indicating a vibrational polaron signature. The kinetics of unbiased de-doping, that is, the relaxation from the doped to the undoped state without any applied bias, have also been characterized.

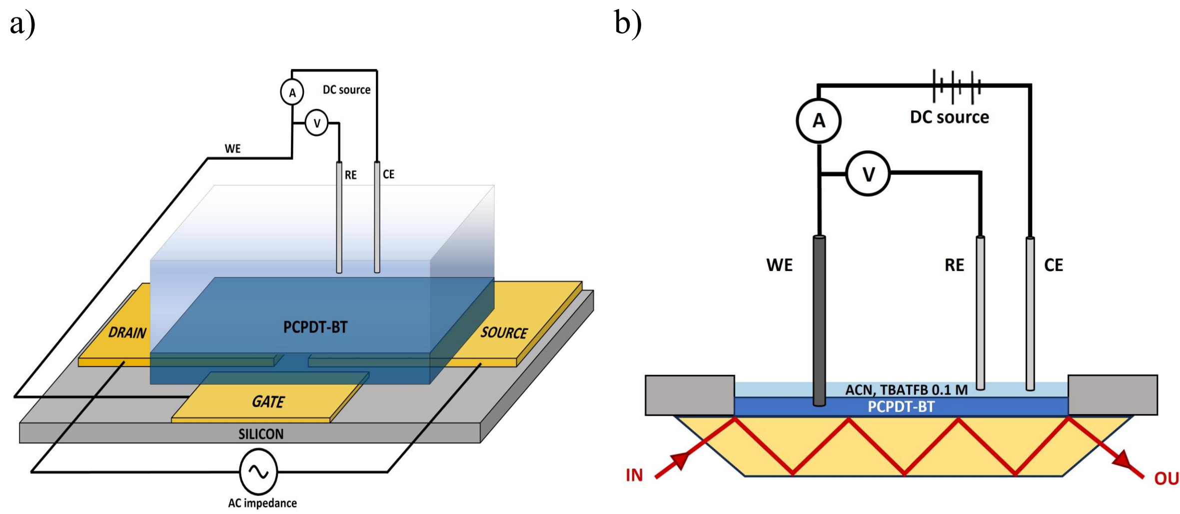

Figure 103 **a)** Schematic representation of the electrochemical-transistor architecture. A thin film of PCPDT-BT is drop-casted onto three gold pads. Two of these terminals serve as the source and drain contacts of the transistor, while the third terminal, the gate, is controlled by applying a direct current potential difference using a three-electrode electrochemical system (a Pt wire as the counter electrode, Ag/AgCl as the reference). **b)** Schematic representation of the experimental set up for “in-situ”/“in-operando” IR spectroelectrochemistry measurements. A dropcasted PCPDT-BT film is the WE. Ag/AgCl/KCl$_{(sat)}$ and a Pt sheet are the RE and CE, respectively. 0.1 M TBATFB is the base electrolyte in ACN.

Figure 104a presents a schematic representation of the measurement cell. Starting from the lower region, the solid-state device consists of a glass substrate (dielectric) on which there 3 gold pads are present (in a "T" design, with a 750 μm separation between the pads). A thin film of PCPTD-BT is dropcasted across these three Au pads. Two terminals serve as the source and drain electrical connections. The third terminal, also connected to the dropcasted PCPDT-BT (which serves as the gate), acts as the working electrode in a conventional three-electrode electrochemical cell, which also includes a platinum wire counter electrode and an Ag/AgCl/KCl$_{sat}$ reference electrode.

The thickness of the PCPDT-BT film falls within the range of 200 to 500 nm and can be controlled by adjusting the concentration of the PCPDT-BT solution and the choice of solvent. Modest variations in the thickness of the drop-casted film do not significantly affect conductivity, primarily due to the 2D PCPDT-BT film in direct contact with the source and drain electrodes.

Figure 104b depicts the experimental setup employed for “in-situ” and “in-operando” measurements of IR spectra during the electrochemical doping of PCPDT-BT (electrochemical oxidation regime). The doping state of a drop-casted PCPDT-BT film, approximately 1 μm thick, is regulated by applying an electrochemical potential bias using a glassy carbon (GC) rod in direct contact with the PCPDT-BT, which serves as the working electrode. The region immediately above the ATR crystal (zinc selenide) has slightly raised edges, which secure the crystal in position (a characteristic of the SPECAC ATR accessory). The space formed by these raised edges is utilized to create an electrochemical cell: a Pt wire functions as the counter electrode (CE), and an Ag/AgCl wire serves as the reference electrode, while a 0.1 M TBATFB solution in ACN acts as the base electrolyte.

### *4.3.2 Results*

#### 4.3.2.1 Electrochemical gating

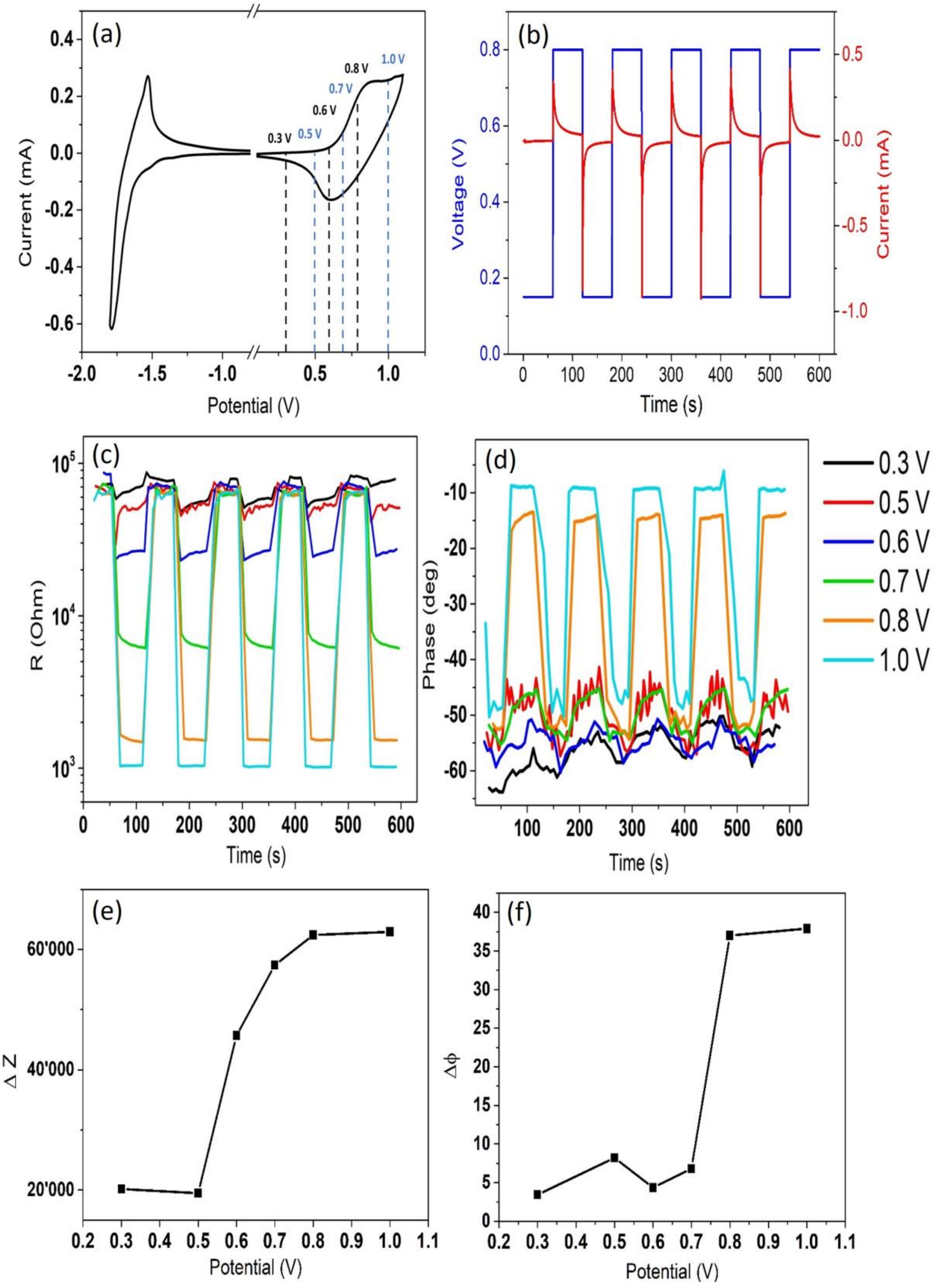

Figure 104 **a)** Cyclic voltammetry of a PCPDT-BT film dropcasted on GC electrode in a conventional three-electrode electrochemical cell. The setup consists of a GC|PCPDT-BT working electrode, a platinum wire counter electrode, and an Ag/AgCl/KCl$_{sat}$ reference electrode. A 0.1 M TBATFB solution in ACN serves as the base electrolyte, with a potential scan rate of 50 mV s$^{-1}$. **b)** Potential vs. time pattern applied to the PCPDT-BT in the electrochemical transistor configuration. For more details on the system setup, refer to Figure 104. **c)** and **d)** Time-dependent in-situ electrochemical impedance spectroscopy measurements. Impedance module and phase are plotted as functions of time. The perturbation signal consists of a sine wave with a constant frequency of 97.7 Hz and a 10 mV peak-to-peak potential difference. **e)** and **f)** Difference between Z and Φ values recorded for E$_{ini}$ and E$_{fin}$ of the applied potential cycles (values are extracted from panels c and d).

Figure 105 displays typical impedance measurements over time for the electrochemical transistor device illustrated in Figure 104. Figure 105a showcases the cyclic voltammetry of PCPDT-BT drop-casted on a glassy carbon electrode as an initial reference measurement. For visualization purposes, a break is present in the curve between -0.8 V and -0.1 V due to the absence of faradaic processes in this potential range (double-layer region). The CV obtained aligns with literature data [351]. Focusing on the oxidation regime (as we are investigating the p-type conductivity of PCPDT-BT), an onset of oxidation current is observed at around 0.65 V, resulting in a peak centered around 0.9 V. This corresponds to the oxidation of PCPDT-BT with the concurrent generation of hole polarons. During the return scan, the induced polaronic state relaxes, and the previously created "cationic" PCPDT-BT units return charge (reversible process), as evidenced by the reduction current peak at -0.6 V. Figure 105b presents a typical potential cycle applied to the gate of our electrochemical transistor for impedance measurements as a function of gating bias. Every 60 seconds, the potential is switched between a constant "off" value, E$_{ini}$ (corresponding to the un-doped state of PCPDT-BT), and a constant "on" value, E$_{fin}$. Suitable E$_{ini}$ and E$_{fin}$ potential values must be selected based on the CV pattern (Figure 105a). For all applied potential cycles, E$_{ini}$ = 0.1 V was chosen as the initial potential (as the current corresponding to this potential is nearly zero). The E$_{fin}$ value is varied in different measurements to determine the potential value that induces the doped state in PCPDT-BT. In the illustrative case of Figure 105b, an E$_{fin}$ value of 0.8 V is reported.

Figure 105c and d depict the resistance and the phase angle as a function of time at a constant frequency of 97.7 Hz, with a 5 mV peak-to-peak potential amplitude. the electronic state of PCPDT-BT, whether it is in an un-doped or doped state, is regulated by the potential applied to the electrochemical cell. This regulation involves 60-seconds potential steps, starting from an initial value (E$_{ini}$, which is consistently set at 0.1 V) and ending at a final value (Ef$_{in)}$. The potential value applied at the gate electrode (E$_{fin}$) is incrementally varied in 100 mV steps, ranging from 0.4 V to 1.0 V. Figure 105c shows that the source-to-drain resistance clearly exhibits modulation in response to the potential applied via the electrochemical cell. A distinct variation in resistance is observed between 0.6 V and 0.8 V. The resistance values at 0.8 V and 1.0 V are nearly coincident, indicating a doped electronic state induced in PCPDT-BT.

Figure 105d displays the phase vs. time (Φ vs. t) pattern corresponding to the same gating voltage cycles presented in Figure 105c. Notably, the phase values prove to be more sensitive to the doping of PCPDT-BT compared to the resistance values. Specifically, considering the black trace in Figure 105d, at low potential values (0.3 V), the phase values approach -90°, indicating that the system behaves almost like an ideal capacitor. Subsequently, for more positive potentials, the phase remains nearly constant, $45 < \phi < 65$ degrees, for 0.5, 0.6, and 0.7 V. The corresponding resistance behaviour as a function of the gating voltage (Figure 105c) does not clearly distinguish between a doped or un-doped state at 0.7 V. At this potential, the resistance is approximately $7 \cdot 10^3$, which falls between the curves at lower potentials and those at 0.8 and 0.9 V (these latter being almost identical). In contrast, the phase more precisely identifies the boundary between the pristine polymer and the polaronic state, exhibiting a sharp discontinuity only between 0.7 V (un-doped) and 0.8 V (doped). Figures 105e and 105f respectively depict the changes in resistance ($\Delta Z$) and phase ($\Delta\phi$) as a function of the gating voltage, highlighting the greater sensitivity of the imaginary part (phase) compared to the real part (resistance) of impedance.

In addition to the results shown in Figure 105, where impedance is recorded at the constant frequency of 97.7 Hz, Figure 106 presents impedance module and phase angle vs. time transients as a function of the perturbation potential frequency (17.7 Hz, 137.7 Hz, 997.7 Hz). The gating voltage is modulated in cycles of 60 seconds between $E_{ini} = 0.1\ V$ (un-doped state) and $E_{fin} = 0.8\ V$ (doped state).

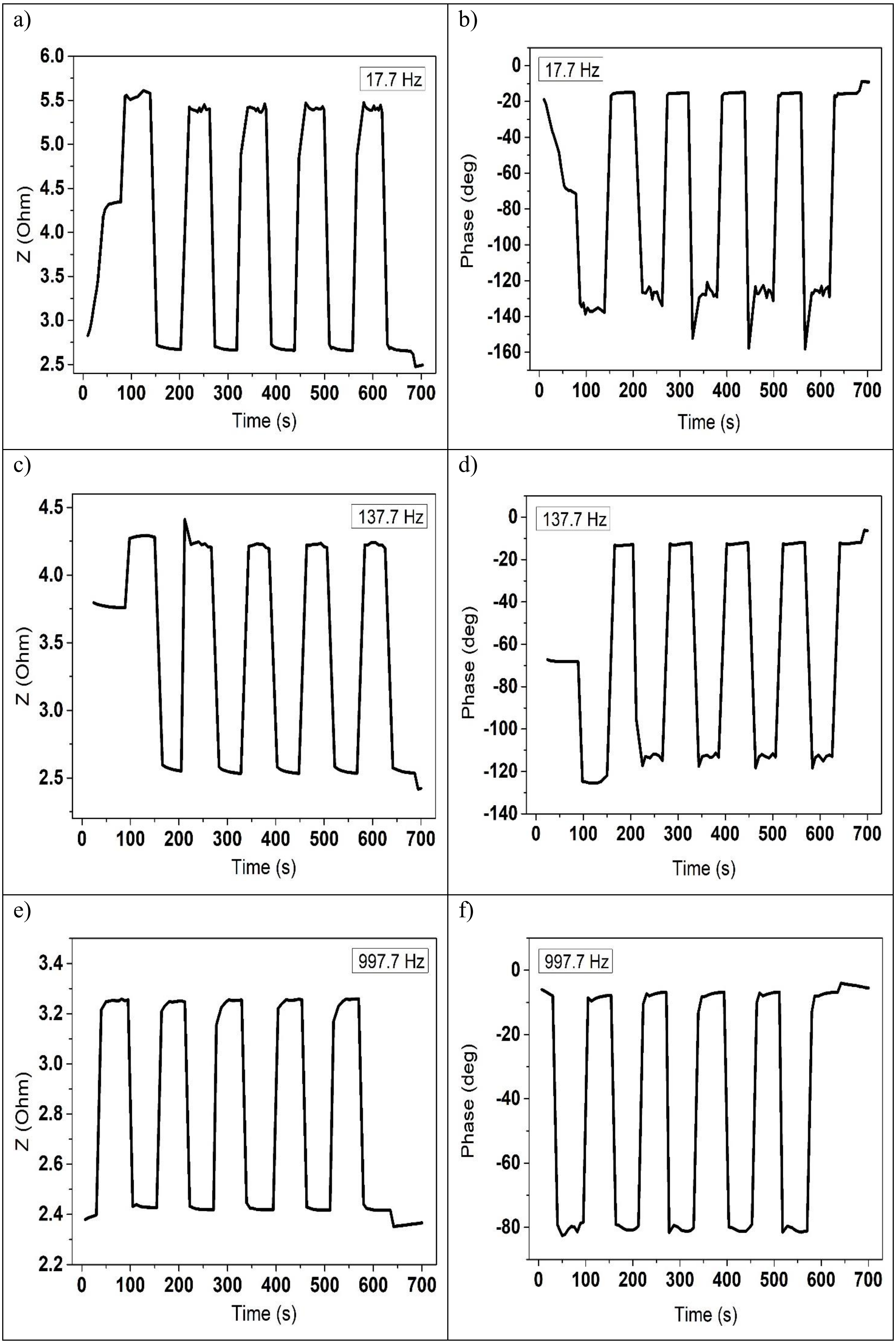
a)
17.7 Hz
Z (Ohm)
6.0
5.5
5.0
4.5
4.0
3.5
3.0
2.5
0
100
200
300
400
500
600
700
Time (s)
b)
17.7 Hz
Phase (deg)
0
-20
-40
-60
-80
-100
-120
-140
-160
0
100
200
300
400
500
600
700
Time (s)
c)
137.7 Hz
Z (Ohm)
4.5
4.0
3.5
3.0
2.5
0
100
200
300
400
500
600
700
Time (s)
d)
137.7 Hz
Phase (deg)
0
-20
-40
-60
-80
-100
-120
-140
0
100
200
300
400
500
600
700
Time (s)
e)
997.7 Hz
Z (Ohm)
3.4
3.2
3.0
2.8
2.6
2.4
2.2
0
100
200
300
400
500
600
700
Time (s)
f)
997.7 Hz
Phase (deg)
0
-20
-40
-60
-80
0
100
200
300
400
500
600
700
Time (s)

Figure 105 Time-dependent variations of impedance (Z) and phase (Φ) as a function of the applied gate voltage. Cycles of constant potential lasting 60 seconds at 0.1 V ($E_{ini}$) followed by 60 seconds at 0.8 V ($E_{fin}$) are applied to the system, and impedance is measured at different frequencies. **a)** and **b)** perturbation sine wave frequency of 17.7 Hz. **c)** and **d)** perturbation sine wave frequency of 137.7 Hz. **e)** and **f)** perturbation sine wave frequency of 997.7 Hz

Observing the trend emerging from Figure 106, it becomes evident that the difference in resistance between the un-doped and doped states decreases as the frequency of the perturbation signal is increased. This observation aligns with the concept that lower frequency impedance measurements preferentially probe interfacial properties, such as conductivity. In contrast, higher frequencies are better suited for investigating bulk properties. The usual frequency range for these measurements falls between 1 to 4 kHz, and generally, the frequency dependence is relatively small within this range. However, for values typically exceeding 10 kHz, the Debye-Falkenhagen effect becomes more pronounced. Notably, ionization in PCPDT-BT is more effective at the interface, in direct contact with the source and drain electrodes, as opposed to the bulk material.

#### 4.3.2.2 De-doping kinetics

The kinetics of the relaxation process from the doped to un-doped state in PCPDT-BT within our Electrochemical Transistor setup is of particular interest, as it complements steady-state conductivity measurements. To investigate this process, the polymer film is polarized to various potential values, and after ≈ 110 seconds of polarization, the system is allowed to relax to its undoped state, corresponding to the open-circuit potential (OCP).

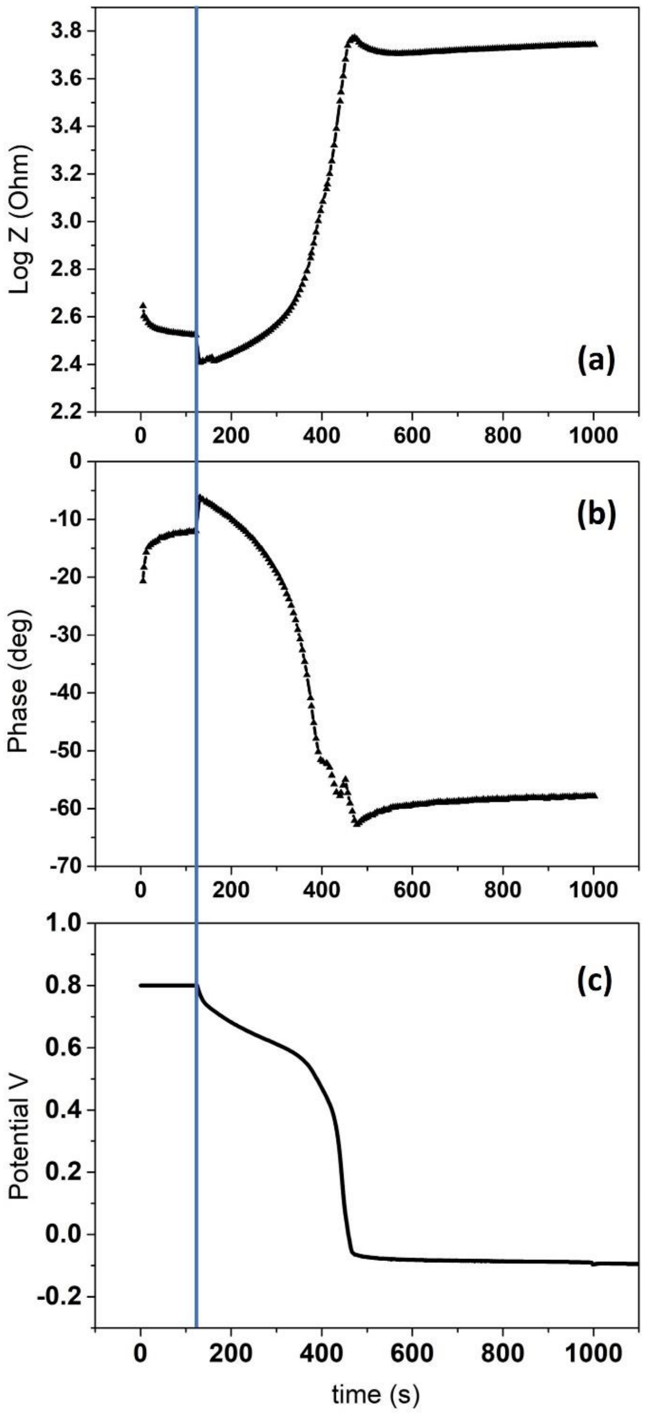

Figure 106 De-doping kinetics: impedance **(a)**, phase **(b)**, and potential of the system **(c)** are displayed as functions of time. At $t \cong 110$ seconds, the constant potential of 0.8 V applied at previous times is disconnected (blue vertical line in the figure). Subsequently, the system is allowed to relax, and the synchronization in the de-doping kinetics of PCPDT-BT for the different variables is shown.

Figure 107 presents the impedance module (Z module), phase angle (Φ), and circuit potential (V) vs. time transients in panels a, b, and c, respectively. In this specific case, the doping bias was set to 0.8 V, as evident from panel c.

At 110 seconds, the potential is disconnected, resulting in a discontinuity in all three curves. Examining the behaviour of the phase angle, it is clear that it provides a more physical and sensitive insight into the state of the system. The Z vs. time pattern appears to be a relatively regular increasing function of time. Two features are noteworthy: an initial decrease in Z and an over-shoot just before reaching the final steady-state plateau value of approximately 5 Kohm. Regarding the Φ vs. t transient, two distinct oscillations are observed around 400 seconds. These oscillations are attributed to a genuine intrinsic system process, as they are consistently found in other measurements, and careful experimental setup ensures that they are not caused by artifacts.

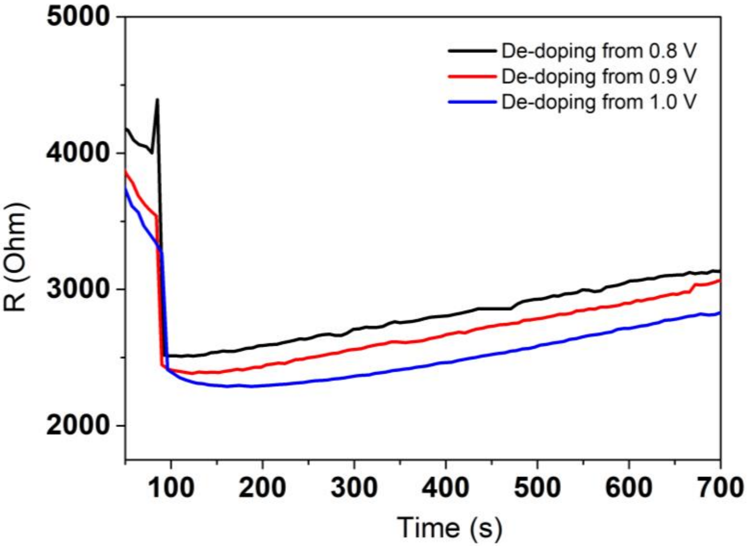

Figure 107 Transient relaxation of resistance over time. The kinetics of de-doping from different electrochemical doping potential values (different $E_{fin}$) are compared. Black trace: de-doping from 0.8 V; red trace: de-doping from 0.9 V; blue trace: de-doping from 1.0 V.

Figure 108 presents relaxation transients recorded for different bias values. The kinetics exhibit essentially the same qualitative pattern, indicating that the doped-to-undoped relaxation kinetics appears to be independent of the electrochemical potential. This behaviour suggests that once a threshold bias value is applied to the system, the doped state becomes essentially a “saturated” positively charged state. Secondly, this implies that the relevant rate-determining step is associated with the spatial rearrangement of ions in the double layer i.e. relaxation of polarization concentration due to ionic diffusion in the double layer region.

#### 4.3.2.3 Polaron IRAV giant response

Figure 109 presents IR spectra recorded in ATR mode for thin films of PCPDT-BT in both the un-doped and doped states.

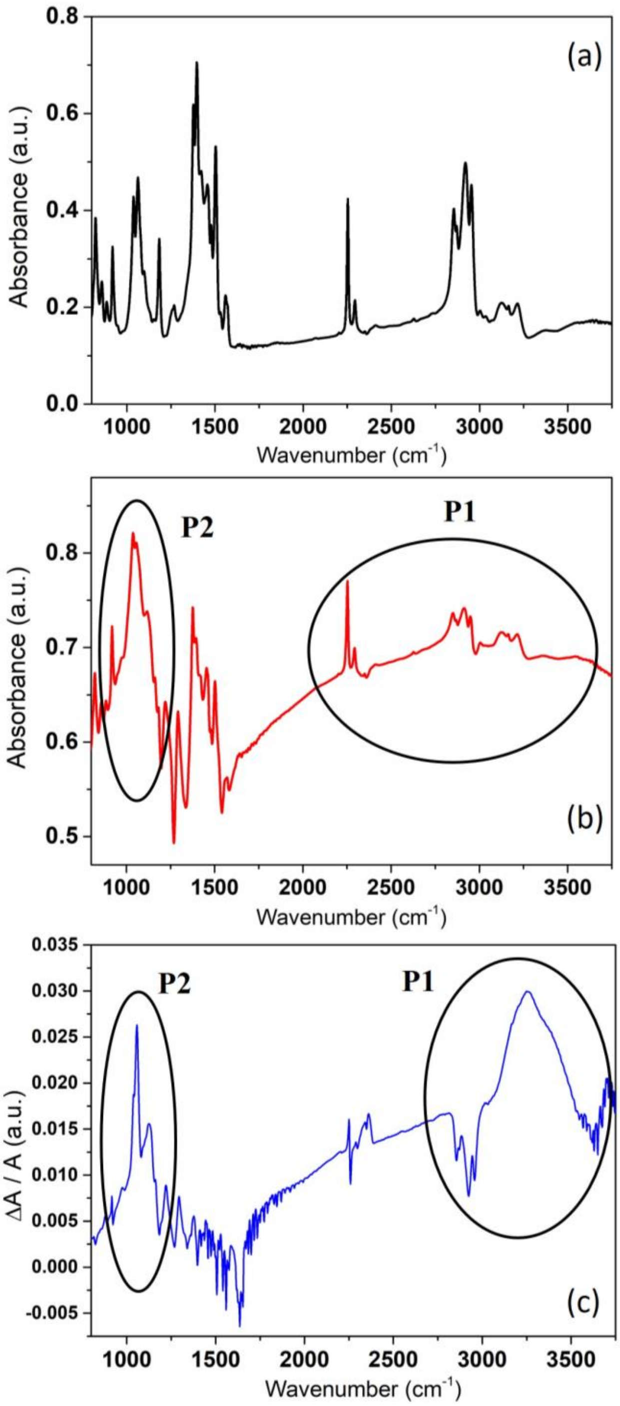

Figure 108 IR spectra of the PCPDT-BT in different oxidation states **a)** un-doped **b)** chemically doped **c)** electrochemically doped.

In Figure 109a, the IR spectrum in the 900 to 4000 cm$^{-1}$ range is shown for the pristine PCPDT-BT film (black trace). This film is directly drop-casted onto the ZnSe crystal of the ATR from a 10 mM DCM solution, and its thickness falls within the range of 1-2 µm. The overall pattern is in perfect agreement with literature data [352]. Figure 109b displays the spectrum of the same film investigated in panel (a) after exposure to iodine vapor ($I_2$, red trace). In contrast to the previous spectrum, there is a noticeable change in the IR signal. A prominent, broad peak is observed around 3200 $cm^{-1}$ (3125 nm), labeled as P1 in Figure 109b. Another significant change occurs at around 1050 $cm^{-1}$ (9523 nm), where a high-intensity structure (labeled as P2) is evident. The band at 1400 $cm^{-1}$ of the polymer is assumed as the reference, in line with the normalization practices employed in the scientific literature for PCPDT-BT IR spectra [353], [354]. It is, therefore, possible to observe that, in panel (b) the relative intensity of the peak at 1050 $cm^{-1}$, which in panel (a) had an intensity approximately half that of the reference peak at 1400 cm-1, is now roughly twice as intense compared to the baseline of absorption. The latter P2 peak is assigned to the so called IRAV giant mode, due to the PCPDT-BT polaron, while the broader P1 structure is the electronic signature of the polaron. Fig. 109b results, obtained by chemical doping of the PCPDT-BT film, serve as a reference for a direct comparison with the spectrum measured by applying an electrochemical bias "in situ" to the PCPDT-BT (FTIR spectroelectrochemistry), corresponding to the electrochemical p-doping of the polymer. Figure 109c displays the IR differential absorbance ($\Delta A/A$) for the electrochemically doped PCPDT-BT deposit (please compare Figure 104b and Section 5.2.10 for the experimental details). A constant potential of 0.9 V (vs Ag/AgCl/KClsat) is applied to the PCPDT-BT film, which serves as the working electrode (WE) in a 3-electrode electrochemical cell. The spectrum recorded in this configuration is processed by subtracting the corresponding spectrum of the neutral polymer (i.e., the system under open-circuit potential conditions, with no applied potential). The structural features associated with the vibrational (P2) and electronic (P1) signature of the polaron are also present in this case (Fig. 109c, blue trace) and closely correspond to the spectrum in Figure 109b (chemical doping, red trace).

Overall, there is a remarkable correlation between cyclic voltammetry/impedance measurements results (electrochemical transistor configuration, as illustrated in Fig. 104a, and IR spectra featuring the application electrochemical potential. When potential values exceed 0.7 V, identified as the doping threshold potential, impedance results exhibit a significant boost in conductivity, accompanied by the appearance of the characteristic giant IRAV mode at around 1100 $cm^{-1}$ in the IR spectrum. Therefore, a comparison of electrochemical outcomes, impedance measurements, and IR vibrational measurements suggests that the enhanced conductivity in the doped state can be attributed to the presence of the PCPDT-BT polaron.

### *4.3.3. Conclusions*

This work introduces a novel device that combines a solid-state transistor layout (with source, drain, and gate) with an electrochemical system. In this innovative setup, a well-studied organic semiconductor, PCPDT-BT, serves as a crucial component, acting as both the gate in the solid-state transistor and the working electrode in the electrochemical cell. The electronic state of the gate, whether it's doped or undoped, is controlled through electrochemical polarization. The source-to-drain conductivity is quantified using impedance spectroscopy. This conductivity is unequivocally assigned to the polaron induced in the PCPDT-BT upon electrochemical polarization, as it is shown by recording ATR IR spectra in both electrochemical "*in-situ*"/"*in-operando*" conditions and via chemical doping (iodine doping). The original electrochemical transistor setup proposed here has the potential for various applications in both scientific and technological fields. Notably, it holds promise as a sensor device, given its sensitivity to analytes in solution, which can be controlled directly through the electrochemical potential applied to transition between undoped and doped electronic states of the organic semiconductor. Moreover, aside from conductivity (essentially an amperometric-based measurement), the phase of the impedance exhibits remarkable sensitivity to the state of the organic semiconductor. This feature could be harnessed to create a capacitor-based sensor device.

## 4.4 Influence of Chiral Compounds on the Oxygen Evolution Reaction (OER) in the Water Splitting Process

### *4.4.1 Introduction and motivation*

While the majority of the experimental work presented in this thesis focuses on charge transport through organic chiral structures, our laboratory has concurrently explored the implications of CISS at the inorganic level. The precise understanding of the source of chirality in inorganic materials, including metals and semiconductors, is still an evolving field, and the concept of "chiral imprinting" has gained significant relevance in this field over the last decade (please refer to the Theoretical Background Section dedicated to chirality, Section 2.3). In the realm of research on charge transport through inorganic chiral interfaces, the "zero step" involves inducing chirality into the system. In this regard, we have pursued two complementary approaches in our research:

In collaboration with my laboratory colleague, Mirko Gazzotti, we achieved a preliminary milestone by producing a chiral Nickel electrode using a co-deposition approach with a bulk chiral agent (which was embedded within the bulk ferromagnetic electrode), in this case, tartaric acid. Results regarding this electrodeposited chiral ferromagnetic Nickel electrode (cNickel) were initially presented in a 2018 Electrochimica Acta article (in which I participated in some experimental measurements during my MSc studies) [161]. In this work, the impact of supramolecular chiral imprinting on the performance of the Nickel electrode is characterized with respect to the reversible nickel oxidation reaction, as a function of the orientation of an external magnetic field (in a classic paradigm of Spin-Dependent Electrochemistry, please compare Figure 110). This field was subsequently expanded upon with a comprehensive characterization in 2021 in Applied Physics Letters (including magnetoresistance measurements) [73].

A second complementary electrochemical approach, which had already been explored in 2018 and is significantly expanded upon here, involves using a chiral compound in bulk solution to induce spin polarization on the surface of the ferromagnetic working electrode. One advantage of this approach is that charge transfer can be directly studied in relation to the (possible) redox reactions of the bulk chiral molecule.

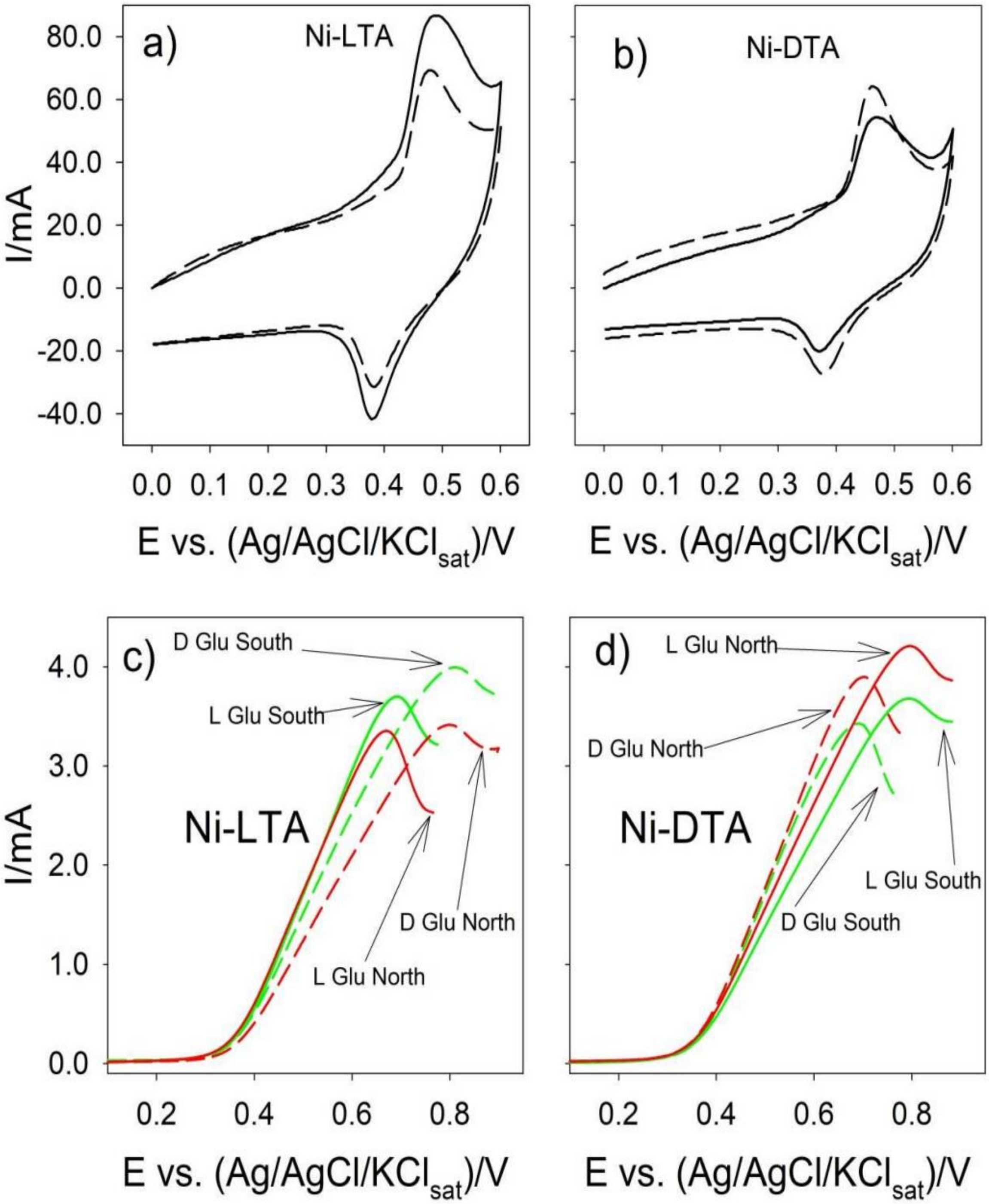

Figure 109 CV curves in 0.1 M KOH aqueous solution: **a)** Ni co-deposited with L-TA acid WE **b)** Ni co-deposited with D-TA WE. Solid line: electrodeposition on the south pole of the magnet. Dashed line: electrodeposition on the north pole of the magnet. **c)** Ni-LTA WE, north and south, in enantiopure solution of 0.1 M L-glu or D-glu. **d)** Ni-LDA WE, north and south, in enantiopure solution of 0.1 M L-glu or D-glu. Solid red line: L-glu on north. Dashed red line: D-(+)-glucose on north. Solid green line: L-glu on south. Dashed green line: D-(+)- glucose on south. Reprinted with permission from ref [161].

In this section, we present results related to a second-order effect linked to CISS, which holds significant technological importance: catalyzing water electrolysis through spin control. The positive impact on WS due to the spin-filter effect has already been demonstrated using a more "classic" experimental archetype, which involves electrodes coated with chiral molecules. Significant results have been achieved by aligning the spin of reactants, both in terms of reducing the overpotential required for OER and suppressing undesired parasitic reactions, such as the production of hydrogen peroxide (a comprehensive overview of the state-of-the-art on the influence of spin control on the OER mechanism and outcomes can be found in the Theoretical Background, Section 2.3).

The novelty introduced by these results lies in observing such catalytic effects on the OER (albeit to a lesser extent) using bulk chiral agents rather than those adsorbed on the electrode (bulk and non-interfacial effect). The bulk chiral environment is achieved by employing chiral molecules in the electrolyte solution. In this context, the performance of a ferromagnetic electrode (Nickel) is compared with that of a stainless-steel electrode (Steel AISI 316L). In the case of the Nickel electrode, the ferromagnetic material acts like a spin-injector as a function of the substrate magnetic field; while in the case of the steel electrode, the possible spin filtering is achieved only from the bulk solution chiral environment.

### *4.4.2 Steel AISI 316L*

#### 4.4.2.1 L-(+)-Tartatic Acid

Figure 111 shows cyclic voltammetry curves, obtained as a function of different concentrations of bulk L-(+)-tartaric acid, on the stainless steel working electrode. In both the forward and backward curves, the current is nearly negligible in the 0.0 to 0.6 V range. In the case of the base electrolyte solution (blue curve, Figure 111), at potential values larger than 0.6 V the current starts to increase almost linearly until reaching a final 2.5 mA value at 0.8 V. Tartaric acid 0.5 mM solution (green curve, Figure 111) shows a lower current, 2.4 mA, at 0.8 V. Tartaric acid 5 mM solution (red curve, Figure 111) shows an initial higher current but at the potential where the OER occurs (around 0.8 V) the current is lower when compared with the previous ones. Tartaric acid 25 mM solution (black curve, Figure 111) shows the lowest current, 1.2 mA, at 0.8 V. The current appears to be correlated to the concentration of the chiral compound with an inverse proportionality. The inset of Figure 111 presents a more detailed CV, in the 0.5 to 0.75 V potential range. The inset shows a small but neat difference between the forward and backward scans. The current for the KOH base electrolyte solution is always higher than the one measured in presence of tartaric acid.

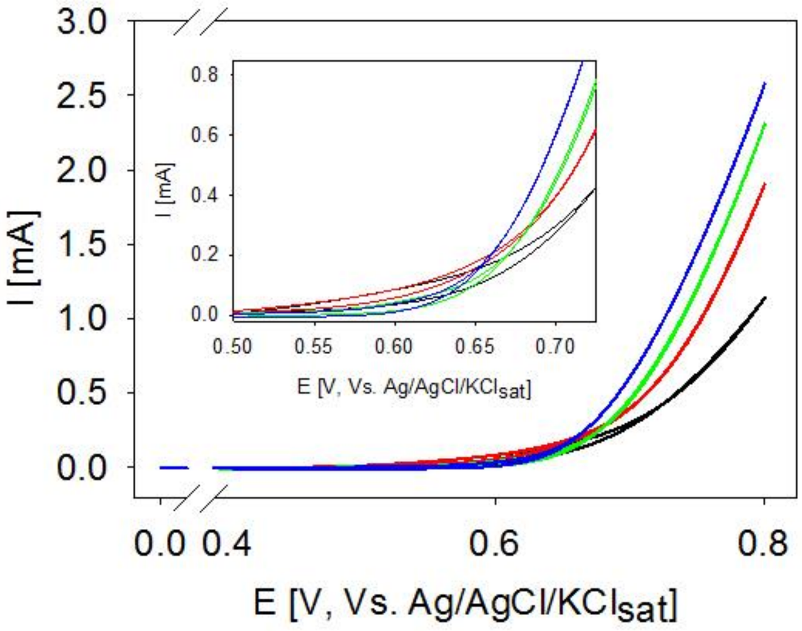

Figure 110 Cyclic voltammetry curves recorded on a steel AISI 316L working electrode (WE). 50 mV/s potential scan rate, Pt sheet as counter (CE) and Ag/AgCl/KClsat as RE. KOH 0.1 M aqueous solution is the base electrolyte. L-(+)-tartaric acid concentration: (blue) 0 mM, (green) 0.5 mM, (red) 5 mM, (black) 25 mM. The inset shows the CV detail in the 0.5 and 0.75 V potential range.

#### 4.4.2.2 . L-(−)-Aspartic Acid

Figure 112 shows CVs in solutions with different concentrations of L-(−)-aspartic acid. Qualitatively, CVs pattern is quite similar to that shown in Figure 111. Quantitatively, all the tartaric acid solutions at different concentration feature a lower current with respect to that of the base electrolyte. Note that no peaks are evident in the backward scan, indicating that any reaction (OER) occurring during the forward scan (oxidation regime) is irreversible.

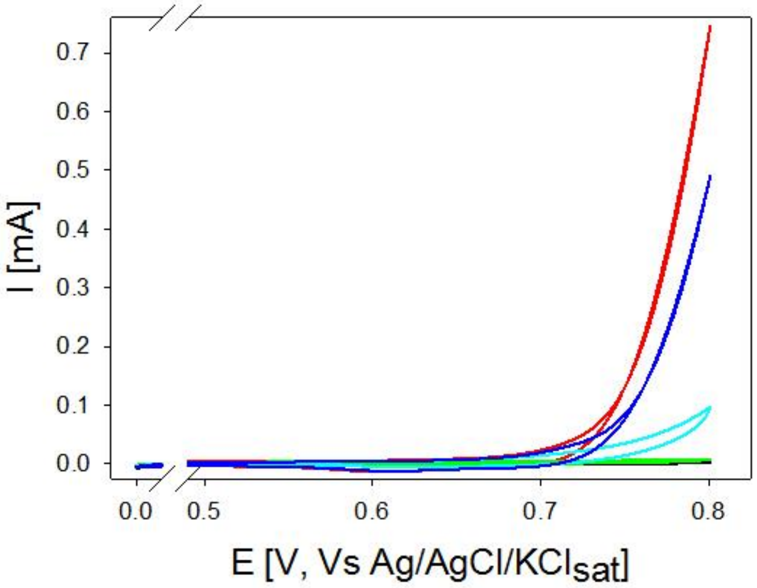

Figure 111 Cyclic voltammetry curves recorded on a steel AISI 316L WE. 50 mV/s potential scan rate, Pt sheet as CE and Ag/AgCl/KClsat as RE. KOH 0.1 M aqueous solution is the base electrolyte. L-(−)-aspartic acid concentration: (red) 0 mM, (blue) 1 mM, (light blue) 10 mM, (green) 50 mM, (black) 100 mM.

In general, concerning the Fig. 111 and Fig. 112 CVs (recorded by using a stainless steel anode), it can be concluded that the L-(+)-tartaric acid and L-(−)-aspartic acid exert a blocking activity on the electrode. The anodic current is found to decrease in response to an increase in the concentration of the acid in the solution. Probably this effect is due to simple coulombic attraction between the anode (charged positively) and the relevant acid anion, which can be adsorbed on the surface eventually leading to a decrease in the overall current.

#### 4.4.2.3 D-(+)-Glucose

Figure 113 shows CVs as function of the concentration of D-(+)-glucose. A systematic variation in the current as a function of the D-(+)-glucose concentration is noted. The maximum efficiency, obtained comparing the current response at fixed potentials, is found for the 10 mM D-(+)-glucose concentration (green curve, Figure 113). The KOH base electrolyte solution is characterized by the lowest current values (red curve, Figure 113).

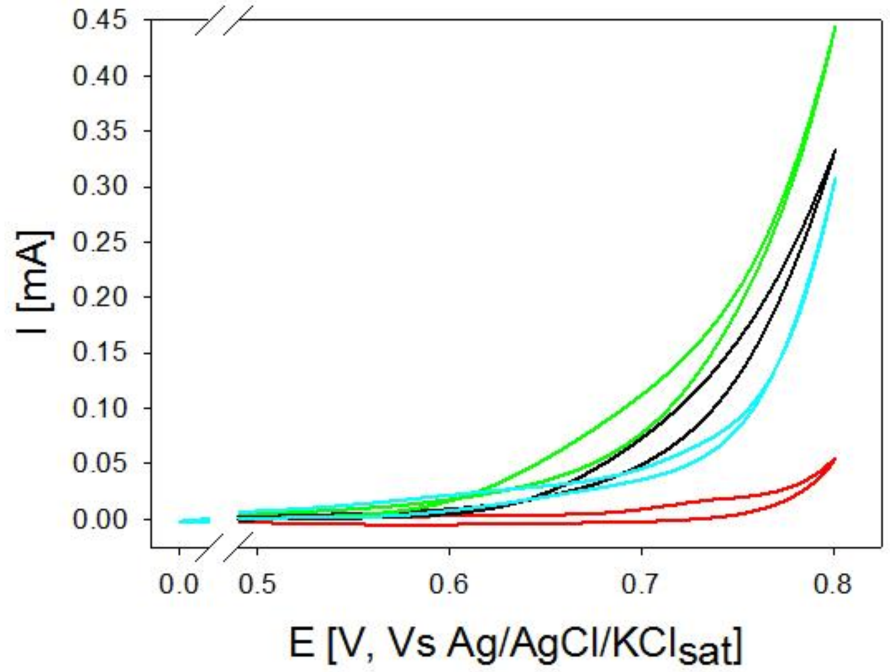

Figure 112 Cyclic voltammetry curves recorded on a steel AISI 316L WE. 50 mV/s potential scan rate, Pt sheet as CE and Ag/AgCl/KClsat as RE. KOH 0.1 M aqueous solution is the base electrolyte. D-(+)-glucose concentration: (red) 0 mM, (light blue) 1 mM, (green) 10 mM, (black) 100 mM.

A non trivial electrochemical behavior is found when the D-(+)-glucose is present in the solution, Figure 113. The current is always found to be larger than that of the base electrolyte, and in terms of efficiency the current increases as a function of the concentration until 10 mM, then starts to decrease for larger concentrations (compare black line, 100 mM, Figure 113).

### *4.4.3 Nickel electrodeposited on magnet*

#### 4.4.3.1 D-(+)-Glucose

Figure 114 shows the cyclic voltammetry of Ni electrodeposited on the north surface of a permanent magnet used as working electrode in two different solutions: D-(+)-glucose 0.1 M in base electrolyte (KOH 0.1 M) and bare base electrolyte. The experimental set-up is the one with the Teflon cell described in Section 5.2.1. Note that values in Figures 114 and 115 are normalized to point out the differences between the current in the solution with the chiral compound and the one with only the support electrolyte KOH. The value that has been used to normalize the data was the current associated to the oxidation of the Ni surface, otherwise the current peak, in the forward scan, in the base electrolyte curve. In the case of pure electrolyte

KOH solution (red curve, Figure 114) the Ni peaks are evident, with the oxidation one happening at 0.55 V in the forward scan while during the backward scan the reduction peak splits in two smaller peaks, one at 0.39 V and the other at 0.46 V. Otherwise, the curve describing the current in the solution containing the chiral compound is completely different, resulting more like the one found with the stainless steel electrode (Figure 113). In particular, the D-(+)-Glucose curve doesn't have the peaks of the Ni nor in forward nor in backward scan. The absence of peaks in the glucose's curve means that the redox process became irreversible if the glucose is added to the KOH solution. The anodic peak current in the solution containing the chiral compound results being 50% higher than the one measured with only the support electrolyte.

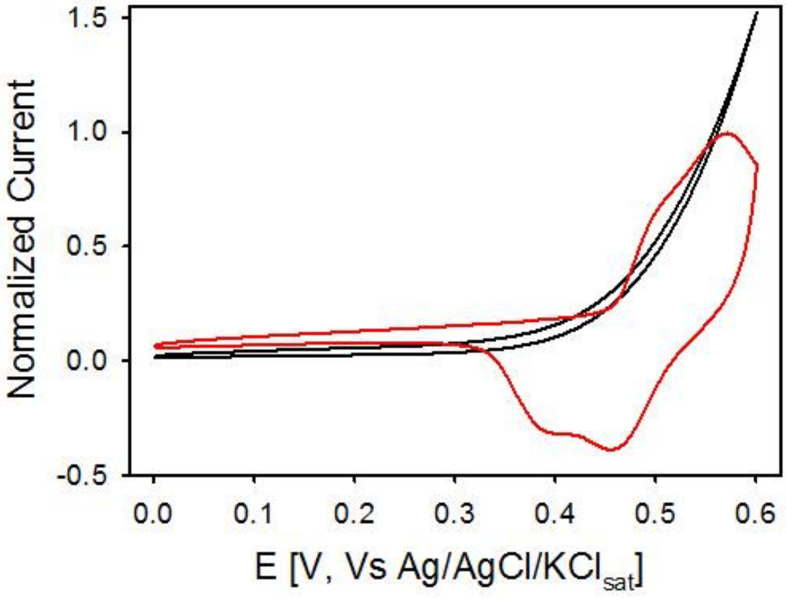

Figure 113. Normalized cyclic voltammetry curves recorded with electrodeposited Ni on the North pole of the magnet. Red curve: KOH 0.1 M aqueous solution. Black curve: 0.1 M of D-(+)-Glucose in KOH 0.1 M aqueous solution. 50 mV/s potential scan rate, a Pt as CE, Ag/AgCl/KClsat as RE.

Figure 115 shows the cyclic voltammetry measured on Ni electrodeposited on the south pole of the permanent magnet used as working electrode; those experiments were carried out with the same solutions of Figure 114, in the same operative conditions. Also in this case D-(+)-Glucose CV curve does not show the characteristic peaks associated to the oxidation and the reduction of the Ni. For what concerns the support electrolyte, the graph shows one peak at 0.55 V in oxidation and one peak and a shoulder in reduction at 0.37 V and 0.45 V respectively, coherent to what has been already seen in Figure 114. Also, in Figure 115 the data relevant to the current, ordinate axis, have been normalized using the value of the current associated to the oxidation peak of the support electrolyte. In comparison to Figure 114, the current of the solution containing the chiral compound is lower in the south pole, resulting having the maximum current in oxidation almost equal to the one measured with the support electrolyte.

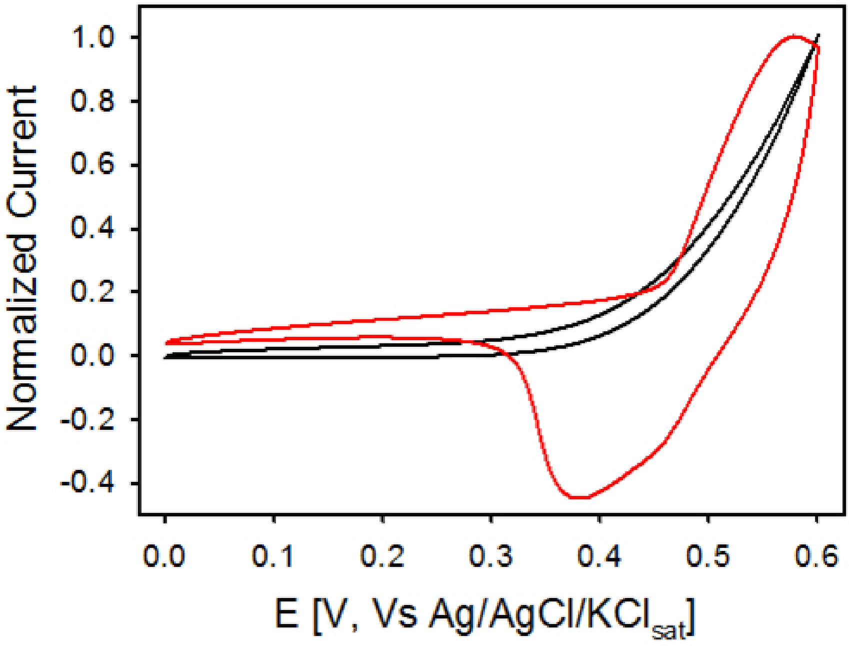

Figure 114 Normalized cyclic voltammetry curves recorded with electrodeposited Ni on the south pole of the magnet. Red curve: KOH 0.1 M aqueous solution. Black curve: 0.1 M of D-(+)-Glucose in KOH 0.1 M aqueous solution. 50 mV/s potential scan rate, Pt as CE, Ag/AgCl/KCl as reference electrodes (RE).

Figure 116 shows the comparison between CVs collected with a Ni electrode on top of north and south magnet polarities, recorded in a wider potential range. Remarkably, at 1.2 V it is present a peak for both the curves and the north pole peak current of the oxidation process is larger than the south pole corresponding value.

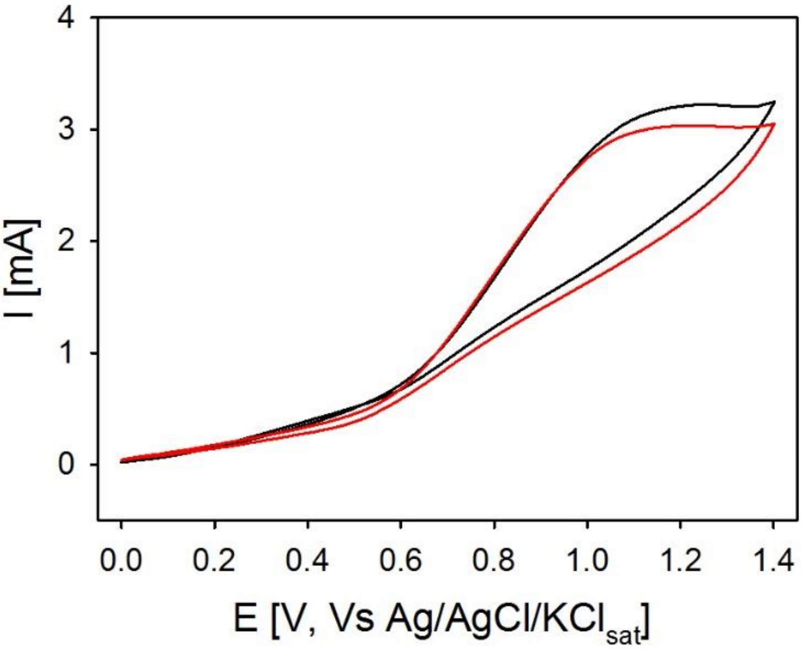

Figure 115 Comparison between cyclic voltammetry curves recorded with electrodeposited Ni on both poles of the magnet. Red curve: South pole with 0.1 M of D-(+)-Glucose in KOH 0.1 M aqueous solution. Black curve: North pole with 0.1 M of D-(+)-Glucose in KOH 0.1 M aqueous solution. 50 mV/s potential scan rate, Pt as CE, Ag/AgCl/KCl as RE.

### *4.4.4 Step and Sweeps*

#### 4.4.4.1 Step and Sweeps on AISI 316L

Step and sweeps were performed using the AISI 316 L steel sheet as working electrode, with the L-(+)-tartaric acid present in bulk solution, reported in Figure 117. The applied potential program as a function of time features a first potential ramp from 0 to 0.75 V at a 50 mVs$^{-1}$ scan rate, followed by eight +0.01 V potential steps, up to 0.83 V. The potential was maintained constant for 10 s before the next step. Tartaric acid concentration 0.5 and 5 mM in bulk solution was used. In the measurements where tartaric acid is added to the solution, a significant increase in the current was observed, indicating a more efficient method of oxygen production. Indeed, visual observation of the anode shows that the oxygen evolution occurs at more negative (smaller) potentials, anticipating the OER between 20 to 30 mV with respect to the pure KOH base electrolyte solution. The comparison of various experiments using this configuration is presented in Table B1. All the B tables presented in Appendix B provide experimental results for dozens of different measurements related to this section, all conducted as physically separate experiments.

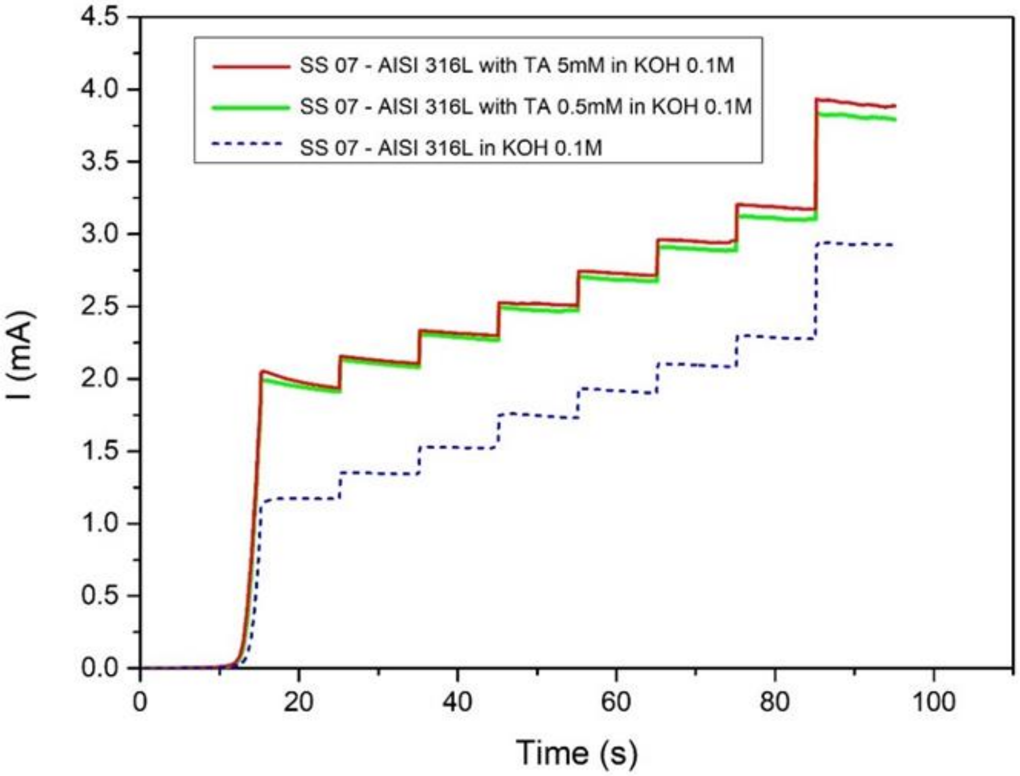

Figure 116 Step and sweeps curves recorded on a steel AISI 316L WE, Pt sheet as CE and Ag/AgCl/KClsat as RE. KOH 0.1 M aqueous solution is the base electrolyte. A potential ramp from 0 to 0.75 V at a 50 mV/s was applied, followed by eight +0.01 V potential steps, up to 0.83 V. The potential was maintained constant for 10 s between each step. L-(+)-tartaric acid concentration: (blue dash) 0 mM, (green) 0.5 mM, (red) 5 mM.

### 4.4.4.2 Step and Sweeps on Nickel

Stepped potential sweeps experiments were recorded also exploiting a ferromagnetic electrode in tight contact with a magnet: The Ni electrodeposited on magnet (Ni-on-magnet) electrode. This to possibly maximize the spin-injection efficiency. Figure 118 shows the anodic current recorded as a function of time: Measurements have been carried out with L-(+)-tartaric acid present in bulk solution, as well as with the pure 0.1 M KOH base electrolyte for reference purposes. The applied potential program as a function of time features a first potential ramp from 0 to 0.70 V at a 50 mVs$^{-1}$ scan rate, followed by +0.01 V potential steps, maintained constant for 15 s. The tartaric acid concentration is 0.5 mM in bulk solution. Results show two different situations depending on the orientation of the substrate magnet. In fact, when the Nickel sheet lays on the south pole of the magnet, the oxidation current results slightly higher for the TA solution than the KOH alone; moreover, a huge current increase can be observed between the chiral solution and the basic one when the North pole of the magnet is used. A significant increase in the current is found, which reflects a more efficient way to produce oxygen. Indeed, for both the North and the South magnet pole visual observation of the anode shows that the oxygen evolution occurs at more negative (smaller) potentials, anticipating the OER between 30 to 50 mV with respect to the pure KOH base electrolyte solution (please compare Table B1 in Appendix B).

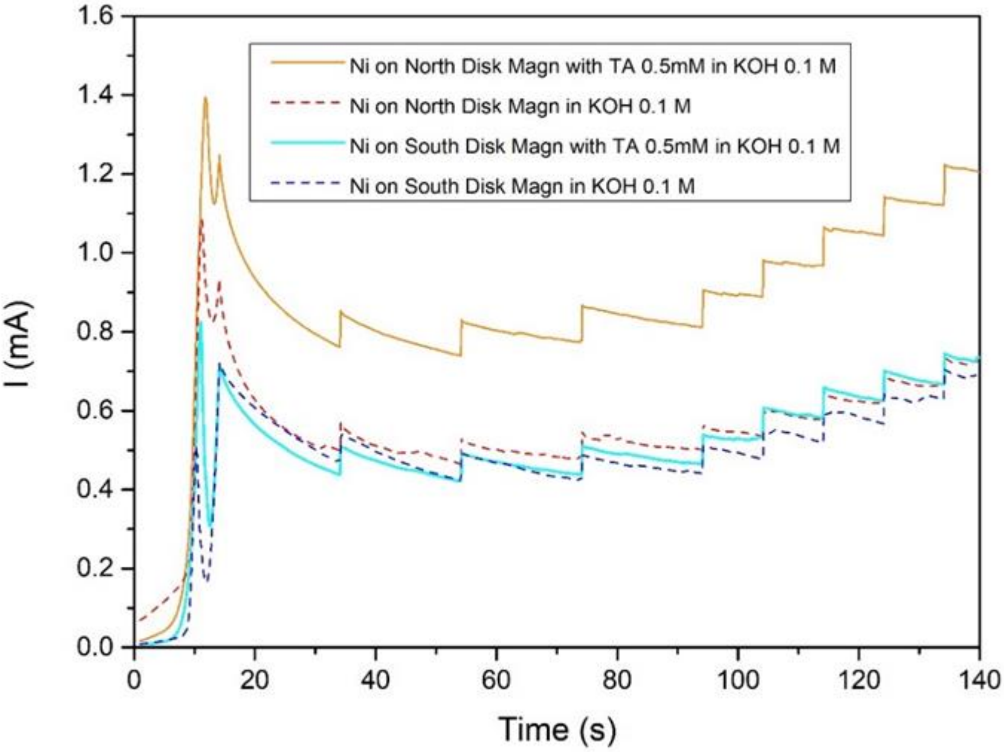

Figure 117 Step and sweeps curves recorded on a Ni deposited on magnet working electrode, a Pt sheet is the CE, Ag/AgCl/KCl is the RE. KOH 0.1 M aqueous solution the base electrolyte. First a potential ramp from 0 to 0.70 V at a 50 mV/s was applied, followed by eight +0.01 V potential steps, up to 0.78 V. The potential was maintained constant for 15 s between each step. L-(+)-tartaric acid concentration: (blue dash) South mag orientation 0 mM, (red dash) South mag orientation 0 mM, (light blue) South mag orientation 0.5 mM, (orange) North mag orientation 0.5mM.

In the case of the L-(+)-tartaric acid, Figure 118, the current recorded in response to potential step and sweeps in the presence of the bulk chiral compound is always larger than that of the base electrolyte. In this peculiar case, the effect of the presence of the chiral compound in bulk solution has been investigated by comparing the peak current values as a function of the magnet orientation (North vs. South), showing significant differences in the values of the current obtained at a fixed potential. Such an analysis is a crucial issue in unravelling the role of the spin. Moreover, to obtain a complete picture, the electrochemical results can be compared for the two enantiomers. Altogether four different situations are to be quantitatively compared: 1)

L-(+)-tartaric acid North 2) L-(+)-tartaric acid south 3) D-(−)-tartaric acid north 4) D-(−)-tartaric acid south. Table B2, B3, B4, and Table B5 report, in the most synthetic way, the current results obtained performing CVs in all four cases (Appendix B). Moreover, Table B6 and Table B7 aim to present in a clear and simple way, as much as possible, the catalytic effect observed in the different combination of enantiomers and the magnet pole. In particular, the sign found in column titled "sgn (Jratio North − Jratio South)" (Table B6 and Table B7, Appendix B) exhibit what is the most efficient combination. Remarkably, the L-(+)-tartaric acid North is more effective than L-(+)-tartaric acid South in a consistent way, while the D-(−)-tartaric acid south combination is found more effective than the D-(−)-tartaric acid North (coherently with the results of the step and sweeps). In the case of the glucose, only the D-(+)-glucose enantiomer was examined and it is found that the current for the D-(+)-glucose north combination is larger than the D-(+)-glucose south one, Figure 114 and Figure 115. Please note that due to fluctuations in the base electrolyte CVs, in Figure 114 and 115 normalized data are presented. Table B8 and Table B9 report the percentage of spin polarization of currents in the experiments carried out on the different Ni surface deposited on the poles of the magnet. Those values are calculated with the formula presented below:

$$\frac{\left(\frac{J_{(Tart)}}{J_{(KOH)}}\right)_{(North)} - \left(\frac{J_{(Tart)}}{J_{(KOH)}}\right)_{(South)}}{\left(\frac{J_{(Tart)}}{J_{(KOH)}}\right)_{(North)} + \left(\frac{J_{(Tart)}}{J_{(KOH)}}\right)_{(South)}} = SP\%$$

### *4.4.5 Conclusions*

This work explored the influence of chiral compounds in bulk solution on the hydrogen production process pursued via water electrolysis, often addressed as "water splitting". To this end two different electrode materials (steel and Ni) and three organic chiral compounds (tartaric acid, aspartic acid, and glucose) were selected. Assessment of the catalytic activity of the different combinations of organic compound and electrode material was performed by measuring CVs under controlled conditions. The KOH 0.1 M aqueous solution base electrolyte was selected as the experimental reference situation to evaluate the catalytic effect on the water splitting process. Chiral compounds have been selected because they are known to enhance the OER efficiency due to spin (Theoretical Background Section, 2.3). The results are encouraging both on steel and on Ni as well. The L-(+)-tartaric acid yields a moderate potential shifting effect (50 mV in the most favorable case), just on the shoulder preceding the current ramp for the OER. On the contrary, the aspartic acid does not seem to exert any prominent effect. In the case of the Ni working electrode the effect of the magnetic field, to select “up” and “down” spin injection, was investigated. Here the most interesting results are obtained. The comparison of the oxidation current peak, essentially due to the oxygen evolution reaction, yields a final consistent picture. Where the L-(+)-tartaric acid is found to enhance the evolution when the north-pole of the magnet is placed in direct contact with the Ni anode surface, the situation is reversed, i.e., larger efficiency for the D-(−)-tartaric acid coupled with the south magnetic field orientation. By and large, it appears that the results obtained using bulk chiral compounds yield a consistent spin filtering effect. Overall, an average 4% spin polarization value is obtained (average obtained by the SP values of each measurement), a value which is definitively less than the 15% to 20% SP range obtained in the case of well-ordered adsorbed monolayers directly on top of the electrode surface. All in all, the results obtained especially on the Ni as a function of the magnet orientation, relate well with results previously presented in the literature. This gives further impulse to the scientific research in the field of spin effects in the OER process.

# 5. Experimental

## 5.1. Chemicals and materials

Merck Dichloromethane solvent (DCM) ≥ 99.5%, Merck Ethanol solvent (EtOH) ≥ 99.5%, Merck Acetonitrile solvent (ACN) ≥ 99.5%, Sigma-Aldrich Sodium Nitrate $NaNO_3$ ≥ 99.0%, Sigma-Aldrich Potassium Sulfate $K_2SO_4$ ≥ 99.0%, Sigma-Aldrich Potassium Chloride KCl, Sigma-Aldrich Ferrocyanide $K_4[Fe(CN)_6]$, Sigma-Aldrich Ferricyanide $K_3[Fe(CN)_6]$, Merck Tetrabutylammonium tetrafluoroborate $(CH_3CH_2CH_2CH_2)_4N(BF_4)$ (TBATFB) 99%, Sigma Aldrich 3,4-Ethylenedioxythiophene (EDOT) 97%, Sigma Aldrich PCPDT-BT, Sigma Aldrich Iodine ($I_2$) ACS reagent ≥ 99.8%, Sigma Aldrich Copper (II) sulfate $CuSO_4$ ≥ 99%, Sigma Aldrich Sulfuric acid $H_2SO_4$ ≥99.9%, Thermo Fisher $LiClO_4$ ≥ 95% Sigma Aldrich Aniline ACS reagent 95%, Sigma Aldrich Iron (III) sulphate hydrate $Fe_2(SO_4)_3$ 97%, Sigma Aldrich Acetic acid $CH_3COOH$ ≥ 99.7%, Sigma Aldrich Sodium hydroxide Na(OH) ≥ 98%, Carlo Erba Boric Acid $H_3BO_3$ ≥ 99%, Carlo Erba Nickel (II) chloride, anhydrous $NiCl_2$ 98%, Sigma Aldrich Nickel (II) sulphate anhydrous $NiSO_4$ 99.99% and Sigma Aldrich Triethanolamine $C_6H_{15}NO_3$ ≥ 99.0%, Merck L-(+)-Tartaric acid ACS reagent ≥ 99.5%, Merck D-(-)-Tartaric acid ACS reagent 99%, Merck L-Aspartic acid 98%, Merck D-Aspartic acid 99%, Merck D-(+)-glucose ≥ 99% were used without further manipulation. 3,4-Dihydroxy-L-phenylalanine (referred as L-DOPA in the text), L-tyrosine 99%, D-tyrosine 99%, (S)-(-)-N,N-dimethyl-1-ferrocenylethylamine 98% (referred as S-FC in the text), (R)-(+)-N,N-dimethyl-1-ferrocenylethylamine 97% (referred as R-FC in the text) are from Alfa Aesar; they were used without further purification. A Ferrocyanide 5 mM, Ferricyanide 5 mM in a KCl 0.1 M aqueous solution is referred as Fe(III)|Fe(II) redox couple in the text. $BT_2T_4$ was synthesized as described in Sannicolò et *al.* [126]. The original synthesis procedure of the chiral oligothiophene N,N'-bis-[2,2';5',2'']tert-thiophen-5-ylmethylcyclohexane-1,2-diamine (2T3N) is reported in a previous work [196]. $BT_2T_4$ was synthesized as described in Sannicolò et *al.*[126]. DM-BEDT-TTF "**1**" and TM-BEDT-TTF "**2**" were prepared according to the published protocols[249], [355]

## 5.2. Techniques and set-ups

### *5.2.1. Electrochemistry*

Electrochemistry serves as the primary technique employed within this study to probe charge transport through both chiral and achiral interfaces. Unless otherwise specified, the employed setup consists of a 3-electrode electrochemical cell, with a commercial Ag/AgCl/KCl$_{sat}$ reference electrode and a platinum sheet as the counter electrode. Before each set of measurements, $N_2$ was used to purge for 15 minutes the electrochemical solution, to achieve oxygen-free electrolyte. All potentials referenced throughout this study are relative to the Ag/AgCl/KCl$_{sat}$ reference electrode. All the electrochemical measurements were conducted by the author of this thesis, utilizing either an Autolab PGSTAT 128N or CH-Instruments CHI660A potentiostat within the laboratories of the DIEF department (Unimore).

In addition to standard electrochemical procedures, this work also employs more sophisticated techniques such as Spin Dependent Electrochemistry (SDE), alongside spectroelectrochemistry measurements, involving the concurrent and synergistic use of electrochemistry with another spectroscopic technique ("in-situ" and/or "in-operando"). These latter and the relevant experimental set-ups are presented below.

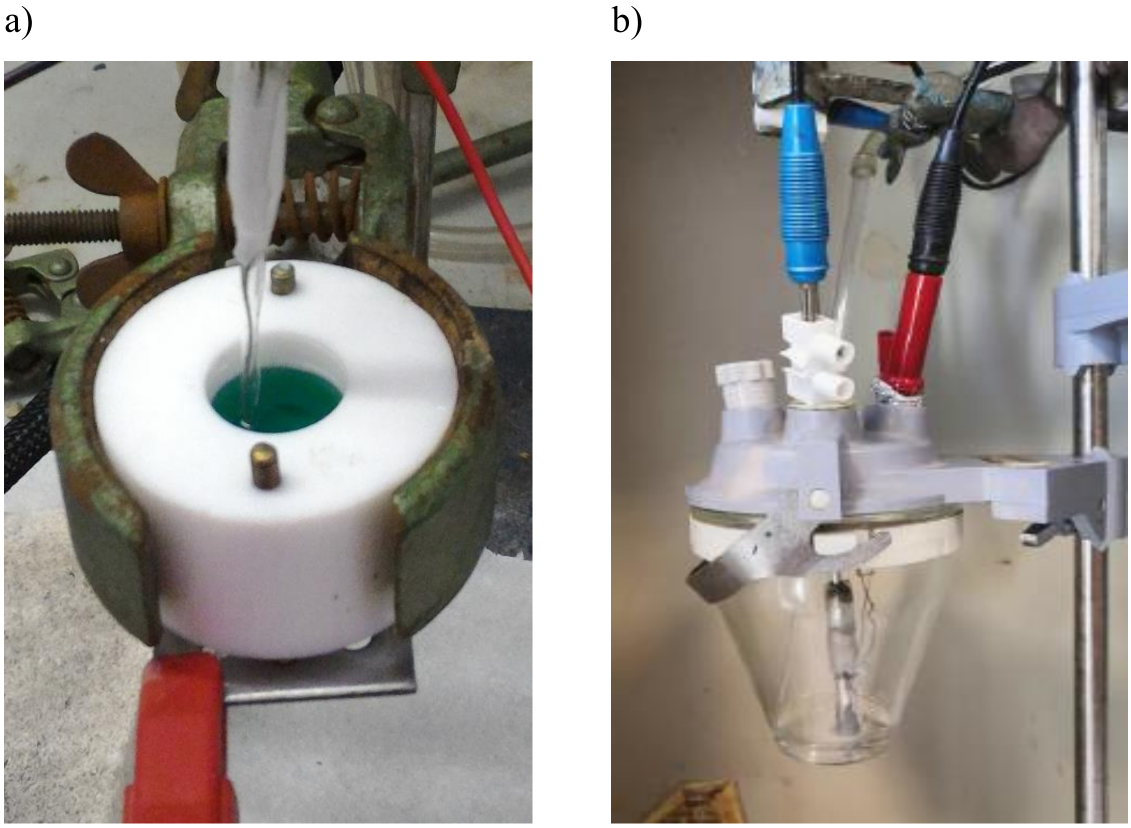

Figure 118 Two examples of three-electrode electrochemical cell used in our measurements. The potential is applied between the working electrode (WE) and the counter electrode (CE) while it is measured between the WE and the reference electrode (RE).

### *5.2.2. Spin-dependent Electrochemistry (SDE)*

Spin Dependent Electrochemistry (SDE) is based on the implementation in an electrochemical system of the spin filtering effect performed by chiral systems (Chiral Induced Spin Selectivity, CISS effect). It can be viewed as the electrochemical counterpart of spintronics, as it encompasses measurements aimed at investigating, identifying, discriminating, and controlling spin orientations. In this work, spin-dependent electrochemical measurements are carried out using a homemade “flat cell”. The cell design is of our own creation and it is realized via lathe-turning of a Teflon rod, for a total cell volume of 3 ml, with a bottom hole of 0.6 cm. Two threaded rods are inserted laterally, in the Teflon cylinder, allowing for the coupling of the cell with a copper plate that serves as a support for the WE. The working electrode is placed at the bottom (typically a shred of about 2 cm length, 1.5 cm width and 0.5 mm thick). A silicon o-ring of 0.7 cm diameter is placed between the bottom cell hole and the WE, avoiding any solution leakage. The external magnetic field is applied through a NdFeB B88X0 Grade N42 K&J Mag-net, Inc. permanent magnet, with a nickel coating. The magnet is placed in direct contact with the bottom surface of the WE, inserted through a hole made in the sample holder plate. The magnetic field at the surface is larger than 0.6 T (6353 Gauss) [161]. All mechanical parts, nuts, bolds and rods are made in brass. An exploded view of the cell is represented in the picture below (Figure 120)

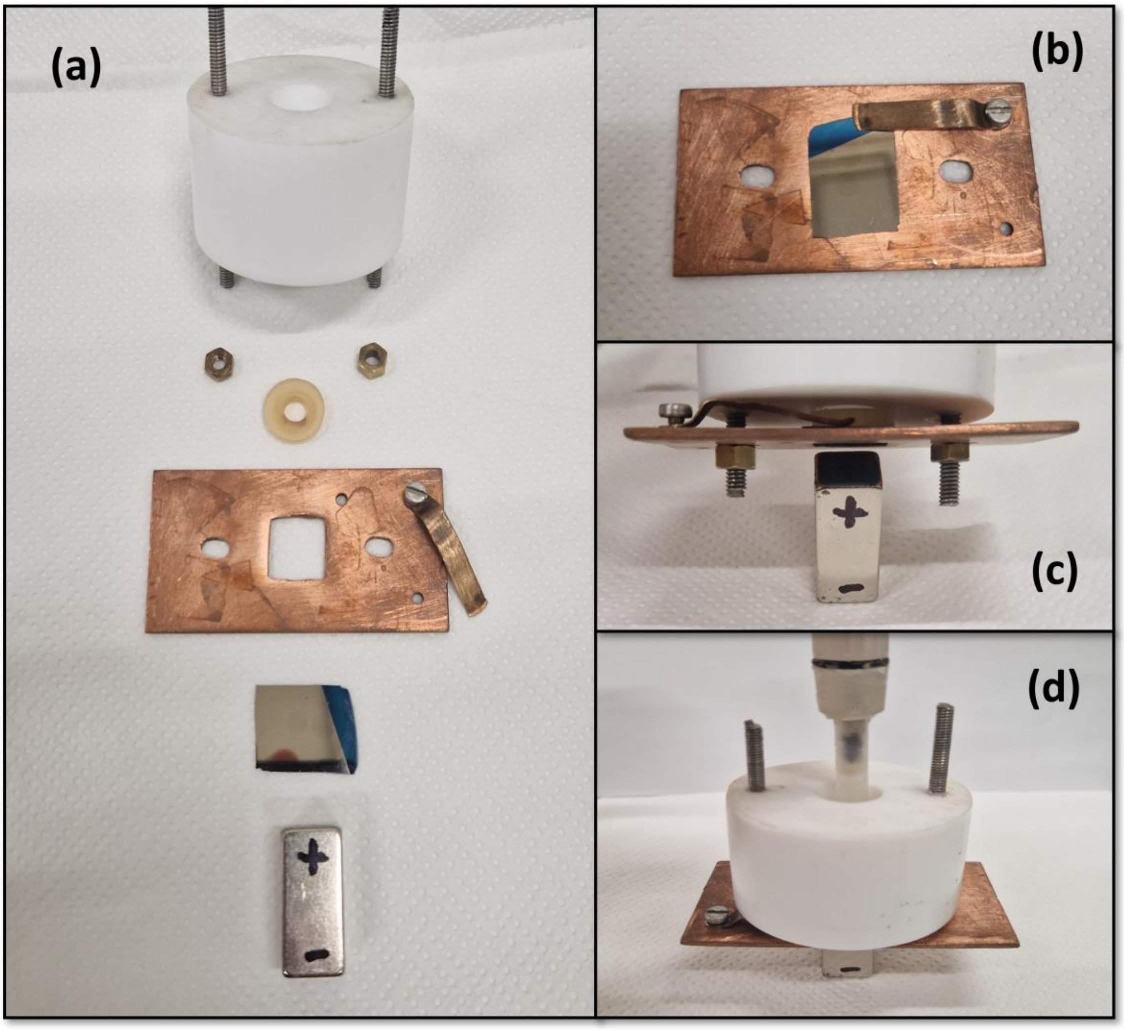

Figure 119 SDE setup: Panels (a) to (d) sequentially show all the components, starting with an exploded view of the cell and continuing as the elements are assembled.

### *5.2.3. Electrochemical Impedance Spectroscopy (EIS) and solid-state impedance measurements*

Impedance measurements were conducted using a CH-Instruments CHI660A potentiostat, both in the electrochemical configuration (with an ionic conductor serving as an electrolyte to complete the circuit between WE and CE) and in the solid-state configuration (in air). The latter configuration was employed, for example, to characterize stacked hybrid systems obtained by sequentially electropolymerizing metallic and polymeric layers. Impedance was then measured 'vertically' between the substrate and the top layer of the sandwich architecture to examine the behavior of coupled interfaces and any short-circuits formed during the process. Contacts were established by connecting thin Copper wires to the sample with a small amount of silver paste or, when possible, by gently touching the coating with a Glassy Carbon wand (Section 4.3.2.3).

A particular setup involving two potentiostats was employed for measurements of the electrochemical transistor system (Section 4.3.2.1). Within a standard electrochemical cell, a glass substrate was utilized, onto which three 100 nm-thick Au pads (with a 10 nm adhesion layer of Chromium) were evaporated. Between these three pads, a polymer (PCPDT-BT) was drop-cast, serving as the gate. Subsequently, two out of the three pads coated with PCPDT-BT were connected as the working electrode (WE) and counter electrode (CE) to the CHI660A potentiostat for impedance measurements, functioning as the source and drain, respectively. The third pad was acted as the WE of the second potentiostat, which applied a DC gating voltage. This allowed impedance spectra to be recorded as a function of the applied gating voltage. A schematic representation of this setup can be found in Figure 121.

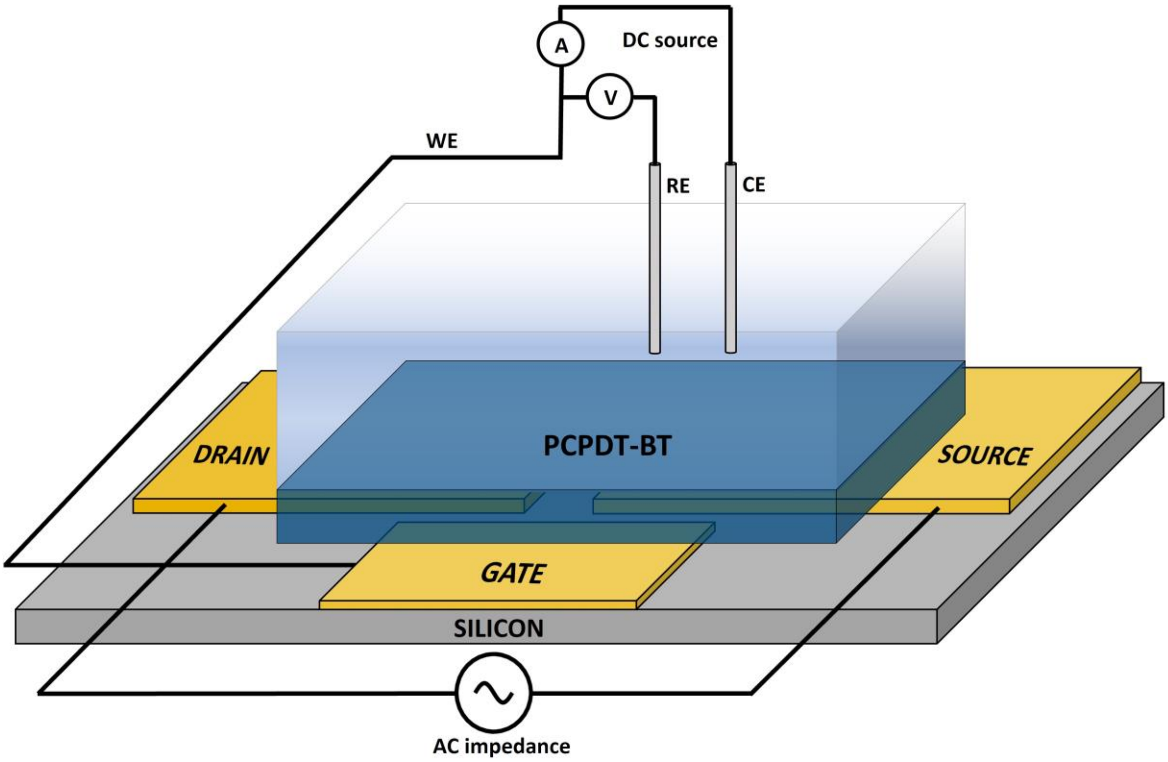

Figure 120 Schematic representation of the electrochemical-transistor architecture. A thin film of PCPDT-BT is drop-casted onto three gold pads. Two of these terminals serve as the source and drain contacts of the transistor, while the third terminal, the gate, is controlled by applying a direct current potential difference using a three-electrode electrochemical system (a Pt wire as the counter electrode, Ag/AgCl as the reference).

### *5.2.4. Ultra-High Vacuum (UHV): XPS, NEXAFS, PECD.*

#### 5.2.4.1 BEAR beamline synchrotron radiation measurements

X-ray synchrotron radiation photoemission spectroscopy measurements (XPS) and near edge X-ray absorption fine structure spectroscopy (NEXAFS) were performed at the BEAR beamline (Elettra synchrotron radiation laboratory, Trieste, Italy) [356]. Photoemission measurements from the Au 4f, C1s and S2p core levels were performed at normal emission with a hemispherical deflection analyzer (66 mm mean radius) driven at constant pass energy, with an overall energy resolution of < 500 meV. The photon energy (hν = 350 eV for C1s and hν = 260 eV for S2p, with the Au4f levels acquired at both 350 eV and 260 eV photon energy for alignment and reference purposes) was chosen in order to measure the photoelectron peaks of the different core levels approximately at the same final kinetic energies (Ek = 90–100 eV). Such a condition was pursued in order to maximise the surface sensitivity, measuring photoelectrons with kinetic energies corresponding to the minimum of the inelastic mean free path ($\Lambda \sim 6$ Å).

NEXAFS spectra were measured at the C 1s edge keeping fixed the incidence angle (20° with respect to surface plane) and varying the direction of the electric field vector from perpendicular to the scattering plane (s-incidence geometry) to parallel to it (p-incidence geometry). This was accomplished by rotating the experimental chamber around the beam axis by an angle $\Psi_C$, from $\Psi_C = 0°$ (s-scattering) to 90° (p-scattering). This guarantees that the illuminated area and the incidence angle remain virtually unchanged for different angles $\Psi_C$. All measurements were performed at room temperature.

#### 5.2.4.2 CiPo beamline synchrotron radiation measurements

X-ray spectroscopy measurements were performed at Elettra, CiPo (Circular Polarization) beamline [357]. CiPo is able to provide variable polarization (linear/circular) synchrotron radiation in the 5 to 900 eV energy range. Photons are yielded by an elliptical electromagnetic wiggler (EEW). Then, by means of a couple of monochromators photons are selected in two beams of low (5 – 40 eV) and high (40 – 900 eV) energies. Measurements based on photoemission techniques such as Core Level Photoemission Spectroscopy (XPS) and Valence Band Photoemission Spectroscopy (UPS) were used for the characterization of both 2T3N film formation and 2T3N|Au interactions. Valence band X-ray Photoelectron natural Circular

Dichroism (PECD) spectra allowed to characterize in detail the optical rotation properties of chemisorbed 2T3N on Au.

#### 5.2.4.3 Conventional X-ray source XPS

X-ray photoemission spectroscopy measurements (XPS) were performed using a conventional MgKα source and a hemispherical Omicron EA125 electron analyzer (LFMS lab, Department of Engineering Enzo Ferrari, University of Modena, Italy). Photoemission measurements were per-formed at normal emission. XPS experimental core-levels spectra have been fitted using Voigt functions (convolution of Gaussian and Lorentzian functions). All measurements were performed at room temperature. Binding energies are referred to the Fermi energy of a gold substrate.

### *5.2.5. UV-vis/NIR and CD spectroscopy*

Absorption and CD spectra in the 300-1200 nm range using a Jasco J-1500 spectrometer and a Perkin-Elmer Lambda 950 UV-Vis spectrophotometer. with a spectral resolution of 3 nm. The employed resolution ranged from 0.5 to 2 nm depending on the specific requirements of each experiment. For each investigated system, baseline subtraction was carried out using previously recorded baselines. This involved the use of only the quartz cuvette and the solvent for liquid samples or solely the ITO glass slide for solid samples. In the case of steady-state systems, the final spectra were derived by averaging five distinct scans. The number of sampling points within the window was manually selected for each spectrum to simultaneously enhance noise reduction and preserve spectral details.

### *5.2.6. FTIR spectroscopy*

Infrared spectra were recorded in both transmission and ATR (Attenuated Total Reflection) modes using a Bruker IFS66 Fourier Transform IR (FT-IR) spectrometer with a vacuum sample chamber. A resolution of 3 cm was utilized. The energy range investigated spanned from 750 to 6000 $cm^{-1}$, employing a Globar source and a liquid nitrogen-cooled mercury cadmium telluride (MCT) detector. Spectra were acquired with baseline subtraction to remove the contribution of water and any minimal substrate absorption. The final spectra were obtained by averaging 30 scans. In the case of transmission measurements, KBr pellets were used, while for ATR acquisitions, a 7-bounce ZnSe crystal was employed.

### 5.2.7. *Raman spectroscopy*

Raman spectra were recorded with a Renishaw RM1000 spectrometer coupled to a Leica DLML microscope equipped with 50×, 20× and 5× objectives. The spectrometer with 250 mm focal length is equipped with a Peltier thermoelectric cooled CCD 1024x256 pixels and a diffraction grating 1800 grooves per mm. The Rayleigh scattering was removed with edge filter centered at 514.5 nm allowing for a minimum Raman shift of approximately 100 $cm^{-1}$. The setup allowed for a spatial resolution of about 1 μm with the 50× objective and a nominal field depth ranging from about 25 to 450 μm and a spectral resolution down to 0.5 $cm^{-1}$. The excitation was from an Argon ion gas laser tuned at 514.5 nm with a nominal power of 25 mW. In all the experiments, the power was reduced by neutral density filters to avoid sample damage.

### 5.2.8. *Magnetic-conductive atomic force microscopy (mc-AFM)*

Magnetic-conductive atomic force microscopy (mc-AFM) measurements were performed at room temperature by using Bruker Scan-analyst Atomic Force Microscopy. The electrical and magnetic module allows conductive samples to be studied both in contact and peak force tuned mode. The mc-AFM was used to map the conductivity of films using both a low noise DC technique and a phase locked AC system. By applying electrical bias in the -3.0 V to 3.0 V range, a variation of intensity in the peak force tune mode of AFM would allow to map conductivity of the sample as a function of the magnetic field direction. In conductive mc-AFM, the sample is electrically biased and the circuit is completed by providing a connection to ground via the mc-AFM probe chip. Magnetic field (0.1 T) was applied, using Nd-Fe-B permanent magnets, on Co/Cr magnetic tip (Bruker-MESP with spring constant 2.6 N/m) during the measurements. This technique provides insight into the grain structure and allows lateral mapping of the conductivity at the nanoscale. All our scans (≈100) on each point have been obtained at room temperature.

### 5.2.9. *Scanning electron microscopy (SEM)*

SEM photomicrographs were captured utilizing a Philips XL40 microscope, enabling observation of both surface morphology and corresponding cross-sections. These images were acquired using both secondary and back-scattered electrons at magnifications of 100x, 200x, 500x, and 1000x. In the case of cross-sections, they were obtained by slicing the samples with a REMET Micromet and subsequently subjected to mechanical polishing via a Buehler Minimet

1000, employing Buehler emery paper and alumina with a grain size of 0.05 μm. Profilometry measurements were executed with a HommelWerke Waveline20 profilometer. Monte Carlo simulations based on the EDS microanalysis data were conducted utilizing the DTSA-|| software [305].

### *5.2.10. Spectroelectrochemistry*

The combination of electrochemistry and spectroscopy is employed to monitor real-time variations in the acquired spectrum as a function of the applied electrochemical procedure (in-situ/in-operando), a technique known as spectroelectrochemistry (SEC) [358].

In synergy with electrochemistry, FTIR spectroscopy (employing the attenuated total reflection, ATR, technique), UV-vis/NIR spectroscopy, and Raman spectroscopy were utilized, now presented in this order. It's worth specifying that, in addition to the additional information presented in this section regarding the combination of electrochemistry and spectroscopy and the specific setups used, the instruments employed, and their relative experimental characteristics and parameters are the same as those in the respective previously presented sections (unless otherwise specified).

Figure 122 presents a schematic illustration of the setup for FTIR spectroelectrochemical measurements, which were used to investigate the p-doped state of the PCPDT-BT polymer by acquiring IR spectra (refer to the specific Results Section, 4.3.2.3). The doped state of a drop-casted film of PCPDT-BT (approximately 1 μm thick) is electrochemically controlled by applying a potential bias via a glassy carbon (GC) rod kept in mechanical contact with the PCPDT-BT. The latter is connected to the potentiostat as the working electrode (WE). The electrochemical cell containing the electrolyte (in this case, ACN with 0.1 M TBATFB as the supporting electrolyte) is physically obtained by exploiting the raised portions of the accessory for supporting the ATR crystal (Gateway ATR System, SPECAC, 7 bounces ZnSe crystal). In this way, a small cavity is created, capable of holding around 4 ml of solution due to the "pool effect". This amount is sufficient to establish contact with a Pt wire (counter electrode, CE) and an Ag/AgCl reference electrode (RE).

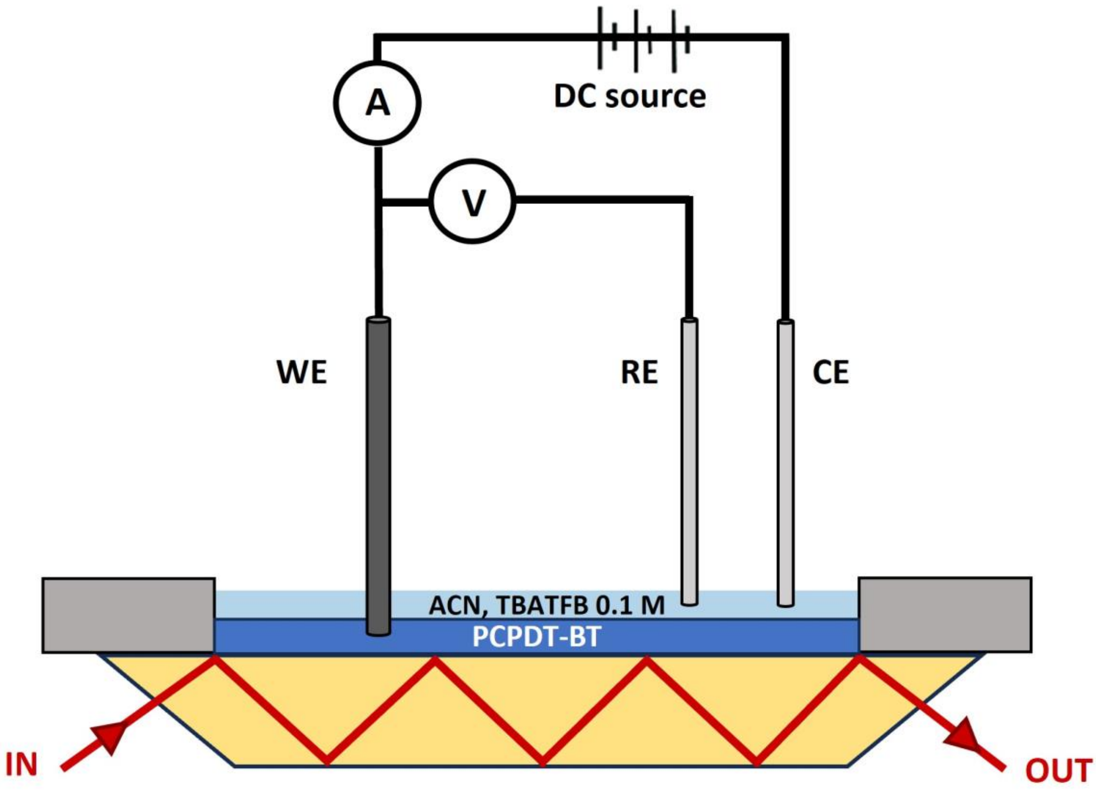

Figure 121 Schematic representation of the experimental set up for “in-situ”/“in-operando” IR spectroelectrochemistry measurements. A dropcasted PCPDT-BT film is the WE. Ag/AgCl/KCl$_{(sat)}$ and a Pt sheet are the RE and CE, respectively. 0.1 M TBATFB is the base electrolyte in ACN.

In the case of UV-vis/NIR spectroelectrochemistry, the spectroelectrochemical cell was directly set up within a standard spectroscopic quartz cuvette. The working electrode was composed of an ITO glass, the auxiliary electrode was a Pt wire, and the reference electrode was an aqueous Ag/AgCl electrode. In this configuration, electrochemistry was employed for two purposes: to polymerize a film on the ITO electrode while recording UV-vis spectra to monitor changes in absorption, and to investigate the p-doped state (and the resulting electronic polaron) of an existing film on the electrode, in an electrolyte support solution (as discussed in Section 4.1.2).

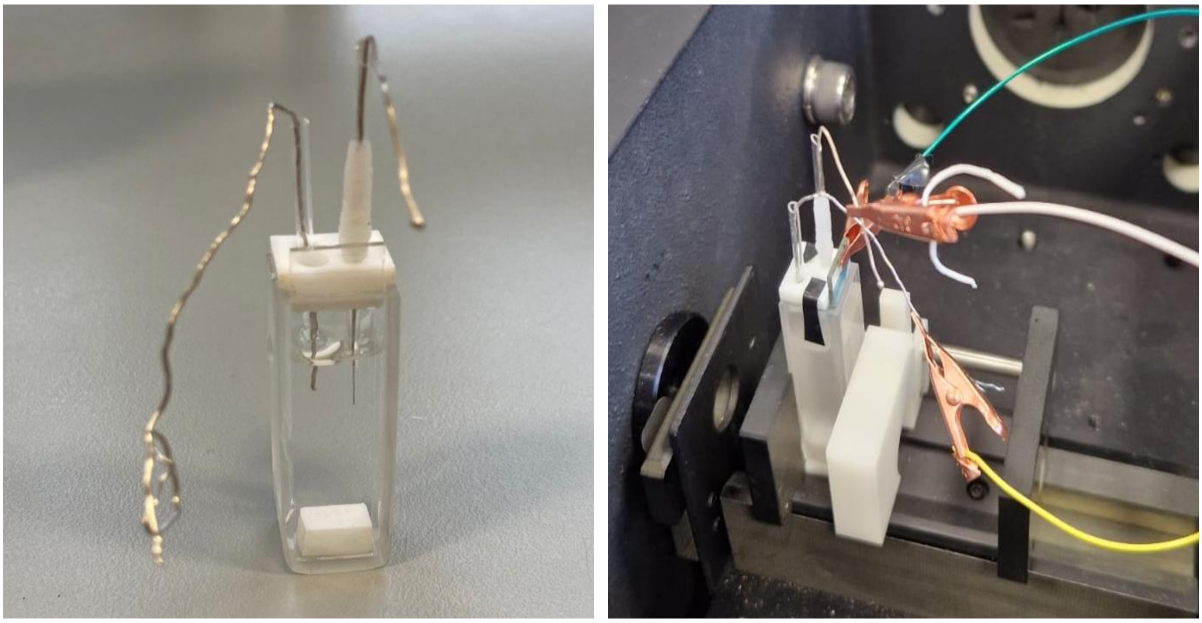

Figure 122 UV-vis/NIR spectroelectrochemistry set-up. The electrochemical cell is created directly within the quartz cuvette using a custom Teflon cover that secures an ITO plate (WE) and two wires, namely Pt and Ag (counter electrode and pseudo-reference).

*"In situ"/"in operando"* Raman spectroelectrochemical measurements were carried using a custom-made Teflon electrochemical cell, capable of accommodating approximately 5 ml of electrolyte solution. The dimensions of this customized cell were designed to create an electrochemical setup with a low profile, allowing for a reduced working distance of just 21 mm, which is suitable for operation with the long-distance 20x objective.

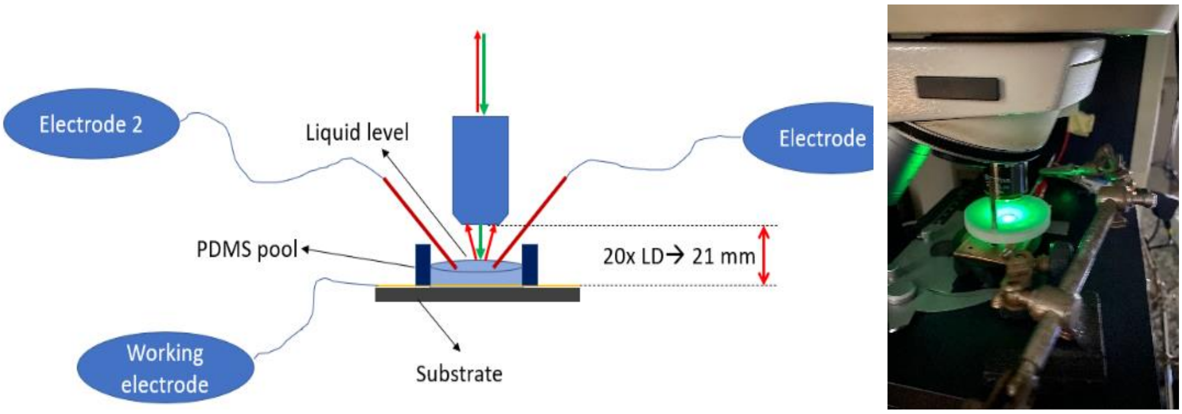

Figure 123 Raman spectroelectrochemistry "in-situ"/"in-operando set-up.

### *5.2.11 Solid-state resistance measurements*

Resistance measurements as a function of the applied magnetic field (Magnetoresistance) and as a function of temperature and of are carried out via a Quantum Design Physical Properties Measurements System (PPMS), using an external Keithley 2636 Source-Meter. Two specimens were mounted on each device holder and connected with a micro-bonder and silver paste to two different channels. Resistance was measured in the temperature range between 300 and 120 K with a slow ramp (1 K/min). Prior to the actual measurements, the ohmic behavior of all the investigated samples is checked by the linearity of the I−V curves. In the two-probe configuration, the voltage bias is fixed at a value in the range of 15−250 mV (depending on the device resistance at room temperature) and measured the current. In the four-probe configuration, we fixed the current in the range of 10 μA and monitored the voltage. No significant differences were observed between two- and four-probe measurements in the whole temperature range.

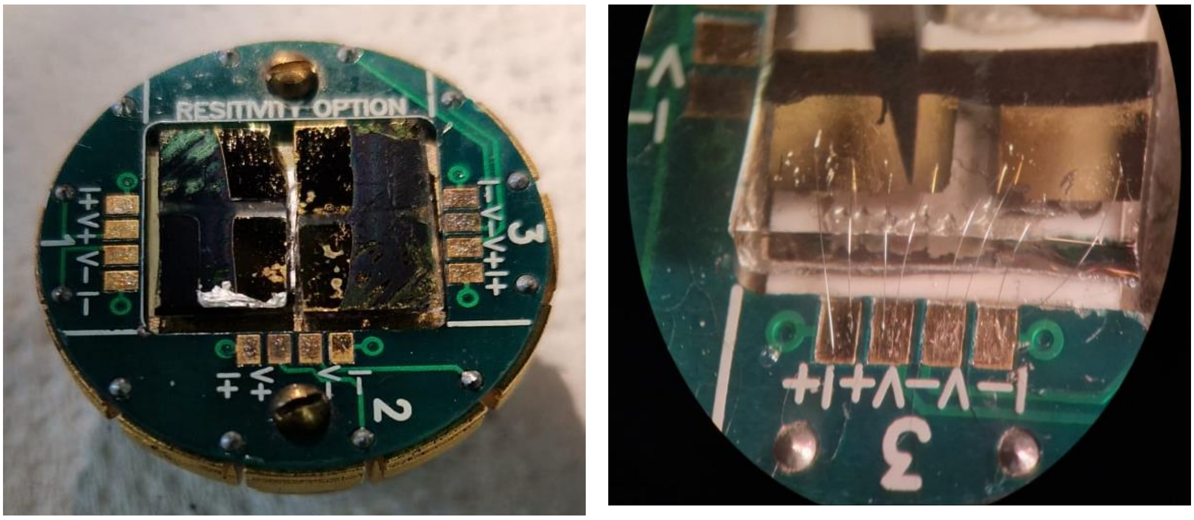

Figure 124 A sample of chiral PANI (cPANI) connected to the four terminals of the PPMS sample holder. Contacts are made on one side to a gold pad and on the other side to a top layer of nickel. The results of the measurements conducted on this system are reported in Section 4.2.2.

### 5.2.12. *Theoretical calculations*

All the theoretical results here reported concerning all possible oxidation states and spin multiplicity of the investigated species are performed in the framework of ab initio quantum mechanical based methods. Unless otherwise indicated, all calculations were performed without any symmetry constraints (C1 point group symmetry) and unrestricted wavefunctions, by using Gaussian [359] and Firefly [360]. Chemcraft [361] is used for visualization purposes, both molecular structures, and ab initio molecular orbitals display. For all the structures investigated and presented, molecular geometries (full optimization) and relevant electronic and vibrational (IR and Raman) spectra are calculated at various theory levels (as specified in the relevant discussion for each specific result, ab-initio DFT B3LYP/cc-pVTZ being the most used one). To account for solute−solvent interaction, geometry optimization is carried out by using the Barone and Cossi's polarizable conductor model (CPCM) [362]. The stability of all the species is checked by Hessian calculation (vibrational frequency spectrum). In the case of reagents, products, and intermediate reaction species, all the frequency values are found as real and positive. Thus, all the optimized geometries are representative of true minima of the potential energy surface (PES). In the case of $BT_2T_4$ and 2T3N, chemisorption was modelled within the so-called embedded cluster approach. The molecule was allowed to relax on top of a (111) surface of the relevant substrate (gold or nickel slab), of fixed geometry (corresponding to the experimental crystalline disposition). In this framework, the slab(111)|molecule clusters optimization and electronic properties have been calculated by using the PM6 Hamiltonian, as implemented within the MOPAC program [363].

# 5.3. Preparations

## *5.3.1. Custom flat electrodes fabrication*

The substrates for the assembling of the organic semiconductor electrochemical transistor (see Section 4.3) and for magnetoresistance (MR) measurements of chiral polyaniline (cPANI, Section 4.2.2) feature gold (Au) pads that serve as electrical contacts (with 2, 3, and 4-pad designs, respectively). Custom 2D geometries for each of these applications were obtained on a glass substrate through thermal evaporation, utilizing self-designed masks produced via additive manufacturing. More specifically: the masks were initially designed using CAD software. Their common architecture consists of a circular base with a thickness of 2 mm, on which 0.9 deep recesses are created to accommodate the 1mm-thick glass substrates. A 1.5 mm thick top-part is also designed, featuring the desired pattern to be transferred onto the electrode (depending on the application) at the locations of the glass slides. The two parts of the mask are fastened together using four screws inserted into dedicated holes at the four ends of the circle.

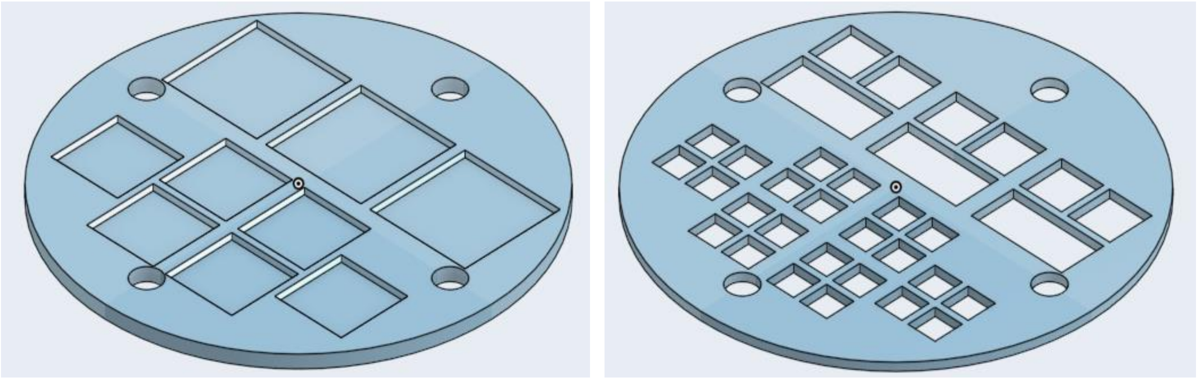

Figure 125 CAD drawings of a customized mask (base and lid) for creating resistance measurements substrates (with 3 or 4 terminals).

The CAD design was processed using slicing software (proprietary to Eiger) to generate a file format recognizable by the 3D printer and to preliminarily verify the feasibility of the designed 2D geometries (the channel between the pads has a variable width ranging from 500 microns to 1 mm, at the printer's sensitivity limit).

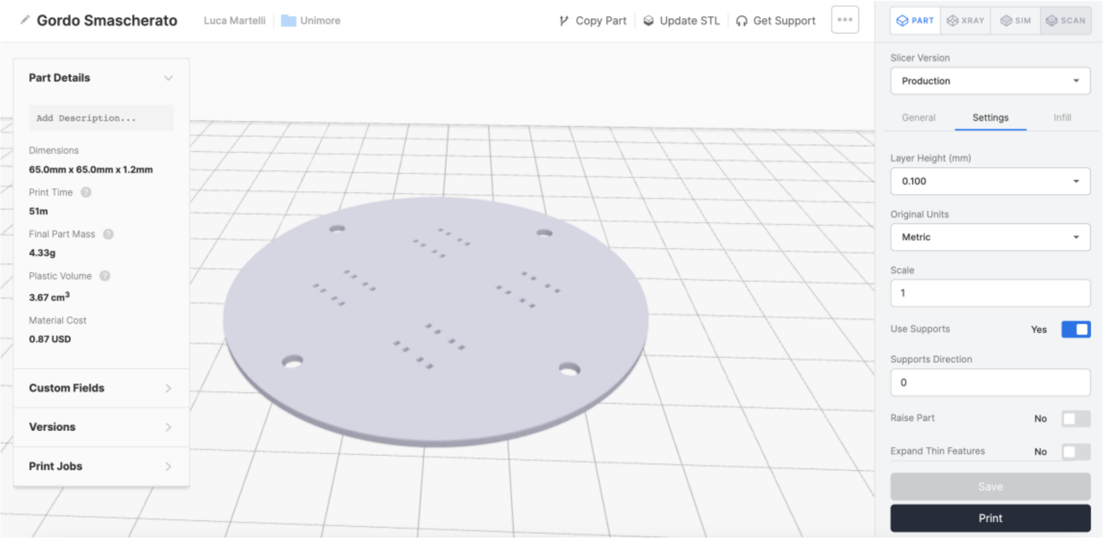

Dimensions: 65.0mm x 65.0mm x 1.2mm
Print Time: 51m
Final Part Mass: 4.33g
Plastic Volume: 3.67 cm$^3$
Material Cost: 0.87 USD

Slicer Version: Production
Layer Height (mm): 0.100
Original Units: Metric
Scale: 1
Use Supports: Yes
Supports Direction: 0
Raise Part: No
Expand Thin Features: No

Figure 126 CAD mask design processed by the 3D printer software

The masks are then fabricated using a Markforged Mark Two 3D printer with Onyx material (a nylon base reinforced with short carbon fibers). The printing is performed in FFF mode, with a layer height of 100 microns, a 37% triangular infill, 2 shells, and 4 bottom/top layers. Printing time ranges from 30 to 60 minutes for each part.

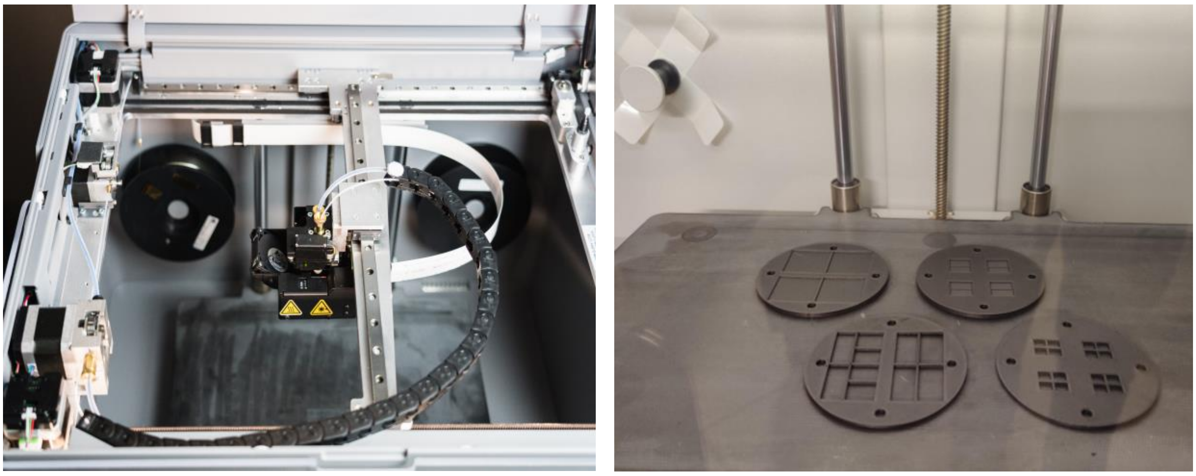

Figure 127 Markforged MarkTwo 3D printer during the production of the custom masks

The glass substrates are cut from 1 mm-thick microscope slides. These substrates undergo a multi-step cleaning process: they are sonicated in absolute ethanol, washed with triply distilled water, and then placed in a solution of 0.5 M NaOH + 10% H2O2 for 10 minutes. Afterward, they are washed as before, transferred to a solution of 33% H2SO4 + 10% H2O2 for another 10 minutes, washed again, and finally soaked in water at 90°C before being dried under an argon stream.

The diameter of the masks is optimized to be coupled with the sample holder plate of a High Vacuum Process thermal evaporator, using the same screws that secure the base and lid. The glass substrates are first mounted on the mask, then attached to the sample holder lid, and finally loaded into the evaporation chamber with the samples facing downward. Utilizing a quartz crystal microbalance for thickness control, 10 nm of Cr (adhesion layer) and 100 nm of Au are evaporated in a two-step process under high vacuum conditions ($10^{-6}$ mbar). This process results in substrates featuring 2, 3, or 4 pads tailored for establishing electrical contacts in MR, Electrochemical Transistor, or VdP measurements. The various stages of the evaporation procedure are depicted in Figure 129.

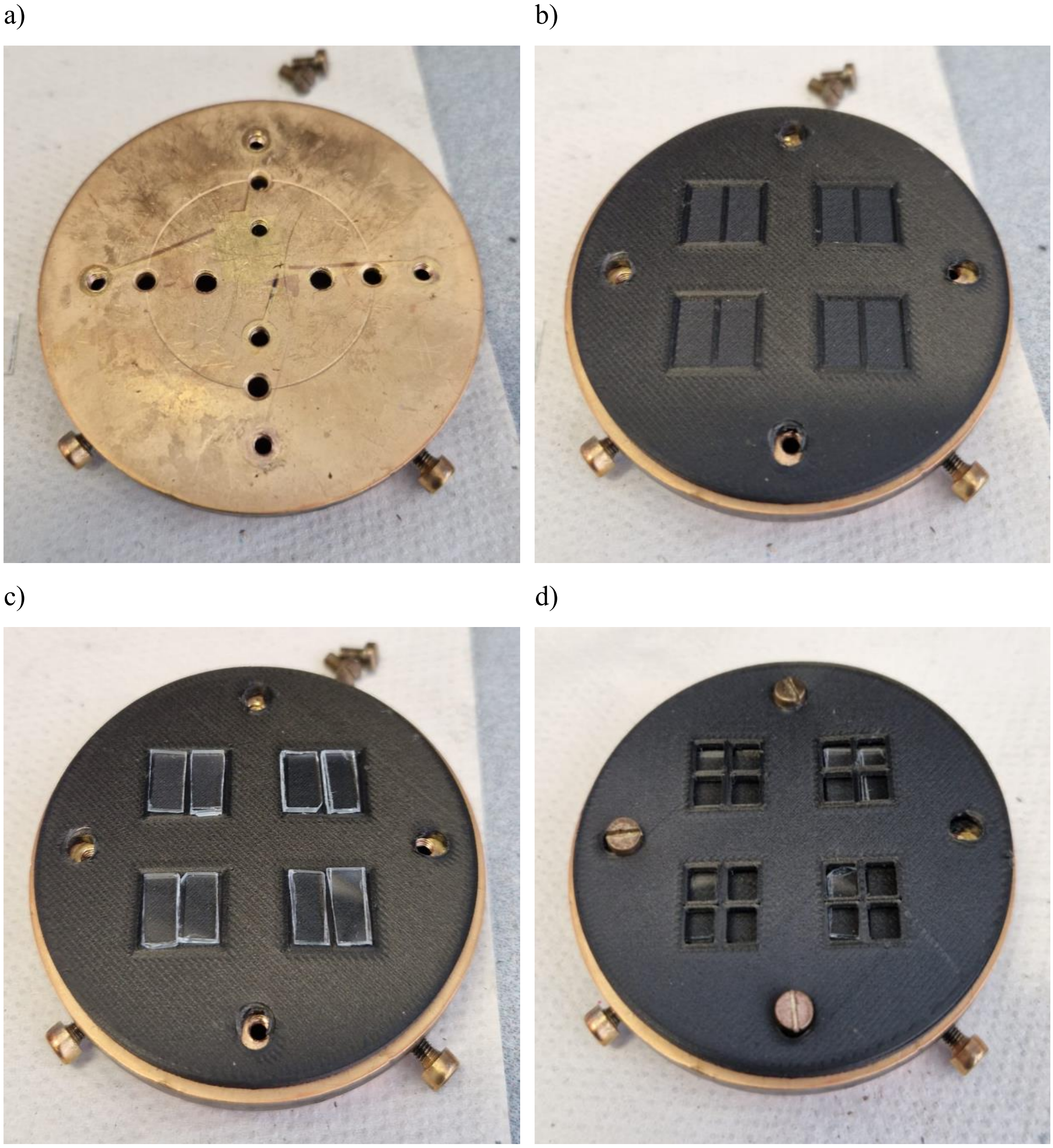

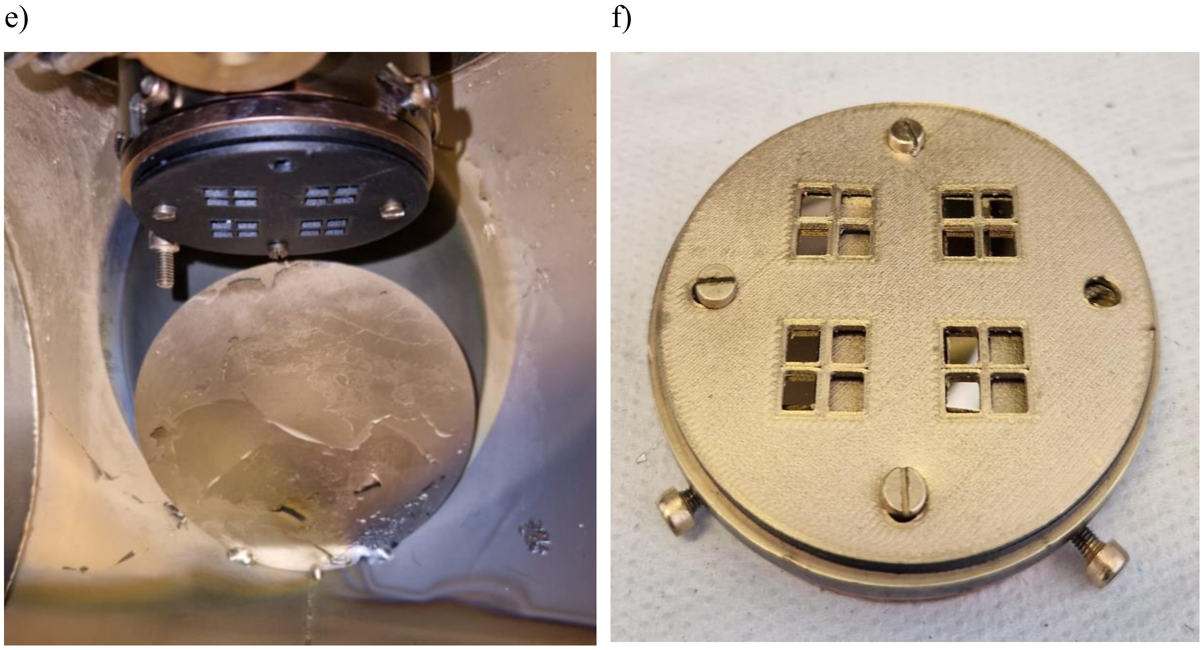

Figure 128 The steps involved in assembling and using the custom-made **a)** Sample holder of the evaporator **b)** The base of the mask is coupled to the sample holder **c)** The glass slides are positioned within the designated slots **d)** The mask cover is secured **e)** The sample holder, connected to the mask, is positioned in the evaporation chamber **f)** At the end of the process, the sample holder is removed from the chamber

### *5.3.2. Gold functionalization*

Gold surfaces were obtained by e-beam evaporation of 100 nm of gold, on a silicon substrate (Siltronix), on top of an 8-nm-thick Cr adhesion layer, grown on top of thermally grown 300 nm $SiO_2$ (100), > 400 Ω $cm^{-2}$. The gold surface is then followed by gentle flame annealing: ethanol flame annealing and cooling in argon according to the rules given by Hamelin[364] (in the following Au stays for Au(111-oriented) [365]. Unless otherwise specified in the relevant paragraph, the functionalization of the gold substrate is achieved by incubating the Au surface in a 5 mM ethanolic solution of the respective investigated chiral molecule ($BT_2T_4$, 2T3N, TTF-derivative, etc.) for 24 hours.

### *5.3.3. Silver nanoparticles preparation*

Silver nanoparticles (AgNPs) were obtained exploiting the electrochemically based method of Starowicz et al. [232], which was successfully used in the production of hybrid thiophene and TTF based architectures, obtaining AgNPs ranging between 20 to 50 nm [233].

### *5.3.4. Hybrid chiral interfaces two-steps preparation*

The Au|BT2T4 interface and the Au|2T3N interfaces, obtained following the suitable gold functionalization (compare Section 5.3.2), were furtherly incubated for 24 hours in the AgNPs suspension. In this way, multilayered interfaces were produced with the thiophene derivative acting as a “molecular thread” between gold and silver (Au|molecule|AgNPs interface).

### *5.3.5. Capped AgNPs preparation*

The electrochemically fabricated AgNPs (vide supra, section 5.3.3) were added to a 5 mM Thiophenic derivative or TTF-derivative ethanolic solution in order to obtain thiophene or TTF capped-silver nanoparticles ($BT_2T_4$@AgNPs, for example). The solution was then left at rest under dark for 24 hours at room temperature. The resulting pale-yellow solution (free of visible precipitate to the naked eye) was subjected to centrifugation at 6000 rpm for 30 minutes, followed by decantation of the supernatant and replacement with fresh solvent. This cycle is repeated twice to purify the AgNPs@thiophene/TTF derivatives from excess, non-adsorbed molecules.

### *5.3.6. Hybrid chiral interface one-step preparation (Au|$BT_2T_4$@AgNPs)*

Au surfaces were incubated within the capped silver nanoparticles ($BT_2T_4$@AgNPs) suspension (compare previous section 5.4.5) for 24 hours in the dark at room temperature. This procedure allows for a one-step preparation of the Au|$BT_2T_4$@AgNPs hybrid interface.

### *5.3.7. Nickel functionalization*

Ni surfaces were obtained by e-beam evaporation of 100 nm of nickel, on a silicon substrate (Siltronix) with thermally grown 300 nm $SiO_2$ (100), > 400 Ω $cm^{-2}$, on an 8-nm-thick Ti adhesion layer. A one-step Ni functionalized preparation strategy was followed [217]. Ni functionalized surfaces were obtained by immersion in a thiophenic or TTF derivative solution in ethanol (yielding a hybrid Ni|molecule chiral interface) or a suspension of thiophene/TTF derivative-capped Ag nanoparticles (yielding a hybrid Ni|molecule@AgNPs chiral interface). During the functionalization process the Ni surface was kept at a negative (reducing) potential of $-0.3\ V$, to avoid nickel oxidation [217].

# 6. Conclusions

In this thesis, a systematic approach has been employed to investigate charge transport through chiral systems. The results are categorized into two main chapters: section 3 and section 4.

In Section 3, the experimental investigation is conducted at the monomer level, exploiting self-assembled monolayers of chiral molecules. For this purpose, most measurements exploit the chemisorption of different S-based (sulphur) structures (thiophenes and TTF derivatives), as opposed to conventional thiols, to anchor molecules to metal surfaces through wet functionalization. This approach yields self-assembled monolayers (SAM) of thiophene and TTF derivatives on gold, silver, and, particularly, nickel (using a novel method based on a synergistic approach with electrochemistry to limit oxidation). The first section of results (3.1) focuses on a chiral thiophene derivative with stereocenters, 2T3N, adsorbed on gold. This monolayer is characterized in great detail, including its nature, order, and features, using synchrotron radiation. The chiral nature of the obtained system is confirmed, especially through photoemission measurements (with dichroic exciting photons) on the valence band of the Au|2T3N complex, demonstrating the “chiralization” of the underlying gold substrate beneath 2T3N. The charge transfer of the system is electrochemically measured using both a bulk redox probe, Fe(III)|Fe(II), and, more significantly, by constructing a molecular junction: a hybrid interface Au|2T3N|AgNPs achieved by adsorbing silver nanoparticles on the Au|2T3N system. The potential of using AgNPs as tunable redox probes is fully exploited in the second section presented in Chapter 3.2, which, in a way, constitutes the core and the most original and impactful result of the entire thesis.

By appropriately functionalizing the AgNPs (by capping them with another *inherently chiral* thiophene derivative, $BT_2T_4$), it is possible to impart chirality to them (similar to the previous Au|2T3N system) to obtain chiral redox probes for both R-$BT_2T_4$@AgNPs and S-$BT_2T_4$@AgNPs enantiomers. These redox probes are used to investigate the chiral recognition properties of chiral interfaces Au|R-$BT_2T_4$ and Au|S-$BT_2T_4$, considering all possible combinations of symmetric and asymmetric interfaces. The effects observed *in the absence of any ferromagnet or magnetic field* align with the results obtained in much more "classical" paradigms for assessing the effects of spin polarization dictated by CISS in the scientific literature, such as measurements involving mc-AFM (using a Ni ferromagnetic tip as a spin injector) and Spin-Dependent Electrochemistry (with a Ni substrate as the spin injector). The complete consistency of the various measurements conducted (reiterating*, both in the absence and presence of spin injection*), along with the meticulous characterization of all the elements involved in the production of the hybrid interfaces (please refer to Section 3.2.3, “Further in-depth characterization”), strongly supports the claim that the Au|$BT_2T_4$ interface acts as a spin injector. Its effect on the electron spin is comparable to that of a ferromagnet in the presence of an external magnetic field. This entire experimental framework finds rationalization in the Chiral Induced Spin Selectivity Effect (CISS) and attests that the spin is the hidden driving force in chiral recognition, which can thus be defined as a spin-driven process. This conclusion unequivocally puts aside obsolete models like the lock and key model or the 3-points interaction model, which were previously used to attempt to explain enantio-selective interactions. It opens the doors to a completely new interpretation of numerous natural biological phenomena, with potentially revolutionary consequences. The same experimental paradigm is thus exploited to investigate charge transport and spin polarization through another important class of S-based chiral molecules: TTF derivatives. These molecules are of particular interest due to their widespread use in charge transfer co-crystal synthesis, often in combination with -TCNQ acceptor species. In this case as well, a multifaceted approach based on enantio-recognition and SDE has revealed the connection between the results of these measurements. Furthermore, consistently, a higher efficiency of spin-dependent transport ($SP \cong 15\%$) is found for the class of molecules with the greatest number of stereocenters, i.e., a more pronounced chiral space. Subsequently, in Section 4, the experimental focus on monomer molecules self-assemblies is abandoned in favour of the investigation of more complex systems: homochiral polymers (p-2T3N), polymers with induced supramolecular chirality (chiral PANI), and hybrid systems of bulk metals coupled to organic chiral agents (such as the use of tartaric acid, aspartic acid, and glucose in combination with steel or nickel electrodes to catalyse the OER in the context of water splitting). The potential to induce chirality in an arbitrary system, including inorganic ones, has the potential to bring about a revolution in the fields of electronics and spintronics, even in the short to medium term. In this regard, this thesis ultimately introduces a novel architecture for creating an electrochemical transistor. At the moment, this type of device has only been tested with a commercial achiral polymer (PCPDT-BT). However, based on the excellent preliminary results obtained, we plan to soon implement its operation with chiral spin-polarizing systems, starting with the p-2T3N and chiral PANI presented in this thesis.

# References

[1] K. Michaeli, V. Varade, R. Naaman, and D. H. Waldeck, ‘A new approach towards spintronics–spintronics with no magnets’, *J. Phys. Condens. Matter*, vol. 29, no. 10, Art. no. 10, 2017, doi: 10.1088/1361-648X/aa54a4.

[2] R. Naaman, Y. Paltiel, and D. H. Waldeck, ‘Chiral molecules and the electron spin’, *Nat. Rev. Chem.*, vol. 3, no. 4, Art. no. 4, Apr. 2019, doi: 10.1038/s41570-019-0087-1.

[3] P. C. Mondal, W. Mtangi, and C. Fontanesi, ‘Chiro-Spintronics: Spin-Dependent Electrochemistry and Water Splitting Using Chiral Molecular Films’, *Small Methods*, vol. 2, no. 4, Art. no. 4, Apr. 2018, doi: 10.1002/smtd.201700313.

[4] V. V. Maslyuk, R. Gutierrez, A. Dianat, V. Mujica, and G. Cuniberti, ‘Enhanced Magnetoresistance in Chiral Molecular Junctions’, *J. Phys. Chem. Lett.*, vol. 9, no. 18, Art. no. 18, Sep. 2018, doi: 10.1021/acs.jpclett.8b02360.

[5] D. H. Waldeck, R. Naaman, and Y. Paltiel, ‘The spin selectivity effect in chiral materials’, *APL Mater.*, vol. 9, no. 4, Art. no. 4, Apr. 2021, doi: 10.1063/5.0049150.

[6] K. Ray, S. P. Ananthavel, D. H. Waldeck, and R. Naaman, ‘Asymmetric Scattering of Polarized Electrons by Organized Organic Films of Chiral Molecules’, *Science*, vol. 283, no. 5403, pp. 814–816, Feb. 1999, doi: 10.1126/science.283.5403.814.

[7] S. Mayer and J. Kessler, ‘Experimental Verification of Electron Optic Dichroism’, *Phys. Rev. Lett.*, vol. 74, no. 24, pp. 4803–4806, Jun. 1995, doi: 10.1103/PhysRevLett.74.4803.

[8] G. L. J. A. Rikken and E. Raupach, ‘Observation of magneto-chiral dichroism’, *Nature*, vol. 390, no. 6659, pp. 493–494, Dec. 1997, doi: 10.1038/37323.

[9] Y. Adhikari *et al.*, ‘Interplay of structural chirality, electron spin and topological orbital in chiral molecular spin valves’, *Nat. Commun.*, vol. 14, no. 1, Art. no. 1, Aug. 2023, doi: 10.1038/s41467-023-40884-9.

[10] B. Gohler *et al.*, ‘Spin Selectivity in Electron Transmission Through Self-Assembled Monolayers of Double-Stranded DNA’, *Science*, vol. 331, no. 6019, Art. no. 6019, Feb. 2011, doi: 10.1126/science.1199339.

[11] I. Carmeli, V. Skakalova, R. Naaman, and Z. Vager, ‘Magnetization of Chiral Monolayers of Polypeptide: A Possible Source of Magnetism in Some Biological Membranes’, *Angew. Chem.*

*Int. Ed.*, vol. 41, no. 5, pp. 761–764, 2002, doi: 10.1002/1521-3773(20020301)41:5<761::AID-ANIE761>3.0.CO;2-Z.

[12] M. Kettner *et al.*, ‘Spin Filtering in Electron Transport Through Chiral Oligopeptides’, *J. Phys. Chem. C*, vol. 119, no. 26, Art. no. 26, Luglio 2015, doi: 10.1021/jp509974z.

[13] D. Mishra *et al.*, ‘Spin-dependent electron transmission through bacteriorhodopsin embedded in purple membrane’, *Proc. Natl. Acad. Sci.*, vol. 110, no. 37, pp. 14872–14876, Sep. 2013, doi: 10.1073/pnas.1311493110.

[14] J. M. Abendroth *et al.*, ‘Spin Selectivity in Photoinduced Charge-Transfer Mediated by Chiral Molecules’, *ACS Nano*, vol. 13, no. 5, pp. 4928–4946, May 2019, doi: 10.1021/acsnano.9b01876.

[15] S. G. Ray, S. S. Daube, G. Leitus, Z. Vager, and R. Naaman, ‘Chirality-Induced Spin-Selective Properties of Self-Assembled Monolayers of DNA on Gold’, *Phys. Rev. Lett.*, vol. 96, no. 3, p. 036101, Jan. 2006, doi: 10.1103/PhysRevLett.96.036101.

[16] M. Á. Niño, I. A. Kowalik, F. J. Luque, D. Arvanitis, R. Miranda, and J. J. de Miguel, ‘Enantiospecific Spin Polarization of Electrons Photoemitted Through Layers of Homochiral Organic Molecules’, *Adv. Mater.*, vol. 26, no. 44, pp. 7474–7479, 2014, doi: 10.1002/adma.201402810.

[17] M. Kettner *et al.*, ‘Chirality-Dependent Electron Spin Filtering by Molecular Monolayers of Helicenes’, *J. Phys. Chem. Lett.*, vol. 9, no. 8, pp. 2025–2030, Apr. 2018, doi: 10.1021/acs.jpclett.8b00208.

[18] A. K. Mondal *et al.*, ‘Spin Filtering in Supramolecular Polymers Assembled from Achiral Monomers Mediated by Chiral Solvents’, *J. Am. Chem. Soc.*, vol. 143, no. 18, pp. 7189–7195, May 2021, doi: 10.1021/jacs.1c02983.

[19] S. Mishra, A. Kumar, M. Venkatesan, L. Pigani, L. Pasquali, and C. Fontanesi, ‘Exchange Interactions Drive Supramolecular Chiral Induction in Polyaniline (Small Methods 10/2020)’, *Small Methods*, vol. 4, no. 10, Art. no. 10, 2020, doi: https://doi.org/10.1002/smtd.202070038.

[20] U. Huizi-Rayo *et al.*, ‘An Ideal Spin Filter: Long-Range, High-Spin Selectivity in Chiral Helicoidal 3-Dimensional Metal Organic Frameworks’, *Nano Lett.*, vol. 20, no. 12, Art. no. 12, Dec. 2020, doi: 10.1021/acs.nanolett.0c02349.

[21] H. Lu *et al.*, ‘Spin-dependent charge transport through 2D chiral hybrid lead-iodide perovskites’, *Sci. Adv.*, vol. 5, no. 12, Art. no. 12, Dec. 2019, doi: 10.1126/sciadv.aay0571.

[22] Y.-H. Kim *et al.*, ‘Chiral-induced spin selectivity enables a room-temperature spin light-emitting diode’, *Science*, vol. 371, no. 6534, pp. 1129–1133, Mar. 2021, doi: 10.1126/science.abf5291.

[23] Q. Qian *et al.*, ‘Chiral molecular intercalation superlattices’, *Nature*, vol. 606, no. 7916, Art. no. 7916, Jun. 2022, doi: 10.1038/s41586-022-04846-3.

[24] H. Al-Bustami *et al.*, ‘Atomic and Molecular Layer Deposition of Chiral Thin Films Showing up to 99% Spin Selective Transport’, *Nano Lett.*, vol. 22, no. 12, pp. 5022–5028, Jun. 2022, doi: 10.1021/acs.nanolett.2c01953.

[25] T. J. Zwang, S. Hürlimann, M. G. Hill, and J. K. Barton, ‘Helix-Dependent Spin Filtering through the DNA Duplex’, *J. Am. Chem. Soc.*, vol. 138, no. 48, Art. no. 48, Dec. 2016, doi: 10.1021/jacs.6b10538.

[26] J. M. Abendroth *et al.*, ‘Analyzing Spin Selectivity in DNA-Mediated Charge Transfer via Fluorescence Microscopy’, *ACS Nano*, vol. 11, no. 7, Art. no. 7, Jul. 2017, doi: 10.1021/acsnano.7b04165.

[27] J. M. Abendroth *et al.*, ‘Spin-Dependent Ionization of Chiral Molecular Films’, *J. Am. Chem. Soc.*, vol. 141, no. 9, Art. no. 9, Mar. 2019, doi: 10.1021/jacs.8b08421.

[28] P. C. Mondal, C. Fontanesi, D. H. Waldeck, and R. Naaman, ‘Field and Chirality Effects on Electrochemical Charge Transfer Rates: Spin Dependent Electrochemistry’, *ACS Nano*, vol. 9, no. 3, pp. 3377–3384, Mar. 2015, doi: 10.1021/acsnano.5b00832.

[29] T. Benincori *et al.*, ‘Highlighting spin selectivity properties of chiral electrode surfaces from redox potential modulation of an achiral probe under an applied magnetic field’, *Chem. Sci.*, vol. 10, no. 9, Art. no. 9, Feb. 2019, doi: 10.1039/C8SC04126A.

[30] C. Kulkarni *et al.*, ‘Highly Efficient and Tunable Filtering of Electrons’ Spin by Supramolecular Chirality of Nanofiber-Based Materials’, *Adv. Mater.*, vol. 32, no. 7, Art. no. 7, 2020, doi: 10.1002/adma.201904965.

[31] M. S. Zöllner, S. Varela, E. Medina, V. Mujica, and C. Herrmann, ‘Insight into the Origin of Chiral-Induced Spin Selectivity from a Symmetry Analysis of Electronic Transmission’, *J. Chem. Theory Comput.*, vol. 16, no. 5, Art. no. 5, May 2020, doi: 10.1021/acs.jctc.9b01078.

[32] E. E. Havinga, M. M. Bouman, E. W. Meijer, A. Pomp, and M. M. J. Simenon, ‘Large induced optical activity in the conduction band of polyaniline doped with (1S)-(+)-10-camphorsulfonic acid’, *Synth. Met.*, vol. 66, no. 1, Art. no. 1, Sep. 1994, doi: 10.1016/0379-6779(94)90168-6.

[33] F. Evers *et al.*, ‘Theory of Chirality Induced Spin Selectivity: Progress and Challenges’, *Adv. Mater.*, vol. 34, no. 13, p. 2106629, 2022, doi: 10.1002/adma.202106629.

[34] C. Fontanesi, A. Kumar, and P. Mondal, ‘Overview on Induced Chirality in Magnetic Field Controlled Electro-Deposition and Induced Magnetic Moment Originating from Chiral Electrodes’, CHEMISTRY, preprint, Jun. 2018. doi: 10.20944/preprints201806.0186.v1.

[35] B. P. Bloom, A. R. Waldeck, and D. H. Waldeck, ‘Homochirality and chiral-induced spin selectivity: A new spin on the origin of life’, *Proc. Natl. Acad. Sci.*, vol. 119, no. 34, p. e2210505119, Aug. 2022, doi: 10.1073/pnas.2210505119.

[36] J. L. Bada, ‘Origins of homochirality’, *Nature*, vol. 374, no. 6523, Art. no. 6523, Apr. 1995, doi: 10.1038/374594a0.

[37] S. Greed, ‘The dawn of asymmetry’, *Nat. Rev. Chem.*, vol. 6, no. 9, Art. no. 9, Sep. 2022, doi: 10.1038/s41570-022-00419-0.

[38] A. Guijarro and M. Yus, *The Origin of Chirality in the Molecules of Life: A Revision from Awareness to the Current Theories and Perspectives of this Unsolved Problem*. Royal Society of Chemistry, 2008.

[39] S. F. Ozturk, Z. Liu, J. D. Sutherland, and D. D. Sasselov, ‘Origin of biological homochirality by crystallization of an RNA precursor on a magnetic surface’, *Sci. Adv.*, vol. 9, no. 23, p. eadg8274, Jun. 2023, doi: 10.1126/sciadv.adg8274.

[40] R. Naaman, Y. Paltiel, and D. H. Waldeck, ‘Chiral Induced Spin Selectivity and Its Implications for Biological Functions’, *Annu. Rev. Biophys.*, vol. 51, no. 1, pp. 99–114, 2022, doi: 10.1146/annurev-biophys-083021-070400.

[41] A. Ziv *et al.*, ‘AFM-Based Spin-Exchange Microscopy Using Chiral Molecules’, *Adv. Mater. Deerfield Beach Fla*, vol. 31, no. 40, p. e1904206, Oct. 2019, doi: 10.1002/adma.201904206.

[42] A. Kumar *et al.*, ‘Chirality-induced spin polarization places symmetry constraints on biomolecular interactions’, *Proc. Natl. Acad. Sci.*, vol. 114, no. 10, pp. 2474–2478, Mar. 2017, doi: 10.1073/pnas.1611467114.

[43] M. Singh, S. Sethi, and R. Bhushan, ‘Liquid chromatographic methods for separation, determination, and bioassay of enantiomers of etodolac: A review’, *J. Sep. Sci.*, vol. 43, no. 1, pp. 18–30, 2020, doi: 10.1002/jssc.201900649.

[44] M. M. Coelho, C. Fernandes, F. Remião, and M. E. Tiritan, ‘Enantioselectivity in Drug Pharmacokinetics and Toxicity: Pharmacological Relevance and Analytical Methods’, *Molecules*, vol. 26, no. 11, Art. no. 11, Jan. 2021, doi: 10.3390/molecules26113113.

[45] N. Davies and X. Teng, ‘Importance of Chirality in Drug Therapy and Pharmacy Practice : Implications for Psychiatry’, 2003. Accessed: Oct. 24, 2023. [Online]. Available: https://www.semanticscholar.org/paper/Importance-of-Chirality-in-Drug-Therapy-and-%3A-for-Davies-Teng/f51eef1c63b18d405e29694767d994a38b7150d2

[46] J. Ceramella *et al.*, ‘A Look at the Importance of Chirality in Drug Activity: Some Significative Examples’, *Appl. Sci.*, vol. 12, no. 21, Art. no. 21, Jan. 2022, doi: 10.3390/app122110909.

[47] J. Pu, H. Wang, C. Huang, C. Bo, B. Gong, and J. Ou, ‘Progress of molecular imprinting technique for enantioseparation of chiral drugs in recent ten years’, *J. Chromatogr. A*, vol. 1668, p. 462914, Apr. 2022, doi: 10.1016/j.chroma.2022.462914.

[48] W. Gong, Z. Chen, J. Dong, Y. Liu, and Y. Cui, ‘Chiral Metal–Organic Frameworks’, *Chem. Rev.*, vol. 122, no. 9, pp. 9078–9144, May 2022, doi: 10.1021/acs.chemrev.1c00740.

[49] P. C. Mondal, D. Asthana, R. K. Parashar, and S. Jadhav, ‘Imprinting chirality in inorganic nanomaterials for optoelectronic and bio-applications: strategies, challenges, and opportunities’, *Mater. Adv.*, vol. 2, no. 23, pp. 7620–7637, 2021, doi: 10.1039/D1MA00846C.

[50] C. Noguez and I. L. Garzón, ‘Optically active metal nanoparticles’, *Chem. Soc. Rev.*, vol. 38, no. 3, pp. 757–771, Feb. 2009, doi: 10.1039/B800404H.

[51] S. Jiang, K. Y. Win, S. Liu, C. P. Teng, Y. Zheng, and M.-Y. Han, ‘Surface-functionalized nanoparticles for biosensing and imaging-guided therapeutics’, *Nanoscale*, vol. 5, no. 8, pp. 3127–3148, Mar. 2013, doi: 10.1039/C3NR34005H.

[52] M. P. Moloney, J. Govan, A. Loudon, M. Mukhina, and Y. K. Gun’ko, ‘Preparation of chiral quantum dots’, *Nat. Protoc.*, vol. 10, no. 4, Art. no. 4, Apr. 2015, doi: 10.1038/nprot.2015.028.

[53] G. Li *et al.*, ‘Fluorescence and Optical Activity of Chiral CdTe Quantum Dots in Their Interaction with Amino Acids’, *ACS Nano*, vol. 14, no. 4, pp. 4196–4205, Apr. 2020, doi: 10.1021/acsnano.9b09101.

[54] N. Suzuki *et al.*, ‘Chiral Graphene Quantum Dots’, *ACS Nano*, vol. 10, no. 2, pp. 1744–1755, Feb. 2016, doi: 10.1021/acsnano.5b06369.

[55] B. Zhou *et al.*, 'Surface engineering strategies of gold nanomaterials and their applications in biomedicine and detection', *J. Mater. Chem. B*, vol. 9, no. 28, pp. 5583–5598, Jul. 2021, doi: 10.1039/D1TB00181G.

[56] H. Jeon, R. Zhu, G. Kim, and Y. Wang, 'Chirality-enhanced transport and drug delivery of graphene nanocarriers to tumor-like cellular spheroid', *Front. Chem.*, vol. 11, 2023, Accessed: Oct. 24, 2023. [Online]. Available: https://www.frontiersin.org/articles/10.3389/fchem.2023.1207579

[57] Q. Yang *et al.*, 'Realization of High Spin Injection Through Chiral Molecules and Its Application in Logic Device', *IEEE Electron Device Lett.*, vol. 43, no. 11, pp. 1862–1865, Nov. 2022, doi: 10.1109/LED.2022.3208856.

[58] P. J. Hore and H. Mouritsen, 'The Radical-Pair Mechanism of Magnetoreception', *Annu. Rev. Biophys.*, vol. 45, no. 1, pp. 299–344, 2016, doi: 10.1146/annurev-biophys-032116-094545.

[59] O. B. Dor, S. Yochelis, S. P. Mathew, R. Naaman, and Y. Paltiel, 'A chiral-based magnetic memory device without a permanent magnet', *Nat. Commun.*, vol. 4, no. 1, Art. no. 1, Aug. 2013, doi: 10.1038/ncomms3256.

[60] Z. Shang *et al.*, 'Chiral-Molecule-Based Spintronic Devices', *Small*, vol. 18, no. 32, p. 2203015, 2022, doi: 10.1002/smll.202203015.

[61] Y. Huai, 'Spin-Transfer Torque MRAM (STT-MRAM): Challenges and Prospects', 2008. Accessed: Oct. 26, 2023. [Online]. Available: https://www.semanticscholar.org/paper/Spin-Transfer-Torque-MRAM-(STT-MRAM)%3A-Challenges-Huai/0322c80c8b69d4efb256482165da7e230752ef43

[62] J. A. Katine and E. E. Fullerton, 'Device implications of spin-transfer torques', *J. Magn. Magn. Mater.*, vol. 320, no. 7, pp. 1217–1226, Apr. 2008, doi: 10.1016/j.jmmm.2007.12.013.

[63] T. Liu *et al.*, 'Linear and Nonlinear Two-Terminal Spin-Valve Effect from Chirality-Induced Spin Selectivity', *ACS Nano*, vol. 14, no. 11, pp. 15983–15991, Nov. 2020, doi: 10.1021/acsnano.0c07438.

[64] M. Agnes, A. Nitti, D. A. V. Griend, D. Dondi, D. Merli, and D. Pasini, 'A chiroptical molecular sensor for ferrocene', *Chem. Commun.*, vol. 52, no. 77, Art. no. 77, Sep. 2016, doi: 10.1039/C6CC05937F.

[65] F. Sannicolò *et al.*, 'Inherently Chiral Spider-Like Oligothiophenes', *Chem. – Eur. J.*, vol. 22, no. 31, Art. no. 31, Jul. 2016, doi: 10.1002/chem.201504899.

[66] L. Dong, Y. Zhang, X. Duan, X. Zhu, H. Sun, and J. Xu, ‘Chiral PEDOT-Based Enantioselective Electrode Modification Material for Chiral Electrochemical Sensing: Mechanism and Model of Chiral Recognition’, *Anal. Chem.*, vol. 89, no. 18, Art. no. 18, Sep. 2017, doi: 10.1021/acs.analchem.7b01095.

[67] B. Liu, F. Wu, H. Gui, M. Zheng, and C. Zhou, ‘Chirality-Controlled Synthesis and Applications of Single-Wall Carbon Nanotubes’, *ACS Nano*, vol. 11, no. 1, pp. 31–53, Jan. 2017, doi: 10.1021/acsnano.6b06900.

[68] T. van Leeuwen, W. Danowski, E. Otten, S. J. Wezenberg, and B. L. Feringa, ‘Asymmetric Synthesis of Second-Generation Light-Driven Molecular Motors’, *J. Org. Chem.*, vol. 82, no. 10, Art. no. 10, May 2017, doi: 10.1021/acs.joc.7b00852.

[69] B. P. Bloom *et al.*, ‘Asymmetric reactions induced by electron spin polarization’, *Phys. Chem. Chem. Phys.*, vol. 22, no. 38, pp. 21570–21582, Oct. 2020, doi: 10.1039/D0CP03129A.

[70] W. Mtangi *et al.*, ‘Control of Electrons’ Spin Eliminates Hydrogen Peroxide Formation During Water Splitting’, *J. Am. Chem. Soc.*, vol. 139, no. 7, Art. no. 7, Feb. 2017, doi: 10.1021/jacs.6b12971.

[71] W. Mtangi, V. Kiran, C. Fontanesi, and R. Naaman, ‘Role of the Electron Spin Polarization in Water Splitting’, *J. Phys. Chem. Lett.*, vol. 6, no. 24, Art. no. 24, Dicembre 2015, doi: 10.1021/acs.jpclett.5b02419.

[72] R. Naaman, Y. Paltiel, and D. H. Waldeck, ‘Chiral Induced Spin Selectivity Gives a New Twist on Spin-Control in Chemistry’, *Acc. Chem. Res.*, vol. 53, no. 11, pp. 2659–2667, Nov. 2020, doi: 10.1021/acs.accounts.0c00485.

[73] S. Mishra, L. Pasquali, and C. Fontanesi, ‘Spin control using chiral templated nickel’, *Appl. Phys. Lett.*, vol. 118, no. 22, Art. no. 22, May 2021, doi: 10.1063/5.0049113.

[74] T. S. Metzger *et al.*, ‘Dynamic Spin-Controlled Enantioselective Catalytic Chiral Reactions’, *J. Phys. Chem. Lett.*, vol. 12, no. 23, pp. 5469–5472, Jun. 2021, doi: 10.1021/acs.jpclett.1c01518.

[75] J. C. Cuevas and E. Scheer, *Molecular electronics: an introduction to theory and experiment*. in World Scientific series in nanoscience and nanotechnology, no. v. 1. Singapore ; Hackensack, NJ: World Scientific, 2010.

[76] S. Li *et al.*, ‘Transition between Nonresonant and Resonant Charge Transport in Molecular Junctions’, *Nano Lett.*, vol. 21, no. 19, pp. 8340–8347, Oct. 2021, doi: 10.1021/acs.nanolett.1c02915.

[77] C. P. De Melo and A. C. L. Moreira, ‘Non-Coherent Charge Transport in Donor–Acceptor Systems: A Self-Consistent Description of the Intramolecular Charge Flow’, *J. Phys. Chem. C*, vol. 116, no. 4, pp. 3122–3131, Feb. 2012, doi: 10.1021/jp207299n.

[78] A. A. Kocherzhenko, F. C. Grozema, and L. D. A. Siebbeles, ‘Single molecule charge transport: from a quantum mechanical to a classical description’, *Phys Chem Chem Phys*, vol. 13, no. 6, pp. 2096–2110, 2011, doi: 10.1039/C0CP01432J.

[79] A. De Sio and C. Lienau, ‘Vibronic coupling in organic semiconductors for photovoltaics’, *Phys. Chem. Chem. Phys.*, vol. 19, no. 29, pp. 18813–18830, 2017, doi: 10.1039/C7CP03007J.

[80] Y. Imry and R. Landauer, ‘Conductance viewed as transmission’, *Rev Mod Phys*, vol. 71, no. 2, 1999.

[81] V. Gasparian, ‘Büttiker–Landauer tunneling time through one-dimensional barriers of arbitrary shape’, *Superlattices Microstruct.*, vol. 23, no. 3, pp. 809–821, Mar. 1998, doi: 10.1006/spmi.1997.0542.

[82] S. Datta, *Quantum Transport: Atom to Transistor*. Cambridge: Cambridge University Press, 2005. doi: 10.1017/CBO9781139164313.

[83] A. Kahn, ‘Fermi level, work function and vacuum level’, *Mater. Horiz.*, vol. 3, no. 1, pp. 7–10, 2016, doi: 10.1039/C5MH00160A.

[84] M. Razavy, *Quantum Theory of Tunneling*. WORLD SCIENTIFIC, 2003. doi: 10.1142/4984.

[85] P. Basnet, ‘METAL OXIDE PHOTOCATALYTIC NANOSTRUCTURES FABRICATED BY DYNAMIC SHADOWING GROWTH’, 2015. doi: 10.13140/RG.2.1.2393.8408.

[86] X. Song, B. Han, X. Yu, and W. Hu, ‘The analysis of charge transport mechanism in molecular junctions based on current-voltage characteristics’, *Chem. Phys.*, vol. 528, p. 110514, Jan. 2020, doi: 10.1016/j.chemphys.2019.110514.

[87] A. Stefani *et al.*, ‘Chiral Recognition: A Spin-Driven Process in Chiral Oligothiophene. A Chiral-Induced Spin Selectivity (CISS) Effect Manifestation’, *Adv. Funct. Mater.*, vol. n/a, no. n/a, p. 2308948, doi: 10.1002/adfm.202308948.

[88] S. J. Tans *et al.*, ‘Individual single-wall carbon nanotubes as quantum wires’, *Nature*, vol. 386, no. 6624, Art. no. 6624, Apr. 1997, doi: 10.1038/386474a0.

[89] J. G. Kushmerick, J. Lazorcik, C. H. Patterson, R. Shashidhar, D. S. Seferos, and G. C. Bazan, ‘Vibronic Contributions to Charge Transport Across Molecular Junctions’, *Nano Lett.*, vol. 4, no. 4, pp. 639–642, Apr. 2004, doi: 10.1021/nl049871n.

[90] Z. Shuai, W. Li, J. Ren, Y. Jiang, and H. Geng, ‘Applying Marcus theory to describe the carrier transports in organic semiconductors: Limitations and beyond’, *J. Chem. Phys.*, vol. 153, no. 8, p. 080902, Aug. 2020, doi: 10.1063/5.0018312.

[91] N. Lu, L. Li, D. Geng, and M. Liu, ‘A review for polaron dependent charge transport in organic semiconductor’, *Org. Electron.*, vol. 61, pp. 223–234, Oct. 2018, doi: 10.1016/j.orgel.2018.05.053.

[92] J. H. Bombile, M. J. Janik, and S. T. Milner, ‘Tight binding model of conformational disorder effects on the optical absorption spectrum of polythiophenes’, *Phys. Chem. Chem. Phys.*, vol. 18, no. 18, pp. 12521–12533, May 2016, doi: 10.1039/C6CP00832A.

[93] P. W. Anderson, ‘The Size of Localized States Near the Mobility Edge’, *Proc. Natl. Acad. Sci.*, vol. 69, no. 5, pp. 1097–1099, May 1972, doi: 10.1073/pnas.69.5.1097.

[94] A. Migliore and A. Nitzan, ‘Nonlinear Charge Transport in Redox Molecular Junctions: A Marcus Perspective’, *ACS Nano*, vol. 5, no. 8, pp. 6669–6685, Aug. 2011, doi: 10.1021/nn202206e.

[95] T. Holstein, ‘Studies of polaron motion: Part I. The molecular-crystal model’, *Ann. Phys.*, vol. 8, no. 3, pp. 325–342, Nov. 1959, doi: 10.1016/0003-4916(59)90002-8.

[96] C. Franchini, M. Reticcioli, M. Setvin, and U. Diebold, ‘Polarons in materials’, *Nat. Rev. Mater.*, vol. 6, no. 7, Art. no. 7, Jul. 2021, doi: 10.1038/s41578-021-00289-w.

[97] J. Potticary *et al.*, ‘An unforeseen polymorph of coronene by the application of magnetic fields during crystal growth’, *Nat. Commun.*, vol. 7, no. 1, p. 11555, May 2016, doi: 10.1038/ncomms11555.

[98] R. A. Marcus, ‘Electrostatic Free Energy and Other Properties of States Having Nonequilibrium Polarization. I’, *J. Chem. Phys.*, vol. 24, no. 5, pp. 979–989, May 1956, doi: 10.1063/1.1742724.

[99] M. Andrea, ‘Marcus Theory for Electron Transfer a short introduction’.

[100] A. A. Voityuk, ‘Electronic coupling for charge transfer in donor–bridge–acceptor systems. Performance of the two-state FCD model’, *Phys. Chem. Chem. Phys.*, vol. 14, no. 40, p. 13789, 2012, doi: 10.1039/c2cp40579b.

[101] R. Saxena *et al.*, ‘Role of the reorganization energy for charge transport in disordered organic semiconductors’, *Phys. Rev. B*, vol. 103, no. 16, p. 165202, Apr. 2021, doi: 10.1103/PhysRevB.103.165202.

[102] M. Sato, A. Kumada, K. Hidaka, T. Hirano, and F. Sato, ‘Can classical marcus theory describe hole transfer in polyethylene?’, *IEEE Trans. Dielectr. Electr. Insul.*, vol. 23, no. 5, pp. 2978–2984, Oct. 2016, doi: 10.1109/TDEI.2016.7736861.

[103] T. Holstein, ‘Studies of polaron motion: Part II. The “small” polaron’, *Ann. Phys.*, vol. 8, no. 3, pp. 343–389, Nov. 1959, doi: 10.1016/0003-4916(59)90003-X.

[104] X. Sun and E. Geva, ‘Equilibrium Fermi’s Golden Rule Charge Transfer Rate Constants in the Condensed Phase: The Linearized Semiclassical Method vs Classical Marcus Theory’, *J. Phys. Chem. A*, vol. 120, no. 19, pp. 2976–2990, May 2016, doi: 10.1021/acs.jpca.5b08280.

[105] K. K. Liang *et al.*, ‘Influence of distortion and Duschinsky effects on Marcus-type theories of electron transfer rate’, *Phys. Chem. Chem. Phys.*, vol. 5, no. 20, pp. 4656–4665, Oct. 2003, doi: 10.1039/B305173K.

[106] ‘Contemporary Issues in Electron Transfer Research | The Journal of Physical Chemistry’. Accessed: Sep. 10, 2023. [Online]. Available: https://pubs.acs.org/doi/10.1021/jp9605663

[107] S. G. Christov, ‘Quantum Theory of Charge-Transfer Processes in Condensed Media’, in *Modern Aspects of Electrochemistry: Volume 28*, B. E. Conway, J. O. Bockris, and R. E. White, Eds., in Modern Aspects of Electrochemistry. , Boston, MA: Springer US, 1996, pp. 167–288. doi: 10.1007/978-1-4899-1718-8_4.

[108] ‘Quantum Mechanics in Chemistry — Northwestern Scholars’. Accessed: Sep. 10, 2023. [Online]. Available: https://www.scholars.northwestern.edu/en/publications/quantum-mechanics-in-chemistry

[109] M. D. Newton, ‘Quantum chemical probes of electron-transfer kinetics: the nature of donor-acceptor interactions’, ACS Publications. Accessed: Sep. 10, 2023. [Online]. Available: https://pubs.acs.org/doi/pdf/10.1021/cr00005a007

[110] J. Jortner, M. Bixon, T. Langenbacher, and M. E. Michel-Beyerle, ‘Charge transfer and transport in DNA’, *Proc. Natl. Acad. Sci.*, vol. 95, no. 22, pp. 12759–12765, Oct. 1998, doi: 10.1073/pnas.95.22.12759.

[111] J. M. Thijssen and H. S. J. Van der Zant, ‘Charge transport and single-electron effects in nanoscale systems’, *Phys. Status Solidi B*, vol. 245, no. 8, pp. 1455–1470, 2008, doi: 10.1002/pssb.200743470.

[112] M. Bixon and J. Jortner, ‘Charge Transport in DNA Via Thermally Induced Hopping’, *J. Am. Chem. Soc.*, vol. 123, no. 50, pp. 12556–12567, Dec. 2001, doi: 10.1021/ja010018p.

[113] A. K. Felts, W. T. Pollard, and R. A. Friesner, ‘Multilevel Redfield Treatment of Bridge-Mediated Long-Range Electron Transfer: A Mechanism for Anomalous Distance Dependence’, ACS Publications. Accessed: Sep. 10, 2023. [Online]. Available: https://pubs.acs.org/doi/pdf/10.1021/j100009a057

[114] J. Jortner, ‘Temperature dependent activation energy for electron transfer between biological molecules’, *J. Chem. Phys.*, vol. 64, no. 12, pp. 4860–4867, Aug. 2008, doi: 10.1063/1.432142.

[115] M. V. Basilevsky, A. V. Soudackov, and M. V. Vener, ‘Electron-proton free-energy surfaces for proton transfer reaction in polar solvents: test calculations for carbon-carbon reaction centres’, *Chem. Phys.*, vol. 200, no. 1, pp. 87–106, Nov. 1995, doi: 10.1016/0301-0104(95)00227-F.

[116] Y.-C. Wei and L.-Y. Hsu, ‘Polaritonic Huang–Rhys Factor: Basic Concepts and Quantifying Light–Matter Interactions in Media’, *J. Phys. Chem. Lett.*, vol. 14, no. 9, pp. 2395–2401, Mar. 2023, doi: 10.1021/acs.jpclett.3c00065.

[117] ‘Recherches sur les Relations qui Peuvent Exister entre la Forme Crystalline, la Composition Chimique et le Sens de la Polarisation Rotatoire’, *Ann Chim Phys*, vol. 24, pp. 442–459, 1848.

[118] ‘Pasteur, M. L. Mémoire sur la Fermentation de l’Acide Tartrique’, *C R Séances Acad Sci*, vol. 46, pp. 615–618.

[119] A. Berthod, ‘Chiral Recognition Mechanisms’, *Anal. Chem.*, vol. 78, no. 7, pp. 2093–2099, Apr. 2006, doi: 10.1021/ac0693823.

[120] W. T. Kelvin, *Baltimore lectures on molecular dynamics and the wave theory of light*. London, Baltimore: C. J. Clay and sons, 1904.

[121] ‘Stereoisomers’. Accessed: Aug. 29, 2023. [Online]. Available: https://www2.chemistry.msu.edu/faculty/reusch/virttxtjml/chapt11.htm

[122] ‘Chirality (chemistry)’, *Wikipedia*. Jun. 30, 2023. Accessed: Aug. 28, 2023. [Online]. Available: https://en.wikipedia.org/w/index.php?title=Chirality_(chemistry)&oldid=1162732602

[123] V. Böhmer, D. Kraft, and M. Tabatabai, ‘Inherently chiral calixarenes’, *J. Incl. Phenom. Mol. Recognit. Chem.*, vol. 19, no. 1, pp. 17–39, Mar. 1994, doi: 10.1007/BF00708972.

[124] ‘Electroactive Inherently Chiral Surfaces at Work: Clues Toward the Elucidation of the Enantioselection Mechanism’. Accessed: Aug. 30, 2023. [Online]. Available: https://air.unimi.it/handle/2434/588609

[125] S. Arnaboldi *et al.*, ‘Inherently chiral electrodes: the tool for chiral voltammetry’, *Chem. Sci.*, vol. 6, no. 3, pp. 1706–1711, Feb. 2015, doi: 10.1039/C4SC03713H.

[126] F. Sannicolò *et al.*, ‘Potential-driven chirality manifestations and impressive enantioselectivity by inherently chiral electroactive organic films’, *Angew. Chem. Int. Ed Engl.*, vol. 53, no. 10, pp. 2623–2627, Mar. 2014, doi: 10.1002/anie.201309585.

[127] S. Arnaboldi *et al.*, ‘Thiahelicene-based inherently chiral films for enantioselective electroanalysis’, *Chem. Sci.*, vol. 10, no. 5, pp. 1539–1548, 2019, doi: 10.1039/C8SC03337D.

[128] E. Flapan, ‘Topological chirality and symmetries of non-rigid molecules’, in *Proceedings of Symposia in Applied Mathematics*, vol. 66, D. Buck and E. Flapan, Eds., Providence, Rhode Island: American Mathematical Society, 2009, pp. 21–45. doi: 10.1090/psapm/066/2508727.

[129] P. Le Guennec, ‘Two-dimensional theory of chirality. I. Absolute chirality’, *J. Math. Phys.*, vol. 41, no. 9, pp. 5954–5985, Sep. 2000, doi: 10.1063/1.1285982.

[130] G. L. J. A. Rikken and E. Raupach, ‘Enantioselective magnetochiral photochemistry’, *Nature*, vol. 405, no. 6789, pp. 932–935, Jun. 2000, doi: 10.1038/35016043.

[131] B. P. Bloom, B. M. Graff, S. Ghosh, D. N. Beratan, and D. H. Waldeck, ‘Chirality Control of Electron Transfer in Quantum Dot Assemblies’, *J. Am. Chem. Soc.*, vol. 139, no. 26, pp. 9038–9043, Jul. 2017, doi: 10.1021/jacs.7b04639.

[132] M. Hu *et al.*, ‘Chiral recognition and enantiomer excess determination based on emission wavelength change of AIEgen rotor’, *Nat. Commun.*, vol. 11, no. 1, Art. no. 1, Jan. 2020, doi: 10.1038/s41467-019-13955-z.

[133] S. F. Mason, ‘The development of concepts of chiral discrimination’, *Chirality*, vol. 1, no. 3, pp. 183–191, 1989, doi: 10.1002/chir.530010302.

[134] I. Meirzada *et al.*, ‘Long-Time-Scale Magnetization Ordering Induced by an Adsorbed Chiral Monolayer on Ferromagnets’, *ACS Nano*, vol. 15, no. 3, pp. 5574–5579, Mar. 2021, doi: 10.1021/acsnano.1c00455.

[135] R. Malatong *et al.*, ‘Highly Durable Spin Filter Switching Based on Self-Assembled Chiral Molecular Motor’, *Small*, vol. 19, no. 32, p. 2302714, 2023, doi: 10.1002/smll.202302714.

[136] V. Kiran, S. P. Mathew, S. R. Cohen, I. Hernández Delgado, J. Lacour, and R. Naaman, ‘Helicenes--A New Class of Organic Spin Filter’, *Adv. Mater. Deerfield Beach Fla*, vol. 28, no. 10, pp. 1957–1962, Mar. 2016, doi: 10.1002/adma.201504725.

[137] T. Jiang *et al.*, ‘Thiophene Derivatives on Gold and Molecular Dissociation Processes’, *J. Phys. Chem. C*, vol. 121, no. 50, Art. no. 50, Dec. 2017, doi: 10.1021/acs.jpcc.7b08006.

[138] V. Malytskyi, V. Gadenne, Y. Ksari, L. Patrone, and J.-M. Raimundo, ‘Synthesis and characterization of thiophene-based push-pull chromophores for tuning the electrical and optical properties of surfaces with controlled SAM formation’, *Tetrahedron*, vol. 73, no. 39, pp. 5738–5744, Sep. 2017, doi: 10.1016/j.tet.2017.08.004.

[139] T. Matsuura, M. Nakajima, and Y. Shimoyama, ‘Growth of Self-Assembled Monolayer of Thiophene on Gold Surface: An Infrared Spectroscopic Study’, *Jpn. J. Appl. Phys.*, vol. 40, no. 12R, p. 6945, Dec. 2001, doi: 10.1143/JJAP.40.6945.

[140] D. Lee, S. Seong, and J. Noh, ‘Formation of a Highly-ordered Thiophene Monolayer on Au(111) via Vapor Phase Deposition’, *Bull. Korean Chem. Soc.*, vol. 40, no. 7, pp. 619–620, 2019, doi: 10.1002/bkcs.11744.

[141] Z. Xie, T. Z. Markus, S. R. Cohen, Z. Vager, R. Gutierrez, and R. Naaman, ‘Spin Specific Electron Conduction through DNA Oligomers’, *Nano Lett.*, vol. 11, no. 11, Art. no. 11, Nov. 2011, doi: 10.1021/nl2021637.

[142] V. Kiran, S. R. Cohen, and R. Naaman, ‘Structure dependent spin selectivity in electron transport through oligopeptides’, *J. Chem. Phys.*, vol. 146, no. 9, p. 092302, Mar. 2017, doi: 10.1063/1.4966237.

[143] B. P. Bloom, V. Kiran, V. Varade, R. Naaman, and David. H. Waldeck, ‘Spin Selective Charge Transport through Cysteine Capped CdSe Quantum Dots’, *Nano Lett.*, vol. 16, no. 7, pp. 4583–4589, Jul. 2016, doi: 10.1021/acs.nanolett.6b01880.

[144] P. C. Mondal, C. Fontanesi, D. H. Waldeck, and R. Naaman, ‘Spin-Dependent Transport through Chiral Molecules Studied by Spin-Dependent Electrochemistry’, *Acc. Chem. Res.*, vol. 49, no. 11, pp. 2560–2568, Nov. 2016, doi: 10.1021/acs.accounts.6b00446.

[145] O. Ben Dor, N. Morali, S. Yochelis, L. T. Baczewski, and Y. Paltiel, ‘Local Light-Induced Magnetization Using Nanodots and Chiral Molecules’, *Nano Lett.*, vol. 14, no. 11, pp. 6042–6049, Nov. 2014, doi: 10.1021/nl502391t.

[146] S. Barman, A. Ganguly, and A. Barman, ‘Configuration and polarization dependent transverse domain wall motion and domain wall switching in ferromagnetic nanowire’, *SPIN*, vol. 03, no. 01, p. 1350001, Mar. 2013, doi: 10.1142/S201032471350001X.

[147] A. C. Aragonès *et al.*, ‘Measuring the Spin-Polarization Power of a Single Chiral Molecule’, *Small Weinh. Bergstr. Ger.*, vol. 13, no. 2, Jan. 2017, doi: 10.1002/smll.201602519.

[148] H. Al-Bustami *et al.*, ‘Single Nanoparticle Magnetic Spin Memristor’, *Small*, vol. 14, no. 30, p. 1801249, 2018, doi: 10.1002/smll.201801249.

[149] G. Bullard *et al.*, ‘Low-Resistance Molecular Wires Propagate Spin-Polarized Currents’, *J. Am. Chem. Soc.*, vol. 141, no. 37, pp. 14707–14711, Sep. 2019, doi: 10.1021/jacs.9b06142.

[150] F. Tassinari *et al.*, ‘Chirality Dependent Charge Transfer Rate in Oligopeptides’, *Adv. Mater. Deerfield Beach Fla*, vol. 30, no. 21, p. e1706423, May 2018, doi: 10.1002/adma.201706423.

[151] J. J. Wei, C. Schafmeister, G. Bird, A. Paul, R. Naaman, and D. H. Waldeck, ‘Molecular chirality and charge transfer through self-assembled scaffold monolayers’, *J. Phys. Chem. B*, vol. 110, no. 3, pp. 1301–1308, Jan. 2006, doi: 10.1021/jp055145c.

[152] C. Fontanesi, ‘Spin-dependent electrochemistry: A novel paradigm’, *Curr. Opin. Electrochem.*, vol. 7, pp. 36–41, Jan. 2018, doi: 10.1016/j.coelec.2017.09.028.

[153] C. Wang, A.-M. Guo, Q.-F. Sun, and Y. Yan, ‘Efficient Spin-Dependent Charge Transmission and Improved Enantioselective Discrimination Capability in Self-Assembled Chiral Coordinated Monolayers’, *J. Phys. Chem. Lett.*, vol. 12, no. 42, pp. 10262–10269, Oct. 2021, doi: 10.1021/acs.jpclett.1c03106.

[154] R. Naaman and D. H. Waldeck, ‘Spintronics and Chirality: Spin Selectivity in Electron Transport Through Chiral Molecules’, *Annu. Rev. Phys. Chem.*, vol. 66, no. 1, pp. 263–281, 2015, doi: 10.1146/annurev-physchem-040214-121554.

[155] S. Mishra *et al.*, ‘Spin Filtering Along Chiral Polymers’, *Angew. Chem. Int. Ed.*, vol. 59, no. 34, pp. 14671–14676, 2020, doi: 10.1002/anie.202006570.

[156] M. Eckshtain-Levi *et al.*, ‘Cold denaturation induces inversion of dipole and spin transfer in chiral peptide monolayers’, *Nat. Commun.*, vol. 7, p. 10744, Feb. 2016, doi: 10.1038/ncomms10744.

[157] R. A. Rosenberg, M. Abu Haija, and P. J. Ryan, ‘Chiral-Selective Chemistry Induced by Spin-Polarized Secondary Electrons from a Magnetic Substrate’, *Phys. Rev. Lett.*, vol. 101, no. 17, p. 178301, Oct. 2008, doi: 10.1103/PhysRevLett.101.178301.

[158] R. A. Rosenberg, D. Mishra, and R. Naaman, ‘Chiral Selective Chemistry Induced by Natural Selection of Spin-Polarized Electrons’, *Angew. Chem. Int. Ed.*, vol. 54, no. 25, Art. no. 25, 2015, doi: https://doi.org/10.1002/anie.201501678.

[159] T. S. Metzger *et al.*, ‘The Electron Spin as a Chiral Reagent’, *Angew. Chem. Int. Ed.*, vol. 59, no. 4, pp. 1653–1658, 2020, doi: 10.1002/anie.201911400.

[160] ‘Chiral Reactions With Chiral Electrons’. Accessed: Sep. 20, 2023. [Online]. Available: https://www.science.org/content/blog-post/chiral-reactions-chiral-electrons

[161] M. Gazzotti *et al.*, ‘Spin-dependent electrochemistry: Enantio-selectivity driven by chiral-induced spin selectivity effect’, *Electrochimica Acta*, vol. 286, pp. 271–278, Oct. 2018, doi: 10.1016/j.electacta.2018.08.023.

[162] I. C. Man *et al.*, ‘Universality in Oxygen Evolution Electrocatalysis on Oxide Surfaces’, *ChemCatChem*, vol. 3, no. 7, pp. 1159–1165, 2011, doi: 10.1002/cctc.201000397.

[163] Q. Lei, B. Wang, P. Wang, and S. Liu, ‘Hydrogen generation with acid/alkaline amphoteric water electrolysis’, *J. Energy Chem.*, vol. 38, pp. 162–169, Nov. 2019, doi: 10.1016/j.jechem.2018.12.022.

[164] A. Vazhayil, L. Vazhayal, J. Thomas, S. Ashok C, and N. Thomas, ‘A comprehensive review on the recent developments in transition metal-based electrocatalysts for oxygen evolution reaction’, *Appl. Surf. Sci. Adv.*, vol. 6, p. 100184, Dec. 2021, doi: 10.1016/j.apsadv.2021.100184.

[165] A. Govind Rajan, J. M. P. Martirez, and E. A. Carter, ‘Why Do We Use the Materials and Operating Conditions We Use for Heterogeneous (Photo)Electrochemical Water Splitting?’, *ACS Catal.*, vol. 10, no. 19, pp. 11177–11234, Oct. 2020, doi: 10.1021/acscatal.0c01862.

[166] A. R. Zeradjanin *et al.*, ‘Rational design of the electrode morphology for oxygen evolution – enhancing the performance for catalytic water oxidation’, *RSC Adv.*, vol. 4, no. 19, pp. 9579–9587, Feb. 2014, doi: 10.1039/C3RA45998E.

[167] A. Grimaud *et al.*, ‘Double perovskites as a family of highly active catalysts for oxygen evolution in alkaline solution’, *Nat. Commun.*, vol. 4, no. 1, Art. no. 1, Sep. 2013, doi: 10.1038/ncomms3439.

[168] Z. W. Seh, J. Kibsgaard, C. F. Dickens, I. Chorkendorff, J. K. Nørskov, and T. F. Jaramillo, ‘Combining theory and experiment in electrocatalysis: Insights into materials design’, *Science*, vol. 355, no. 6321, p. eaad4998, Jan. 2017, doi: 10.1126/science.aad4998.

[169] M. S. Burke, L. J. Enman, A. S. Batchellor, S. Zou, and S. W. Boettcher, ‘Oxygen Evolution Reaction Electrocatalysis on Transition Metal Oxides and (Oxy)hydroxides: Activity Trends and Design Principles’, *Chem. Mater.*, vol. 27, no. 22, pp. 7549–7558, Nov. 2015, doi: 10.1021/acs.chemmater.5b03148.

[170] S. Ghosh, B. P. Bloom, Y. Lu, D. Lamont, and D. H. Waldeck, ‘Increasing the Efficiency of Water Splitting through Spin Polarization Using Cobalt Oxide Thin Film Catalysts’, *J. Phys. Chem. C*, vol. 124, no. 41, pp. 22610–22618, Oct. 2020, doi: 10.1021/acs.jpcc.0c07372.

[171] S. Chrétien and H. Metiu, ‘O2 evolution on a clean partially reduced rutile TiO2(110) surface and on the same surface precovered with Au1 and Au2: The importance of spin conservation’, *J. Chem. Phys.*, vol. 129, no. 7, p. 074705, Aug. 2008, doi: 10.1063/1.2956506.

[172] E. Torun, C. M. Fang, G. A. de Wijs, and R. A. de Groot, ‘Role of Magnetism in Catalysis: RuO2 (110) Surface’, *J. Phys. Chem. C*, vol. 117, no. 12, pp. 6353–6357, Mar. 2013, doi: 10.1021/jp4020367.

[173] F. A. Garcés-Pineda, M. Blasco-Ahicart, D. Nieto-Castro, N. López, and J. R. Galán-Mascarós, ‘Direct magnetic enhancement of electrocatalytic water oxidation in alkaline media’, *Nat. Energy*, vol. 4, no. 6, Art. no. 6, Jun. 2019, doi: 10.1038/s41560-019-0404-4.

[174] X. Ren *et al.*, ‘Spin-polarized oxygen evolution reaction under magnetic field’, *Nat. Commun.*, vol. 12, no. 1, Art. no. 1, May 2021, doi: 10.1038/s41467-021-22865-y.

[175] L. Elias and A. Chitharanjan Hegde, ‘Effect of Magnetic Field on HER of Water Electrolysis on Ni–W Alloy’, *Electrocatalysis*, vol. 8, no. 4, pp. 375–382, Jul. 2017, doi: 10.1007/s12678-017-0382-x.

[176] Z. Zeng *et al.*, ‘Magnetic Field-Enhanced 4-Electron Pathway for Well-Aligned Co3O4/Electrospun Carbon Nanofibers in the Oxygen Reduction Reaction’, *ChemSusChem*, vol. 11, no. 3, pp. 580–588, 2018, doi: 10.1002/cssc.201701947.

[177] E. Katz, O. Lioubashevski, and I. Willner, ‘Magnetic Field Effects on Bioelectrocatalytic Reactions of Surface-Confined Enzyme Systems: Enhanced Performance of Biofuel Cells’, *J. Am. Chem. Soc.*, vol. 127, no. 11, pp. 3979–3988, Mar. 2005, doi: 10.1021/ja044157t.

[178] W. Zhang, K. Banerjee-Ghosh, F. Tassinari, and R. Naaman, ‘Enhanced Electrochemical Water Splitting with Chiral Molecule-Coated Fe3O4 Nanoparticles’, *ACS Energy Lett.*, vol. 3, no. 10, pp. 2308–2313, Oct. 2018, doi: 10.1021/acsenergylett.8b01454.

[179] ‘5.19: Chiral Catalysts for Production of Enantiomerically Pure Compounds’, Chemistry LibreTexts. Accessed: Oct. 19, 2023. [Online]. Available: https://chem.libretexts.org/Bookshelves/General_Chemistry/Book%3A_Structure_and_Reactivity_in_Organic_Biological_and_Inorganic_Chemistry_(Schaller)/I%3A__Chemical_Structure_and_Properties/05%3A_Stereochemistry/5.19%3A_Chiral_Catalysts_for_Production_of_Enantiomerically_Pure_Compounds

[180] D. Di Nuzzo *et al.*, ‘High Circular Polarization of Electroluminescence Achieved via Self-Assembly of a Light-Emitting Chiral Conjugated Polymer into Multidomain Cholesteric Films’, *ACS Nano*, vol. 11, no. 12, Art. no. 12, Dec. 2017, doi: 10.1021/acsnano.7b07390.

[181] G. Yang, S. Zhang, J. Hu, M. Fujiki, and G. Zou, ‘The Chirality Induction and Modulation of Polymers by Circularly Polarized Light’, *Symmetry*, vol. 11, no. 4, Art. no. 4, Apr. 2019, doi: 10.3390/sym11040474.

[182] X. Li *et al.*, ‘Chiral polyaniline with superhelical structures for enhancement in microwave absorption’, *Chem. Eng. J.*, vol. 352, pp. 745–755, Nov. 2018, doi: 10.1016/j.cej.2018.07.096.

[183] D. Di Nuzzo, L. Cui, J. L. Greenfield, B. Zhao, R. H. Friend, and S. C. J. Meskers, ‘Circularly Polarized Photoluminescence from Chiral Perovskite Thin Films at Room Temperature’, *ACS Nano*, vol. 14, no. 6, Art. no. 6, Jun. 2020, doi: 10.1021/acsnano.0c03628.

[184] J. A. Switzer, H. M. Kothari, P. Poizot, S. Nakanishi, and E. W. Bohannan, ‘Enantiospecific electrodeposition of a chiral catalyst’, *Nature*, vol. 425, no. 6957, Art. no. 6957, Oct. 2003, doi: 10.1038/nature01990.

[185] K. Banerjee-Ghosh *et al.*, ‘Separation of enantiomers by their enantiospecific interaction with achiral magnetic substrates’, *Science*, vol. 360, no. 6395, Art. no. 6395, Jun. 2018, doi: 10.1126/science.aar4265.

[186] C. Wattanakit *et al.*, ‘Enantioselective recognition at mesoporous chiral metal surfaces’, *Nat. Commun.*, vol. 5, p. ncomms4325, Feb. 2014, doi: 10.1038/ncomms4325.

[187] I. Mogi, R. Morimoto, and R. Aogaki, ‘Surface chirality effects induced by magnetic fields’, *Curr. Opin. Electrochem.*, vol. 7, pp. 1–6, Jan. 2018, doi: 10.1016/j.coelec.2017.09.029.

[188] E. W. Bohannan, H. M. Kothari, I. M. Nicic, and J. A. Switzer, ‘Enantiospecific Electrodeposition of Chiral CuO Films on Single-Crystal Cu(111)’, *J. Am. Chem. Soc.*, vol. 126, no. 2, Art. no. 2, Jan. 2004, doi: 10.1021/ja039422+.

[189] K. Maeda and E. Yashima, ‘Helical Polyacetylenes Induced via Noncovalent Chiral Interactions and Their Applications as Chiral Materials’, *Top. Curr. Chem.*, vol. 375, no. 4, Art. no. 4, Jul. 2017, doi: 10.1007/s41061-017-0161-4.

[190] K. Morino, N. Watase, K. Maeda, and E. Yashima, ‘Chiral Amplification in Macromolecular Helicity Assisted by Noncovalent Interaction with Achiral Amines and Memory of the Helical Chirality’, *Chem. – Eur. J.*, vol. 10, no. 19, Art. no. 19, 2004, doi: 10.1002/chem.200400381.

[191] L. Durán Pachón, I. Yosef, T. Z. Markus, R. Naaman, D. Avnir, and G. Rothenberg, ‘Chiral imprinting of palladium with cinchona alkaloids’, *Nat. Chem.*, vol. 1, no. 2, Art. no. 2, May 2009, doi: 10.1038/nchem.180.

[192] H. Behar-Levy, O. Neumann, R. Naaman, and D. Avnir, ‘Chirality Induction in Bulk Gold and Silver’, *Adv. Mater.*, vol. 19, no. 9, pp. 1207–1211, 2007, doi: 10.1002/adma.200601702.

[193] Y. Dang, X. Liu, Y. Sun, J. Song, W. Hu, and X. Tao, ‘Bulk Chiral Halide Perovskite Single Crystals for Active Circular Dichroism and Circularly Polarized Luminescence’, *J. Phys. Chem. Lett.*, vol. 11, no. 5, pp. 1689–1696, Mar. 2020, doi: 10.1021/acs.jpclett.9b03718.

[194] T. J. Lawton *et al.*, ‘Long Range Chiral Imprinting of Cu(110) by Tartaric Acid’, *J. Phys. Chem. C*, vol. 117, no. 43, pp. 22290–22297, Oct. 2013, doi: 10.1021/jp402015r.

[195] M. Gazzotti, A. Stefani, M. Bonechi, W. Giurlani, M. Innocenti, and C. Fontanesi, ‘Influence of Chiral Compounds on the Oxygen Evolution Reaction (OER) in the Water Splitting Process’, *Molecules*, vol. 25, no. 17, Art. no. 17, Jan. 2020, doi: 10.3390/molecules25173988.

[196] M. Bandini, M. Melucci, F. Piccinelli, R. Sinisi, S. Tommasi, and A. Umani-Ronchi, ‘New chiral diamino-bis(tert-thiophene): an effective ligand for Pd- and Zn-catalyzed asymmetric transformations’, *Chem. Commun.*, no. 43, pp. 4519–4521, Oct. 2007, doi: 10.1039/B711666G.

[197] H. O. Finklea, ‘Self-Assembled Monolayers on Electrodes’, in *Encyclopedia of Analytical Chemistry*, John Wiley & Sons, Ltd, 2006. Accessed: Apr. 11, 2015. [Online]. Available: http://onlinelibrary.wiley.com/doi/10.1002/9780470027318.a5315/abstract

[198] C. D. Bain, E. B. Troughton, Y. T. Tao, J. Evall, G. M. Whitesides, and R. G. Nuzzo, ‘Formation of monolayer films by the spontaneous assembly of organic thiols from solution onto gold’, *J. Am. Chem. Soc.*, vol. 111, no. 1, Art. no. 1, Jan. 1989, doi: 10.1021/ja00183a049.

[199] R. C. Salvarezza and P. Carro, 'The electrochemical stability of thiols on gold surfaces', *J. Electroanal. Chem.*, vol. 819, pp. 234–239, Jun. 2018, doi: 10.1016/j.jelechem.2017.10.046.

[200] S. Sek, A. Misicka, and R. Bilewicz, 'Effect of Interchain Hydrogen Bonding on Electron Transfer through Alkanethiol Monolayers Containing Amide Bonds', *J. Phys. Chem. B*, vol. 104, no. 22, Art. no. 22, Giugno 2000, doi: 10.1021/jp000376z.

[201] J. Noh, E. Ito, K. Nakajima, J. Kim, H. Lee, and M. Hara, 'High-Resolution STM and XPS Studies of Thiophene Self-Assembled Monolayers on Au(111)', *J. Phys. Chem. B*, vol. 106, no. 29, pp. 7139–7141, Jul. 2002, doi: 10.1021/jp020482w.

[202] P. Morvillo *et al.*, 'Low band gap polymers for application in solar cells: synthesis and characterization of thienothiophene-thiophene copolymers', *Polym. Chem.*, 2013, doi: 10.1039/C3PY01618H.

[203] M. Innocenti, F. Loglio, L. Pigani, R. Seeber, F. Terzi, and R. Udisti, 'In situ atomic force microscopy in the study of electrogeneration of polybithiophene on Pt electrode', *Electrochimica Acta*, vol. 50, no. 7, Art. no. 7, Feb. 2005, doi: 10.1016/j.electacta.2004.10.034.

[204] F. Terzi *et al.*, 'New Insights on the Interaction between Thiophene Derivatives and Au Surfaces. The Case of 3,4-Ethylenedioxythiophene and the Relevant Polymer', *J. Phys. Chem. C*, vol. 115, no. 36, Art. no. 36, Sep. 2011, doi: 10.1021/jp203219b.

[205] E. Ito, J. Noh, and M. Hara, 'Adsorption states and thermal desorption behaviors of thiophene derivative self-assembled monolayers on Au(111)', *Surf. Sci.*, vol. 602, no. 21, Art. no. 21, Nov. 2008, doi: 10.1016/j.susc.2008.08.025.

[206] J. Zhang and X. Bu, 'Chiralization of Diamond Nets: Stretchable Helices and Chiral and Achiral Nets with Nearly Identical Unit Cells', *Angew. Chem. Int. Ed.*, vol. 46, no. 32, pp. 6115–6118, 2007, doi: 10.1002/anie.200701374.

[207] G. Zhu, O. J. Kingsford, Y. Yi, and K. Wong, 'Review—Recent Advances in Electrochemical Chiral Recognition', *J. Electrochem. Soc.*, vol. 166, no. 6, p. H205, Apr. 2019, doi: 10.1149/2.1121906jes.

[208] K. A. Schug and W. Lindner, 'Chiral molecular recognition for the detection and analysis of enantiomers by mass spectrometric methods', *J. Sep. Sci.*, vol. 28, no. 15, pp. 1932–1955, 2005, doi: 10.1002/jssc.200500232.

[209] N. M. Maier, P. Franco, and W. Lindner, ‘Separation of enantiomers: needs, challenges, perspectives’, *J. Chromatogr. A*, vol. 906, no. 1, pp. 3–33, Jan. 2001, doi: 10.1016/S0021-9673(00)00532-X.

[210] A. Stefani *et al.*, ‘Spin-dependent charge transmission through chiral 2T3N self-assembled monolayer on Au’, *J. Chem. Phys.*, vol. 159, no. 10, p. 104701, Sep. 2023, doi: 10.1063/5.0151350.

[211] R. Dell’Anna *et al.*, ‘The role of incidence angle in the morphology evolution of Ge surfaces irradiated by medium-energy Au ions’, *J. Phys. Condens. Matter*, vol. 30, no. 32, p. 324001, Jul. 2018, doi: 10.1088/1361-648X/aacf5f.

[212] N. Wang *et al.*, ‘Graphitic Nitrogen Is Responsible for Oxygen Electroreduction on Nitrogen-Doped Carbons in Alkaline Electrolytes: Insights from Activity Attenuation Studies and Theoretical Calculations’, *ACS Catal.*, vol. 8, no. 8, pp. 6827–6836, Aug. 2018, doi: 10.1021/acscatal.8b00338.

[213] G. Contini *et al.*, ‘Transfer of chirality from adsorbed chiral molecules to the substrate highlighted by circular dichroism in angle-resolved valence photoelectron spectroscopy’, *Phys. Rev. B*, vol. 86, no. 3, p. 035426, Jul. 2012, doi: 10.1103/PhysRevB.86.035426.

[214] L. Ferrari *et al.*, ‘Electronic properties and photoelectron circular dichroism of adsorbed chiral molecules’, *Phys. Rev. B*, vol. 91, no. 8, p. 085408, Feb. 2015, doi: 10.1103/PhysRevB.91.085408.

[215] T. Pajkossy, M. U. Ceblin, and G. Mészáros, ‘Dynamic electrochemical impedance spectroscopy for the charge transfer rate measurement of the ferro/ferricyanide redox couple on gold’, *J. Electroanal. Chem.*, vol. 899, p. 115655, Oct. 2021, doi: 10.1016/j.jelechem.2021.115655.

[216] P. C. Mondal, N. Kantor-Uriel, S. P. Mathew, F. Tassinari, C. Fontanesi, and R. Naaman, ‘Chiral Conductive Polymers as Spin Filters’, *Adv. Mater.*, vol. 27, no. 11, pp. 1924–1927, Mar. 2015, doi: 10.1002/adma.201405249.

[217] C. Fontanesi *et al.*, ‘New One-Step Thiol Functionalization Procedure for Ni by Self-Assembled Monolayers’, *Langmuir*, vol. 31, no. 11, pp. 3546–3552, Mar. 2015, doi: 10.1021/acs.langmuir.5b00177.

[218] N. Liu, B. Yang, Z.-Z. Yin, W. Cai, J. Li, and Y. Kong, ‘A chiral sensing platform based on chiral metal-organic framework for enantiodiscrimination of the isomers of tyrosine and tryptophan’, *J. Electroanal. Chem.*, vol. 918, p. 116445, Aug. 2022, doi: 10.1016/j.jelechem.2022.116445.

[219] P. C. Mondal, C. Fontanesi, D. H. Waldeck, and R. Naaman, ‘Spin-Dependent Transport through Chiral Molecules Studied by Spin-Dependent Electrochemistry’, *Acc. Chem. Res.*, Oct. 2016, doi: 10.1021/acs.accounts.6b00446.

[220] S. Fireman-Shoresh, I. Turyan, D. Mandler, D. Avnir, and S. Marx, ‘Chiral Electrochemical Recognition by Very Thin Molecularly Imprinted Sol–Gel Films’, *Langmuir*, vol. 21, no. 17, pp. 7842–7847, Aug. 2005, doi: 10.1021/la050240y.

[221] S. Arnaboldi, M. Magni, and P. R. Mussini, ‘Enantioselective selectors for chiral electrochemistry and electroanalysis: Stereogenic elements and enantioselection performance’, *Curr. Opin. Electrochem.*, vol. 8, pp. 60–72, Mar. 2018, doi: 10.1016/j.coelec.2018.01.002.

[222] E. T. Kang, K. G. Neoh, and K. L. Tan, ‘X-ray photoelectron spectroscopic studies of poly(2,2’-bithiophene) and its complexes’, *Phys. Rev. B*, vol. 44, no. 19, pp. 10461–10469, Nov. 1991, doi: 10.1103/PhysRevB.44.10461.

[223] A.-S. Duwez, ‘Exploiting electron spectroscopies to probe the structure and organization of self-assembled monolayers: a review’, *J. Electron Spectrosc. Relat. Phenom.*, vol. 134, no. 2, pp. 97–138, Feb. 2004, doi: 10.1016/j.elspec.2003.10.005.

[224] L. Pasquali *et al.*, ‘Adsorption of 3,4-ethylenedioxythiophene (EDOT) on noble metal surfaces: A photoemission and X-ray absorption study’, *J. Electron Spectrosc. Relat. Phenom.*, vol. 172, no. 1, pp. 114–119, May 2009, doi: 10.1016/j.elspec.2009.03.014.

[225] C. Vericat, M. E. Vela, G. A. Benitez, J. A. M. Gago, X. Torrelles, and R. C. Salvarezza, ‘Surface characterization of sulfur and alkanethiol self-assembled monolayers on Au(111)’, *J. Phys. Condens. Matter*, vol. 18, no. 48, pp. R867–R900, Nov. 2006, doi: 10.1088/0953-8984/18/48/R01.

[226] G. Liu, J. A. Rodriguez, J. Dvorak, J. Hrbek, and T. Jirsak, ‘Chemistry of sulfur-containing molecules on Au(111): thiophene, sulfur dioxide, and methanethiol adsorption’, *Surf. Sci.*, vol. 505, pp. 295–307, May 2002, doi: 10.1016/S0039-6028(02)01377-8.

[227] C. J. Powell and A. Jablonski, ‘Evaluation of Calculated and Measured Electron Inelastic Mean Free Paths Near Solid Surfaces’, *J. Phys. Chem. Ref. Data*, vol. 28, no. 1, pp. 19–62, Jan. 1999, doi: 10.1063/1.556035.

[228] M. P. Seah and W. A. Dench, ‘Quantitative electron spectroscopy of surfaces: A standard data base for electron inelastic mean free paths in solids’, *Surf. Interface Anal.*, vol. 1, no. 1, pp. 2–11, Feb. 1979, doi: 10.1002/sia.740010103.

[229] A. Jablonski and C. J. Powell, ‘Relationships between electron inelastic mean free paths, effective attenuation lengths, and mean escape depths’, *J. Electron Spectrosc. Relat. Phenom.*, vol. 100, no. 1, pp. 137–160, Oct. 1999, doi: 10.1016/S0368-2048(99)00044-4.

[230] L. Qie *et al.*, ‘Sulfur-Doped Carbon with Enlarged Interlayer Distance as a High-Performance Anode Material for Sodium-Ion Batteries’, *Adv. Sci.*, vol. 2, no. 12, p. advs.201500195, Dec. 2015, doi: 10.1002/advs.201500195.

[231] D. Chateau *et al.*, ‘Controlled surface modification of gold nanostructures with functionalized silicon polymers’, *J. Sol-Gel Sci. Technol.*, vol. 81, no. 1, pp. 147–153, Jan. 2017, doi: 10.1007/s10971-016-4116-y.

[232] M. Starowicz, B. Stypu\la, and J. Banaś, ‘Electrochemical synthesis of silver nanoparticles’, *Electrochem. Commun.*, vol. 8, no. 2, pp. 227–230, 2006.

[233] F. Tassinari, E. Tancini, M. Innocenti, L. Schenetti, and C. Fontanesi, ‘On the Hybrid Glassy Carbon Electrode/OligoThiophene/Ag(NP) Interface’, *Langmuir*, vol. 28, no. 44, pp. 15505–15512, Oct. 2012, doi: 10.1021/la3025777.

[234] Y.-J. Choi and T.-J. M. Luo, ‘Electrochemical Properties of Silver Nanoparticle Doped Aminosilica Nanocomposite’, *Int. J. Electrochem.*, vol. 2011, p. e404937, Sep. 2011, doi: 10.4061/2011/404937.

[235] F. Liu *et al.*, ‘A facile method to prepare noble metal nanoparticles modified Self-Assembly (SAM) electrode’, *J. Exp. Nanosci.*, vol. 13, no. 1, pp. 1–10, Jan. 2018, doi: 10.1080/17458080.2017.1373202.

[236] A. Ulman, ‘An Introduction to Ultrathin Organic Films, 1st Edition, Academic Press, Boston, 1991.’ Accessed: Nov. 06, 2013. [Online]. Available: http://store.elsevier.com/product.jsp?isbn=9780127082301&_requestid=130432

[237] A. Maeland and T. B. Flanagan, ‘Lattice spacings of gold–palladium alloys’, *Can. J. Phys.*, vol. 42, no. 11, pp. 2364–2366, Nov. 1964, doi: 10.1139/p64-213.

[238] T. Jiang *et al.*, ‘Controlling In-Plane Isotropic and Anisotropic Orientation of Organic Semiconductor Molecules on Ionic Fluoride Dielectrics’, *J. Phys. Chem. C*, vol. 121, no. 8, pp. 4426–4433, Mar. 2017, doi: 10.1021/acs.jpcc.6b12926.

[239] J. Speight, *Lange’s Handbook of Chemistry, Seventeenth Edition*. Accessed: Dec. 17, 2022. [Online]. Available: https://www.mhprofessional.com/lange-s-handbook-of-chemistry-seventeenth-edition-9781259586095-usa

[240] S. Mayer, C. Nolting, and J. Kessler, ‘Electron scattering from chiral molecules’, *J. Phys. B At. Mol. Opt. Phys.*, vol. 29, no. 15, pp. 3497–3511, Aug. 1996, doi: 10.1088/0953-4075/29/15/021.

[241] Aragonès Albert C. *et al.*, ‘Measuring the Spin-Polarization Power of a Single Chiral Molecule’, *Small*, vol. 13, no. 2, p. 1602519, Jan. 2017, doi: 10.1002/smll.201602519.

[242] J. M. Dreiling, F. W. Lewis, and T. J. Gay, ‘Spin-polarized electron transmission through chiral halocamphor molecules’, *J. Phys. B At. Mol. Opt. Phys.*, vol. 51, no. 21, p. 21LT01, Oct. 2018, doi: 10.1088/1361-6455/aae1bd.

[243] V. V. Maslyuk, R. Gutierrez, and G. Cuniberti, ‘Spin–orbit coupling in nearly metallic chiral carbon nanotubes: a density-functional based study’, *Phys. Chem. Chem. Phys.*, vol. 19, no. 13, Art. no. 13, Mar. 2017, doi: 10.1039/C7CP00059F.

[244] N. Avarvari and J. D. Wallis, ‘Strategies towards chiral molecular conductors’, *J. Mater. Chem.*, vol. 19, no. 24, pp. 4061–4076, Jun. 2009, doi: 10.1039/B820598A.

[245] F. Pop, N. Zigon, and N. Avarvari, ‘Main-Group-Based Electro- and Photoactive Chiral Materials’, *Chem. Rev.*, vol. 119, no. 14, pp. 8435–8478, Jul. 2019, doi: 10.1021/acs.chemrev.8b00770.

[246] F. Pop, P. Auban-Senzier, E. Canadell, G. L. J. A. Rikken, and N. Avarvari, ‘Electrical magnetochiral anisotropy in a bulk chiral molecular conductor’, *Nat. Commun.*, vol. 5, no. 1, p. 3757, May 2014, doi: 10.1038/ncomms4757.

[247] C. Réthoré, N. Avarvari, E. Canadell, P. Auban-Senzier, and M. Fourmigué, ‘Chiral Molecular Metals: Syntheses, Structures, and Properties of the AsF6- Salts of Racemic (±)-, (R)-, and (S)-Tetrathiafulvalene−Oxazoline Derivatives’, *J. Am. Chem. Soc.*, vol. 127, no. 16, pp. 5748–5749, Apr. 2005, doi: 10.1021/ja0503884.

[248] F. Pop, P. Auban-Senzier, E. Canadell, and N. Avarvari, ‘Anion size control of the packing in the metallic versus semiconducting chiral radical cation salts (DM-EDT-TTF)2XF6 (X = P, As, Sb)’, *Chem. Commun.*, vol. 52, no. 84, pp. 12438–12441, Oct. 2016, doi: 10.1039/C6CC06706A.

[249] J. D. Wallis, A. Karrer, and J. D. Dunitz, ‘Chiral Metals - A Chiral Substrate for Organic Conductors and Superconductors’, *Helv. Chim. Acta*, vol. 69, no. 1, Art. no. 1, 1986, Accessed: Oct. 08, 2023. [Online]. Available: https://irep.ntu.ac.uk/id/eprint/13468/

[250] S. Yang *et al.*, ‘Charge transfer complexes and radical cation salts of chiral methylated organosulfur donors’, *CrystEngComm*, vol. 16, no. 19, pp. 3906–3916, 2014, doi: 10.1039/C3CE42539H.

[251] J. R. Galán-Mascarós *et al.*, 'A Chiral Ferromagnetic Molecular Metal', *J. Am. Chem. Soc.*, vol. 132, no. 27, pp. 9271–9273, Jul. 2010, doi: 10.1021/ja103147k.

[252] F. Pop, S. Laroussi, T. Cauchy, C. J. Gomez-Garcia, J. D. Wallis, and N. Avarvari, 'Tetramethyl-Bis(ethylenedithio)-Tetrathiafulvalene (TM-BEDT-TTF) Revisited: Crystal Structures, Chiroptical Properties, Theoretical Calculations, and a Complete Series of Conducting Radical Cation Salts', *Chirality*, vol. 25, no. 8, pp. 466–474, 2013, doi: 10.1002/chir.22210.

[253] F. Pop *et al.*, 'Unusual stoichiometry, band structure and band filling in conducting enantiopure radical cation salts of TM-BEDT-TTF showing helical packing of the donors', *J. Mater. Chem. C*, vol. 9, no. 33, pp. 10777–10786, Aug. 2021, doi: 10.1039/D1TC01112J.

[254] J. S. Zambounis *et al.*, 'Crystal structure and electrical properties of κ-((S,S)-DMBEDT–TTF)2ClO4', *Adv. Mater.*, vol. 4, no. 1, pp. 33–35, 1992, doi: 10.1002/adma.19920040106.

[255] N. Mroweh *et al.*, 'In Search of Chiral Molecular Superconductors: κ-[(S,S)-DM-BEDT-TTF]2ClO4 Revisited', *Adv. Mater.*, vol. 32, no. 36, p. 2002811, 2020, doi: 10.1002/adma.202002811.

[256] E. Gomar-Nadal *et al.*, 'Self-assembled monolayers of tetrathiafulvalene derivatives on au(111): Organization and electrical properties', *J. Phys. Chem. B*, vol. 108, no. 22, pp. 7213–7218, Jun. 2004, doi: 10.1021/jp0495949.

[257] B. C. Wiegand and C. M. Friend, 'Model studies of the desulfurization reactions on metal surfaces and in organometallic complexes', *Chem. Rev.*, vol. 92, no. 4, pp. 491–504, Jun. 1992, doi: 10.1021/cr00012a001.

[258] 'Azahelicenes: an Attractive Family of Inherently Chiral Electroactive Molecular Tools'. Accessed: Oct. 17, 2023. [Online]. Available: https://air.unimi.it/handle/2434/949791

[259] F. Yang *et al.*, 'Electrochemical Evidences of Chiral Molecule Recognition Using L/D-Cysteine Modified Gold Electrodes', *Electrochimica Acta*, vol. 237, pp. 22–28, May 2017, doi: 10.1016/j.electacta.2017.03.180.

[260] F. Pop *et al.*, 'Chirality Driven Metallic versus Semiconducting Behavior in a Complete Series of Radical Cation Salts Based on Dimethyl-Ethylenedithio-Tetrathiafulvalene (DM-EDT-TTF)', *J. Am. Chem. Soc.*, vol. 135, no. 45, pp. 17176–17186, Nov. 2013, doi: 10.1021/ja408350r.

[261] S. Grecchi *et al.*, 'Widening the Scope of "Inherently Chiral" Electrodes: Enantiodiscrimination of Chiral Electroactive Probes with Planar Stereogenicity', *ChemElectroChem*, vol. 7, no. 16, pp. 3429–3438, 2020, doi: 10.1002/celc.202000657.

[262] A. Kumar, P. C. Mondal, and C. Fontanesi, ‘Chiral Magneto-Electrochemistry’, *Magnetochemistry*, vol. 4, no. 3, Art. no. 3, Sep. 2018, doi: 10.3390/magnetochemistry4030036.

[263] F. Pop and N. Avarvari, ‘Chiral metal-dithiolene complexes’, *Coord. Chem. Rev.*, vol. 346, pp. 20–31, Sep. 2017, doi: 10.1016/j.ccr.2016.11.015.

[264] A. Abhervé *et al.*, ‘Conducting chiral nickel(II) bis(dithiolene) complexes: structural and electron transport modulation with the charge and the number of stereogenic centres’, *J. Mater. Chem. C*, vol. 9, no. 12, pp. 4119–4140, Apr. 2021, doi: 10.1039/D1TC00439E.

[265] E. K. Joice, S. Rison, K. B. Akshaya, and A. Varghese, ‘Platinum decorated polythiophene modified stainless steel for electrocatalytic oxidation of benzyl alcohol’, *J. Appl. Electrochem.*, vol. 49, no. 9, pp. 937–947, Sep. 2019, doi: 10.1007/s10800-019-01336-9.

[266] Y. Li, S. Deng, P. Cai, C. Wang, H. Wang, and Y. Shen, ‘Synthesis, electropolymerization, and electrochromic performances of two novel tetrathiafulvalene–thiophene assemblies’, *E-Polym.*, vol. 20, no. 1, pp. 382–392, Jan. 2020, doi: 10.1515/epoly-2020-0044.

[267] E. A. Bazzaoui, S. Aeiyach, and P. C. Lacaze, ‘Low potential electropolymerization of thiophene in aqueous perchloric acid’, *J. Electroanal. Chem.*, vol. 364, no. 1, pp. 63–69, Jan. 1994, doi: 10.1016/0022-0728(93)02910-A.

[268] X. Liu *et al.*, ‘Enhanced electrochemical enantiorecognition of tryptophan enantiomers based on synergistic effect of porous β-CD-containing polymers and multiwalled carbon nanotubes’, *Microchem. J.*, vol. 155, p. 104688, Jun. 2020, doi: 10.1016/j.microc.2020.104688.

[269] M. Chahma, ‘Doped Polythiophene Chiral Electrodes as Electrochemical Biosensors’, *Electrochem*, vol. 2, no. 4, Art. no. 4, Dec. 2021, doi: 10.3390/electrochem2040042.

[270] H. Gao, Z. Lu, and Y. Xiao, ‘An electrochemical chiral sensor for amino acids based on cyclodextrin modified thiophene-based copolymer’, *Carbohydr. Polym.*, vol. 297, p. 120012, Dec. 2022, doi: 10.1016/j.carbpol.2022.120012.

[271] S. Arnaboldi, S. Grecchi, M. Magni, and P. Mussini, ‘Electroactive chiral oligo- and polymer layers for electrochemical enantiorecognition’, *Curr. Opin. Electrochem.*, vol. 7, pp. 188–199, Jan. 2018, doi: 10.1016/j.coelec.2018.01.001.

[272] ‘Electropolymerization of Thiophene-Based Monomers with Different Spatial Structures: The Impact of Monomer Structure on Electrochromic Properties - Zhang - 2022 - Macromolecular Chemistry and Physics - Wiley Online Library’. Accessed: Oct. 28, 2023. [Online]. Available: https://onlinelibrary.wiley.com/doi/abs/10.1002/macp.202100341

[273] K. Tanaka, T. Shichiri, S. Wang, and T. Yamabe, ‘A study of the electropolymerization of thiophene’, *Synth. Met.*, vol. 24, no. 3, pp. 203–215, May 1988, doi: 10.1016/0379-6779(88)90258-5.

[274] Y. Wei, C. C. Chan, J. Tian, G. W. Jang, and K. F. Hsueh, ‘Electrochemical polymerization of thiophenes in the presence of bithiophene or terthiophene: kinetics and mechanism of the polymerization’, *Chem. Mater.*, vol. 3, no. 5, pp. 888–897, Sep. 1991, doi: 10.1021/cm00017a026.

[275] A. H. Majeed *et al.*, ‘A Review on Polyaniline: Synthesis, Properties, Nanocomposites, and Electrochemical Applications’, *Int. J. Polym. Sci.*, vol. 2022, p. e9047554, Oct. 2022, doi: 10.1155/2022/9047554.

[276] K. M. Molapo *et al.*, ‘Electronics of Conjugated Polymers (I): Polyaniline’, *Int. J. Electrochem. Sci.*, vol. 7, no. 12, pp. 11859–11875, Dec. 2012, doi: 10.1016/S1452-3981(23)16509-6.

[277] Y. Mei *et al.*, ‘Perovskite Solar Cells with Polyaniline Hole Transport Layers Surpassing a 20% Power Conversion Efficiency’, *Chem. Mater.*, vol. 33, no. 12, pp. 4679–4687, Jun. 2021, doi: 10.1021/acs.chemmater.1c01176.

[278] M. A. Deyab, G. Mele, E. Bloise, and Q. Mohsen, ‘Novel nanocomposites of Ni-Pc/polyaniline for the corrosion safety of the aluminum current collector in the Li-ion battery electrolyte’, *Sci. Rep.*, vol. 11, no. 1, Art. no. 1, Jun. 2021, doi: 10.1038/s41598-021-91688-0.

[279] A. K. Ghasemi, M. Ghorbani, M. S. Lashkenari, and N. Nasiri, ‘Controllable synthesis of zinc ferrite nanostructure with tunable morphology on polyaniline nanocomposite for supercapacitor application’, *J. Energy Storage*, vol. 51, p. 104579, Jul. 2022, doi: 10.1016/j.est.2022.104579.

[280] A. A. Yaqoob *et al.*, ‘Utilizing Biomass-Based Graphene Oxide–Polyaniline–Ag Electrodes in Microbial Fuel Cells to Boost Energy Generation and Heavy Metal Removal’, *Polymers*, vol. 14, no. 4, Art. no. 4, Jan. 2022, doi: 10.3390/polym14040845.

[281] J. Upadhyay, T. M. Das, and R. Borah, ‘Electrochemical performance study of polyaniline and polypyrrole based flexible electrodes’, *Int. J. Polym. Anal. Charact.*, vol. 26, no. 4, pp. 354–363, May 2021, doi: 10.1080/1023666X.2021.1891799.

[282] C. H. Abdul Kadar, M. Faisal, N. Maruthi, N. Raghavendra, B. P. Prasanna, and S. R. Manohara, ‘Corrosion-Resistant Polyaniline-Coated Zinc Tungstate Nanocomposites with Enhanced Electric

Properties for Electromagnetic Shielding Applications', *Macromol. Res.*, vol. 30, no. 9, pp. 638–649, Sep. 2022, doi: 10.1007/s13233-022-0067-z.

[283] A. Samadi, M. Xie, J. Li, H. Shon, C. Zheng, and S. Zhao, 'Polyaniline-based adsorbents for aqueous pollutants removal: A review', *Chem. Eng. J.*, vol. 418, p. 129425, Aug. 2021, doi: 10.1016/j.cej.2021.129425.

[284] X. Zhang, Y. Wang, D. Fu, G. Wang, H. Wei, and N. Ma, 'Photo-thermal converting polyaniline/ionic liquid inks for screen printing highly-sensitive flexible uncontacted thermal sensors', *Eur. Polym. J.*, vol. 147, p. 110305, Mar. 2021, doi: 10.1016/j.eurpolymj.2021.110305.

[285] G. P. Oliveira, B. H. Barboza, and A. Batagin-Neto, 'Polyaniline-based gas sensors: DFT study on the effect of side groups', *Comput. Theor. Chem.*, vol. 1207, p. 113526, Jan. 2022, doi: 10.1016/j.comptc.2021.113526.

[286] Zh. A. Boeva and V. G. Sergeyev, 'Polyaniline: Synthesis, properties, and application', *Polym. Sci. Ser. C*, vol. 56, no. 1, pp. 144–153, Sep. 2014, doi: 10.1134/S1811238214010032.

[287] J. Tanaka, N. Mashita, K. Mizoguchi, and K. Kume, 'Molecular and electronic structures of doped polyaniline', *Synth. Met.*, vol. 29, no. 1, pp. 175–184, Mar. 1989, doi: 10.1016/0379-6779(89)90294-4.

[288] G. G. Wallace, P. R. Teasdale, G. M. Spinks, and L. A. P. Kane-Maguire, *Conductive Electroactive Polymers: Intelligent Materials Systems, Second Edition*, 0 ed. CRC Press, 2002. doi: 10.1201/9781420031898.

[289] M. M. Gvozdenović, B. Z. Jugović, J. S. Stevanović, T. L. Trišović, and B. N. Grgur, *Electrochemical Polymerization of Aniline*. IntechOpen, 2011. doi: 10.5772/28293.

[290] G. Inzelt, M. Pineri, J. W. Schultze, and M. A. Vorotyntsev, 'Electron and proton conducting polymers: recent developments and prospects', *Electrochimica Acta*, vol. 45, no. 15, pp. 2403–2421, May 2000, doi: 10.1016/S0013-4686(00)00329-7.

[291] Lj. D. Arsov, W. Plieth, and G. Koßmehl, 'Electrochemical and Raman spectroscopic study of polyaniline; influence of the potential on the degradation of polyaniline', *J. Solid State Electrochem.*, vol. 2, no. 5, pp. 355–361, Aug. 1998, doi: 10.1007/s100080050112.

[292] A. M. P. Hussain and A. Kumar, 'Electrochemical synthesis and characterization of chloride doped polyaniline', *Bull. Mater. Sci.*, vol. 26, no. 3, pp. 329–334, Apr. 2003, doi: 10.1007/BF02707455.

[293] M. Łapkowski, ‘Electrochemical synthesis of linear polyaniline in aqueous solutions’, *Synth. Met.*, vol. 35, no. 1, pp. 169–182, Feb. 1990, doi: 10.1016/0379-6779(90)90041-I.

[294] G. de T. Andrade, M. Jesús Aguirre, and S. R. Biaggio, ‘Influence of the first potential scan on the morphology and electrical properties of potentiodynamically grown polyaniline films’, *Electrochimica Acta*, vol. 44, no. 4, pp. 633–642, Sep. 1998, doi: 10.1016/S0013-4686(98)00185-6.

[295] Z. Mandić, L. Duić, and F. Kovačiček, ‘The influence of counter-ions on nucleation and growth of electrochemically synthesized polyaniline film’, *Electrochimica Acta*, vol. 42, no. 9, pp. 1389–1402, Jan. 1997, doi: 10.1016/S0013-4686(96)00362-3.

[296] S. Mu and J. Kan, ‘The effect of salts on the electrochemical polymerization of aniline’, *Synth. Met.*, vol. 92, no. 2, pp. 149–155, Jan. 1998, doi: 10.1016/S0379-6779(98)80104-5.

[297] A. Malinauskas and R. Holze, ‘Suppression of the “first cycle effect” in self-doped polyaniline’, *Electrochimica Acta*, vol. 43, no. 5, pp. 515–520, Jan. 1998, doi: 10.1016/S0013-4686(97)00093-5.

[298] K. Bade, V. Tsakova, and J. W. Schultze, ‘Nucleation, growth and branching of polyaniline from microelectrode experiments’, *Electrochimica Acta*, vol. 37, no. 12, pp. 2255–2261, Sep. 1992, doi: 10.1016/0013-4686(92)85120-A.

[299] S. Mishra, V. S. Poonia, C. Fontanesi, R. Naaman, A. M. Fleming, and C. J. Burrows, ‘The effect of oxidative damage on charge and spin transport in DNA’, *J. Am. Chem. Soc.*, Dec. 2018, doi: 10.1021/jacs.8b12014.

[300] A. C. V. de Araújo *et al.*, ‘Synthesis, characterization and magnetic properties of polyaniline-magnetite nanocomposites’, *Synth. Met.*, vol. 160, no. 7, pp. 685–690, Apr. 2010, doi: 10.1016/j.synthmet.2010.01.002.

[301] ‘Polyaniline Stabilized Magnetite Nanoparticle Reinforced Epoxy Nanocomposites | ACS Applied Materials & Interfaces’. Accessed: Jul. 27, 2022. [Online]. Available: https://pubs.acs.org/doi/10.1021/am301529t

[302] C. Janáky, A. Kormányos, and C. Visy, ‘Magnetic hybrid modified electrodes, based on magnetite nanoparticle containing polyaniline and poly(3,4-ethylenedioxythiophene)’, *J. Solid State Electrochem.*, vol. 15, no. 11, pp. 2351–2359, Dec. 2011, doi: 10.1007/s10008-011-1401-0.

[303] A. Keyhanpour, S. M. Seyed Mohaghegh, and A. Jamshidi, ‘Electropolymerization and characterization of polyaniline, poly(2-anilinoethanol) and poly(aniline-co-2-anilinoethanol)’, *Iran. Polym. J.*, vol. 21, no. 5, pp. 307–315, May 2012, doi: 10.1007/s13726-012-0032-3.

[304] W. Giurlani, M. Innocenti, and A. Lavacchi, ‘X-ray Microanalysis of Precious Metal Thin Films: Thickness and Composition Determination’, *Coatings*, vol. 8, no. 2, Art. no. 2, Feb. 2018, doi: 10.3390/coatings8020084.

[305] ‘NIST DTSA-II’. Accessed: Jul. 28, 2022. [Online]. Available: https://www.cstl.nist.gov/div837/837.02/epq/dtsa2/index.html

[306] S. Mishra and C. Fontanesi, ‘Combined effect of organic-inorganic heterostructure to enhance electrochemical capacitance’, *Mater. Chem. Phys.*, vol. 238, p. 121943, Dec. 2019, doi: 10.1016/j.matchemphys.2019.121943.

[307] A. T. Özyılmaz, M. Erbil, and B. Yazıcı, ‘The influence of polyaniline (PANI) top coat on corrosion behaviour of nickel plated copper’, *Appl. Surf. Sci.*, vol. 252, no. 5, pp. 2092–2100, Dec. 2005, doi: 10.1016/j.apsusc.2005.04.001.

[308] O. Koysuren, C. Du, N. Pan, and G. Bayram, ‘Preparation and comparison of two electrodes for supercapacitors: Pani/CNT/Ni and Pani/Alizarin-treated nickel’, *J. Appl. Polym. Sci.*, vol. 113, no. 2, pp. 1070–1081, 2009, doi: 10.1002/app.29924.

[309] R. Salmimies, M. Mannila, J. Juha, and A. Häkkinen, ‘Acidic Dissolution of Magnetite: Experimental Study on The Effects of Acid Concentration and Temperature’, *Clays Clay Miner.*, vol. 59, no. 2, pp. 136–146, Apr. 2011, doi: 10.1346/CCMN.2011.0590203.

[310] J.-J. Han, N. Zhang, D.-L. Liu, H. Ma, T. Han, and D.-D. Sun, ‘Cyclic voltammetry for the determination of the selectivity of PANI-HClO4 sensor to different acids’, *Ionics*, vol. 26, no. 2, pp. 1029–1038, Feb. 2020, doi: 10.1007/s11581-019-03238-4.

[311] S.-H. Jeon, G. D. Song, and D. Hur, ‘Effects of Deposition Potentials on the Morphology and Structure of Iron-Based Films on Carbon Steel Substrate in an Alkaline Solution’, *Adv. Mater. Sci. Eng.*, vol. 2016, pp. 1–9, Jan. 2016, doi: 10.1155/2016/9038478.

[312] M. R. Majidi, L. A. P. Kane-Maguire, and G. G. G. Wallace, ‘Facile synthesis of optically active polyaniline and polytoluidine’, *Polymer*, vol. 37, no. 2, pp. 359–362, Jan. 1996, doi: 10.1016/0032-3861(96)81111-6.

[313] S. He, X. Shang, W. Lu, Y. Tian, Z. Xu, and W. Zhang, ‘Electrochemical enantioselective sensor for effective recognition of tryptophan isomers based on chiral polyaniline twisted nanoribbon’, *Anal. Chim. Acta*, vol. 1147, pp. 155–164, Feb. 2021, doi: 10.1016/j.aca.2020.12.058.

[314] Y. Yan, Z. Yu, Y. W. Huang, W. X. Yuan, and Z. X. Wei, ‘Helical Polyaniline Nanofibers Induced by Chiral Dopants by a Polymerization Process’, *Adv. Mater.*, vol. 19, no. 20, pp. 3353–3357, 2007, doi: 10.1002/adma.200700846.

[315] V. Egan, R. Bernstein, L. Hohmann, T. Tran, and R. B. Kaner, ‘Influence of water on the chirality of camphorsulfonic acid-doped polyaniline’, *Chem. Commun.*, no. 9, pp. 801–802, Jan. 2001, doi: 10.1039/B008996F.

[316] H. (谷 红波) Gu *et al.*, ‘Separating positive and negative magnetoresistance for polyaniline-silicon nanocomposites in variable range hopping regime’, *Appl. Phys. Lett.*, vol. 102, no. 21, p. 212403, May 2013, doi: 10.1063/1.4807787.

[317] P. Pipinys and A. Kiveris, ‘Positive temperature coefficient of resistivity of polyaniline films in the framework of phonon-assisted tunnelling model’, *Phys. B Condens. Matter*, vol. 370, no. 1, pp. 168–171, Dec. 2005, doi: 10.1016/j.physb.2005.09.007.

[318] K. Lee, S. Cho, S. Heum Park, A. J. Heeger, C.-W. Lee, and S.-H. Lee, ‘Metallic transport in polyaniline’, *Nature*, vol. 441, no. 7089, Art. no. 7089, May 2006, doi: 10.1038/nature04705.

[319] Y. Long, Z. Chen, N. Wang, Z. Zhang, and M. Wan, ‘Resistivity study of polyaniline doped with protonic acids’, *Phys. B Condens. Matter*, vol. 325, pp. 208–213, Jan. 2003, doi: 10.1016/S0921-4526(02)01526-0.

[320] A. B. Kaiser *et al.*, ‘Comparison of electronic transport in polyaniline blends, polyaniline and polypyrrole’, *Synth. Met.*, vol. 84, no. 1, pp. 699–702, Jan. 1997, doi: 10.1016/S0379-6779(96)04112-4.

[321] A. B. Kaiser, ‘Electronic transport properties of conducting polymers and carbon nanotubes’, *Rep. Prog. Phys.*, vol. 64, no. 1, p. 1, Jan. 2001, doi: 10.1088/0034-4885/64/1/201.

[322] Y. Long *et al.*, ‘Electrical conductivity of a single conducting polyaniline nanotube’, *Appl. Phys. Lett.*, vol. 83, no. 9, pp. 1863–1865, Aug. 2003, doi: 10.1063/1.1606864.

[323] V. Varade *et al.*, ‘Bacteriorhodopsin based non-magnetic spin filters for biomolecular spintronics’, *Phys. Chem. Chem. Phys.*, vol. 20, no. 2, pp. 1091–1097, Jan. 2018, doi: 10.1039/C7CP06771B.

[324] Y. Sang *et al.*, 'Temperature Dependence of Charge and Spin Transfer in Azurin', *J. Phys. Chem. C*, vol. 125, no. 18, pp. 9875–9883, May 2021, doi: 10.1021/acs.jpcc.1c01218.

[325] A. Jonsson *et al.*, 'Therapy using implanted organic bioelectronics', *Sci. Adv.*, vol. 1, no. 4, p. e1500039, May 2015, doi: 10.1126/sciadv.1500039.

[326] S. Mishra *et al.*, 'Recent advances in salivary cancer diagnostics enabled by biosensors and bioelectronics', *Biosens. Bioelectron.*, vol. 81, pp. 181–197, Jul. 2016, doi: 10.1016/j.bios.2016.02.040.

[327] A. Marks, S. Griggs, N. Gasparini, and M. Moser, 'Organic Electrochemical Transistors: An Emerging Technology for Biosensing', *Adv. Mater. Interfaces*, vol. 9, no. 6, p. 2102039, 2022, doi: 10.1002/admi.202102039.

[328] L. Bai, C. G. Elósegui, W. Li, P. Yu, J. Fei, and L. Mao, 'Biological Applications of Organic Electrochemical Transistors: Electrochemical Biosensors and Electrophysiology Recording', *Front. Chem.*, vol. 7, 2019, Accessed: Oct. 29, 2023. [Online]. Available: https://www.frontiersin.org/articles/10.3389/fchem.2019.00313

[329] B. D. Paulsen, K. Tybrandt, E. Stavrinidou, and J. Rivnay, 'Organic mixed ionic-electronic conductors', *Nat. Mater.*, vol. 19, no. 1, pp. 13–26, Jan. 2020, doi: 10.1038/s41563-019-0435-z.

[330] J. Song, H. Liu, Z. Zhao, P. Lin, and F. Yan, 'Flexible Organic Transistors for Biosensing: Devices and Applications', *Adv. Mater.*, vol. n/a, no. n/a, p. 2300034, doi: 10.1002/adma.202300034.

[331] R. B. Rashid, W. Du, S. Griggs, I. P. Maria, I. McCulloch, and J. Rivnay, 'Ambipolar inverters based on cofacial vertical organic electrochemical transistor pairs for biosignal amplification', *Sci. Adv.*, vol. 7, no. 37, p. eabh1055, Sep. 2021, doi: 10.1126/sciadv.abh1055.

[332] D. Khodagholy *et al.*, 'Organic electronics for high-resolution electrocorticography of the human brain', *Sci. Adv.*, vol. 2, no. 11, p. e1601027, Nov. 2016, doi: 10.1126/sciadv.1601027.

[333] D. Khodagholy *et al.*, 'In vivo recordings of brain activity using organic transistors', *Nat. Commun.*, vol. 4, no. 1, Art. no. 1, Mar. 2013, doi: 10.1038/ncomms2573.

[334] D. Ohayon *et al.*, 'Biofuel powered glucose detection in bodily fluids with an n-type conjugated polymer', *Nat. Mater.*, vol. 19, no. 4, pp. 456–463, Apr. 2020, doi: 10.1038/s41563-019-0556-4.

[335] A.-M. Pappa *et al.*, 'Organic Transistor Arrays Integrated with Finger-Powered Microfluidics for Multianalyte Saliva Testing', *Adv. Healthc. Mater.*, vol. 5, no. 17, pp. 2295–2302, Sep. 2016, doi: 10.1002/adhm.201600494.

[336] W. Hai *et al.*, 'Human influenza virus detection using sialyllactose-functionalized organic electrochemical transistors', *Sens. Actuators B Chem.*, vol. 260, pp. 635–641, May 2018, doi: 10.1016/j.snb.2018.01.081.

[337] R.-X. He *et al.*, 'Detection of bacteria with organic electrochemical transistors', *J. Mater. Chem.*, vol. 22, no. 41, pp. 22072–22076, Oct. 2012, doi: 10.1039/C2JM33667G.

[338] J. Gladisch *et al.*, 'Reversible Electronic Solid–Gel Switching of a Conjugated Polymer', *Adv. Sci.*, vol. 7, no. 2, p. 1901144, 2020, doi: 10.1002/advs.201901144.

[339] D. Melling, J. G. Martinez, and E. W. H. Jager, 'Conjugated Polymer Actuators and Devices: Progress and Opportunities', *Adv. Mater.*, vol. 31, no. 22, p. 1808210, 2019, doi: 10.1002/adma.201808210.

[340] K. Lieberth *et al.*, 'Current-Driven Organic Electrochemical Transistors for Monitoring Cell Layer Integrity with Enhanced Sensitivity', *Adv. Healthc. Mater.*, vol. 10, no. 19, p. 2100845, 2021, doi: 10.1002/adhm.202100845.

[341] M. Moser *et al.*, 'Controlling Electrochemically Induced Volume Changes in Conjugated Polymers by Chemical Design: from Theory to Devices', *Adv. Funct. Mater.*, vol. 31, no. 26, p. 2100723, 2021, doi: 10.1002/adfm.202100723.

[342] S. Muench, A. Wild, C. Friebe, B. Häupler, T. Janoschka, and U. S. Schubert, 'Polymer-Based Organic Batteries', *Chem. Rev.*, vol. 116, no. 16, pp. 9438–9484, Aug. 2016, doi: 10.1021/acs.chemrev.6b00070.

[343] L. R. Savagian, A. M. Österholm, J. F. Ponder, K. J. Barth, J. Rivnay, and J. R. Reynolds, 'Balancing Charge Storage and Mobility in an Oligo(Ether) Functionalized Dioxythiophene Copolymer for Organic- and Aqueous- Based Electrochemical Devices and Transistors', *Adv. Mater. Deerfield Beach Fla*, vol. 30, no. 50, p. e1804647, Dec. 2018, doi: 10.1002/adma.201804647.

[344] D. Moia *et al.*, 'Design and evaluation of conjugated polymers with polar side chains as electrode materials for electrochemical energy storage in aqueous electrolytes', *Energy Environ. Sci.*, vol. 12, no. 4, pp. 1349–1357, Apr. 2019, doi: 10.1039/C8EE03518K.

[345] H. S. White, G. P. Kittlesen, and M. S. Wrighton, 'Chemical derivatization of an array of three gold microelectrodes with polypyrrole: fabrication of a molecule-based transistor', *J. Am. Chem. Soc.*, vol. 106, no. 18, pp. 5375–5377, Sep. 1984, doi: 10.1021/ja00330a070.

[346] I. Gualandi, M. Tessarolo, F. Mariani, D. Tonelli, B. Fraboni, and E. Scavetta, ‘Organic Electrochemical Transistors as Versatile Analytical Potentiometric Sensors’, *Front. Bioeng. Biotechnol.*, vol. 7, p. 354, Nov. 2019, doi: 10.3389/fbioe.2019.00354.

[347] L. Li, H. Li, Y. Song, W. Xu, W. Hu, and D. Zhu, ‘Air-stable ambipolar field-effect transistors based on copper phthalocyanine and tetracyanoquinodimethane’, *Res. Chem. Intermed.*, vol. 34, no. 2, pp. 147–153, Feb. 2008, doi: 10.1163/156856708783623537.

[348] J. C. Ribierre, S. Watanabe, M. Matsumoto, T. Muto, and T. Aoyama, ‘Majority carrier type conversion in solution-processed organic transistors and flexible complementary logic circuits’, *Appl. Phys. Lett.*, vol. 96, no. 8, p. 083303, Feb. 2010, doi: 10.1063/1.3310025.

[349] Y. Wang and Y. Liu, ‘Insight into conjugated polymers for organic electrochemical transistors’, *Trends Chem.*, vol. 5, no. 4, pp. 279–294, Apr. 2023, doi: 10.1016/j.trechm.2023.01.006.

[350] Y. Yao *et al.*, ‘Flexible and Stretchable Organic Electrochemical Transistors for Physiological Sensing Devices’, *Adv. Mater.*, vol. 35, no. 35, p. 2209906, 2023, doi: 10.1002/adma.202209906.

[351] J. Hou, T. L. Chen, S. Zhang, and Y. Yang, ‘Poly[4,4-bis(2-ethylhexyl)cyclopenta[2,1- *b* ;3,4- *b′* ]dithiophene-2,6-diyl- *alt* -2,1,3- benzoselenadiazole-4,7-diyl], a New Low Band Gap Polymer in Polymer Solar Cells’, *J. Phys. Chem. C*, vol. 113, no. 4, pp. 1601–1605, Jan. 2009, doi: 10.1021/jp808255b.

[352] B. Y. Jeon *et al.*, ‘Strong Bathochromic Shift of Conjugated Polymer Nanowires Assembled with a Liquid Crystalline Alkyl Benzoic Acid via a Film Dispersion Process’, *ACS Omega*, vol. 6, no. 50, pp. 34876–34888, Dec. 2021, doi: 10.1021/acsomega.1c05556.

[353] D. Di Nuzzo *et al.*, ‘How intermolecular geometrical disorder affects the molecular doping of donor–acceptor copolymers’, *Nat. Commun.*, vol. 6, Mar. 2015, doi: 10.1038/ncomms7460.

[354] M. Anderson *et al.*, ‘Displacement of polarons by vibrational modes in doped conjugated polymers’, *Phys. Rev. Mater.*, vol. 1, no. 5, Art. no. 5, Oct. 2017, doi: 10.1103/PhysRevMaterials.1.055604.

[355] J. Yamada, K. Aoki, S. Nakatsuji, H. Nishikawa, I. Ikemoto, and K. Kikuchi, ‘Preparation of 4,5-(alkylmethylenedithio)-1,3-dithiole-2-chalcogenones: Building blocks for the mono-alkylated TTF donors’, *Tetrahedron Lett.*, vol. 40, no. 36, pp. 6635–6638, Sep. 1999, doi: 10.1016/S0040-4039(99)01328-3.

[356] L. Pasquali, ‘The UHV Experimental Chamber For Optical Measurements (Reflectivity and Absorption) and Angle Resolved Photoemission of the BEAR Beamline at ELETTRA’, in *AIP*

*Conference Proceedings*, San Francisco, California (USA): AIP, 2004, pp. 1142–1145. doi: 10.1063/1.1758001.

[357] A. Derossi, F. Lama, M. Piacentini, T. Prosperi, and N. Zema, ‘High flux and high resolution beamline for elliptically polarized radiation in the vacuum ultraviolet and soft x-ray regions’, *Rev. Sci. Instrum.*, vol. 66, no. 2, Art. no. 2, Feb. 1995, doi: 10.1063/1.1145828.

[358] J. J. A. Lozeman, P. Führer, W. Olthuis, and M. Odijk, ‘Spectroelectrochemistry, the future of visualizing electrode processes by hyphenating electrochemistry with spectroscopic techniques’, *Analyst*, vol. 145, no. 7, pp. 2482–2509, Mar. 2020, doi: 10.1039/C9AN02105A.

[359] J. A. Pople, *Gaussian suite of programs*. Wallingford, Connecticut, 2017. Accessed: Apr. 18, 2017. [Online]. Available: http://gaussian.com/

[360] A. Granovsky A., *Firefly version 8.0.0, http://classic.chem.msu.su/gran/firefly/index.html*. 2016. [Online]. Available: http://classic.chem.msu.su/gran/gamess/index.html

[361] G. A. Andrienko and Chemcraft - graphical software for visualization of quantum chemistry computations., ‘Chemcraft - graphical software for visualization of quantum chemistry computations.’, https://www.chemcraftprog.com. [Online]. Available: https://www.chemcraftprog.com

[362] M. Cossi, N. Rega, G. Scalmani, and V. Barone, ‘Energies, structures, and electronic properties of molecules in solution with the C-PCM solvation model’, *J. Comput. Chem.*, vol. 24, no. 6, pp. 669–681, 2003, doi: 10.1002/jcc.10189.

[363] James J.P. Stewart, ‘MOPAC2016’, MOPAC2016. [Online]. Available: HTTP://OpenMOPAC.net

[364] A. Hamelin, L. Doubova, D. Wagner, and H. Schirmer, ‘A modification of the last step of surface preparation for gold and silver single crystal faces’, *J. Electroanal. Chem. Interfacial Electrochem.*, vol. 220, no. 1, pp. 155–160, Mar. 1987, doi: 10.1016/0022-0728(87)88010-5.

[365] K. Pekmez, E. Avci, H. G. Baumgärtel, and C. Donner, ‘The Under Potential Deposition of Cu on Au (111) in Nonaqueous Acetonitrile’, *Z. Für Phys. Chem.*, vol. 226, no. 9–10, pp. 953–963, Oct. 2012, doi: 10.1524/zpch.2012.0306.

# Appendix A: Calculation Details

## A.1. Average projected area of the adsorbate on the electrode surface

### *A.1.1. Au|2T3N*

Figure 40 in section 3.1.5 shows cyclic voltammetry curves relevant to the 2T3N electrodesorption experiment. Integration of the current vs. potential area relevant to the $E_{des}$ current peak found at about -1.0 V allows to calculate the charge associated to the 2T3N electrodesorption: $Q_{electrodedesorb} \cong 5.59 * 10^{-7}$ C . Then, it is possible to estimate the mean surface area occupied by adsorbed 2T3N, assuming that the electrodesorption of one molecule is due to a single electron transfer, A1 reaction, once known the electrode surface area:

$$2T3N_{ads} - Au + e^{-} \rightarrow Au + 2T3N_{slz}^{-} \tag{A1}$$

The number of desorbed molecules $n_{desorb}$ is:

$$n_{desorb} = {Q_{desorb}}/{Q_{e^-}} = {5.59 * 10^{-7}\,[C]}/{1.60218 * 10^{-19}\,[C]} = 3.489 * 10^{12}$$

Where: $Q_{desorb}$ is the charge obtained by the integration of the desorption peak in Figure 40, $Q_{e^-}$ is the electron elementary charge.

The working electrode is a cylindrical gold rod of 1.5 mm radius, thus the geometrical area is

$$A_{electrode} = \pi * (1.5)^2\, mm^2 = 7.07\, mm^2 = 7.07 * 10^{14}\ \text{Å}^2$$

Thus, the average surface area occupied by a 2T3N adsorbed molecule is about

$$A_{molC11} = {A_{desorb}}/{n_{desorb}} \cong 200\ {\text{Å}^2}/{molecule}$$

The latter value is in just larger than the area obtained considering the 2T3N adsorbed in a flat disposition, compare Figure A1 where the plane of the page represent the electrode surface. The value calculated from the electrodesorption experiment, which is slightly larger than the van Der Waals project value, suggests a SAM not well ordered, which is indeed expected due to the irregular shape of the 2T3N.

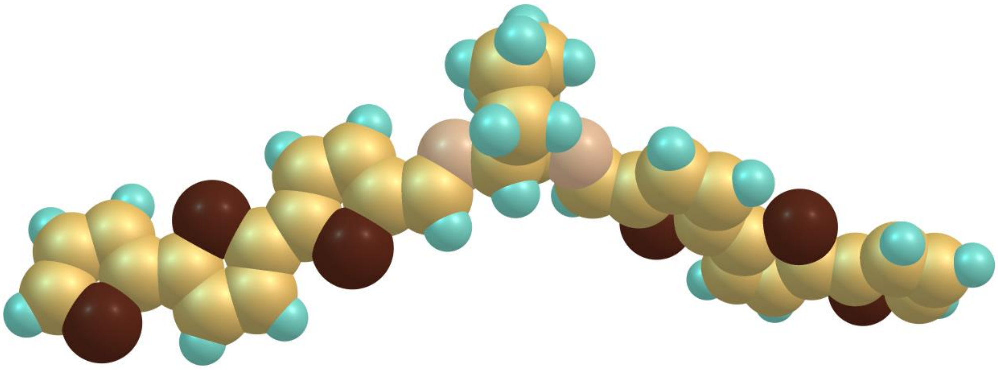

Figure A1 2T3N molecular model, van Der Waals atomic radii representation, as projected orthogonal with respect to the electrode surface.

### *A.1.2. Au|C11*

Following exactly the same procedure as for the *Au|2T3N* interface (previous paragraph, A.1.1), in the case of the Au|C11 system (relevant for comparison with the electrochemical results of the Au|2T3N interface, as shown in Figure 41), the results obtained from the electrodesorption measurement are:

$$n_{desorb} = Q_{desorb}/Q_{e^-} = 9.23 * 10^{-6}\ [C]/1.60218 * 10^{-19}\ [C] = 5.761 * 10^{13}$$

$$A_{electrode} = \pi * (1.5)^2\ mm^2 = 7.07\ mm^2 = 7.07 * 10^{14}\ \text{Å}^2$$

$$A_{molC11} = A_{desorb}/n_{desorb} \cong 13\ \text{Å}^2/molecule$$

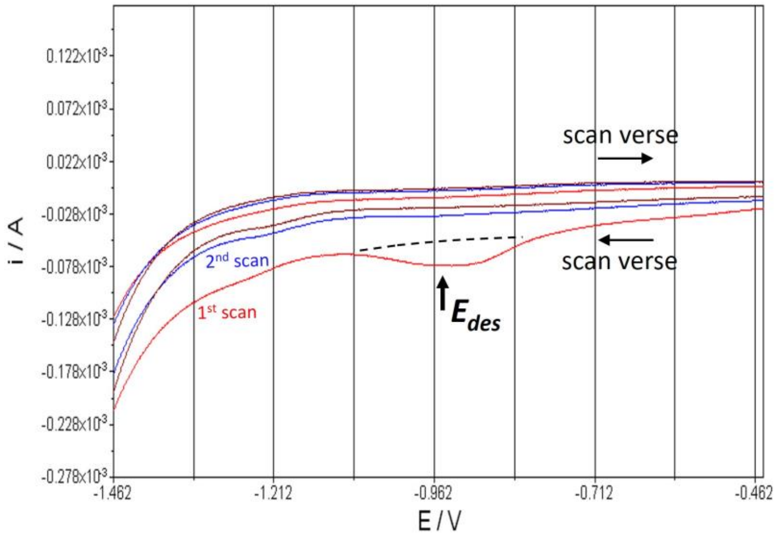

Figure A2 Detail of the desorption peak (first reduction potential scan) in the case of the CV measurements of the Au|C11 interface (WE), in a classic three-electrode electrochemical setup (with Pt wire as the CE and Ag/AgCl/KClsat as the RE). The electrodesorption procedure is identical to that conducted for the Au|2T3N interface (refer to Figures 40 and 41 in Section 3.1.5)

### A.1.3. Au|(S)-1 and Au|(S)-2 (TTF derivatives)

Figures 71b and 71d in section 3.3.2 show cyclic voltammetry curves relevant to (*S*)-**2** and (*S*)-**1** molecules electrodesorption experiment. Integration of the current vs. potential area relevant to the desorption current peaks ($E_{des\,1}$ and $E_{des\,2}$) found in both measurements at about -1.1 V allows to calculate the charge associated to the two species electrodesorption.

Figure A3 presents panels (d) and (b) from Figure 71, zooming in on the region of interest of the curves and highlighting the area under the electro-desorption peaks (associated with a certain desorption charge, $Q_{des}$)

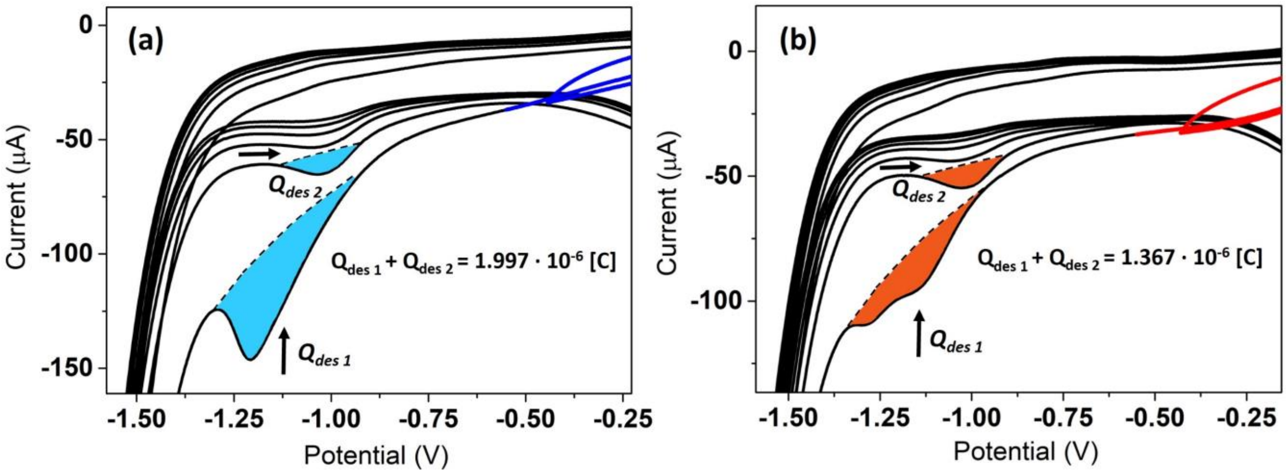

Figure A3 Detail obtained by zooming in on the regions of interest from Figure 71 of this thesis, panels (d) and (b), respectively. The areas beneath the peaks of electrode desorption are highlighted to emphasize the underlined area, corresponding to the charge associated with the desorption ($Q_{des}$).

It is possible to estimate the mean surface area occupied by adsorbed (*S*)-**1** and (*S*)-**2** , assuming that the electrodesorption of one molecule is due to a single electron transfer once known the electrode surface area.

In the case of (*S*)-**1** (Figure A3a):

$$(S)\mathbf{1}_{ads} - Au + e^{-} \rightarrow Au + (S)\mathbf{1}_{slz}^{-} \qquad \text{(A2)}$$

The analysis of the desorption peaks yields a total charge of

$$Q_{desorb} = Q_{des\,1} + Q_{des\,2} \cong 1.997 * 10^{-6}\ \mathrm{C}$$

The number of desorbed molecules $n_{desorb}$ is:

$$n_{desorb} = {}^{Q_{desorb}}\!/_{Q_{e^-}} = {}^{1.997 * 10^{-6}\,[C]}\!/_{1.60218 * 10^{-19}\,[C]} = 1.246 * 10^{13}$$

Where: $Q_{desorb}$ is the charge obtained by the integration of the desorption peak in Figure 71, $Q_{e^-}$is the electron elementary charge.

The working electrode is a cylindrical gold rod of 1.5 mm radius, thus the geometrical area is

$$A_{electrode} = \pi * (1.5)^2\ mm^2 = 7.07\ mm^2 = 7.07 * 10^{14}\ \text{Å}^2$$

Thus, the average surface area occupied by a 2T3N adsorbed molecule is about

$$A_{(\boldsymbol{S})1} = {}^{A_{electrode}}\!/_{n_{desorb}} \cong 55\ {}^{\text{Å}^2}\!/_{molecule}$$

The same procedure is followed for (*S*)-**2** (Figure A3b):

$$(S)\mathbf{2}_{ads} - Au + e^- \rightarrow Au + (S)\mathbf{2}^-_{slz} \tag{A3}$$

$$Q_{desorb} = Q_{des\,1} + Q_{des\,2} \cong 1.367 * 10^{-6}$$

$$n_{desorb} = {}^{Q_{desorb}}\!/_{Q_{e^-}} = {}^{1.367 * 10^{-6}\,[C]}\!/_{1.60218 * 10^{-19}\,[C]} = 8.532 * 10^{12}$$

$$A_{(S)\mathbf{2}} = {}^{A_{electrode}}\!/_{n_{desorb}} \cong 80\ {}^{\text{Å}^2}\!/_{molecule}$$

## A.2. Valence Band Photoelectron CD (PECD) calculations

Valence band photoelectron CD (PECD) spectra reported in Fig. 35, Section 3.1.4 were obtained by suitable elaboration of Valence Band circularly polarized synchrotron radiation measurements. The Au|R-2T3N VB dichroic spectrum PECD reported in Fig. 35 upper panel was calculated by using equation A4:

$$PECD\ (\%) = \frac{2 \cdot (Av_M - Av_P)}{Av_M + Av_P} \tag{A4}$$

Where: $Av_M$ and $Av_P$ are the average signals recorded by using left-handed and right-handed circularly polarized photons, respectively. The recording of each left-/right- circular polarization VB spectra was reiterated three times; the exciting photon polarization was switched (left-/right-) following each VB photoemission spectrum. This procedure was implemented in order to minimize instrumental artifacts. Fig. A4 shows the Valence Band photoelectron circularly polarized synchrotron radiation measurements raw data, which were used as $Av_M$ and $Av_P$ data in the calculations relying on Equation A4.

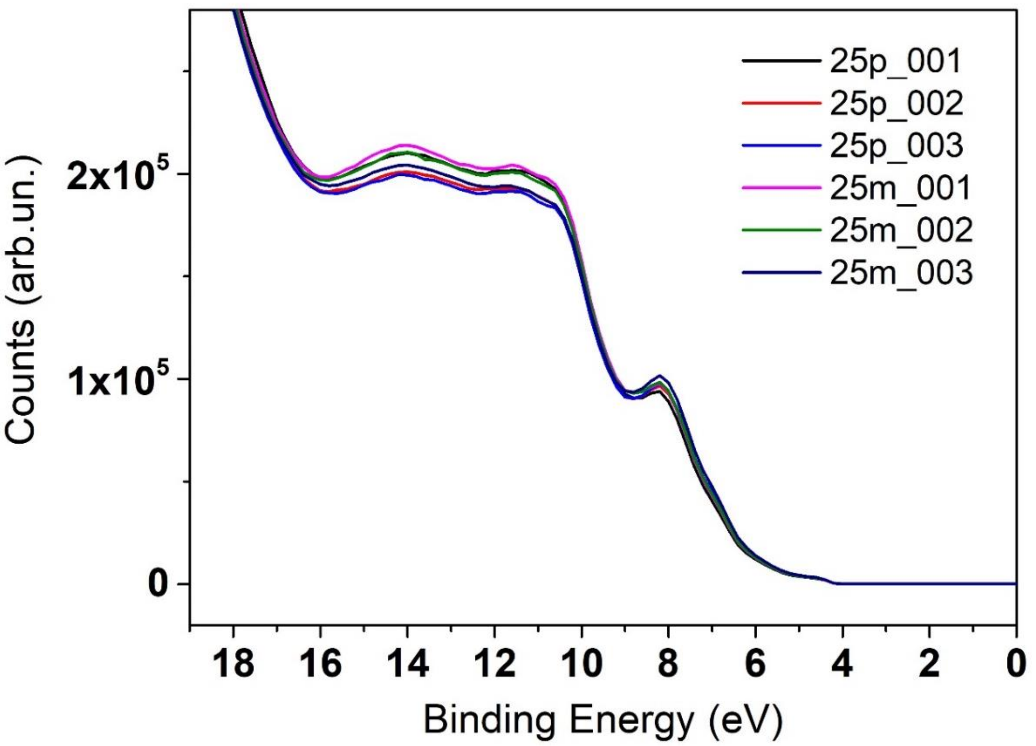

Figure A4 Au|R-2T3N interface. VB photoemission measurements recorded with a 25 eV emitted photon. Left- and right-handed polarizations are labelled 25m and 25p respectively.

# Appendix B: Water Splitting Tables

***Table B1.*** *First column: name of the experiment for its unambiguous identification. Second Column: type of electrolyte. Third column: surface used as working electrode. Fourth column: potential at which the oxygen evolution is detected by eye with bubbles formation. Fifth column: stepped sweeps potential vs time function.*

| Test Name | Electrolyte | Working Electrode | OER [V] | E [V] vs t [s] function |
|---|---|---|---|---|
| SeS01 | KOH 0.1 M | AISI 316L | 0.78 | |
| SeS01 | TA 0.5mM in KOH 0.1M | AISI 316L | 0.75 | 1 |
| SeS01 | TA 5mM in KOH 0.1M | AISI 316L | 0.80 | |
| SeS02 | KOH 0.1 M | AISI 316L | 0.78 | 2 |
| SeS02 | TA 0.5mM in KOH 0.1M | AISI 316L | 0.72 | |
| SeS02 | TA 5mM in KOH 0.1M | AISI 316L | 0.81 | 1 |
| SeS03 | KOH 0.1 M | AISI 316L | 0.78 | 1 |
| SeS03 | TA 0.5mM in KOH 0.1M | AISI 316L | 0.71 | |
| SeS03 | TA 5mM in KOH 0.1M | AISI 316L | 0.80 | |
| SeS04 | KOH 0.1 M | AISI 316L | 0.78 | |
| SeS01 | KOH 0.1 M | Ni on North Pole Disk Magnet | 0.76 | A |
| SeS02 | KOH 0.1 M | Ni on North Pole Disk Magnet | 0.76 | A |
| SeS03 | KOH 0.1 M | Ni on North Pole Disk Magnet | 0.72 | E |
| SeS04 | KOH 0.1 M | Ni on North Pole Disk Magnet | 0.72 | E |
| SeS05 | KOH 0.1 M | Ni on North Pole Disk Magnet | 0.71 | B |
| SeS06 | KOH 0.1 M | Ni on North Pole Disk Magnet | 0.71 | B |
| SeS01 | KOH 0.1 M | Ni on South Pole Disk Magnet | 0.75 | A |
| SeS02 | KOH 0.1 M | Ni on South Pole Disk Magnet | 0.75 | A |
| SeS03 | KOH 0.1 M | Ni on South Pole Disk Magnet | 0.73 | E |
| SeS04 | KOH 0.1 M | Ni on South Pole Disk Magnet | 0.74 | E |
| SeS05 | KOH 0.1 M | Ni on South Pole Disk Magnet | 0.72 | B |
| SeS06 | KOH 0.1 M | Ni on South Pole Disk Magnet | 0.71 | B |
| SeS01 | TA 0.5mM in KOH 0.1M | Ni on North Pole Disk Magnet | 0.75 | A |
| SeS02 | TA 0.5mM in KOH 0.1M | Ni on North Pole Disk Magnet | 0.75 | A |
| SeS05 | TA 0.5mM in KOH 0.1M | Ni on North Pole Disk Magnet | 0.70 | B |
| SeS06 | TA 0.5mM in KOH 0.1M | Ni on North Pole Disk Magnet | 0.70 | B |
| SeS07 | TA 0.5mM in KOH 0.1M | Ni on North Pole Disk Magnet | 0.66 | C |
| SeS08 | TA 0.5mM in KOH 0.1M | Ni on North Pole Disk Magnet | 0.66 | C |
| SeS09 | TA 0.5mM in KOH 0.1M | Ni on North Pole Disk Magnet | 0.63 | D |
| SeS10 | TA 0.5mM in KOH 0.1M | Ni on North Pole Disk Magnet | 0.63 | D |
| SeS01 | TA 0.5mM in KOH 0.1M | Ni on South Pole Disk Magnet | 0.75 | A |
| SeS02 | TA 0.5mM in KOH 0.1M | Ni on South Pole Disk Magnet | 0.75 | A |
| SeS05 | TA 0.5mM in KOH 0.1M | Ni on South Pole Disk Magnet | 0.71 | B |
| SeS06 | TA 0.5mM in KOH 0.1M | Ni on South Pole Disk Magnet | 0.71 | B |

| | | | | |
|---|---|---|---|---|
| SeS07 | TA 0.5mM in KOH 0.1M | Ni on South Pole Disk Magnet | 0.69 | C |
| SeS08 | TA 0.5mM in KOH 0.1M | Ni on South Pole Disk Magnet | 0.69 | C |
| SeS09 | TA 0.5mM in KOH 0.1M | Ni on South Pole Disk Magnet | 0.69 | |
| SeS01 | KOH 0.1 M | Ni on North Pole Disk Magnet | 0.76 | A |
| SeS02 | KOH 0.1 M | Ni on North Pole Disk Magnet | 0.75 | A |
| SeS03 | KOH 0.1 M | Ni on North Pole Disk Magnet | 0.71 | E |
| SeS04 | KOH 0.1 M | Ni on North Pole Disk Magnet | 0.71 | E |
| SeS05 | KOH 0.1 M | Ni on North Pole Disk Magnet | 0.70 | B |
| SeS06 | KOH 0.1 M | Ni on North Pole Disk Magnet | 0.70 | B |
| SeS01 | KOH 0.1 M | Ni on South Pole Disk Magnet | 0.76 | A |
| SeS02 | KOH 0.1 M | Ni on South Pole Disk Magnet | 0.76 | A |
| SeS03 | KOH 0.1 M | Ni on South Pole Disk Magnet | 0.76 | E |
| SeS04 | KOH 0.1 M | Ni on South Pole Disk Magnet | 0.75 | E |
| SeS05 | KOH 0.1 M | Ni on South Pole Disk Magnet | 0.76 | B |
| SeS06 | KOH 0.1 M | Ni on South Pole Disk Magnet | 0.78 | B |
| SeS01 | TA 0.5mM in KOH 0.1M | Ni on North Pole Disk Magnet | 0.75 | A |
| SeS02 | TA 0.5mM in KOH 0.1M | Ni on North Pole Disk Magnet | 0.75 | A |
| SeS05 | TA 0.5mM in KOH 0.1M | Ni on North Pole Disk Magnet | 0.70 | B |
| SeS06 | TA 0.5mM in KOH 0.1M | Ni on North Pole Disk Magnet | 0.70 | B |
| SeS07 | TA 0.5mM in KOH 0.1M | Ni on North Pole Disk Magnet | 0.67 | C |
| SeS08 | TA 0.5mM in KOH 0.1M | Ni on North Pole Disk Magnet | 0.67 | C |
| SeS09 | TA 0.5mM in KOH 0.1M | Ni on North Pole Disk Magnet | 0.63 | G |
| SeS10 | TA 0.5mM in KOH 0.1M | Ni on North Pole Disk Magnet | 0.64 | G |
| SeS01 | TA 0.5mM in KOH 0.1M | Ni on South Pole Disk Magnet | 0.76 | A |
| SeS02 | TA 0.5mM in KOH 0.1M | Ni on South Pole Disk Magnet | 0.76 | A |
| SeS05 | TA 0.5mM in KOH 0.1M | Ni on South Pole Disk Magnet | 0.73 | B |
| SeS06 | TA 0.5mM in KOH 0.1M | Ni on South Pole Disk Magnet | 0.73 | B |
| SeS07 | TA 0.5mM in KOH 0.1M | Ni on South Pole Disk Magnet | 0.70 | C |
| SeS08 | TA 0.5mM in KOH 0.1M | Ni on South Pole Disk Magnet | 0.70 | C |
| SeS09 | TA 0.5mM in KOH 0.1M | Ni on South Pole Disk Magnet | | |
| SeS01 | KOH 0.1 M | Ni on North Pole Disk Magnet | 0.76 | A |
| SeS01 | TA 0.5mM in KOH 0.1M | Ni on North Pole Disk Magnet | 0.75 | |
| SeS01 | TA 5mM in KOH 0.1M | Ni on North Pole Disk Magnet | 0.76 | |
| SeS05 | KOH 0.1 M | Ni on North Pole Disk Magnet | 0.70 | B |
| SeS05 | TA 0.5mM in KOH 0.1M | Ni on North Pole Disk Magnet | 0.70 | |
| SeS05 | TA 5mM in KOH 0.1M | Ni on North Pole Disk Magnet | 0.70 | |
| SeS01 | KOH 0.1 M | Ni on South Pole Disk Magnet | 0.76 | A |
| SeS01 | TA 0.5mM in KOH 0.1M | Ni on South Pole Disk Magnet | 0.76 | |
| SeS01 | TA 5mM in KOH 0.1M | Ni on South Pole Disk Magnet | 0.77 | |
| SeS05 | KOH 0.1 M | Ni on South Pole Disk Magnet | 0.71 | B |
| SeS05 | TA 0.5mM in KOH 0.1M | Ni on South Pole Disk Magnet | 0.72 | |
| SeS05 | TA 5mM in KOH 0.1M | Ni on South Pole Disk Magnet | 0.72 | |
| SeS01 | KOH 0.1 M | Ni on North Pole Parallelepiped Magnet | 0.75 | |
| SeS02 | KOH 0.1 M | Ni on North Pole Parallelepiped Magnet | 0.75 | |

| | | | | |
|---|---|---|---|---|
| SeS06 | KOH 0.1 M | Ni on North Pole Parallelepiped Magnet | 0.70 | |
| SeS01 | KOH 0.1 M | Ni on South Pole Parallelepiped Magnet | 0.75 | |
| SeS05 | KOH 0.1 M | Ni on South Pole Parallelepiped Magnet | 0.70 | |
| SeS01 | TA 0.5mM in KOH 0.1M | Ni on North Pole Parallelepiped Magnet | 0.75 | |
| SeS05 | TA 0.5mM in KOH 0.1M | Ni on North Pole Parallelepiped Magnet | 0.70 | |
| SeS07 | TA 0.5mM in KOH 0.1M | Ni on North Pole Parallelepiped Magnet | 0.66 | |
| SeS09 | TA 0.5mM in KOH 0.1M | Ni on North Pole Parallelepiped Magnet | 0.63 | |
| SeS01 | TA 0.5mM in KOH 0.1M | Ni on South Pole Parallelepiped Magnet | 0.75 | |
| SeS05 | TA 0.5mM in KOH 0.1M | Ni on South Pole Parallelepiped Magnet | 0.70 | |
| SeS07 | TA 0.5mM in KOH 0.1M | Ni on South Pole Parallelepiped Magnet | 0.67 | |
| SeS04 | TA 0.5mM in KOH 0.1M | AISI 316L | 0.71 | |
| SeS04 | TA 5mM in KOH 0.1M | AISI 316L | 0.81 | |
| SeS05 | KOH 0.1 M | AISI 316L | 0.77 | |
| SeS05 | TA 0.5mM in KOH 0.1M | AISI 316L | 0.70 | |
| SeS05 | TA 5mM in KOH 0.1M | AISI 316L | 0.80 | |
| SeS06 | KOH 0.1 M | AISI 316L | 0.76 | 2 |
| SeS06 | TA 0.5mM in KOH 0.1M | AISI 316L | 0.70 | 3 |
| SeS06 | TA 5mM in KOH 0.1M | AISI 316L | 0.76 | 2 |
| SeS07 | KOH 0.1 M | AISI 316L | 0.76 | |
| SeS07 | TA 0.5mM in KOH 0.1M | AISI 316L | 0.76 | 2 |
| SeS07 | TA 5mM in KOH 0.1M | AISI 316L | 0.76 | |
| SeS08 | KOH 0.1 M | AISI 316L | 0.74 | |
| SeS08 | TA 0.5mM in KOH 0.1M | AISI 316L | 0.76 | |
| SeS08 | TA 5mM in KOH 0.1M | AISI 316L | 0.74 | |
| SeS09 | KOH 0.1 M | AISI 316L | 0.73 | |
| SeS09 | TA 0.5mM in KOH 0.1M | AISI 316L | 0.72 | |
| SeS09 | TA 5mM in KOH 0.1M | AISI 316L | 0.73 | |
| SeS10 | KOH 0.1 M | AISI 316L | 0.73 | |
| SeS10 | TA 0.5mM in KOH 0.1M | AISI 316L | 0.71 | |
| SeS10 | TA 5mM in KOH 0.1M | AISI 316L | 0.72 | 3 |
| SeS11 | TA 5mM in KOH 0.1M | AISI 316L | 0.72 | |

***Table B2*** - *CV of Ni electrodeposited on both side of the magnet B88X0 of K&J Magnet Inc, used as WE. The table presents current peaks and related potential values, for both the electrolytes support tested. All the CVs are made with Ag/AgCl/KClsat as RE and Pt as CE, with a scan rate of 50 mV/s.*

| | NORTH POLE | | | |
|---|---|---|---|---|
| | L-(+)-Tartaric Acid 0.5 mM in KOH 0.1 M | | KOH 0.1 M | |
| Test Name | J Anodic [A] | E Anodic [V] | J Anodic [A] | E Anodic [V] |
| CV01_Scan1 | 6.958E-04 | 0.569 | 4.987E-04 | 0.522 |
| CV01_Scan3 | 6.177E-04 | 0.554 | 3.772E-04 | 0.510 |
| CV01_Scan5 | 6.055E-04 | 0.552 | 3.902E-04 | 0.513 |
| CV02_Scan1 | 6.815E-04 | 0.559 | 5.185E-04 | 0.532 |
| CV02_Scan3 | 6.378E-04 | 0.552 | 4.862E-04 | 0.522 |
| CV02_Scan5 | 6.412E-04 | 0.549 | 5.075E-04 | 0.522 |
| CV03_Scan1 | 7.251E-04 | 0.554 | 5.884E-04 | 0.535 |
| CV03_Scan3 | 6.744E-04 | 0.547 | 5.765E-04 | 0.527 |
| CV03_Scan5 | 6.784E-04 | 0.544 | 5.942E-04 | 0.527 |

| | SOUTH POLE | | | |
|---|---|---|---|---|
| | L-(+)-Tartaric Acid 0.5 mM in KOH 0.1 M | | KOH 0.1 M | |
| Test Name | J Anodic [A] | E Anodic [V] | J Anodic [A] | E Anodic [V] |
| CV01_Scan1 | 1.198E-03 | 0.574 | 9.909E-04 | 0.544 |
| CV01_Scan3 | 1.021E-03 | 0.552 | 8.646E-04 | 0.552 |
| CV01_Scan5 | 9.998E-04 | 0.549 | 8.804E-04 | 0.522 |
| CV02_Scan1 | 1.129E-03 | 0.559 | 9.518E-04 | 0.530 |
| CV02_Scan3 | 1.046E-03 | 0.549 | 9.210E-04 | 0.525 |
| CV02_Scan5 | 1.061E-03 | 0.547 | 9.439E-04 | 0.525 |
| CV03_Scan1 | 1.277E-03 | 0.556 | 1.031E-03 | 0.532 |
| CV03_Scan3 | 1.134E-03 | 0.547 | 9.952E-04 | 0.527 |
| CV03_Scan5 | 1.137E-03 | 0.547 | 1.013E-03 | 0.527 |

**Table B3** - CV of Ni electrodeposited on both side of the magnet B88X0 of K&J Magnet Inc, used as WE. The table presents current peaks and related potential values, for both the electrolytes support tested. All the CVs are made with Ag/AgCl/KCl$_{sat}$ as RE and Pt as CE, with a scan rate of 50 mV/s

| | NORTH POLE | | | |
|---|---|---|---|---|
| | L-(+)-Tartaric Acid 0.5 mM in KOH 0.1 M | | KOH 0.1 M | |
| Test Name | J Anodic [A] | E Anodic [V] | J Anodic [A] | E Anodic [V] |
| CV01_Scan1 | 6.485E-04 | 0.554 | 3.607E-04 | 0.525 |
| CV01_Scan3 | 5.655E-04 | 0.544 | 3.144E-04 | 0.513 |
| CV01_Scan5 | 5.490E-04 | 0.542 | 3.336E-04 | 0.513 |
| CV02_Scan1 | 6.259E-04 | 0.549 | 3.733E-04 | 0.518 |
| CV02_Scan3 | 5.740E-04 | 0.542 | 3.755E-04 | 0.515 |
| CV02_Scan5 | 5.820E-04 | 0.542 | 3.915E-04 | 0.515 |
| CV03_Scan1 | 6.482E-04 | 0.547 | 4.525E-04 | 0.518 |
| CV03_Scan3 | 6.046E-04 | 0.542 | 4.633E-04 | 0.518 |
| CV03_Scan5 | 6.043E-04 | 0.540 | 4.735E-04 | 0.518 |

| | SOUTH POLE | | | |
|---|---|---|---|---|
| | L-(+)-Tartaric Acid 0.5 mM in KOH 0.1 M | | KOH 0.1 M | |
| Test Name | J Anodic [A] | E Anodic [V] | J Anodic [A] | E Anodic [V] |
| CV01_Scan1 | 7.272E-04 | 0.570 | 4.802E-04 | 0.601 |
| CV01_Scan3 | 6.479E-04 | 0.559 | 4.060E-04 | 0.537 |
| CV01_Scan5 | 6.360E-04 | 0.557 | 4.263E-04 | 0.535 |
| CV02_Scan1 | 7.111E-04 | 0.566 | 5.008E-04 | 0.547 |
| CV02_Scan3 | 6.580E-04 | 0.562 | 4.668E-04 | 0.537 |
| CV02_Scan5 | 6.512E-04 | 0.559 | 4.792E-04 | 0.537 |
| CV03_Scan1 | 6.924E-04 | 0.564 | 5.222E-04 | 0.549 |
| CV03_Scan3 | 6.598E-04 | 0.559 | 5.136E-04 | 0.542 |
| CV03_Scan5 | 6.699E-04 | 0.559 | 5.261E-04 | 0.540 |

**Table B4** - CV of Ni electrodeposited on both side of the magnet B88X0 of K&J Magnet Inc, used as WE. The table presents current peaks and related potential values, for both the electrolytes support tested. All the CVs are made with Ag/AgCl/$KCl_{sat}$ as RE and Pt as CE, with a scan rate of 50 mV/s.

| | NORTH POLE | | | |
|---|---|---|---|---|
| | D-(-)-Tartaric Acid 0.5 mM in KOH 0.1 M | | KOH 0.1 M | |
| Test Name | J Anodic [A] | E Anodic [V] | J Anodic [A] | E Anodic [V] |
| CV01_Scan1 | 3.850E-04 | 0.600 | 2.606E-04 | 0.600 |
| CV01_Scan3 | 3.600E-04 | 0.600 | 2.306E-04 | 0.600 |
| CV01_Scan5 | 3.515E-04 | 0.600 | 2.297E-04 | 0.600 |
| CV02_Scan1 | 8.200E-04 | 0.700 | 5.441E-04 | 0.684 |
| CV02_Scan3 | 7.529E-04 | 0.688 | 5.270E-04 | 0.659 |
| CV02_Scan5 | 7.452E-04 | 0.686 | 5.487E-04 | 0.659 |
| CV03_Scan1 | 7.761E-04 | 0.688 | 5.875E-04 | 0.664 |
| CV03_Scan3 | 7.294E-04 | 0.686 | 5.481E-04 | 0.659 |
| CV03_Scan5 | 7.266E-04 | 0.688 | 5.518E-04 | 0.662 |

| | SOUTH POLE | | | |
|---|---|---|---|---|
| | D-(-)-Tartaric Acid 0.5 mM in KOH 0.1 M | | KOH 0.1 M | |
| Test Name | J Anodic [A] | E Anodic [V] | J Anodic [A] | E Anodic [V] |
| CV01_Scan1 | 3.852E-04 | 0.600 | 2.745E-04 | 0.600 |
| CV01_Scan3 | 2.962E-04 | 0.600 | 1.772E-04 | 0.600 |
| CV01_Scan5 | 2.776E-04 | 0.600 | 1.657E-04 | 0.600 |
| CV02_Scan1 | 5.728E-04 | 0.679 | 3.300E-04 | 0.675 |
| CV02_Scan3 | 5.231E-04 | 0.667 | 3.100E-04 | 0.649 |
| CV02_Scan5 | 5.188E-04 | 0.664 | 3.261E-04 | 0.647 |
| CV03_Scan1 | 6.137E-04 | 0.676 | 3.911E-04 | 0.657 |
| CV03_Scan3 | 5.515E-04 | 0.671 | 3.600E-04 | 0.649 |
| CV03_Scan5 | 5.527E-04 | 0.671 | 3.708E-04 | 0.652 |

**Table B5** - CV of Ni electrodeposited on both side of the magnet B88X0 of K&J Magnet Inc, used as WE. The table presents current peaks and related potential values, for both the electrolytes support tested. All the CVs are made with Ag/AgCl/KCl$_{sat}$ as RE and Pt as CE, with a scan rate of 50 mV/s.

| | NORTH POLE | | | |
|---|---|---|---|---|
| | D-(-)-Tartaric Acid 0.5 mM in KOH 0.1 M | | KOH 0.1 M | |
| Test Name | J Anodic [A] | E Anodic [V] | J Anodic [A] | E Anodic [V] |
| CV01_Scan1 | 5.066E-04 | 0.600 | 3.719E-04 | 0.574 |
| CV01_Scan3 | 4.323E-04 | 0.600 | 2.816E-04 | 0.562 |
| CV01_Scan5 | 4.153E-04 | 0.600 | 2.825E-04 | 0.564 |
| CV02_Scan1 | 7.373E-04 | 0.688 | 3.315E-04 | 0.669 |
| CV02_Scan3 | 6.662E-04 | 0.674 | 4.292E-04 | 0.654 |
| CV02_Scan5 | 6.560E-04 | 0.671 | 4.552E-04 | 0.654 |
| CV03_Scan1 | 6.897E-04 | 0.674 | 5.014E-04 | 0.659 |
| CV03_Scan3 | 6.323E-04 | 0.671 | 4.644E-04 | 0.657 |
| CV03_Scan5 | 6.299E-04 | 0.671 | 4.687E-04 | 0.657 |

| | SOUTH POLE | | | |
|---|---|---|---|---|
| | D-(-)-Tartaric Acid 0.5 mM in KOH 0.1 M | | KOH 0.1 M | |
| Test Name | J Anodic [A] | E Anodic [V] | J Anodic [A] | E Anodic [V] |
| CV01_Scan1 | 3.825E-04 | 0.600 | 2.703E-04 | 0.600 |
| CV01_Scan3 | 3.353E-04 | 0.600 | 1.794E-04 | 0.600 |
| CV01_Scan5 | 3.201E-04 | 0.600 | 1.694E-04 | 0.600 |
| CV02_Scan1 | 5.978E-04 | 0.674 | 3.315E-04 | 0.669 |
| CV02_Scan3 | 5.408E-04 | 0.659 | 3.409E-04 | 0.645 |
| CV02_Scan5 | 5.377E-04 | 0.659 | 3.409E-04 | 0.645 |
| CV03_Scan1 | 6.055E-04 | 0.667 | 3.849E-04 | 0.649 |
| CV03_Scan3 | 5.640E-04 | 0.664 | 3.798E-04 | 0.647 |
| CV03_Scan5 | 5.768E-04 | 0.664 | 4.044E-04 | 0.649 |

**Table B6** - Ratio of anodic current peaks during CVs of Ni electrodeposited on north and south pole of magnet B88X0 of K&J Magnetic, Inc used as WE with solution of 0.5 mM L-(+)-Tartaric Acid in KOH 0.1 M and KOH 0.1 M as electrolyte support. All the CV are run using Ag/AgCl/KCl$_{sat}$ as RE and Pt as CE, with a scan rate of 50 mV/s. Last column shows the result of the sign function of the difference between the two values in the associated row (North – South).

| | ANODIC CURRENT RATIO | | sgn ( $J_{ratio}$ North - $J_{ratio}$ South) |
|---|---|---|---|
| | $J_{ratio}$ North | $J_{ratio}$ South | |
| Test Name | $J_{Tart}$ / $J_{KOH}$ | $J_{Tart}$ / $J_{KOH}$ | |
| CV01_Scan1 | 1.798 | 1.514 | 1 |
| CV01_Scan3 | 1.799 | 1.596 | 1 |
| CV01_Scan5 | 1.646 | 1.492 | 1 |
| CV02_Scan1 | 1.677 | 1.420 | 1 |
| CV02_Scan3 | 1.529 | 1.410 | 1 |
| CV02_Scan5 | 1.487 | 1.359 | 1 |
| CV03_Scan1 | 1.432 | 1.326 | 1 |
| CV03_Scan3 | 1.305 | 1.285 | 1 |
| CV03_Scan5 | 1.276 | 1.273 | 1 |
| | | | |
| CV01_Scan1 | 1.798 | 1.514 | 1 |
| CV01_Scan3 | 1.799 | 1.596 | 1 |
| CV01_Scan5 | 1.646 | 1.492 | 1 |
| CV02_Scan1 | 1.677 | 1.420 | 1 |
| CV02_Scan3 | 1.529 | 1.410 | 1 |
| CV02_Scan5 | 1.487 | 1.359 | 1 |
| CV03_Scan1 | 1.432 | 1.326 | 1 |
| CV03_Scan3 | 1.305 | 1.285 | 1 |
| CV03_Scan5 | 1.276 | 1.273 | 1 |

**Table B7**- Ratio of anodic current peaks during CV of Ni electrodeposited on north and south pole of magnet B88X0 of K&J Magnetic, Inc used as WE with solution of 0.5 mM D-(-)-Tartaric Acid in KOH 0.1 M and KOH 0.1 M as electrolyte support. All the CV are run using Ag/AgCl/KClsat as RE and Pt as CE, with a scan rate of 50 mV/s. Last column shows the result of the sign function of the difference between the two values in the associated row (North – South).

| | ANODIC CURRENT RATIO | | sgn ( $J_{ratio}$ North - $J_{ratio}$ South) |
|---|---|---|---|
| | $J_{ratio}$ North | $J_{ratio}$ South | |
| Test Name | $J_{Tart}$ / $J_{KOH}$ | $J_{Tart}$ / $J_{KOH}$ | |
| CV01_Scan1 | 1.477 | 1.403 | 1 |
| CV01_Scan3 | 1.561 | 1.672 | -1 |
| CV01_Scan5 | 1.530 | 1.675 | -1 |
| CV02_Scan1 | 1.507 | 1.736 | -1 |
| CV02_Scan3 | 1.429 | 1.687 | -1 |
| CV02_Scan5 | 1.358 | 1.591 | -1 |
| CV03_Scan1 | 1.321 | 1.569 | -1 |
| CV03_Scan3 | 1.331 | 1.532 | -1 |
| CV03_Scan5 | 1.317 | 1.491 | -1 |
| | | | |
| CV01_Scan1 | 1.362 | 1.415 | -1 |
| CV01_Scan3 | 1.535 | 1.869 | -1 |
| CV01_Scan5 | 1.470 | 1.890 | -1 |
| CV02_Scan1 | 2.224 | 1.803 | 1 |
| CV02_Scan3 | 1.552 | 1.586 | -1 |
| CV02_Scan5 | 1.441 | 1.577 | -1 |
| CV03_Scan1 | 1.376 | 1.573 | -1 |
| CV03_Scan3 | 1.362 | 1.485 | -1 |
| CV03_Scan5 | 1.344 | 1.426 | -1 |

**Table B8** – Table of the values of spin polarization (SP%) of the current in the measurement made with L-(+)-tartaric acid. The values used to calculate SP% are the ones recorded and reported in tables **B2** and **B3** for what concerns the current peaks. Table **B6**, instead, reports the “anodic current ratio”.

| | ANODIC CURRENT RATIO | | Spin Polarization Percentage in L-(+)-tartaric acid |
|---|---|---|---|
| | North Pole | South Pole | |
| Test Name | $J_{Tart} / J_{KOH}$ | $J_{Tart} / J_{KOH}$ | $SP\% = \frac{\left(\frac{J(Tart)}{J(KOH)}\right)_{(North)} - \left(\frac{J(Tart)}{J(KOH)}\right)_{(South)}}{\left(\frac{J(Tart)}{J(KOH)}\right)_{(North)} + \left(\frac{J(Tart)}{J(KOH)}\right)_{(South)}}$ |
| CV01_Scan1 | 1.798 | 1.514 | 8.56% |
| CV01_Scan3 | 1.799 | 1.596 | 5.98% |
| CV01_Scan5 | 1.646 | 1.492 | 4.90% |
| CV02_Scan1 | 1.677 | 1.420 | 8.29% |
| CV02_Scan3 | 1.529 | 1.410 | 4.05% |
| CV02_Scan5 | 1.487 | 1.359 | 4.49% |
| CV03_Scan1 | 1.432 | 1.326 | 3.86% |
| CV03_Scan3 | 1.305 | 1.285 | 0.78% |
| CV03_Scan5 | 1.276 | 1.273 | 0.11% |
| | | | |
| CV01_Scan1 | 1.798 | 1.514 | 8.56% |
| CV01_Scan3 | 1.799 | 1.596 | 5.98% |
| CV01_Scan5 | 1.646 | 1.492 | 4.90% |
| CV02_Scan1 | 1.677 | 1.420 | 8.29% |
| CV02_Scan3 | 1.529 | 1.410 | 4.05% |
| CV02_Scan5 | 1.487 | 1.359 | 4.49% |

| | | | |
|---|---|---|---|
| CV03_Scan1 | 1.432 | 1.326 | 3.86% |
| CV03_Scan3 | 1.305 | 1.285 | 0.78% |
| CV03_Scan5 | 1.276 | 1.273 | 0.11% |

**Table B9** - Table of the values of spin polarization (SP%) of the current in the measurement made with D-(-)-tartaric acid. The values used to calculate SP% are the ones recorded and reported in Table 4SI and Table 5SI for what concerns the current peaks. Table 7SI, instead, reports the "anodic current ratio".

| | ANODIC CURRENT RATIO | | Spin Polarization Percentage in D-(-)-tartaric acid |
|---|---|---|---|
| | North Pole | South Pole | |
| Test Name | $J_{Tart}$ / $J_{KOH}$ | $J_{Tart}$ / $J_{KOH}$ | $SP\% = \dfrac{\left(\frac{J_{(Tart)}}{J_{(KOH)}}\right)_{(South)} - \left(\frac{J_{(Tart)}}{J_{(KOH)}}\right)_{(North)}}{\left(\frac{J_{(Tart)}}{J_{(KOH)}}\right)_{(North)} + \left(\frac{J_{(Tart)}}{J_{(KOH)}}\right)_{(South)}}$ |
| CV01_Scan1 | 1.362 | 1.415 | 1.90% |
| CV01_Scan3 | 1.535 | 1.869 | 9.81% |
| CV01_Scan5 | 1.470 | 1.890 | 12.49% |
| CV02_Scan1 | 2.224 | 1.803 | -10.45% |
| CV02_Scan3 | 1.552 | 1.586 | 1.09% |
| CV02_Scan5 | 1.441 | 1.577 | 4.51% |
| CV03_Scan1 | 1.376 | 1.573 | 6.70% |
| CV03_Scan3 | 1.362 | 1.485 | 4.34% |
| CV03_Scan5 | 1.344 | 1.426 | 2.97% |
| | | | |

| | | | |
|---|---|---|---|
| CV01_Scan1 | 1.477 | 1.403 | -2.57% |
| CV01_Scan3 | 1.561 | 1.672 | 3.42% |
| CV01_Scan5 | 1.530 | 1.675 | 4.53% |
| CV02_Scan1 | 1.507 | 1.736 | 7.05% |
| CV02_Scan3 | 1.429 | 1.687 | 8.30% |
| CV02_Scan5 | 1.358 | 1.591 | 7.89% |
| CV03_Scan1 | 1.321 | 1.569 | 8.59% |
| CV03_Scan3 | 1.331 | 1.532 | 7.03% |
| CV03_Scan5 | 1.317 | 1.491 | 6.19% |

# Appendix C: List of Abbreviations

| | |
|---|---|
| **DOS** | Density Of States |
| **TD** | Time-Dependent |
| **SRLTM** | Single Resonant Level Tunneling Model |
| **PES** | Potential Energy Surface |
| **CT** | Charge Transfer |
| **SS** | Solid-State |
| **DHO** | Displaced Harmonic Oscillator |
| **EGH** | Energy Gap Hamiltonian) |
| **FGR** | Fermi Golden Rule |
| **FC** | Frank-Condon |
| **HR** | Huang-Rhys |
| **FCWD** | Franck-Condon Weighted Density Of States |
| **S-FC** | (S)-(-)-N,N-Dimethyl-1-Ferrocenylethylamine |
| **R-FC** | (R)-(+)-N,N-Dimethyl-1-Ferrocenylethylamine |
| **SAM** | Self-Assembled Monolayer |
| **SDE** | Spin-Dependent Electrochemistry |
| **SDCR** | Spin-Dependent Charge Reorganization |
| **CW** | Clockwise |
| **ACW** | Anticlockwise |
| **TCR** | Temperature Coefficient of Resistance |
| **OECT** | Organic Electrochemical Transistor |
| **ECT** | Electrochemical Transistor |
| **OMIEC** | Organic Mixed Ionic-Electronic Conductors |
| **BEDT** | bis(ethylenedithio) |

| | |
|---|---|
| **eMChA** | Electrical MagnetoChiral Anisotropy |
| **1** | DM-BEDT-TTF = dimethyl-bis(ethylenedithio)-tetrathiafulvalene |
| **2** | TM-BEDT-TTF = tetramethyl-bis(ethylenedithio)-tetrathiafulvalene |
| **SEM** | Scanning Electron Microscope |
| **PANI** | Polyaniline |
| **cPANI** | Chiral Polyaniline |
| **SEC** | Spectroelectrochemistry |
| **HOMO** | Highest Occupied Molecular Orbital |
| **LUMO** | Lowest Unoccupied Molecular Orbital |
| **MO** | Molecular Orbital |
| **CISS** | Chiral Induced Spin Selectivity |
| **CV** | Cyclic Voltammetry |
| **WE** | Working Electrode |
| **CE** | Counter Electrode |
| **RE** | Reference Electrode |
| **2T3N** | N,N'-bis-[2,2';5',2″]tert-thiophene-5-yl methylcyclohexane-1,2-diamine |
| **BT2T4** | 2,2′-bis(2,2′-bithiophene-5-yl)-3,3′-bibenzothiophene |
| **OER** | Oxygen Evolution Reaction |
| **HER** | Hydrogen Evolution Reaction |
| **MIT** | Molecularly Imprinted Technique |
| **MRAM** | Magnetic Ransom Access Memory |
| **mc-AFM** | Magneto-conductive AFM |
| **SP** | Spin Polarization |
| **CMOF** | Chiral Metal-Organic Framework |
| **TTF** | Tetrathiafulvalene |
| **SDCR** | Spin-Dependent Charge Reorganization |
| **DHO** | Displaced Harmonic Oscillator |

| | |
|---|---|
| **EGH** | Energy Gap Hamiltonian |
| **HR** | Huang-Rhys factor |
| **FC** | Franck-Condon |
| **VdW** | Van der Waals |
| **VB** | Valence Band |
| **PECD** | PhotoElectron Circular Dichroism |
| **XPS** | X-ray Photoelectron Spectroscopy |
| **EDS** | Energy Dispersive X-ray Spectroscopy |